

Sheffield Hallam University

Investigation of Pretreatment Primer Performance by Electrochemical Techniques and Environmental Weathering

NGO, Son

Available from the Sheffield Hallam University Research Archive (SHURA) at:

<http://shura.shu.ac.uk/25600/>

A Sheffield Hallam University thesis

This thesis is protected by copyright which belongs to the author.

The content must not be changed in any way or sold commercially in any format or medium without the formal permission of the author.

When referring to this work, full bibliographic details including the author, title, awarding institution and date of the thesis must be given.

Please visit <http://shura.shu.ac.uk/25600/> and <http://shura.shu.ac.uk/information.html> for further details about copyright and re-use permissions.

**Investigation of Pretreatment Primer Performance by Electrochemical
Techniques and Environmental Weathering**

Son Ngo

A thesis submitted in partial fulfilment of the requirements of
Sheffield Hallam University
for the degree of Doctor of Philosophy

10 April 2019

Abstract

Four systems, based on a solventborne polyester/ melamine topcoat applied over one benchmark solventborne primer and three related experimental pretreatment primers, were exposed in natural and accelerated environments. Their performances were characterised by electrochemical impedance spectroscopy (EIS) and focused ion beam/scanning electron microscope (FIB/SEM) analysis to determine the extent and mode of corrosion.

The coatings performance were evaluated by measuring the impedance modulus $|Z|$, phase angles, the degree of blistering and analysis of exposed area. The solventborne primer performed excellently in natural and accelerated environments. However, non-pigmented waterborne pretreatment primer performed poorly in natural environment, but performed similarly to the two other waterborne pretreatment primers in accelerated tests. The two waterborne pretreatment primers containing anticorrosive pigments with and without conversion technology, show some improvement in the corrosion protection of hot dipped galvanised steel.

The performance of different coatings tested in electrochemical cells, neutral salt spray, humidity and under outdoor weathering conditions in Bohus Malmön, Sweden (BM) were characterised using EIS. Impedance modulus, $|Z|$, indicates the overall performance of the system, and phase angles were indicative of the presence of corrosion product. The total impedance was a good indicator in distinguishing the performance of different coatings. The other components in equivalent circuit models were also useful in determining the performance of coatings

FIB/SEM analysis developed in this project was found to be a useful technique to study cross-sections of pre-painted metal. Information from secondary and the backscatter electron images can reveal the thickness, the quality of the coating and specific areas of interest such as defects, contamination and corroded areas. EDS measures the distribution and quantitation of elements within coatings can also be studied.

FIB/SEM was found to correlate to EIS data and supports the work of other researchers whereby they used total impedance values to indicate the presence of corrosion underneath the coating. Corrosion starts at defects in the zinc layer, not necessarily at the zinc/ primer interface. Corrosion products were found to separate away from the zinc layer and not from the coating as previously understood for blisters and delaminated coatings.

Contents

Abstract	1
Contents.....	2
List of tables	20
Nomenclature	21
Candidate's Statement.....	26
Chapter 1. Introduction	27
1.1. Motivation.....	27
1.2. Aim	32
1.3. Objectives.....	32
Chapter 2. Literature review.....	34
2.1. Corrosion process	34
2.1.1. Definition of corrosion	34
2.1.2. Thermodynamics.....	35
2.1.3. The free energy and electrode potential relationship	36
2.1.4. Corrosion kinetics	37
2.1.5. Electrochemical processes	38
2.1.6. Types of corrosion	39
2.2. Corrosion of steel	39
2.3. Corrosion of Zn [2].....	40
2.4. Corrosion process on HDG steel.....	43
2.4.1. How does zinc protect steel from corrosion?	43
2.4.2. Atmospheric corrosion	44
2.4.3. Effects of corrodants	46
2.4.4. Corrosion products	46
2.5. Pretreatment	47
2.6. Purpose of organic coatings	49
2.6.1. Purpose of primers	49
2.6.2. Barrier properties of primers	50
2.6.3. Resistance to ionic current by organic coatings.....	51
2.6.4.1. Chromate pigments	52

2.6.4.2. Chromate-free pigments	54
2.7. Waterborne coatings	56
2.7.1. Waterborne acrylics	56
2.7.2. Film formation mechanisms	58
2.8. Failure mechanisms of coatings	62
2.8.1. Blistering	62
2.8.2. Delamination.....	65
2.9. Corrosion detection techniques	66
2.9.1 Accelerated and natural weathering tests	67
2.9.2 Electrochemical Impedance Spectroscopy (EIS) [95]	70
2.9.3. Focused ion beam/scanning electron microscope.....	86
Chapter 3. Methodology.....	91
3.1. Materials	91
3.1.1. Steel substrates.....	91
3.1.2. System information	91
3.1.3. Primer information	92
3.1.4. Topcoat.....	92
3.2. Cleaning of substrate	92
3.3. Paint application, panel preparation, and EIS cell constructions.	93
3.3.1. Paint application and panel preparation.	93
3.3.2. Preparation for EIS cells on panels.	94
3.3.3. Preparation for EIS cells on panels exposed in humidity and neutral salt spray chambers.	95
3.3.4. Preparation for EIS cells on panels exposed in Bohus Malmö.....	96
3.3.5. Degree of blistering assessment.....	97
3.4. EIS measurements of coated panels	99
3.4.1. EIS measurement of a dummy cell	99
3.4.2. EIS measurements of coated panels with cells.	99
3.4.3. EIS measurements of coated panels exposed in neutral salt spray and humidity chambers.....	100
3.4.4. EIS measurements of coated panels exposed in Bohus Malmö.....	101
3.4.5. Fitting of Nyquist and Bode spectra.....	102
3.5. FIB/SEM.....	104

3.5.1. Development of FIB/SEM technique to observe corroded coated panels .	104
3.5.1.1. Samples.....	104
3.5.1.2. FIB/SEM analysis	104
3.5.1.3. Elemental analysis.....	105
3.5.2. FIB/SEM technique used to observe corroded coated panels	106
3.5.2.1. Sample preparation.....	106
3.5.2.2. FIB/SEM.....	106
Chapter 4. Results & discussions	110
4.1. EIS measurements	110
4.1.1. Organic coatings	110
4.2. Panels exposed in accelerated weathering chambers and cells	113
4.2.1. EIS cell.....	113
4.2.1. Open circuit potential	113
4.2.1.2. Exposed panels characterised by EIS	115
4.2.1.3. Exposed panels assessed by visual inspection for degree of blistering.....	120
4.2.2. Neutral salt spray test.....	125
4.2.2.1. Open circuit potential	125
4.2.2.2. Panels exposed in NSS chamber and characterised by EIS.....	126
4.2.2.3. Exposed panels in NSS assessed by visual inspection for degree of blistering.....	130
4.2.3. Humidity test.....	135
4.2.3.1. Open circuit potential	135
4.2.3.2. Panels exposed in humidity chamber and characterised by EIS.....	136
4.2.3.3. Exposed panels in humidity assessed by visual inspection	140
4.3. Panels exposed in outdoor weathering	145
4.3.1. North facing panels characterised by EIS	145
4.3.2. North facing panels assessed by visual inspection for degree of blistering.....	147
4.3.3. South facing panels characterised by EIS	149
4.3.4. South facing panels assessed by visual inspection for degree of blistering.....	150
4.3.5. ECM of North & South facing panels exposed in Bohus Malmö.....	152

4.4. Summary of accelerated and outdoor weathering tests	155
4.5. Development of FIB/SEM technique to observe corroded coated panels	156
4.5.1. Results and discussion.....	156
4.5.5. Summary.....	166
4.6. Panels investigated by FIB/SEM analysis	167
4.6.1. Unexposed panels	167
4.6.1.1. Unexposed panel of system 1 (Solventborne primer with anti-corrosive pigment)	167
4.6.1.2. Unexposed panel of system 2 (Waterborne pretreatment primer with no anti-corrosive pigment)	170
4.6.1.3. Unexposed panel of system 3 (Waterborne pretreatment primer with anti-corrosive pigment)	172
4.6.1.4. Unexposed panel of system 4 (Waterborne pretreatment primer with anti-corrosive pigment and pretreatment technology)	175
4.6.2. Exposed panels.....	178
4.6.2.1. Exposed panels of system 1 (Solvent-borne primer with anti-corrosive pigment)	178
4.6.2.1.1. System 1 submerged in a cell from 0 to 1000 hours.	178
4.6.2.1.2. System 1 submerged in a cell for 408 hours.	179
4.6.2.1.3. System 1 submerged in a cell for 1000hours.	180
4.6.2.2. Exposed panels of System 2 (Waterborne pretreatment primer with no anti-corrosive pigment)	182
4.6.2.2.1. System 2 submerged in a cell from 0 to 1000 hours.	182
4.6.2.2.2. System 2 submerged in a cell for 192 hours.	183
4.6.2.2.3. System 2 submerged in a cell for 408 hours, area A.	185
4.6.2.2.4. System 2 submerged in a cell for 408 hours, area B.	188
4.6.2.2.5. System 2 submerged in a cell for 1000 hours.	191
4.6.2.3. Exposed panels of system 3 (Waterborne pretreatment primer with anti-corrosive pigment)	193
4.6.2.3.1. System 3 submerged in a cell from 0 to 1000 hours.	193
4.6.2.3.2. System 3 submerged in a cell for 192 hours.	194
4.6.2.3.3. System 3 submerged in a cell for 408 hours.	196
4.6.2.3.4. System 3 submerged in a cell for 1000 hours.	200

4.6.2.4. Exposed panels of system 4 (Waterborne pretreatment primer with anti-corrosive pigment and pretreatment technology)	204
4.6.2.4.1. System 4 submerged in a cell from 0 to 1000 hours.	204
4.6.2.4.2. System 4 submerged in a cell for 192 hours.	205
4.6.2.4.3. System 4 submerged in a cell for 408 hours.	206
4.6.2.4.4. System 4 submerged in a cell for 1000 hours.	210
4.6.2.4.5. Systems submerged in a cell up to 1000 hours.	213
4.7.1. Correlation of total impedance and corrosion products	214
4.7.1.1. Total impedance $>1 \times 10^8 \Omega \text{ cm}^2$ and the cross-sectioned area found. .	214
4.7.1.2. Total impedance $\sim 1 \times 10^7 \Omega \text{ cm}^2$ and the cross-sectioned area found. .	215
4.7.1.3. Total impedance $\sim 1 \times 10^6 \Omega \text{ cm}^2$ and the cross-sectioned area found. .	215
4.7.1.4. Total impedance $\sim 1 \times 10^5 \Omega \text{ cm}^2$ and the cross-sectioned area found. .	216
4.7.1.5. Total impedance $\sim 1 \times 10^4 \Omega \text{ cm}^2$ and the cross-sectioned area found. .	217
Chapter 5. Conclusions and future work.....	219
5.1. Conclusions	219
5.2. Further work.....	225
References	226
Word count	237
Appendix I – Supplementary information to chapter 4.6.1.....	238
Appendix II – Supplementary information to chapter 4.6.2.	240

List of figures

Figure 1. Photographs showing precoated metal in facade cladding of buildings [3].	27
Figure 2. Schematic diagram showing a typical coil coating line [5].....	28
Figure 3. Schematic diagram showing a typical hot dipped galvanised steel line [9].	29
Figure 4. Schematic diagram showing a roll coater coating the top and back side of the metal coil sheet [10].	29
Figure 5. Schematic diagram showing a standard coil coating system on HDG steel [11].....	30
Figure 6. Schematic diagram showing anodes and cathodes in dry (a) and wet (b) corrosion processes [17].....	34
Figure 7. Schematic diagram showing a thermodynamic energy profile for metals and their compounds [2].....	35
Figure 8. Schematic diagram showing the potential of Zn in distilled water as a function of pH adjusted by NaOH or HCl [2].	41
Figure 9. Schematic diagram showing the corrosion rate of Zn in distilled water as a function of pH (pH was adjusted with addition of NaOH or HCl) [19].	42
Figure 10. Schematic diagram showing the corrosion process of HDG steel [2].	43
Figure 11. Most common zinc corrosion products [23].....	44
Figure 12. Graph showing the resistance behaviour of coatings over time [39].....	51
Figure 13. Schematic diagram showing how chromates inhibit corrosion at the cut edge of a coated panel in near neutral and alkaline conditions by forming chromium (III) hydroxide [37].	52
Figure 14. Schematic diagram showing how chromates inhibit corrosion at the cut edge of a coated panel in acid conditions by dissolving to form dichromate ions and then reduce to Cr^{3+} ions. Cr^{3+} ions are transported to the metal surface to form chromium (III) hydroxide [37].	53
Figure 15. Schematic diagram showing how calcium ion exchange silica pigment inhibit corrosion at the cut edge of a coated panel [37] [65].....	55
Figure 16. Schematic diagram of a waterborne acrylic and solventborne polymers [66] [67].	56

Figure 17. Schematic diagram of the different stages in the film formation process for solventborne coating [68].	58
Figure 18. Schematic diagram showing the different stages in the film formation of waterborne coating [68].	60
Figure 19. Schematic diagram showing side chain and group movements [81].	61
Figure 20. Photograph and schematic diagram of blisters [84].	63
Figure 21. Schematic diagram showing an osmotic blistering process caused by contaminated substrate [42].	64
Figure 22. Schematic diagram of the blistering and delamination processes [89].	65
Figure 23. Photograph of filiform corrosion on a painted aluminium sample [90].	65
Figure 24. Schematic diagram of a cathodic delamination mechanism [91]. The anodic site is represented by the defect area on the left. The cathodic site is represented by the delaminated coating area in the middle.	66
Figure 25. Photograph of a typical salt spray chamber [92].	67
Figure 26. Photograph of a typical humidity chamber [94].	68
Figure 27. Photograph of Bohus Malmö exposure site with exposure racks at 45° South facing.	69
Figure 28. Photograph of Bohus Malmö exposure site with exposure rack at 90° North facing.	69
Figure 29. Schematic diagram showing the waveforms of the applied potential (E) and the response of the current in AC circuit.	70
Figure 30. Schematic diagram showing a vector in terms of one (X and Y coordinates), two (angle (θ) and magnitude ($ Z $) coordinates) and three (real (Z') and imaginary (Z'') coordinates).	71
Figure 31. Schematic diagram showing an equivalent circuit containing RC in series (a). Nyquist (b) and Bode (c) impedance plots of this circuit.	72
Figure 32. Schematic diagram showing coating physical properties circuit model of a perfect painted metal [97].	74
Figure 33. Schematic diagram showing an equivalent circuit containing RC in parallel (a). Nyquist (b) and Bode (c) impedance plots of this circuit.	75
Figure 34. Schematic diagram showing an equivalent electrical circuit model of metal/ solution interface (a) and its Nyquist (b) and Bode impedance (c) plots.	75

Figure 35. Schematic diagram showing coating physical properties circuit model of an intact painted metal [97].	76
Figure 36. Schematic diagram showing an example of a double layer [101].	77
Figure 37. Schematic diagram showing an equivalent electrical circuit model of painted metal/ solution interface with distinctive separation of the paint film and metal components (a), and its Nyquist (b) and Bode impedance (c) plots.	78
Figure 38. Schematic diagram showing an equivalent electrical circuit model of painted metal/ solution interface without distinctive separation of the paint film and metal components (a), and its Nyquist (b) and Bode impedance (c) plots.	79
Figure 39. Schematic diagram showing coating physical properties circuit model of degraded painted metal [97].	80
Figure 40. Schematic diagram showing an equivalent electrical circuit model of painted metal/ solution interface in the presence of diffusion (a) and the effect of varying diffusion coefficient on the curve shapes in Nyquist (b) and Bode impedance (c) plots.	81
Figure 41. EIS spectra of (a) Cr containing and (b) Cr-free coil coating systems.	83
Figure 42. EIS spectra obtained for an unstrained (a) and strained (b) coil coatings exposed for 50 days.	84
Figure 43. Schematic diagram showing typical components of a scanning electron microscope system [110].	86
Figure 44. Schematic showing spatial resolution of SEM sources [111].	87
Figure 45. Schematic diagram showing typical components of a focused ion beam system [110].	88
Figure 46. Photograph showing an FEI Quanta 3D FEG FIB/SEM system.	89
Figure 47. Schematic diagram showing a FIB/SEM system [118].	89
Figure 48. Photographs showing a stage with a sample (left) and chamber containing different sources (right).	89
Figure 49. Photograph showing a sample tilted at 53° for milling.	90
Figure 50. Photograph showing a cleaning tank with DI water collection.	93
Figure 51. Photograph showing a panel of system 1 with 3 cells.	94
Figure 52. Photographs showing system 1 panel of which one was unexposed (left) and the same one after exposure in humidity with a cell sealed with Blu Tack (right).	95

Figure 53. Photographs showing system 1 panels were unexposed (left) and the same one after exposure in neutral salt spray with a cell sealed with Blu Tack (right).	95
Figure 54. Photographs showing South (left) and North (right) facing panels of system 1.....	96
Figure 55. Illustration of blisters size 2 classification.	97
Figure 56. Illustration of blister size 5 classification.	98
Figure 57. Photograph showing a dummy cell with connection points for the different electrodes.	99
Figure 58. Photograph showing a classical three electrodes arrangement consisting of a saturated Calomel electrode (+0.242 V vs. SHE), a platinum counter electrode, and the testing sample as a working electrode.....	101
Figure 59. Schematic diagram showing an equivalent circuit model used for fitting. [107].....	102
Figure 60. Photograph showing a coated HDG steel sample mounted onto an SEM stub.....	106
Figure 61. FIB images showing sample deposited with Pt (left) and the same sample with a polygon shape on the surface to represent the milling area shown in yellow (right).	107
Figure 62. FIB image of sample after milling (left) and SEM image of the same sample after polishing (right).	107
Figure 63. SEM images of main cross-sectioned area (left) and topcoat/ primer interface (right). The boxes in white represented area of EDS analysis.	108
Figure 64. SEM images of primer/ zinc interface (left) and zinc/ steel interface (right). The boxes in white represented area of EDS analysis.	108
Figure 65. Q_f vs. time plots of systems measured at the start (a) and then 2 hours (b) later.	110
Figure 66. R_f vs. time plots of systems measured at the start (a) and 2 hours (b) later	111
Figure 67. $Z_{0.1Hz}$ vs. time plots of systems measured at the start (a) and 2 hours (b) later.	111
Figure 68. Open circuit potential (OCP) of 4 systems and HDG steels (untreated and pretreated with 1455T) submerged in cells over time.	113

Figure 69. Bode impedance modulus (a) and phase angle (b) plots of 4 systems (labelled as 1 to 4) submerged in cells tested for 1000 hours.	115
Figure 70. $Z_{0.1\text{Hz}}$ (a) and X_o (b) vs. time plots of systems submerged in cells.	117
Figure 71. Q_{pf} (a) and R_{pf} (b) vs. time plots of systems submerged in cells.	118
Figure 72. Q_d (a) and R_t (b) vs. time plots of systems submerged in cells.....	119
Figure 73. Photographs of triplets (a, b and c) of system 1 submerged in cells for 1000 hours.	120
Figure 74. Photographs of triplets (a, b and c) of system 2 submerged in cells for 1000 hours.	121
Figure 75 Enlarge photographs of S2A submerged in cell for 0, 408 and 1000 hours.	122
Figure 76. Photographs of triplets (a, b and c) of system 3 submerged in cells for 1000 hours	122
Figure 77. Photographs of triplets (a, b and c) of system 4 submerged in cell for 1000 hours.....	123
Figure 78. Degree of blistering vs. time plot of 4 systems submerged in cells for 1000 hours.	124
Figure 79. Open circuit potential of 4 systems tested in NSS chamber compared to HDG steels, untreated and treated with 1455T Cr-free pretreatment.	125
Figure 80. Bode impedance modulus (a) and phase angle (b) plots of 4 systems (labelled as 1 to 4) tested in a neutral salt spray chamber over time.	126
Figure 81. $Z_{0.1\text{Hz}}$ (a) and X_o (b) vs. time plots of systems exposed in NSS chamber.	128
Figure 82. Q_{pf} (a) and R_{pf} (b) vs. time plots of systems exposed in NSS chamber. .	129
Figure 83. Q_d (a) and R_t (b) vs. time plots of systems exposed in NSS chamber.....	129
Figure 84. Photographs of panels with 3 areas (a, b and c) of EIS measurements. System 1 was exposed in NSS chamber for 1000 hours and measured by EIS.	130
Figure 85. Photographs of panels with 3 areas (a, b and c) of EIS measurements. System 2 was exposed in NSS chamber for 1000 hours and measured by EIS.	131
Figure 86. Photographs of panels with 3 areas (a, b and c) of EIS measurements. System 3 was exposed in NSS chamber for 1000 hours and measured by EIS.	132
Figure 87. Photographs of panels with 3 areas (a, b and c) of EIS measurements. System 4 was exposed in NSS chamber for 1000 hours and measured by EIS.	133

Figure 88. Photographs of System 1 to 4 after 1000 hours of exposure in NSS.	133
Figure 89. Degree of blistering vs. time plot of 4 systems exposed in NSS cabinet for 1000 hours.	134
Figure 90. Open circuit potential of 4 systems tested in NSS over compared to HDG steels.	135
Figure 91. Bode impedance modulus (a) and phase angle (b) plots of 4 systems (labelled as 1 to 4) tested in a humidity chamber over time.	136
Figure 92. $Z_{0.1\text{Hz}}$ (a) and X_o (b) vs. time plots of systems exposed in humidity chamber.	138
Figure 93. Q_{pf} (a) and R_{pf} (b) vs. time plots of systems exposed in humidity chamber.	139
Figure 94. Q_d (a) and R_t (b) vs. time plots of systems exposed in humidity chamber.	139
Figure 95. Photographs of panels with 3 areas (a, b and c) of EIS measurements. System 1 was exposed in humidity chamber for 1000 hours and measured by EIS.	141
Figure 96. Photographs of panels with 3 areas (a, b and c) of EIS measurements. System 2 was exposed in humidity chamber for 1000 hours and measured by EIS.	141
Figure 97. Photographs of panels with 3 areas (a, b and c) of EIS measurements. System 3 was exposed in humidity chamber for 1000 hours and measured by EIS.	142
Figure 98. Photographs of panels with 3 areas (a, b and c) of EIS measurements. System 4 was exposed in humidity chamber for 1000 hours and measured by EIS.	143
Figure 99. Degree of blistering vs. time plot of 4 systems exposed in a humidity cabinet for 1000 hours.	144
Figure 100. Bode impedance modulus (a) & phase angle (b) plots of 4 systems (labelled as S1, S2, S3 and S4) exposed at 90° North facing in Bohus Malmö for 2 years.	145
Figure 101. Photographs of panels of 4 systems exposed at 90° North facing in Bohus Malmö for 2 years.	147

Figure 102. Degree of blistering vs. time plot of 4 systems exposed at 90° North facing in Bohus Malmön for 2 years.....	148
Figure 103. Bode impedance modulus (a) and phase angle (b) plots of 4 systems (labelled as S1, S2, S3 and S4) exposed at 45° South facing in Bohus Malmön for 2 years.	149
Figure 104. Photographs of panels of the 4 systems exposed at 45° South facing in Bohus Malmön for 2 years.	151
Figure 105. Degree of blistering vs. time plot of 4 systems exposed at 45° South facing in Bohus Malmön for 2 years.....	151
Figure 106. $Z_{0.1\text{Hz}}$ vs. time plots of 4 systems exposed at 90° North (a) and 45° South (b) facing in Bohus Malmön for 2 years.	152
Figure 107. X_o vs. time plots of 4 systems exposed at 90° North (a) and 45° South (b) facing in Bohus Malmön for 2 years.....	152
Figure 108. Q_{pf} vs. time plots of 4 systems exposed at 90° North (a) and 45° South (b) facing in Bohus Malmön for 2 years.	153
Figure 109. R_{pf} vs. time plots of 4 systems exposed at 90° North (a) and 45° South (b) facing in Bohus Malmön for 2 years.	153
Figure 110. Q_d vs. time plot of 4 systems exposed at 90° North (a) and 45° South (b) facing in Bohus Malmön for 2 years.....	154
Figure 111. R_t vs. time plot of 4 systems exposed at 90° North (a) and 45° South (b) facing in Bohus Malmön for 2 years.....	154
Figure 112. Schematic representation of sample position and beam geometry [121]. Sample stage at 52° so that the ion beam is 90° to the top surface of the sample (a).	156
Figure 113. Secondary electron SEM images of milled (a) and polished areas (b) at the centre of sample. The red box indicates the area where EDS elemental mapping was performed (See Fig. 117 for results)	157
Figure 114 EDS element map for carbon after polishing. Cross-section taken from sample centre. Illustration showing shadowing effect caused by the wall of the milled area.	158
Figure 115. Secondary electron SEM image of milled area (a). Backscattered electron (BSED) SEM image of milled area (b). Number annotations are described in	

the text. The white box indicates the area where EDS elemental mapping was performed. (See Fig. 119 for results)	159
Figure 116. EDS element map for carbon. Cross-section taken at sample edge. Illustration highlights the shadowing effect caused by the wall of the milled area (annotation 2).....	159
Figure 117. Ga ⁺ ion FIB image of edge of sample before milling (a). White annotation indicates milling location. Secondary electron SEM image of first milled area without polishing (b).	160
Figure 118. Ga ⁺ ion FIB image of edge of sample after first mill (a). White annotation indicates milling location. Secondary electron SEM image of cross-sectioned area after second mill (b).	161
Figure 119. Secondary electron (a) and backscattered SEM (b) images of cross-sectioned area after polishing. The red box indicates the area where EDS elemental mapping was performed (See Fig. 120-124 for results)	162
Figure 120. Secondary electron SEM image of polished area that was mapped using EDS analysis (See Fig. 124 for EDS analysis method development and Fig. 125 for all elements identified in this cross-section).	163
Figure 121. EDS carbon element maps acquired from area shown in Fig. 120 at 53.5° tilt (A), 60° tilt (B) and 60° tilt and -9° rotation (C). Illustrations show how the shadowing effect (marked 1 on map) was eliminated by changing the tilt and rotation.	163
Figure 122. EDS maps for elements identified in the cross-section shown in Fig. 121c. Differences between topcoat, primer and substrate can be observed.	164
Figure 123. EDS spectrum of a sample in Fig. 121c.	165
Figure 124. Semi-quantitative elemental results of sample in Fig. 121c. The statistical error, sigma quoted is less than 0.5 for all elements.	165
Figure 125. Secondary electron SEM images of an unexposed panel of system 1, area 1. Cross-sectioned area (A), topcoat/ primer/ zinc interface (B) and primer/ zinc interface (C).....	167
Figure 126. EDS spectra and mapping results of an unexposed panel of system 1 analysed from Fig. 125b.....	168
Figure 127. EDS mapping results of individual elements of an unexposed panel of system 1 analysed from Fig. 125b.	169

Figure 128. Secondary electron SEM images of an unexposed panel of system 2. Cross-sectioned area (A), topcoat/ primer/ zinc interface (B) and primer/ zinc interface (C). Red arrows represent the phase difference between topcoat and primer. A white square shows area of EDS analysis.	170
Figure 129. Secondary electron SEM image of an unexposed panel of system 2 that was mapped.	171
Figure 130. EDS spectrum of an unexposed panel of system 2 in Fig. 128.	172
Figure 131. Secondary electron SEM images of an unexposed panel of system 3, area 2. Cross-sectioned area (a), topcoat/ primer/ zinc area (b) and primer/ zinc area (c). A white square shows area of EDS analysis.	172
Figure 132. Secondary electron SEM image (a) and the results of EDS mapping (b) of an unexposed panel of system 3 from Fig. 131A.	173
Figure 133. EDS spectra of an unexposed panel of system 3 from Fig. 132 with 3 areas of analysis.	174
Figure 134. Secondary electron SEM images of an unexposed panel of system 4, area 2. Cross-sectioned area (a), topcoat/ primer/ zinc area (b) and primer/ zinc area (c). A red arrow represents the phase difference between the topcoat and primer. A white square shows area of EDS analysis.	175
Figure 135. Secondary electron SEM image (a) and the results of EDS mapping (b) of an unexposed panel of system 4 from Fig. 134a.	176
Figure 136. EDS spectra of an unexposed panel of system 4 from Fig. 135 with 3 locations of analysis.	177
Figure 137. Secondary electron & backscattered electron SEM images of unexposed and exposed panels of system 1 submerged in a cell for 0 hr (A), 408 hrs (B) and 1000 hrs, SE (C) and BSED (D) images. White squares show area of EDS analysis.	178
Figure 138. Secondary electron SEM image (a) and the results of EDS mapping (b) of an exposed panel of system 1 submerged in a cell for 408 hours from Fig. 137b.	179
Figure 139. EDS spectra of an exposed panel of system 1 submerged in a cell 408 hours from Fig. 138 with 2 areas of analysis.	180
Figure 140. Secondary electron SEM image of an exposed panel of system 1 submerged in a cell for 1000 hours.	181

Figure 141. EDS spectra of an exposed panel of system1 submerged in a cell for 1000 hours. Spectrum 3 and 4 are the results of areas located in Fig. 140.	181
Figure 142. Secondary electron SEM images of unexposed and exposed panels of system 2 submerged in a cell for 0 hr (A), 192 hrs (B), 408 hrs (C) and 1000 hrs (D).	182
Figure 143. Secondary (a & c) & backscattered (b) electron images of an exposed panel of system 2 submerged in a cell for 192 hours. Cross-sectioned area with 2 white squares (a) zoom in area 1 (b) and zoom in area 2 (c).	183
Figure 144. Secondary electron SEM image (image 11) of the areas that were analysed. The result is shown in Fig. 147.	184
Figure 145. EDS spectrum of an exposed panel of system 2 submerged in a cell for 192 hours.	185
Figure 146. A panel of system 2 submerged in a cell for 408 hours.	185
Figure 147. Secondary electron SEM images of a cross-section at edge of a blister, located in Fig. 146a.	186
Figure 148. Secondary electron SEM image (a) and the results of EDS mapping (b) of a cross-sectioned area.	187
Figure 149. EDS spectra (map and spectrum 9) of Fig. 148.	188
Figure 150. Secondary electron SEM images of a cross-section area closed to a blister, located in Fig. 146b. Cross-sectioned area (A), defected area in the zinc layer (B) and primer/zinc interface (C)	189
Figure 151. Secondary electron SEM image of areas going to be analysed using point & ID EDS analysis.	190
Figure 152. EDS spectra of areas 8 and 13 in Fig. 151.	190
Figure 153. Secondary electron SEM image of an exposed panel of system 2 submerged in a cell for 1000 hours. Cross-section of milled area (A), topcoat/ primer area (B) and topcoat/ primer/ zinc area (C).	191
Figure 154. Secondary electron SEM images of unexposed and exposed panels of system 3 submerged in a cell for 0 hr (A), 192 hrs (B), 408 hrs (C) and 1000 hrs (D).	193
Figure 155. Secondary (A) & backscattered electron (B & C) SEM images of an exposed panel of system 3 submerged in a cell for 192 hours. Cross-section of milled	

area (A), primer/ zinc interface (B) and another example of primer/ zinc interface (C).	194
Figure 156. Secondary electron SEM image of areas was analysed using point & ID EDS analysis.....	195
Figure 157. EDS spectra of spectrum 5 and 6 in Fig. 156.	196
Figure 158. Secondary (A & C) & BSED (B) SEM images of an exposed panel of system 3 submerged in a cell for 408hrs. Cross-section of milled area (A), BSED image of primer/ zinc area (B) and SE image of primer/ zinc area (C).	197
Figure 159. Secondary electron SEM image (left) and the results of EDS mapping (right).	198
Figure 160. EDS spectra of maps 30 and 31 from Fig. 161.	198
Figure 161. Secondary electron SEM image (a) and the results of EDS mapping (b).	199
Figure 162. EDS spectra of maps 2 and 8 from Fig. 163.....	200
Figure 163. Secondary electron SEM images of an exposed panel of system 3 submerged in a cell for 1000hrs. Cross-section of milled area (A), topcoat/ primer interface (B) and primer/ zinc interface (C).	201
Figure 164. EDS mapping results of area of primer and zinc region in Fig. 163...	202
Figure 165. EDS line scan results of area of primer/ zinc interface in Fig. 163.	203
Figure 166. Secondary electron SEM images of unexposed and exposed panels of system 4 submerged in a cell for 0 hr (A), 192 hrs (B), 408 hrs (C) and 1000 hrs (D).	204
Figure 167. Secondary (a & c) & backscattered (b) electron SEM images of an exposed panel of system 4 submerged in a cell for 192 hrs. Cross-section of milled area (a), topcoat/ primer/ zinc area (b) and topcoat/ primer/ zinc area (c).	205
Figure 168. Secondary (A & C) & backscattered (B) electron SEM images of an exposed panel of system 4 submerged in a cell for 408hrs. Cross-section of milled area (A), primer/ zinc interface (B) and primer/ zinc interface (C).	207
Figure 169. Secondary electron SEM image (A) and the results of EDS mapping (B) of that image.	208
Figure 170. EDS spectra of maps 1, 2, and 3 from Fig. 169.	209

Figure 171. Secondary electron SEM images of an exposed panel of system 4 submerged in a cell for 1000 hrs. Cross-section of delaminated area (a), topcoat/ primer interface (b) and delamination of zinc interface (c).	210
Figure 172. EDS mapping results of delaminated area.....	211
Figure 173. Secondary electron SEM image of delaminated area analysed by point and ID.....	212
Figure 174. EDS spectrum of area 14 from Fig. 175.....	212
Figure 175. Secondary electron SEM images of exposed panel of systems 1 to 4.	213
Figure 176. Bode impedance modulus (A) & Nyquist (B) plots of total impedance of $>1 \times 10^8 \Omega \text{ cm}^2$ and the cross-sectioned area observed for system 1 (C).....	214
Figure 177. Bode impedance modulus (A) & Nyquist (B) plots of total impedance of $\sim 1 \times 10^7 \Omega \text{ cm}^2$ and the cross-sectioned area observed (C).....	215
Figure 178. Modulus Bode (A) & Nyquist (B) plots of total impedance of $\sim 1 \times 10^6 \Omega \text{ cm}^2$ and the cross-sectioned area observed (C).	216
Figure 179. Modulus Bode (A) & Nyquist (B) plots of total impedance of $\sim 1 \times 10^5 \Omega \text{ cm}^2$ and the cross-section area observed (C).....	216
Figure 180. Modulus Bode (A) & Nyquist (B) plots of total impedance of $\sim 1 \times 10^4 \Omega \text{ cm}^2$ and the cross-sectioned area observed (C).	217
Figure 181. Secondary electron SEM images of an unexposed panel of system 1, area 2. Cross-section area (a), topcoat/ primer/ zinc area (b) and primer/ zinc area (c).	238
Figure 182. Secondary electron SEM images of an unexposed panel of system 2. Cross-section area (a) , topcoat/ primer/ zinc area (b) and primer/ zinc area (c). A red arrow represents the phase differene between topcoat and primer.	238
Figure 183. Secondary electron & back scattered electron SEM images of an unexposed panel of system 3, area1. Cross-section area (a), topcoat/ primer/ zinc area (b) and primer/ zinc area (c). A red arrow represents the phase differene between topcoat and primer.	239
Figure 184. Secondary electron SEM images of an unexposed panel of system 4, area 1. Cross-section area (a), topcoat/ primer/ zinc interface (b) and primer/ zinc interface (c). Red arrow pointing towards the phase difference between topcoat and primer.	239

Figure 185. Secondary electron images of an exposed panel of system 2 submerged in a cell for 408 hours. A blister in the centre of image (a), cross-section of a blister in A (b) and zoom in corroded area in B (c).	240
Figure 186. Secondary electron SEM image (left) and the results of EDS mapping (right) of an exposed panel of system 2 submerged in a cell for 408 hours. Results are shown in Fig. 187.....	241
Figure 187. EDS spectra of an exposed panel from Fig. 186.....	242
Figure 188. Secondary (a & c) & backscattered (b) electron SEM images of an exposed panel of system 2 submerged in a cell for 408 hours, area 2. Cross-sectioned area (a), BSED image of zoom in area (b) and SE image of zoom in area (c).....	243
Figure 189. Secondary electron SEM image showing areas that was mapped.	244
Figure 190. EDS spectra of analysed areas in Fig. 189.	244
Figure 191. Secondary electron SEM image of system 2 submerged in a cell for 408 hours.....	245
Figure 192. EDS line scan 2 of Fig. 191.	245
Figure 193. Secondary (a & c) & backscattered electron (b) SEM images of an exposed panel of system 3 submerged in a cell for 408 hrs. Cross-section of milled area (a), primer/ zinc interface (b) and another example of primer/ zinc interface (c).	246
Figure 194. Secondary electron SEM images of an exposed panel of system 4 submerged in a cell for 408 hrs. Cross-section of milled area (a), topcoat/ primer/ zinc interface (b) and primer/ zinc interface (c).	247
Figure 195. Secondary electron SEM image of primer and zinc area that was mapped at the primer/ zinc interface.....	248
Figure 196. EDS spectrum results at the primer/ zinc interface of Fig. 195.....	248

List of tables

Table 1. Types of corrosion [17].	39
Table 2. Typical monomers used in polymerisation of waterborne acrylic [68].....	57
Table 3. Information of the 4 systems.	91
Table 4. Composition of the 4 primers.	92
Table 5. The mean, standard error, and % RSE of Q_f component of the 4 systems at the start (a) and then 2 hours after (b).	110
Table 6. The mean, standard error, and % RSE of R_f component of the 4 systems at the start (a) and 2 hours after (b).	111
Table 7. The mean, standard error and % RSE of $Z_{0.1Hz}$ of 4 systems at the start (a) and 2 hours after (b).	112
Table 8. Summary of accelerated and outdoor weathering tests characterised by EIS and assessed by degree of blistering.	155

Nomenclature

Abbreviations

%RSE: Percentage relative standard error

2D: 2 dimensional

3D: 3 dimensional

AC: Alternating current

ASTM: American society for testing and materials

BM-N: Bohus Malmön North facing

BM-S: Bohus Malmön South facing

BS: British standard

C_R : Corrosion rate

DC: Direct current

DMA: Dynamic mechanical analysis

DSC: Differential scanning calorimetry

ECM: Equivalent circuit models

ECN: Electrochemical noise

EDS: Energy dispersive X-ray spectroscopy

EIS: Electrochemical impedance spectroscopy

EN: Norme Europeenne/ Europäische Norm (European standard)

FIB/SEM: Focused ion beam/scanning electron microscope

h: Hour

HDG: Hot dipped galvanised (steel)

ISO: International organisation for standardisation

MFFT: Minimum film formation temperature

OCP: Open circuit potential

PET: Polyethylene terephthalate

pH: Power of hydrogen
PMT: Peak metal temperature
PVC: Polyvinylchloride
PVdF: Polyvinylidene fluoride
RSE: Relative standard error
Rms: Root mean square
SHE: Standard hydrogen electrode
SDC: Scanning droplet cell
SKP: Scanning Kelvin probe
SVET: Scanning vibrating electrode technique
TEM: Transmission electron microscopy
TMA: Thermomechanical analysis
Tg: Glass transition temperature
Yr: Year

Greek alphabet

μm : micrometre
 μS : microsiemens
 ΔG^* : Activation energy
 ΔG : Net change of energy in a reaction
 ΔG° : Change in free energy
 ϵ_0 : Electrical permittivity
 ϵ_r : Relative electrical permittivity
 θ : Angle
 θ : Phase angle
 ρA : picoampere

σ : Warburg impedance coefficient

$\Omega \text{ cm}^2$: Ohm square centimetre

ω : Angular frequency

Latin alphabet

A: Surface of one plate or sample

A: Undefined constant

A_s : Exposed area

A_w : Metal molar mass

C: Capacitor

C_d : Double layer capacitance

C_f : Film capacitance

$C_{m,0}$: Measured capacitance at zero time

C_m : Measured capacitance at any time t

CPE: Constant phase element

d: Distance between two plates or coating thickness

dm/dt: Rate of mass loss

e: Electron

E: Potential

E°_{cell} : Standard electrode potential

F: Faraday

F: Faraday's constant

f: Frequency

g/m^2 : Gram per square metre

I: Current

i_{corr} : Corrosion current density

I' : Real coordinate

I'' : Imaginary coordinate

J: Imaginary unit

K_{corr} : Rate of corrosion

KeV: Photon energy

kV: Kilovolt

M(s): Metal

m/min: Metre per minute

M^{2+} : Metal ions

n: An exponent which equals 1 for an ideal capacitor

n: Number of moles of electrons transferred in the cell reaction per mole of product

nA: nanoampere

nm: nanometre

$^{\circ}\text{C}$: Degree Celsius

p: Metal density

Q_d : Constant phase element of dual layer capacitance

Q_f : Constant phase element of film capacitance

R: Resistor

R: Universal gas constant

R_t : Charge transfer resistance

R_f : Film resistance

T: Absolute temperature

$\tan \theta$: Phase angle

T_{β} : Beta transition

T_{γ} : Gamma transition

wt%: Weight percentage

X_v : Percentage of water absorbed in an organic coating

Z : Alternating current impedance

$Z_{0.1\text{Hz}}$: Total or maximum impedance

Candidate's Statement

My main objectives were to gain scientific knowledge and understanding in the field of corrosion protection of precoated HDG steel. To develop and understand EIS and FIB/SEM so that corrosion process can be investigated. To use my existing skills from industry and develop into academia. To be able to plan and manage a project.

First, I would like to thank my partner Julie Hiley for the support, help and encouragement in completing this PhD project. Especially the time she helped and supported me to look after my father.

Second, I would like to thank my industrial supervisor and manager Dr Chris Lowe for his continuous guidance and support throughout this project for 7 long years. Included in this is Becker Industrial Coating for the time, financial support and the use of equipment.

Third, I would like to thank my university supervisor Dr Oliver Lewis and Dr David Greenfield for their continuous guidance and support throughout this project. Included in this is staff from MERI department for their help and advice during the time I attended the university. Particularly the help from Stuart Creasey in the use of FIB/SEM.

Fourth, I would like to thank all my colleagues at Becker Industrial Coatings in the support and advice throughout this project. Also having the patience and time to listen to my work and personal issues.

Finally, I would like to thank all the people who have not contributed much but listen and support me throughout this project.

Chapter 1. Introduction

1.1. Motivation

Metals have been used by the engineering and construction industries for hundreds of years. One of the problems of using metals is their tendency to corrode, particularly ferrous metals, including steel. The corrosion mechanisms of metals have been extensively studied for more than 150 years [1]. They occur naturally and involve an electrochemical process in which a metal reacts with its environment to form oxides or other compounds. The process requires an electrochemical cell which has four essential constituents: an anode, a cathode, an electrolyte (which is an electrically conducting solution), and an electrical connection. The result of the electrochemical reaction is metal loss [2].

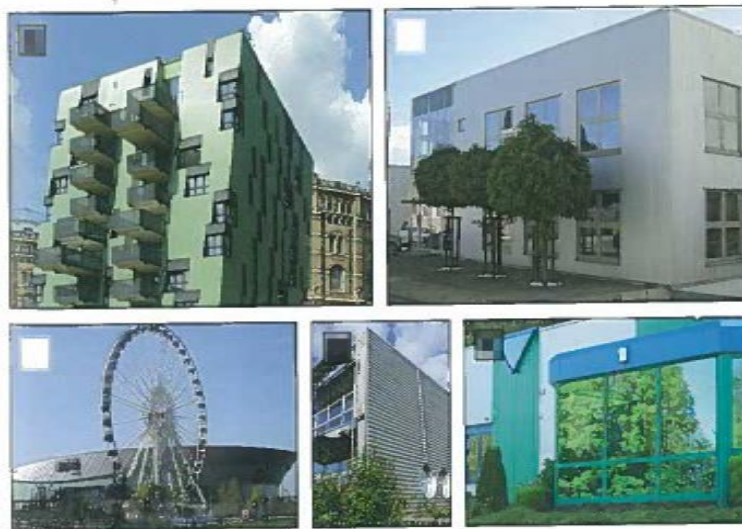


Figure 1. Photographs showing pre-coated metal in facade cladding of buildings [3].

Coated metal panels are used on the facades and roofs of many buildings (See Fig. 1). The paints are normally used for both aesthetic purposes and to protect metal surfaces from corrosion. They are cheap to produce and easy to apply onto different metal substrates. They are made from five main components, which are binder, solvents, pigments and fillers, and additives. The binder is the film forming component and gives the basic physical and chemical properties of the paint. The solvents are used to dissolve the binder and disperse the other constituents in the formulation. They allow the viscosity to be controlled and enable the paints to be applied. The colour pigments, non-soluble particles, are used to enhance the paints, most providing colour,

but some inhibit corrosion. Fillers such barium sulphate and calcium carbonate are added to reduce the cost of the paints and improve certain properties such as hardness. Finally additives are added in small quantities into the paint to enhance certain properties.

Paints are used to precoat metal strips on coil coating lines. The first coil coating line was developed in the mid 1930's to coat Venetian blind slats [4]. It is a continuous process whereby production costs are cut to a minimum and environmental impact [4] is reduced compared to post painting processes.

Today, coil coating lines are highly automated, operating at very high speed (100-180 m/min.). The technology is known as 'pre-finishing' [4]. A coil line consists of many stages (See Fig. 2) .First the metal coil, commonly hot dip galvanised (HDG) steel or aluminium is unwound, cleaned, and degreased with alkaline based cleaners.

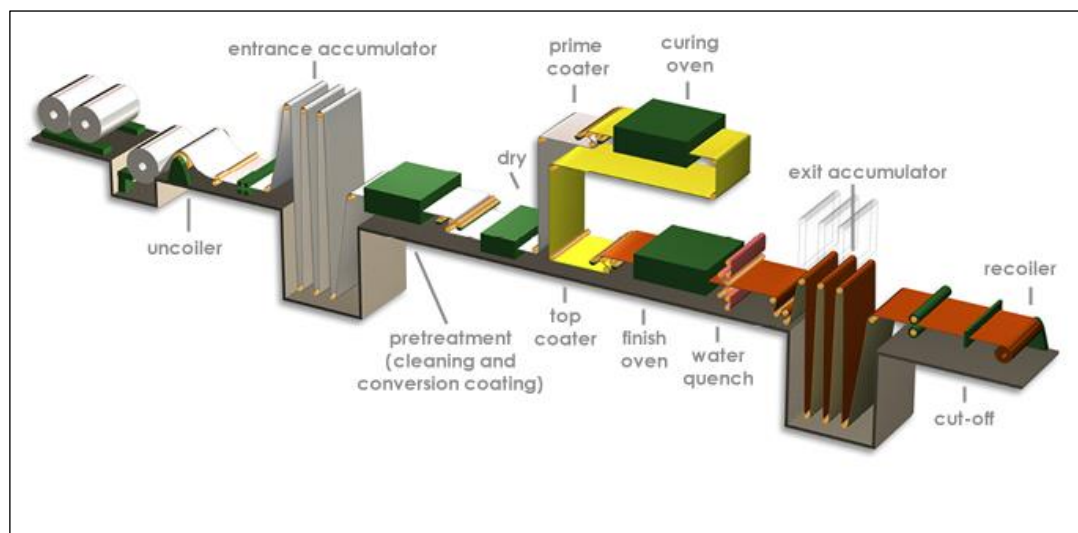


Figure 2. Schematic diagram showing a typical coil coating line [5].

The HDG steel is produced on a galvanising line by dipping the steel strip into molten zinc bath at 450 °C (See Fig. 3). The zinc forms a good metallurgical bond with the steel. A small amount of aluminium (0.1 - 0.3 % wt.) is added to the zinc bath to suppress the growth of brittle intermetallic phases of Fe-Zn at the steel/ zinc interface [6]. The Al addition improves the adhesion of zinc to the steel by producing an inhibition layer of $Fe_2Al_5(Zn)$ 50 nm thick [7]. The thickness of the zinc is controlled by air knives. Lower zinc thicknesses are used for less severe environments

because the thickness has an effect on the protection of the steel [8]. A zinc coat weight of 275 g/m^2 , equivalent to $20 \text{ }\mu\text{m}$ on both sides of the strip is normally used for exterior applications.

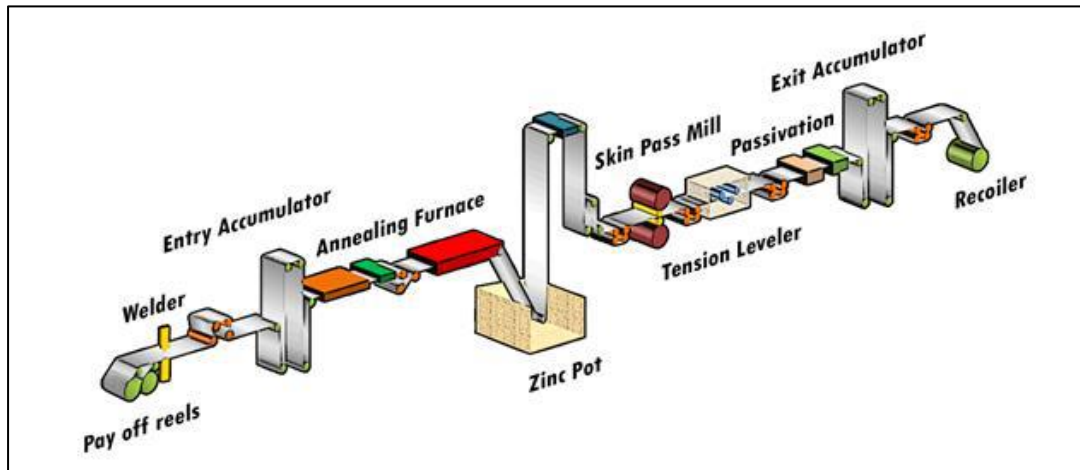


Figure 3. Schematic diagram showing a typical hot dipped galvanised steel line [9].

The metal is normally cleaned with an alkaline solution so that impurities and inert aluminium oxide are removed [6] [8]. It is then pretreated with a chromate or chromate-free conversion coating by immersion, spray, squeegee rolls or, the most common, a roll coater. The pretreatment helps the solvent based primer to adhere to the substrate.

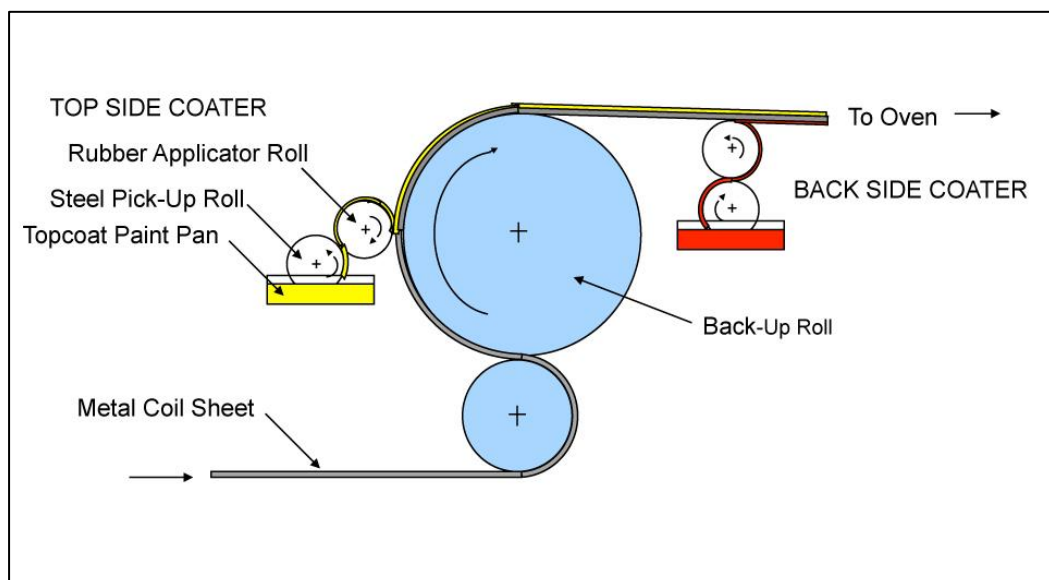


Figure 4. Schematic diagram showing a roll coater coating the top and back side of the metal coil sheet [10].

A roll coater is used to apply the primer onto the metal (See Fig. 4) which is cured in an oven, generally for around 30 seconds, at a peak metal temperature (PMT) of between 216 to 232 °C. The primed surface is then overcoated with a topcoat and also cured in an oven generally for around 30 seconds but this time at a PMT of between 216 to 250 °C. The process occurs concurrently on both sides of the metal strip.

Primers are used to protect the steel or aluminium from corrosion where adhesion and anticorrosive performance are the essential properties. The topcoat provides the final aesthetic appearance, mechanical, and durability performance of a coil coated product [4].

The paints are typically solvent based, thermosetting systems dominated mainly by polyester resins cured with either an alkoxy methyl melamine crosslinker or one based on an isocyanate [8]. They have a market share of around 83% in Europe and can be tailored to the end-user requirements very easily [8]. Polyvinylchloride (PVC) plastisol and polyvinylidene fluoride (PVdF) take second and third place respectively [8]. PVC plastisol and PVdF are mainly based on thermoplastic systems and have a market share of around 14%. Epoxies, acrylics, silicone-modified polyesters, and alkyds cover the rest of the 3% market share [8].

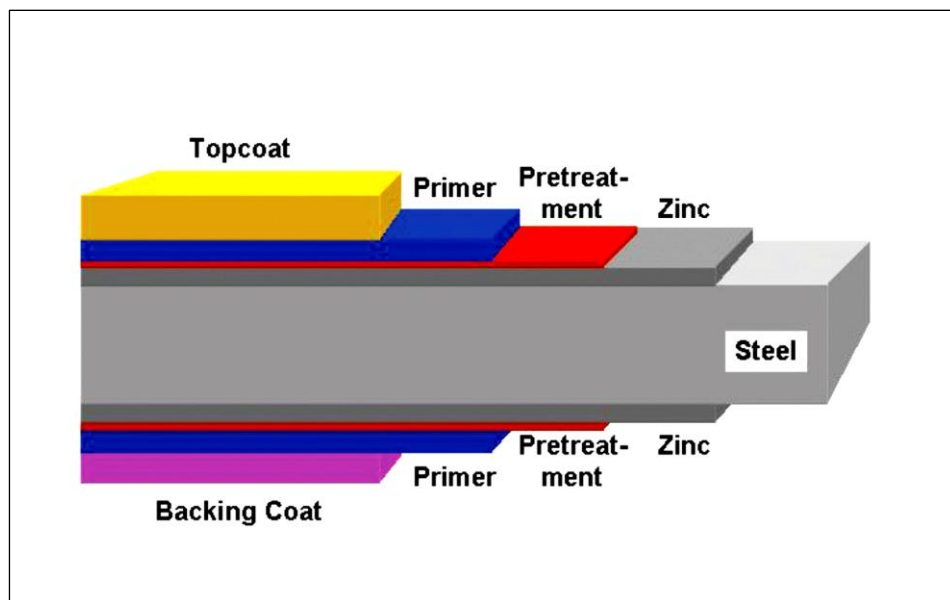


Figure 5. Schematic diagram showing a standard coil coating system on HDG steel

Following the cure of the topcoat, the painted metal is then quenched with water, cooled, and rewound into another coil. The coated metal coil is normally formed before shearing for use as roofing or facades for the construction industry or for carcasses of domestic appliances. About 70% of coil products are used for buildings [4]. The coatings provided excellent protection from the environment for a long period of time with a less than 0.5% failure rate [12] of which 75% is linked to corrosion, especially the edge areas of cut sheets [13]. Most exterior products are coated with a 20-25 μm topcoat, 5-8 μm primer, and sub-micrometres layer of pretreatment (See Fig. 5). The rest of the coil products are for automotive, appliance, furniture, and other applications.

The corrosion performance of coil coated products is commonly evaluated by accelerated laboratory tests. Neutral salt spray (ASTM B117-09) and humidity (BS3900 Part F2: 1973) tests are widely used by the industry to predict the lifetime of the products intended for exterior applications. Although the correlation between the accelerated tests and natural exposures is poor [14] [15], many architects, and builders like the tests due to lengthy historical experience of how precoated metal performs in them. The tests are embedded in internal documents, procedures, and specifications.

In the last few years, the industry has move towards cyclic tests (ASTM G85-96 and ASTM D5894-96) so that actual environmental conditions can be more closely replicated. These tests involve a series of wet and dry cycles, and some have additional exposure conditions such as heat, humidity, and ultraviolet light. In short term testing, cyclic tests generally have reasonably good correlation with natural weathering tests [16].

Established products normally consist of hot dip galvanised steel coated with a pretreatment, a primer, and a topcoat. Coating companies are increasingly interested in adopting a pretreatment primer: pretreatments that can also act as primers - in order to cut costs by eliminating a process and reducing emissions and effluents [8]. It allows also for existing coil lines to have the ability to add an extra coat to the layers when the pretreatment stage is used to run a pretreatment primer. Then the primer stage can be replaced with a basecoat or topcoat [8], or the topcoat stage can be replaced with a clear coat, or other functional coating [8].

Beckers has tried to develop a pretreatment primer for a number of years and has achieved the very stringent customer specifications of fast curing and being solvent free, but corrosion performance has been variable. A range of waterborne chemistries such as epoxies, polyurethane dispersions, phenolics, and acrylics have been evaluated. Problems of removing water, poor mechanical properties and more recently, corrosion resistance were faced but the root causes of these problems are not known. Film formation, surfactant, adhesion, and others may be the cause.

1.2. Aim

The aim of this project was to gain knowledge and understanding of the corrosion mechanisms of coil coated products that utilised a novel waterborne pretreatment primer using electrochemical impedance spectroscopy and focused ion beam/scanning electron microscope.

The project will focus on a range of related experimental coatings compared to a benchmark product and how they protect hot dipped galvanised (HDG) steel in accelerated and outdoor environments. Electrochemical impedance spectroscopy (EIS) is used to characterise the corrosion process during the testing in an electrochemical cell, neutral salt spray, humidity, and under outdoor weathering conditions on the Swedish West coast.

Focused ion beam/scanning electron microscope (FIB/SEM) is used to observe, monitor, and detect the corrosion products during exposure. The results from the different accelerated and outdoor weathering tests are correlated to determine the significance of the results.

1.3. Objectives

The objectives of this project are to observe, monitor, and investigate the corrosion failure mechanisms of waterborne chromate free pretreatment primers, to aid the development of that coating so that two layer systems will have similar weathering characteristic to a commercial three layer system on HDG steel.

More precisely it is to study the behaviour of a range of related experimental coatings and a benchmark product in accelerated tests such as an electrochemical cell, neutral salt spray, humidity, and under outdoor weathering conditions on the Swedish

West coast. In addition, correlation of the results from EIS and FIB/SEM will be attempted.

The first task is to monitor the consistency of EIS measurements for a dummy cell and for four coating systems over periods of time. Three locations will be measured on each panel and tested for periods of time. Then fitting software will be used to model the behaviour during that period of testing.

The second task is to monitor and characterise the four systems in accelerated tests for periods of time by EIS and then model the behaviour using fitting software. Also included is the assessment of the degree of blistering on the panels during the tests.

The third task is to monitor and characterise the four systems in outdoor weathering on the Swedish West coast for a number of years by EIS and then model the behaviour using fitting software. Also included is the assessment of the degree of blistering on the panels during that period.

The fourth task is to develop and optimise FIB/SEM technique so that pigment dispersion, interfacial properties, and changes occurring after exposure can be studied. Energy dispersive X-ray spectroscopy (EDS) analysis will be included to investigate the chemical composition inside the areas of investigation.

The fifth task is to observe, monitor, and investigate the four systems in an accelerated test for periods of time by FIB/SEM analysis. EDS analysis will be included to investigate the chemical composition inside the coatings and the possible formation of corrosion products formed during the exposure.

The final task is to analyse and correlate EIS results with FIB/SEM analysis to determine the significance of the results.

Chapter 2. Literature review

2.1. Corrosion process

2.1.1. Definition of corrosion

In its simplest form, corrosion is defined as the degradation of a metal by an electrochemical reaction with its environment [2]. There are two types of classification of corrosion processes in metals [17]. Dry corrosion is a process that occurs without water or aqueous solution when metals are exposed to gas or vapour. Whereas wet corrosion is a process that occurs when metals are exposed to an aqueous solution.

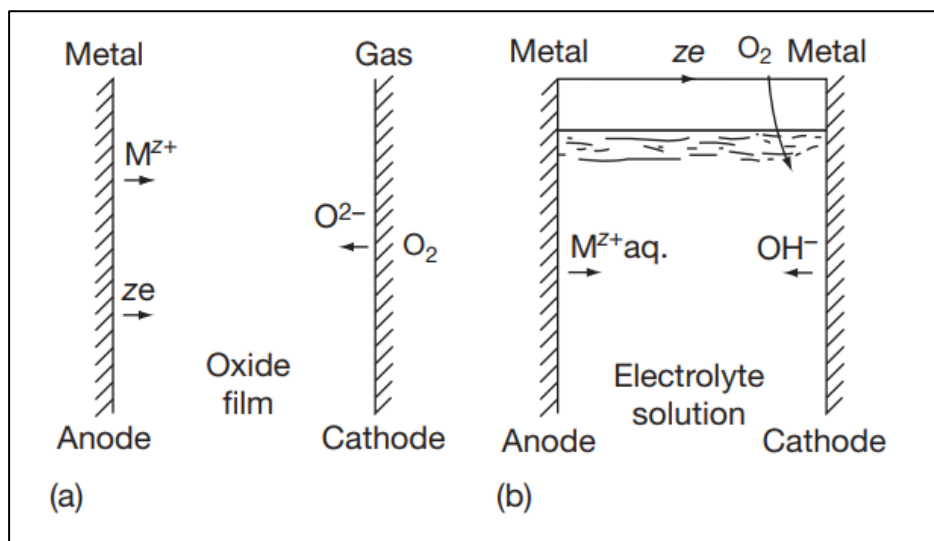


Figure 6. Schematic diagram showing anodes and cathodes in dry (a) and wet (b) corrosion processes [17].

Dry corrosion [17] occurs when metal reacts with a gas or vapour such as oxygen, halogens, hydrogen sulfide, sulphur vapour, etc, resulting in oxidation, scaling, and tarnishing (See Fig. 6a). The reaction involves the initial oxidation of the metal (donate electrons), the reduction (accept electrons) of the nonmetal, and the formation of the compound at the metal-nonmetal interface. A further interaction at the interface is possible if the compound is volatile, or discontinuous, and in most cases, the reaction rate mainly remains the same over a period of time. Whereas for a continuous film, a barrier to the reactants is formed. The reactants can travel through the film by diffusion of the nonmetal or by diffusion and migration of ions of the reactants.

Wet corrosion [17] occurs when different parts of a metal are oxidised and the species are reduced in solution resulting in an electron transfer through the metal from the anode to the cathode (See Fig. 6b). The reaction forms a thermodynamically stable solid compounds or hydrated ions of either cations or anions at the metal-solution interface. The compounds that form at the metal-solution interface may be transported away by processes such as migration, diffusion, and natural or forced convection. Further reaction can occur with the solution; if the stable solid phase formed falls away from the interface then it can not be protective. For a stable oxide formed on the metal surface to be protective, it must be a film or a precipitate.

2.1.2. Thermodynamics

Metals are thermodynamically unstable due to the absorbed energy obtained when metals are extracted from their ores. They corrode to release this free energy so forming a stable energy state corrosion product. The free energy is the single factor which determines whether or not corrosion will take place spontaneously [2].

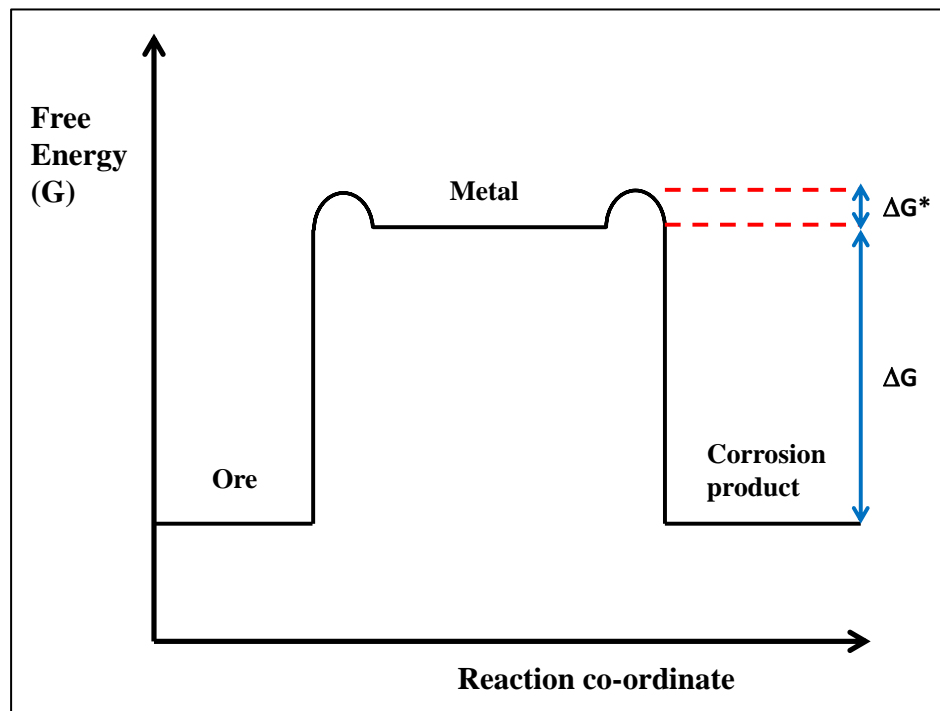


Figure 7. Schematic diagram showing a thermodynamic energy profile for metals and their compounds [2].

This is illustrated in Fig. 7 which is a thermodynamic energy profile diagram that shows the tendency of the metal to corrode and the rate of corrosion which is represented by the activation energy (ΔG^*).

ΔG = Net change of energy in a reaction

ΔG^* = Free energy of activation (Activation energy)

Therefore:

$\Delta G < 0$ = Reaction is spontaneous

$\Delta G = 0$ = Reaction is in equilibrium

$\Delta G > 0$ = Reaction is non-spontaneous

The rate of corrosion is controlled by the size of the activation energy as expressed in (1) [2]. It acts as an obstacle by slowing the corrosion process. A high value results in very slow corrosion rate and the opposite effect occurs for a low value. For example, the corrosion mechanism proceeds at a faster rate when water and electrolyte are present by lowering the activation energy of the reaction.

$$K_{\text{corr}} = A \exp(-\Delta G^*/RT) \quad (1)$$

A = Undefined constant

ΔG^* = Activation energy (KJ/mol)

R = Universal gas constant (8.314 J/mol. K)

T = Absolute temperature (Kelvin)

2.1.3. The free energy and electrode potential relationship

In equation (2) [2], there is a direct relationship between the standard electrode potential (E^0), and the thermodynamic quantity of Gibbs free energy change (ΔG^0). It indicates that the more positive the electrode potentials are, the more thermodynamically favourable the reactions will be. Whereas a negative electrode potential indicates no reaction has taken place. The thermodynamic driving force of

the electrochemical process is determined by the difference in the electrode potentials between the anodic reaction, and cathodic reaction.

$$\Delta G^\circ = -nFE^\circ_{\text{cell}} \quad (2)$$

ΔG° = Change in free energy (J)

n = Number of moles of electrons transferred in the cell reaction per mole of product (mol)

F = Faraday's constant (96847 C/mol)

E°_{cell} = Standard electrode potential (V)

Therefore the following rules apply:

The reaction is spontaneous when $E^\circ_{\text{cell}} > 0$

The reaction is nonspontaneous when $E^\circ_{\text{cell}} < 0$

$\Delta G^\circ < 0$ and E°_{cell} must be positive in order to have a spontaneous reaction, where:

$$E^\circ_{\text{cell}} = E^\circ_{\text{cathode}} - E^\circ_{\text{anode}}$$

The data values of electrode potentials can be obtained in a table of standard electrode potentials. E°_{anode} is the standard potential at the anode and E°_{cathode} is the standard potential at the cathode.

2.1.4. Corrosion kinetics

The electrode potential difference between the anodic and cathodic half reactions can be used to determine the thermodynamic tendency of metals to corrode. The number of electrons transferred in any time period can be used to determine the rate of corrosion. Hence the rate of corrosion is directly related to the current (I) flowing between the anode and cathode. The corrosion rate (C_R) is basically the rate of metal oxidation and can be measured by the rate of mass loss (dm/dt) during an electrochemical reaction that involved electrons transfer between the anode and cathode, which is expressed in (3).

$$dm/dt = i/nF \quad (3)$$

dm/dt = The rate of mass loss (g/s) also known as the weight loss in the literature.

i = current flow

n = Number of electrons transferred during one oxidation reaction

F = Faraday's constant (96847 C/mol)

$$C_R = 1/A_s \rho \cdot dm/dt = IA_w / nFA_s \rho \quad (4)$$

$$C_R = iA_w / nF\rho \quad (5)$$

$i = I/A_s$ = Current density (A/cm²)

A_s = Exposed area (cm²); A_w = Metal molar mass (g/mol); ρ = Metal density (g/cm³)

The theoretical engineering rate of penetration as the corrosion rate in 4 and 5 is obtained by dividing equation 3 with the product, $A_s \rho$ [18].

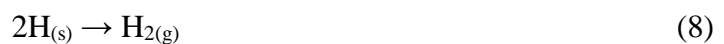
2.1.5. Electrochemical processes

Corrosion involves an electrochemical process in which the metal reacts with its environment by transferring electrons between species to bring about chemical change. The process consists of two half cell reactions. At the anode, the metal oxidises and forms metal ions (M^{Z+}) and electrons (ze^-). This process is called anodic dissolution:



The valency of the metal is governed by the number of electrons available to be released by the atom and is generally between 1 and 3.

At the cathode, the electrons that have travelled through the metal from the anode are consumed and the reduction reactions are dependent on the pH levels. At low pH, hydrogen ions, H^+ , undergo a two step process to produce hydrogen gas:



At near neutral conditions, the process consumes dissolved oxygen and produces hydroxyl ions:



Other cathodic processes may be possible if the energy changes are favourable and the reactions are able to consume the electrons generated by the anodic dissolution. An ionic conducting solution and an electrically conducting pathway between the anode and cathode are the other essential constituents of the corrosion process. The removal of any one of the four components will stop the corrosion reaction [2].

2.1.6. Types of corrosion

There are 5 types of corrosion, which are: uniform, localised, pitting, selective dissolution, and conjoint action of corrosion and a mechanical factor. They are detailed in Table 1 [17].

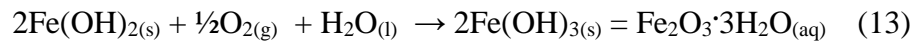
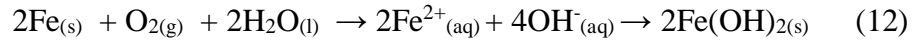
<i>Type</i>	<i>Characteristic</i>	<i>Examples</i>
1. Uniform (or almost uniform)	All areas of the metal corrode at the same (or similar) rate	Oxidation and tarnishing; active dissolution in acids; anodic oxidation and passivity; chemical and electrochemical polishing; atmospheric and immersed corrosion in certain cases
2. Localized	Certain areas of the metal surface corrode at higher rates than others due to 'heterogeneities' in the metal, the environment or in the geometry of the structure as a whole. Attack can range from being slightly localized to pitting	Crevice corrosion; filiform corrosion; deposit attack; bimetallic corrosion; intergranular corrosion; weld decay
3. Pitting	Highly localized attack at specific areas resulting in small pits that penetrate into the metal and may lead to perforation	Pitting of passive metals such as the stainless steels, aluminum alloys, etc., in the presence of specific ions, for example, Cl^- ions
4. Selective dissolution	One component of an alloy (usually the most active) is selectively removed from an alloy	Dezincification; dealuminification; graphitization
5. Conjoint action of corrosion and a mechanical factor	Localized attack or fracture due to the synergistic action of a mechanical factor and corrosion	Erosion – corrosion, fretting corrosion, impingement attack, cavitation damage; stress corrosion cracking, hydrogen cracking, corrosion fatigue

Table 1. Types of corrosion [17].

2.2. Corrosion of steel

The atmospheric corrosion of steel occurs when the metal is oxidised at the anodic sites (10) to form ferrous ions resulting in a release of electrons. The electrons are then consumed at on adjacent cathodic site (11) by oxygen and water to form hydroxyl ions. The ferrous ions react with the hydroxyl ions to produce ferrous hydroxide $\text{Fe}(\text{OH})_2$ (12) which is unstable and known as rust. Further oxidation

reaction occurs with air containing moisture to produce red rust of ferric hydroxide (with Fe^{3+} cations) and hydrated ferric oxide (13) [18].



In the case of HDG steel, corrosion occurs by galvanic effect only when the steel is exposed whereby the zinc corrodes preferentially when in contact with the steel and in the presence of an electrolyte solution. See section 2.4 for further explanation of how zinc protects steel.

2.3. Corrosion of Zn [2]

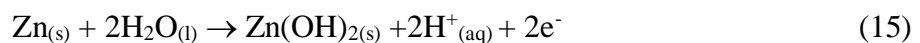
There are five important reactions that can occur when zinc corrodes in water. The study was made by Marcel Pourbaix, whereby he characterised the differences between a corroding condition and a non-corroding condition by the magnitude of the potential. He successfully correlated the dependence on pH and the potential of the electrode with the condition of the electrode.

In solution with Zn ion concentration of $\geq 10^{-6}$ M, the metal is considered to be in a corroding condition. The metal is considered to be in a condition of immunity when the concentration of the ions is $<10^{-6}$ M. The third condition is passivity whereby the corroding product forms a film on the metal surface and prevents electrolyte contacting the metal which results in a reduced corrosion rate.

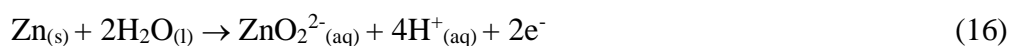
Usual anodic reaction:



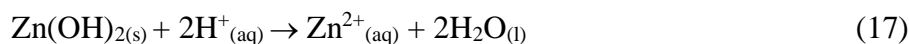
Formation of an insoluble zinc hydroxide:



Formation of a soluble zincate from zinc metal:



Dissolution of zinc hydroxide by acid:



Dissolution of zinc hydroxide by alkali to a soluble zincate:



Electron transfer is involved in reactions 14, 15, and 16 and this is related to the potential of the metal and is influenced by the change in electrode potential. Hydrogen ions are formed in reactions 15 to 18, which are influenced by the acidity of the solution and therefore controlled by the pH. The potential and pH controlled reactions 15 and 16. The outcome of Pourbaix's work is a chart that illustrates how a metal, in this case zinc, behaves in a range of pH at different potentials. The diagram (See Fig. 8) shows that zinc can be immune, passivated or corroding in different conditions of pH and potential.

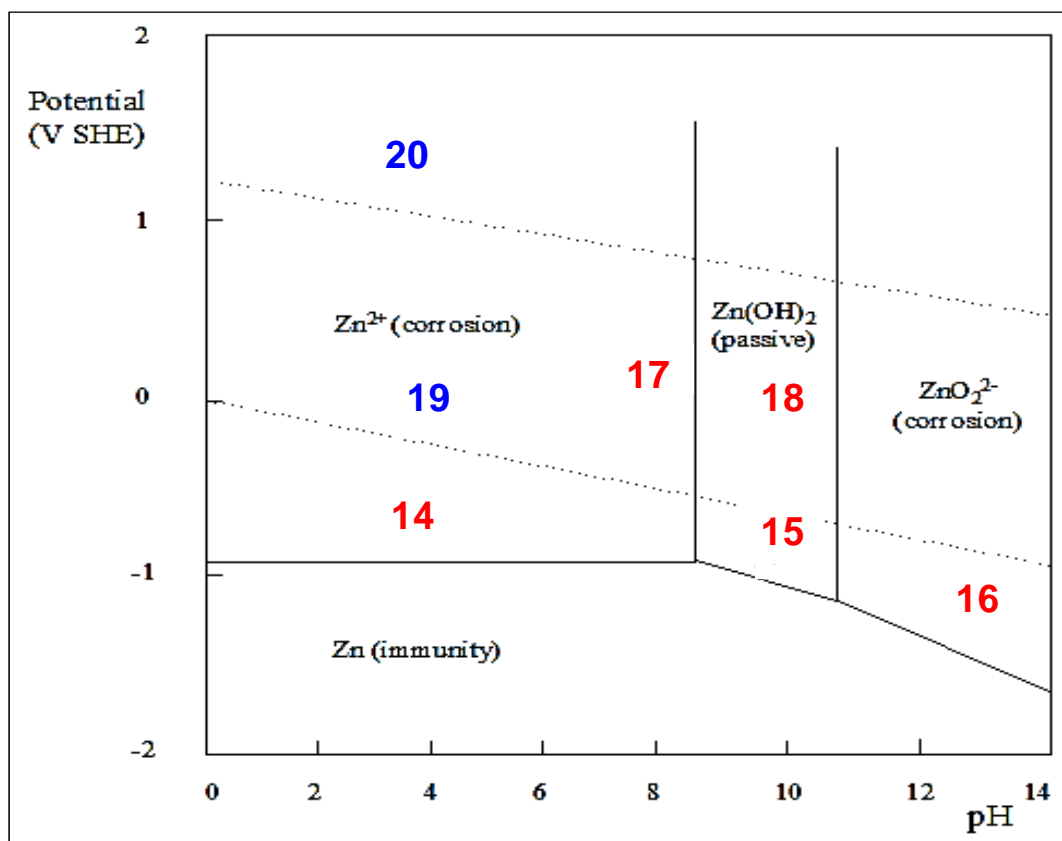
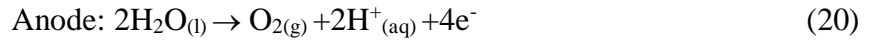


Figure 8. Schematic diagram showing the potential of Zn in distilled water as a function of pH adjusted by NaOH or HCl [2].

The two dashed lines represent the reduction of hydrogen ions to liberate hydrogen gas (19) and oxidation of water to liberate oxygen gas (20).



The Pourbaix diagram shows that over the whole pH range, Zn is thermodynamically unstable in water and tends to dissolve with hydrogen evolution. A passivation layer of hydroxide film is formed on the surface of the zinc in pH range of 8.5 to 10.5, which inhibits the dissolution process of zinc. At above pH 10.5, Zn corrodes to form ZnO_2^{2-} ions and below pH 8.5, Zn corrodes to form Zn^{2+} ions at certain potentials.

Changes to the pH of distilled water by adjusting with additions of NaOH or HCl can also affect the rate of corrosion of zinc. The diagram in Fig. 9 shows the corrosion rate increases substantially when pH values are lower than 6 or higher than 12. At pH between 6 and 12, the corrosion rate is relatively low.

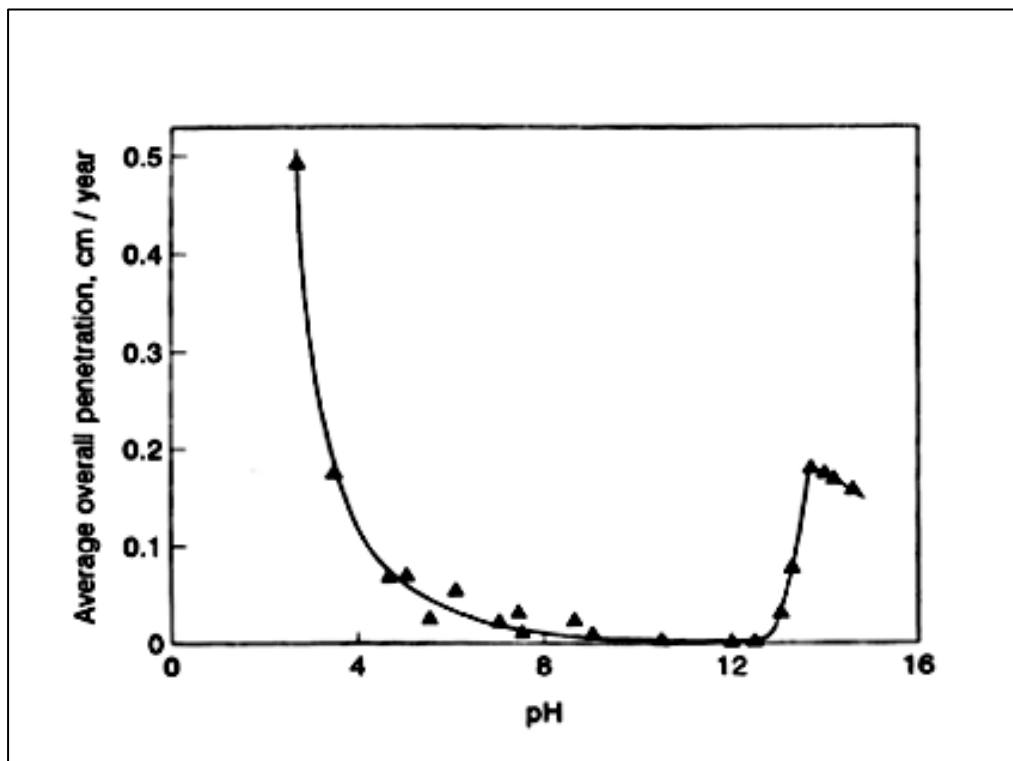


Figure 9. Schematic diagram showing the corrosion rate of Zn in distilled water as a function of pH (pH was adjusted with addition of NaOH or HCl) [19].

2.4. Corrosion process on HDG steel

2.4.1. How does zinc protect steel from corrosion?

One of the most common and inexpensive ways to protect steel from corrosion in natural environments is to coat the steel with zinc. The zinc coating has two functions in protecting the steel. It mainly acts as a barrier, stopping corrodants contacting, and attacking the steel. The other purpose is to protect the exposed steel by galvanic protection when the zinc coating above is damaged due to voids, scratches and cut edges of the coating. The zinc behaves as a sacrificial anode and the steel acts as the cathode (See Fig. 10). This can be seen in the galvanic series, where zinc is more reactive than steel in most environments at ambient temperatures and preferentially corrodes.

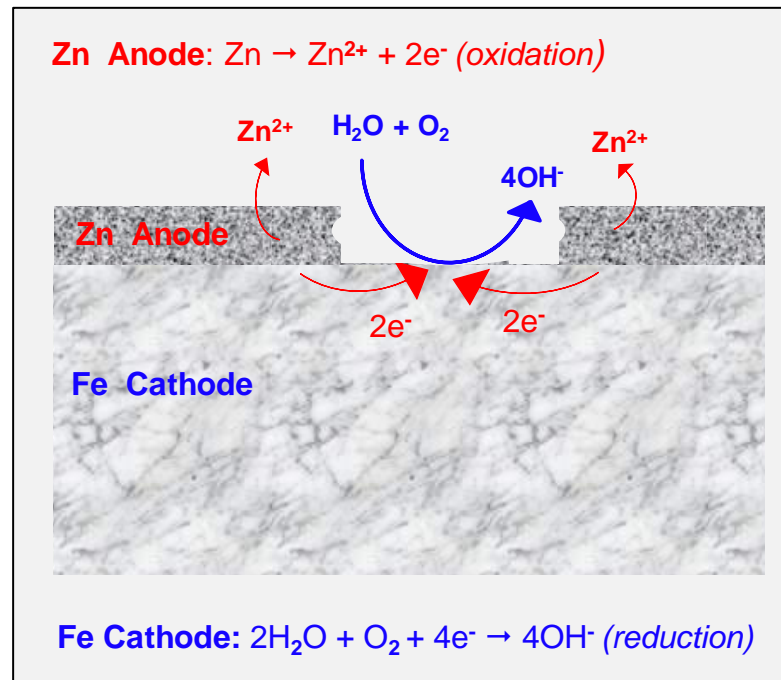
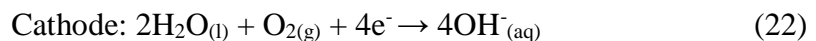
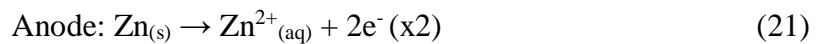


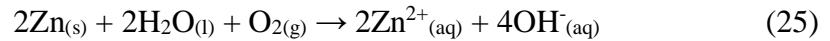
Figure 10. Schematic diagram showing the corrosion process of HDG steel [2].



Porous zinc oxide formation at anodic areas [20]:



Zinc hydroxide (white rust) formation at cathodic areas [20]:



At the surface of the uncovered steel, a porous zinc oxide sacrificial layer is formed by a dissolution/ reprecipitation mechanism (24). This leads to preferential corrosion pathways across the high porosity areas and results in a linear corrosion rate [20]. A secondary barrier layer of zinc hydroxide precipitate (25) is formed at the cathodic areas of the exposed steel after the dissolution of zinc. This leads to the zinc coating corroding at a slower rate than the steel substrate.

Zinc corrodes much less than steel in most atmospheric environments by a factor of 10 to 100 times [21] [22]. The protective layer formed consists of a mixture of Zn oxide, Zn hydroxide, and various basic Zn salts depending on the environment it is exposed in (See Fig. 11).

Corrosion product	Crystal structure	Formula
Hydrozincite	Monoclinic	$\text{Zn}_5(\text{CO}_3)_2(\text{OH})_6$
Simonkollite	Hexagonal	$\text{Zn}_5\text{Cl}_2(\text{OH})_8 \cdot \text{H}_2\text{O}$
Smithsonite	Trigonal	ZnCO_3
Wurtsite	Hexagonal	B-ZnS
Zincite	Hexagonal	ZnO
Zinc hydroxide	Tetragonal	$\text{Zn}(\text{OH})_2$
Zinc nitrate	Trigonal	$\text{Zn}(\text{NO}_3)_2$
Zinkosite	Orthorhombic	ZnSO_4

Figure 11. Most common zinc corrosion products [23].

2.4.2. Atmospheric corrosion

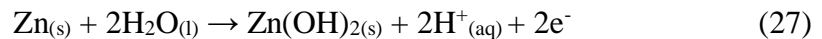
Rural, urban, industrial, and marine are the four types of categories used to characterise atmospheric corrosion. Only a small amount of industrial pollutants are present in the atmosphere of rural and urban areas due to low industrial activity. However more pollutants of SO_x and NO_x are present in the atmosphere of urban area due to higher emissions from motor vehicles. A lot of air contaminants consisting of

Cl₂, CO₂, SO_x, NO₃, or O₃ may be present in an industrial atmosphere. In a marine area there is a high concentration of chloride present in the atmosphere which, together with wind speed makes it a very corrosive environment [24].

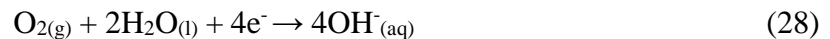
For atmospheric corrosion to occur and at a significant rate, water has to be present to complete the components of a wet electrochemical process. The corrosion rate depends on a number of factors such as the kinetics of anodic/ cathodic processes, the conductivity of the electrolyte, and the conductivity of the solid state. Other factors influencing the atmospheric corrosion rate are the different air pollutants, relative humidity, temperature, and weather changes [25].

Zinc in contact with moisture such as rain, mist, or dew will corrode to form zinc hydroxide on the surface of the metal [23] (27), zinc has a low electrical conductivity and reduces the oxygen to form hydroxide (28) and hence the corrosion reaction in (27) is suppressed.

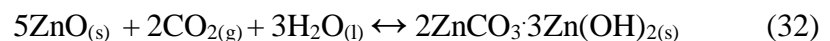
Anodic reaction:



Cathodic reactions:



The zinc hydroxide will be dehydrated into zinc oxide over a period of time, ranging from a few days to a few weeks by reaction (30). The corrosion process continues as zinc oxide does not totally suppress the oxygen reduction reaction (29), as it is an n-type semiconductor. It can react with carbon dioxide in the water to form the less soluble Zn carbonate.



Corrosion of the steel could be stopped or slowed down if reaction (30) was eliminated. This has been seen in zinc alloys containing one or combination of these elements of Al, Mg, Ni, Co, and Mn. They retard reaction in (30) and by doing so, the metallic coating improves its resistance to corrosion [26].

Zinc oxide, hydroxide, and basic carbonates are the main corrosion products formed, which provide a barrier layer on the surface of the steel. This reduces the rate of corrosion of the zinc to levels below those of the steel. The acidity and alkalinity of the environment affect the type of mechanistic attack, the rate of corrosion, and the different products produced.

2.4.3. Effects of corrodants

Air pollutants containing carbon dioxide will result in the formation of carbonates. The film formed passivates the zinc but is unstable at certain acidity levels, hence can be dissolved because CO_2 is soluble in moisture and will lower the pH [23]. CO_2 without the presence of NaCl can increase the corrosion rate slightly due to the acidification of the surface electrolyte, which gives rise to higher surface conductivity, and increases the rate of dissolution of the surface film [27]. The corrosion rate decreases rapidly when CO_2 is added in the presence of NaCl by enhancing the formation of simonkolleite, $\text{Zn}_5(\text{OH})_8\text{Cl}_2 \cdot \text{H}_2\text{O}$ [28].

A significant increase in the corrosion rate of Zn is obtained when NaCl and SO_2 are present together in the atmosphere [22] [28]. The SO_2 is soluble in moisture to form sulphurous acid by an oxidation reaction and a reduction reaction of hydrogen ions in the moisture. This increases the corrosion of Zn [23]. Laboratory studies of atmospheric corrosion show heavy corrosion pitting of metal on the Zn surface when in the presence of NaCl [27] [28]. Pitting corrosion occurs when there is a breakdown of the protective layer of either an organic coating or passive oxide film [7].

2.4.4. Corrosion products

When zinc corrodes, the corrosion process, and formation of products are dependent on the various types of atmospheric environments [29] [30] [31]. In a rural environment, zinc hydroxysulphate, $\text{Zn}_4\text{SO}_4(\text{OH})_6 \cdot 4\text{H}_2\text{O}$ was formed under sheltered condition by transforming from zinc hydroxycarbonate, $\text{Zn}_5(\text{CO}_3)_2(\text{OH})_6$ in the initial phase [29]. For unsheltered conditions there was no phase change, zinc

hydroxycarbonate remained the same over a period of time because it was stable. In an urban and an industrial environment, zinc chlorohydroxysulphate, $(\text{Zn}_4\text{Cl}_2(\text{OH})_4\text{SO}_4 \cdot 5\text{H}_2\text{O})$ was produced in the final phase, with the initial phase being zinc hydroxycarbonate and the intermediate phase being zinc hydroxysulphate [30]. Sodium zinc chlorohydroxysulfate, $\text{NaZn}_4\text{Cl}(\text{OH})_6\text{SO}_4 \cdot 6\text{H}_2\text{O}$ was formed in the final phase in a marine environment. The initial formation consisted of basic Zn carbonate, $\text{Zn}_5(\text{CO}_3)_2(\text{OH})_6$ transformed into zinc hydroxychloride, $\text{Zn}_5(\text{OH})_8\text{Cl}_2 \cdot \text{H}_2\text{O}$ for the intermediate phase [31].

Corrosion products can influence the corrosion behaviour of the metal significantly by acting as a barrier between the metal and the environment. Zn compounds are insoluble, compact, adherent, and insulating. However not all zinc compounds have the same protective properties because of the structure of the compounds or the inhibitive property of the corrosion products.

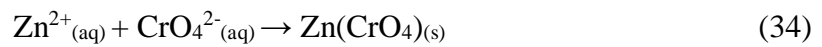
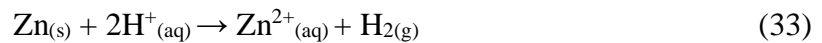
2.5. Pretreatment

Conversion coatings developed during chromating processes are mainly used in the pretreatment stage whereby hexavalent chromium or trivalent chromium are applied by a no rinse process onto the clean HDG steel strip, reacted, and dried off at between 50 and 100 °C [4] [8]. Previously the preferred method was based on alkaline passivation and then rinsed with chromic acid containing chromium (III) ions as well as sugar used as a reducing agent to achieve sufficient corrosion protection; this was expensive and wasteful compared to the no rinse process [3].

The alkaline passivation solution contained caustic soda (NaOH), iron (Fe), and cobalt (Co) compounds and other soluble compounds [3]. Sometime nickel ions were used instead of cobalt. A zinc oxide coating was produced during the course of the reaction which had Fe, and Co (or Ni) ions incorporated in a spinel type lattice structure. The conversion coating delivers excellent organic coating adhesion, which allows the steel to withstand extreme deformation without the breaking of the protection layer. Typical specific coating weights range between 0.2 and 0.4 g/m² [3].

Conversion coating by chromating forms a submicron layer of zinc chromates or chromium hydroxide on the metal surface in reactions (39) to (41) [3]. It ensures good adhesion of the primer to the substrate and gives enhanced corrosion protection

[8]. The chromate acts as a passivation layer and has the ability to behave both as an anodic and a cathodic inhibitor. In anodic inhibition, the rate of zinc dissolution is reduced [32] by the formation of zinc chromate. In cathodic inhibition, the rate of the oxygen reduction reaction on the metal surface is lowered by a thin layer of conversion coating, and the formation of blisters is avoided in the organic coating [32] [33]. Also reported is the healing effect of using chromate conversion coatings whereby the chromium ions, being slightly soluble, leach to the damage area, and form a passive layer in turn protecting the substrate [34].

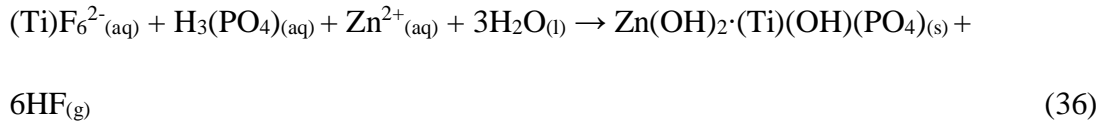
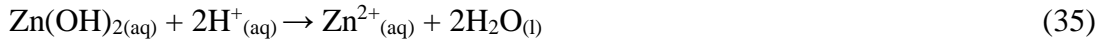


For HDG steel, the passive layer contains Zn(II) and Cr(III) oxides. However, another study has demonstrated that $\text{Cr}(\text{OH})_3 \cdot 2\text{H}_2\text{O}$ is the main component of the passive layer formed when reduced from CrO_4^{2-} (see Fig. 11) and the zinc amount is minor component enabling zinc dissolution to permeate and cause corrosion [32].

Chromate based pretreatments have been used for a long time, however many European countries want to outlaw the use of the process because of the harmful effects of hexavalent chromium, a suspected carcinogen [35], in spite of their good anticorrosive properties [32]. Chromate free pretreatments are the alternative method in use today. They were developed and introduced during the early 1990s [4]. They are mainly based on aqueous solutions of titanium and zirconium fluoro complexes, manganese phosphate, phosphoric acid, and water-soluble organic polymers to enhance paint adhesion [4]. 4-10 mg Ti/m² are normally applied on HDG steel to have the optimum corrosion protection [6].

In the first stage of chromate-free conversion coating, a solution of phosphoric, and fluorotitanic acid is used to initiate the formation of the layer on the surface of the substrate. The pH ranges from 2 to 5 which helps the dissolution of zinc hydroxide to release zinc ions into the treatment bath (42).

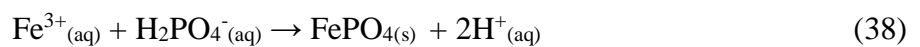
In the second stage, a precipitate of a hydrated mixed oxide/ phosphate compound is formed by the reaction of zinc ions with other ions contained in the solution (i.e. Mn^{2+} , H_2PO_4^- , Ti^{4+}) as in reaction (35) [3].



Researchers have found that chromate-free conversion coating protect the HDG steel by decreasing the corrosion current density (i_{corr}). They also limit the oxygen diffusion to the HDG steel [6] [36]. The surface morphology is noticeably different when there is an absence of either manganese phosphate or the organic compound. However, the chromate-free conversion coatings lack the self-healing ability of the chromate versions and produce a thinner layer too [6] [36].

Zinc or iron phosphates have also been used, but are now mainly used in the United States [3]. The solutions are sprayed onto the steel coil to achieve a specific coating weight between 0.2 and 0.5 g/m². This allows the conversion coating to have a basic level of corrosion protection. A final rinse of a sealant, including chromate chemicals, is needed to improve the performance of the conversion coating.

The surface of the steel is treated with an acidic solution of sodium phosphate (dihydrogen phosphate) which dissolves the iron and forms a thin layer of amorphous iron phosphate as shown in equation 37 and 38. Oxidants like molybdate, chlorate, or organic nitro compounds are used to increase the thickness of the conversion coatings by inhibiting the formation of hydrogen, thereby accelerating the next reaction [8].



2.6. Purpose of organic coatings

Coil coating paints mainly consisted of a topcoat and a primer. The topcoat provides the final aesthetic appearance, mechanical, and durability performance of a coil coated product [4]. Primers main purposes are to prepare the surface for the topcoat and provide protection to the substrate [8].

2.6.1. Purpose of primers

a) Prepare the surface for the topcoat [8] [37]:

- Give good adhesion to the substrate in our case metal
- Be formable so that they can bridge cracks in the underlying metal
- Allow good intercoat adhesion with the topcoat

b) Provide protection to the substrate:

- Coatings based on high glass transition temperature (T_g) resins are stiff and provide greater barrier to moisture and corrodants
- Other methods can also be used in addition such as high molecular weight and linear structure resins
- Provide a reservoir of anticorrosive pigments to protect against corrosion

The primers protect in two ways, as a barrier, and through an electrochemical process [38]. The barrier mechanism works by slowing the progress of corrosive environmental agent (such as ions) travelling towards the metal surface. It was found that the resistance of a coating to the flow of ionic current is a limiting factor to corrosion [39] [40]. The original thinking was based on how the coating protected the metal from the attack of environmental water and oxygen [41].

Anticorrosive pigments are used to reduce or inhibit the electrochemical reactions on the metal. The two mechanisms do not work in isolation and that which is dominant will depend on the properties of the coating, for example the barrier property of the binder or chemical nature of the anticorrosive pigment used.

2.6.2. Barrier properties of primers

The basic principle involved is the limiting of transport of a gas or vapour through an organic coating. The ease of permeation will depend on the solubility of the contaminants within the polymer matrix and how easy it is for them to diffuse through it [41].

The restriction of the passage of gases, vapours, and organic liquids through a coating will depend on the type of polymer, the functional groups, chain symmetry, and crystallinity. The orientation of the polymer, the cross-link density, plasticisation, and T_g also have a significant influence on the coating permeability [41].

The barrier properties of waterborne coatings depend on the chemical structure of the binders and the extent of film forming. Cross-linking and the T_g , in relation to the prevailing conditions have an influence on the film formation process [38] and hence the porosity/ permeability. A properly formed coating should not have pores present in the coating.

It was originally assumed that the purpose of an organic coating is to act as a barrier to water and oxygen. However, evidence from scientific research has shown that the resistance to the flow of ionic current is the limiting factor in the protective function of barrier coatings [39] [40] [42].

2.6.3. Resistance to ionic current by organic coatings

In a study by Bacon, Smith, and Rugg whereby the direct current (DC) resistance of over 300 different coating systems were investigated, a direct correlation was found between the ability of the coatings to protect the steel from corrosion and their resistance values. Good, fair and poor were the three general classifications established and these were based on the resistance values over a period of time (See Fig. 12) [39] [42]. The results were: Good coatings = $\text{Log } R = 9 \Omega \text{ cm}^2$. Coatings

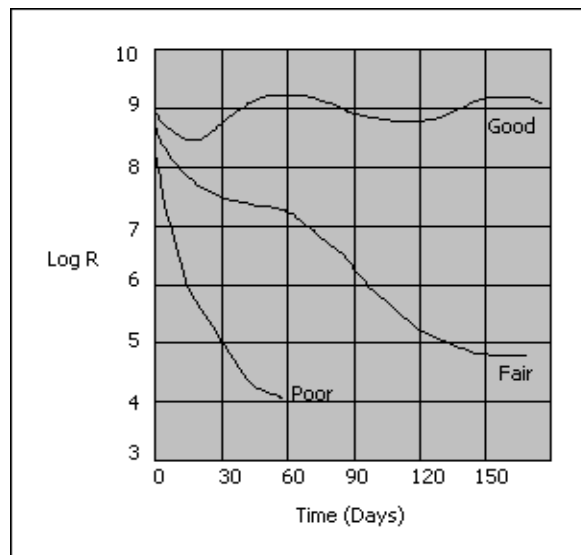


Figure 12. Graph showing the resistance behaviour of coatings over time [39].

providing good corrosion protection $\geq 10^8 \Omega \text{ cm}^2$ over time. Coatings providing poor corrosion protection $\leq 10^6 \Omega \text{ cm}^2$ over time. Initial decreases in resistance values were found for all coatings.

2.6.4. Anti-corrosive pigments in primers

2.6.4.1. Chromate pigments

Traditionally chromates and ‘red lead’ (Pb_3O_4) were used as pigment corrosion inhibitors in primers with organic binders. The oldest anti-corrosive pigment is red lead which is highly toxic but it has the ability to be reactive when dispersed in an oxidisable medium [43]. Strontium and zinc chromates are also widely used. The chromate ions are soluble in water and then migrate to the metal surface where it react to form a passive metal oxide film, which inhibits the corrosion [44]. They are more effective at suppressing the cathodic reaction than anodic zinc dissolution. The extent of inhibition depends on factors such as chloride: chromate ratio, pH, and degree of aeration. However, chromate pigments are toxic and can cause dermatitis, skin sensitisation, asthma, and cancer. Red lead pigments can cause lead poisoning, and mental retardation in children [45].

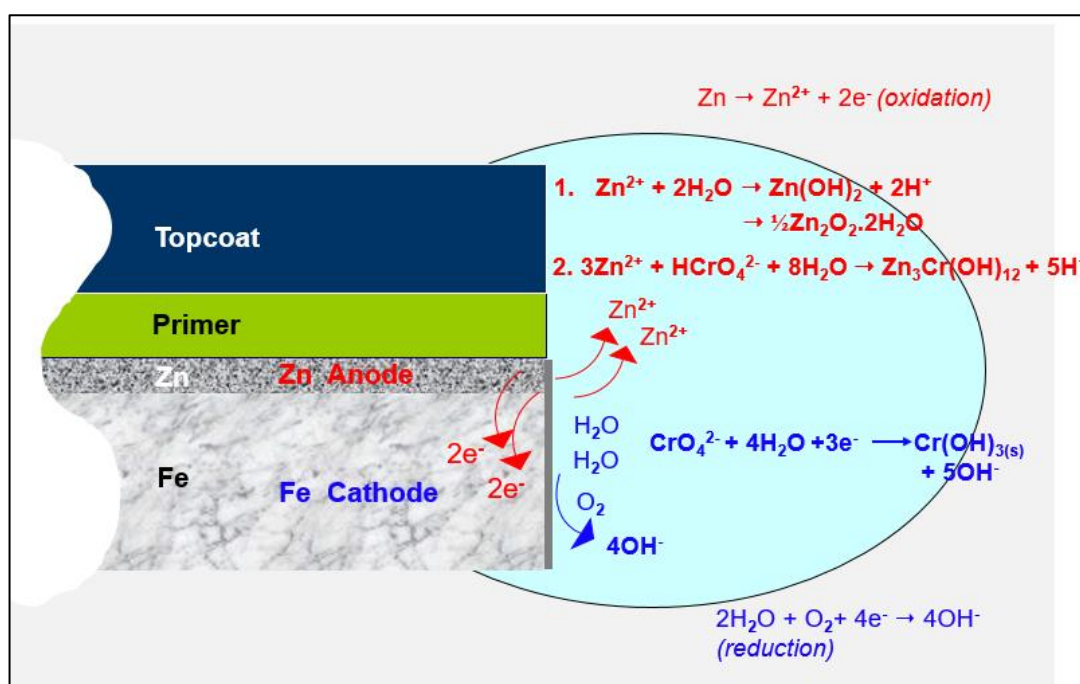


Figure 13. Schematic diagram showing how chromates inhibit corrosion at the cut edge of a coated panel in near neutral and alkaline conditions by forming chromium (III) hydroxide [37].

In near neutral and alkaline conditions, chromates inhibit corrosion at the cathodic region (oxygen reduction) by reducing Cr^{6+} to Cr^{3+} , form an irreversible layer

of near-monolayer thickness of Cr^{3+} hydroxide or oxide ($\text{Cr}(\text{OH})_3$ or Cr_2O_3) at the metal surface [46]. Even at high chloride: chromate ratios, chromate is a very powerful cathodic inhibitor. At the anodic region, two possible mechanisms can occur. One, zinc ions react with water to form zinc hydroxide and further reacts with H^+ ions to form hydrated zinc oxide. Two, chromate ions react with zinc to form a mixed zinc chromium (III) hydroxide (See Fig. 13) [37].

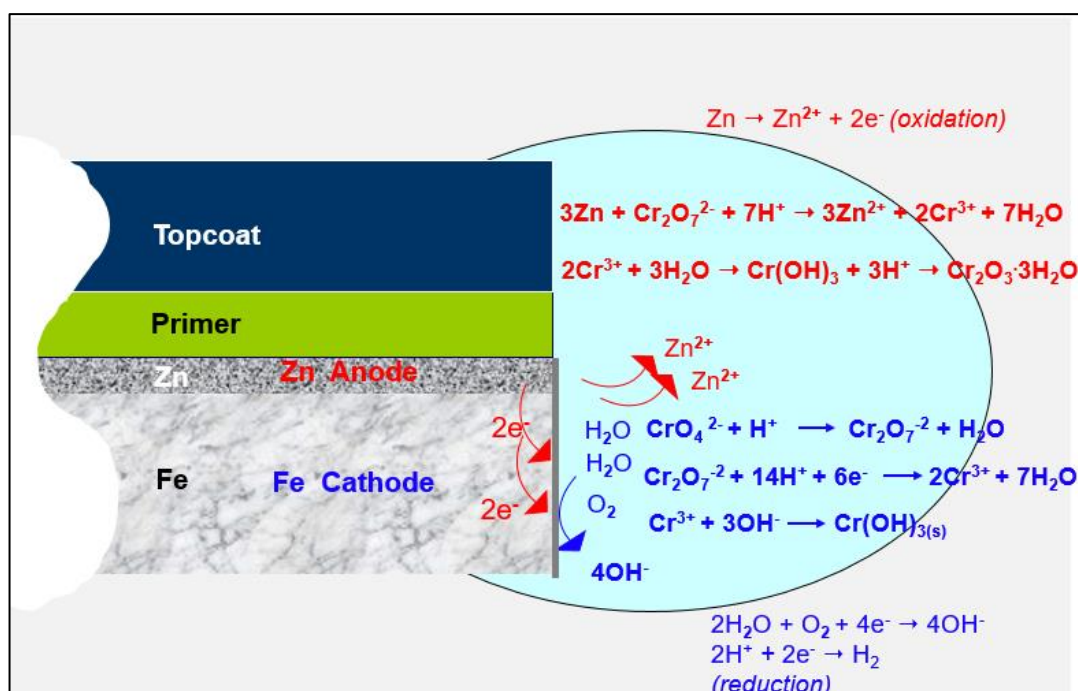


Figure 14. Schematic diagram showing how chromates inhibit corrosion at the cut edge of a coated panel in acid conditions by dissolving to form dichromate ions and then reduce to Cr^{3+} ions. Cr^{3+} ions are transported to the metal surface to form chromium (III) hydroxide [37].

Chromates are relatively soluble in acidic conditions. This can happen at the anodic region whereby the pH is decreased from neutral to acidic condition by the dissolution of zinc. Chromates inhibit at the anodic region by forming soluble dichromate ions ($\text{Cr}_2\text{O}_7^{2-}$) which are then reduced to Cr^{3+} ions [46]. These are then transported to the metal surface to form $\text{Cr}(\text{OH})_3$ which further reacts with H^+ ions to form a protective layer of hydrated chromium (III) oxide (See Fig. 12). At the cathodic region, the dichromate ions are formed from the reaction of chromate ions with H^+

ions and then reduced to Cr^{3+} ions, which reacts with OH^- ions to form a protective layer of chromium (III) hydroxide.

2.6.4.2. Chromate-free pigments

The strict environmental regulations in the last decade have forced the coating industry to move away from these toxic pigments towards environmentally friendly pigments and inhibitors [45]. Phosphates, ferrites, and ion-exchange pigments are now most frequently used by the industry [45].

There are many types of phosphates and polyphosphates in use today. The anions are combined with one, or more cations of aluminium, calcium, lithium, magnesium, strontium, and zinc [47] [48] [49] [50] [51]. The pigments in small quantities are soluble in water and can release free ions to the damaged area of the coating by passivating the exposed metal surface, or by forming a barrier layer of precipitated salt film.

Zinc is the most common cation due to the low solubility and reactivity of the pigment with different binders. It works by the phosphatisation of the metal surface. The phosphate first reacts with either hydroxyl or carboxyl groups on the binder and with the products of the corrosion [48] [49] [50] [51] to form a passivation layer. Oxides, hydroxyoxides, and iron phosphate compounds are normally formed in the passive layer of iron and their salts have limited solubility which results in the polarisation of the cathodic regions [52] [53] [54] hence slowing the rate of corrosion. Other views are that due to the low solubility of zinc phosphate, especially in near neutral conditions of between 6.5-8 pH it will be difficult to produce a passivation layer [55] [56] [57].

Aluminium triphosphate, calcium zinc phosphate, zinc polyphosphate, and calcium phosphate are also used and the mechanism to stop corrosion is similar to zinc phosphate. However, these pigments have not been as extensively studied as zinc phosphate [58] [59].

Ion-exchange pigments are mainly based on calcium ion exchange silica. They undergo a two stage mechanism to protect metal surfaces. In acidic conditions, hydrogen ions penetrate the coating from the environment and are exchanged with

calcium ions which neutralise the acidic compound. Subsequent transport of the calcium compound to the metal occurs where they form a protective layer of calcium and metal silicate on the surface of the substrates [58] [60] [61] [62] [63] [64].

Figure 15 shows zinc is oxidised at the anodic site to form zinc ions (Zn^{2+}) and enter into the solution. Oxygen reduction reaction occurs at the cathodic site, whereby the water and oxygen present at the metal surface consume the four electrons to produce hydroxyl ions (OH^-). In alkaline solutions, silica can be soluble depending on the alkalinity in the coating and dissolve as silicate ions (SiO_3^{2-}) at the cathodic region. Parallel to the silicate ion reaction, silica releases calcium ions (Ca^{2+}) in exchange for cations such as H^+ or Na^+ . Ca^{2+} reacts with silicate ions to form a calcium silicate film in alkaline regions on the metal surface. At the anodic region silicate ions react with zinc ions and form zinc silicate. The zinc silicate and calcium silicate combined to form mixed zinc silicate and calcium silicate ($ZnSiO_3CaSiO_3$) protective layer [65].

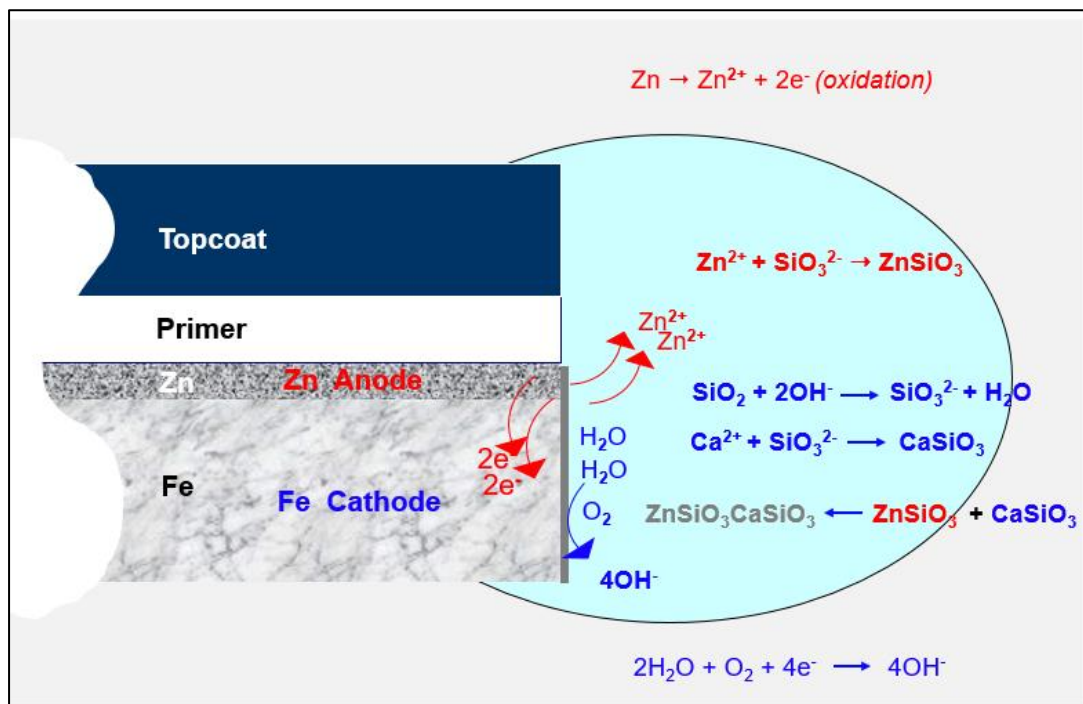


Figure 15. Schematic diagram showing how calcium ion exchange silica pigment inhibit corrosion at the cut edge of a coated panel [37] [65].

2.7. Waterborne coatings

Strict environmental regulations have forced the coating industry to develop coatings that are solvent free with non-toxic pigments for protection against corrosion. Waterborne coatings with chromate-free pigments have been used in the last 20 years [45]. They are based on water which acts as a vehicle in which to disperse the resin. A small amount of co-solvents are often added. Two types of binder are used in waterborne coatings [66], they are:

- 1) Polymer in solution. These are soluble resins that are completely dissolved in water.
- 2) Polymer in dispersion. These are insoluble resins and they exist as particles that are suspended in water using emulsifiers. The particles can range between 10 nm and 150 μm in diameter.

In this study dispersion resins will be the main focus. They are based on variety of different technologies. The main resin types in use are acrylics.

2.7.1. Waterborne acrylics

Waterborne acrylics are made up of small insoluble particles dispersed in water. They have higher molecular weight than solvent based resins and the difference can be up to 100 times larger. Due to their high molecular weight, acrylics do not need crosslinking reactions to form a coherent and homogeneous film.

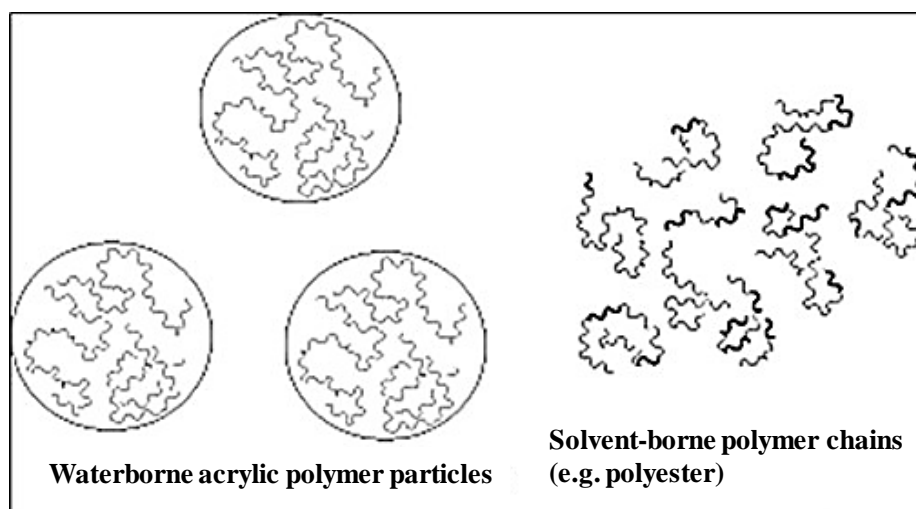


Figure 16. Schematic diagram of a waterborne acrylic and solventborne polymers

[66] [67].

The particles produced are in the size range of between 20 and 1000 nm containing a number of acrylic polymer chains in each particle [68].

Figure 16 shows how polymer chains of solvent based resins are dissolved in solvents whereas small, spherical particles are dispersed in water which contain several acrylic polymer chains in each particle [66] [67] .

The choice of monomer and the type of stabiliser used will produce specific properties. The resins are generally made up of a blend between acrylic monomers and vinyl monomers to produce desired properties of adhesion, exterior durability, chemical resistance, hardness, flexibility and cost [68] (See Table 2).

Chemical type	Example	Function
Vinyl ester	Vinyl acetate	General purpose, hardening
	Vinyl versatate	Flexibilising
Acrylic and methacrylic ester	Methyl methacrylate	General purpose, hardening
	Glycidyl methacrylate Dimethyl amino ethyl methacrylate	Adhesion promotion
	Ethyl, butyl, 2-ethylhexyl acrylate	Flexibilising
Aromatic	Styrene	Hardness, gloss
Olefin	Ethylene	Flexibilising
Miscellaneous	Acrylamide, n-methylol acrylamide	Crosslinking

Table 2. Typical monomers used in polymerisation of waterborne acrylic [68].

For a coating to form a film at ambient temperature, the glass transition temperature (T_g), of the resin has a major influence on the minimum film formation temperature (MFFT). T_g is the region where the polymer undergoes a change from brittle to soft, and pliable. The amounts and types of co-solvents and coalescing agents,

plasticisers and other additives added to the polymer or to the coating formulation have a big influence on the MFFT [68]. Therefore most resulting polymers have Tg range between 0 and 10 °C. Below the Tg region, the polymer is hard, and has issues with coalescing and adhesion. Above the Tg region, the polymer is soft, and has issues with abrasion resistance and dirt collection [68].

2.7.2. Film formation mechanisms

The film formation process of dissolved and suspended resins is very different [69] [70]. Emulsions are much more difficult to control and the process of film formation is critical to achieving optimum performance [70]. This is not the case for solvent based coatings.

2.7.2.1. Film formation of solvent-borne coatings

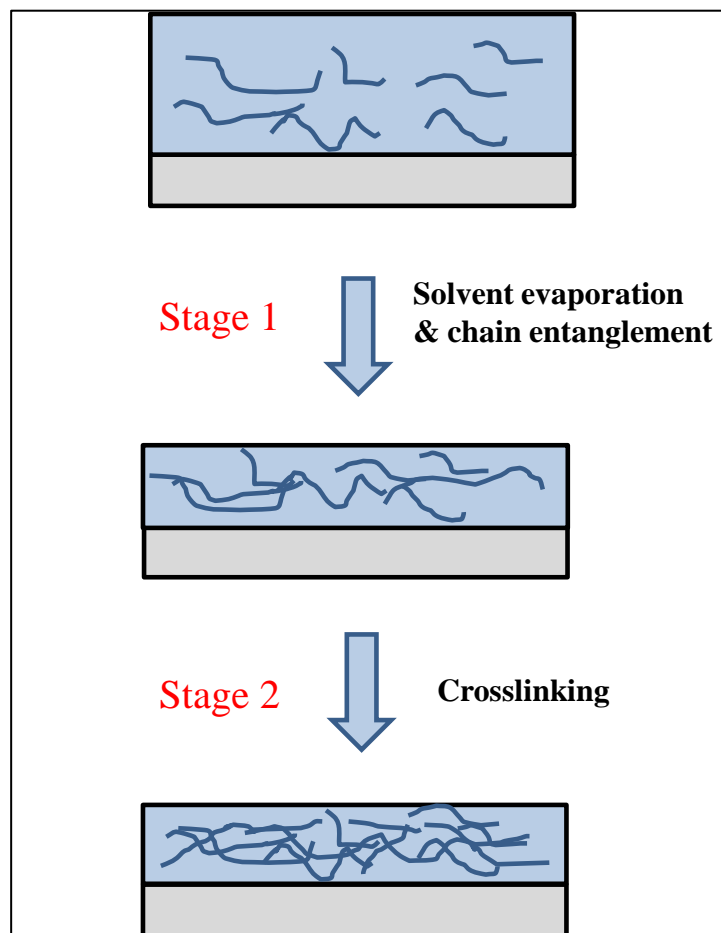


Figure 17. Schematic diagram of the different stages in the film formation process for solventborne coating [68].

Solvent based coatings have two stages in forming a film [66] (See Fig. 17). Stage one is the bulk evaporation of the solvents from the coating to produce a solid film. The process is very rapid and the rate of evaporation depends on the solvents and the environmental conditions.

The long polymer chains entangle and form a tight network. About ninety percent of the solvent is lost [71]. Stage two is the diffusive evaporation process whereby the remaining solvents are lost over a longer period of time. The process is slow and is hindered by the formation of the tighter polymer network in stage one. To overcome this, heating at elevated temperatures is mostly used, which forces the solvents to completely escape from the coating, and form a three-dimensional polymer network.

2.7.2.2. Film formation of waterborne coatings

Waterborne emulsions in contrast have three stages before a complete film is formed (See Fig. 18) [66] [72]. However, some researchers have mentioned four stages, whereby they split stage two into two parts [71]. The exact film formation mechanism is still open for discussion [69]. Stage one is the evaporation of the water from the coating until the particles come together into close contact. A least 36% volume of water and additives are still left in the film [71].

A continuation of evaporation of water occurs at stage two and this results in voids within the interstitial boundaries of the particles. The rate of water removal can be affected by the polar part of the hydrophilic dispersion additives, e.g. surfactants which interact with the water molecules [73] will slow down the rate of water evaporation. For packing of deformed particles to occur and form a polyhedral structure [74], the forming temperature (T) must be above that of the minimum film forming temperature (MFFT) so that the forces accompanying the drying process exceed the modulus of the particle and deform the particles to fill the voids left by the evaporation of water.

In stage three, the polymer particle boundaries inter-diffuse and coalesce to form a homogeneous and coherent film. Completion of the process may never occur and the time dependency of the latex film formation can be explained this behaviour [75]. Most researchers have mentioned that for inter-diffusion to occur and for a film

to be formed, the annealing temperature (temperature that alters the physical property of a material) must be above that of the polymers glass transition temperature (T_g) [69] [76] [77] [78]. The molecular weight of the polymer [77], the time of annealing [76] [77], the spatial distribution of chains ends near the interface [79], and the steric and electrostatic stabilisation [80] of the latex also have strong influence on the inter-diffusion capability.

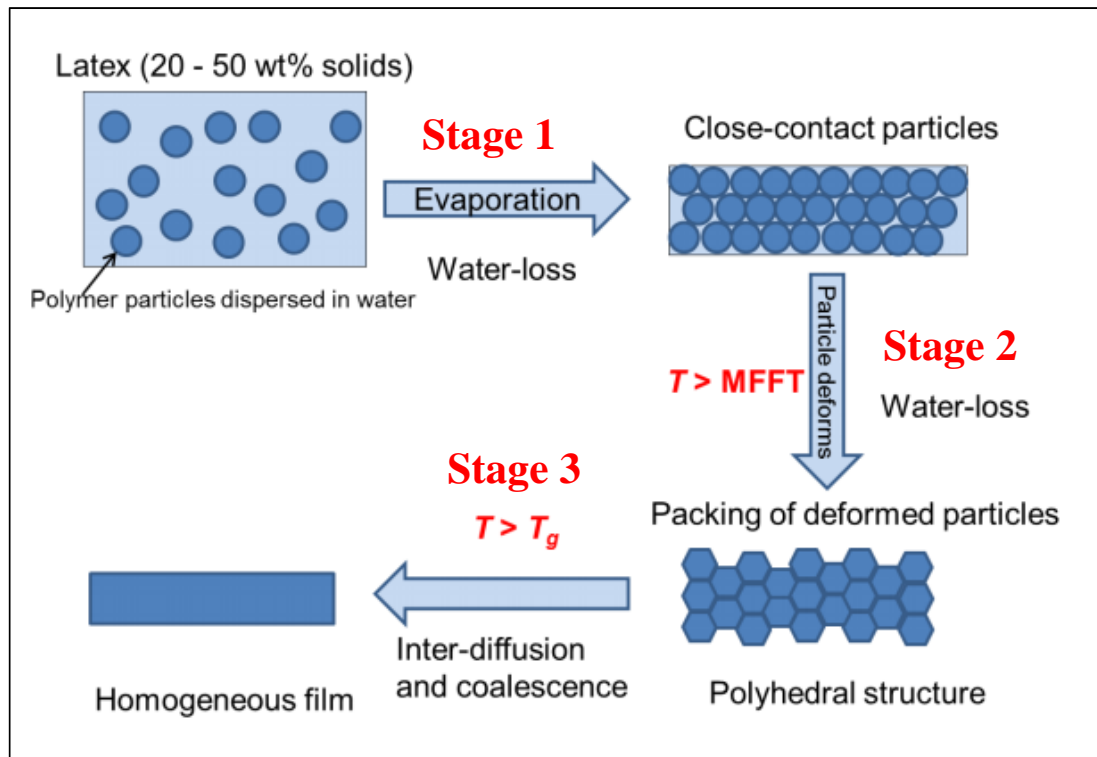


Figure 18. Schematic diagram showing the different stages in the film formation of waterborne coating [68].

The main difference in film formation between the two coatings is the slower drying of the waterborne coating and this may have a detrimental effect on the performance of a pretreatment primer.

2.7.2.3. Glass transition temperature (T_g)

Glass transition temperature is a temperature range, which the hard brittle glassy state of a polymer or coating changes to a rubbery one. T_g is influenced by the “rigidity in the polymer chain, side groups that sterically hinder the chain’s movement, and molecular weight” [68]. Increases in these parameters will increase the T_g . However, the disadvantage of higher T_g is generally a decrease in ductility.

Internal stress occurs during curing and cooling stages of coating, especially when quenching. The magnitude of the stress is influenced by the T_g of the cured coating and is directly proportional to the difference between the T_g of the coating and the ambient temperature to which it cools. This can affect the ability of the coating to adhere to the substrate.

The simplest and easiest methods of determining T_g for polymers or coatings are differential scanning calorimetry (DSC) and thermomechanical analysis (TMA). DMA is another important method used to determine the T_g of coatings. It indicates the physical mechanical properties of the coating, for example a high T_g coating will be brittle in ambient temperature whereas a low T_g coating will be flexible when undergoes forming process.

Glass transition can be explained by either kinetic or equilibrium theories, which were developed over a number of years. Kinetic theories are based on dynamic process whereby the “freezing” of the movements of chain segments (kinetic units) causes vitrification, or glassification. The first (solid-state) transition occurs when localised bonds and side chains start to move at low temperatures by bending and stretching. This point is called gamma transition (T_γ). As the temperature increases, material undergoes beta transition (T_β) whereby it starts to develop some toughness due to the activation of localised motions that involve the whole side chain and localised group movements (See Fig. 19). T_g is then reached with further heating. At this transition a dramatic change in properties of the material is observed due to the large scale coordinated motions of the polymer chains.

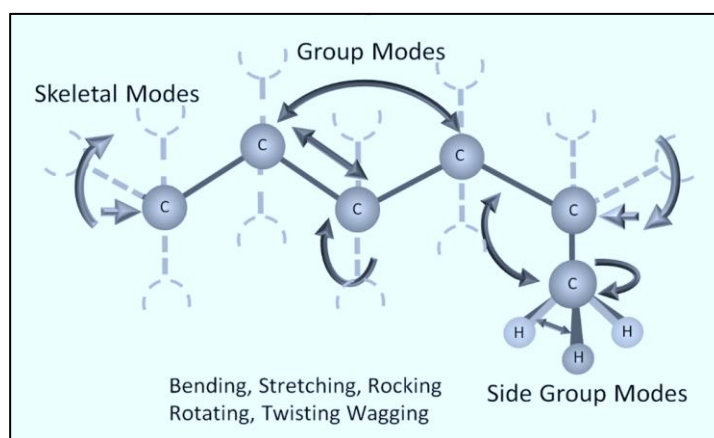


Figure 19. Schematic diagram showing side chain and group movements [81].

The first equilibrium is another theory for T_g developed by Gibbs and DiMarzio [81]. They estimated that the increase in temperature will change the conformational entropy and suggested that a thermodynamic second-order transition is reached when conformational entropy becomes zero. All conformations are essentially "frozen" when temperature is below this position.

2.8. Failure mechanisms of coatings

Blistering and delamination are the most common failure mechanism found in organic coatings. They have apparently similar mechanisms however it is unclear if the phenomena are the same. In each mode of failure, there are sub classes of failures.

2.8.1. Blistering

There are four common features associated with the blistering mechanism of coatings upon exposure to aqueous environments [82], they are:

1. Fewer blisters are generated when the concentrations of ions are the greatest in the immersion liquid.
2. In seawater immersion, the fluid in the blisters formed is always alkaline. The amount of chlorine in the blister is lower compared to seawater.
3. The steel under the blisters area is normally bright and contains no corrosion.
4. Blistered areas are commonly related to adjacent corrosion areas.

Points 3 and 4 are normally observed in exposed coated panels.

In the majority of situations, at the weakest point in the coating some corrosion is observed before any blistering occurred and where there is no corrosion present an insignificant number of blisters is formed. This leads to the suggestion for the formation of blistering is as follows [42]:

1. Water containing some dissolved salts is absorbed by the coating immersed in solution.
2. Primary corrosion sites at the interface are activated when a sufficient amount of liquid containing chloride passes through to the underlying metal.

3. A cathodic area surrounds this and has a build-up of hydroxyl ions. At the anodic area in the centre of the blister metal oxidation occurs.
4. At the cathodic site, the alkaline environment will weaken and destroy the adhesion of the film. The resulting product causes osmotic pressure at the coating metal interface.
5. The substance at the interface formed during the cathodic reaction causes the water to travel through a film by osmotic process [83].

Points 3, 4 and 5 are normally observed in coated panels on exposure.

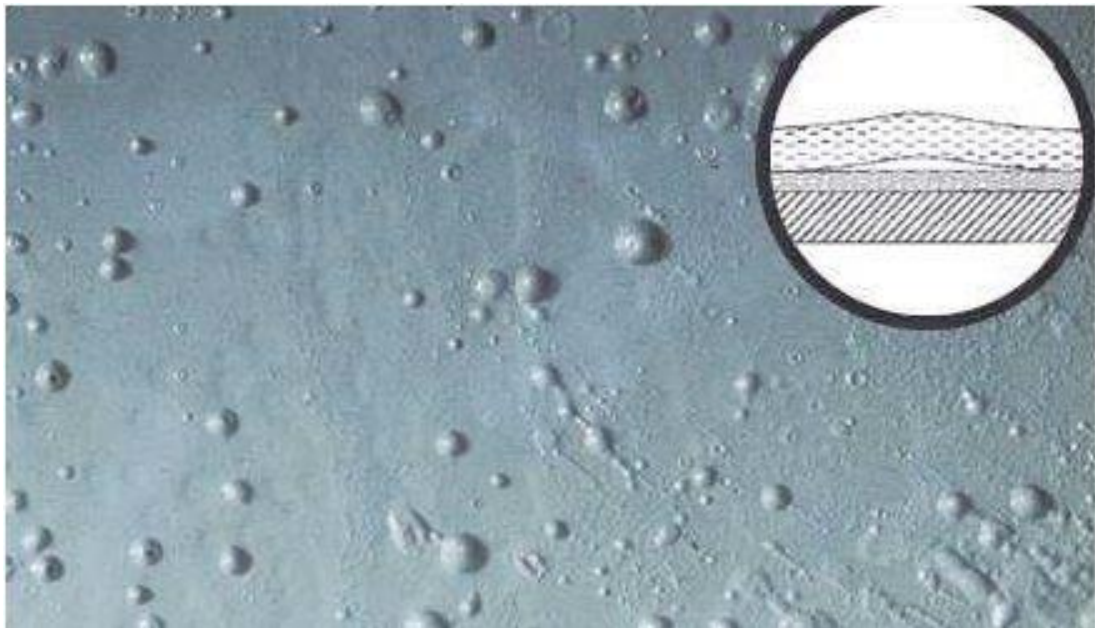


Figure 20. Photograph and schematic diagram of blisters [84].

There are three types of blister formation in a coating (See Figs. 20, 21 and 22), which are osmotic blistering, anodic blistering, and cathodic blistering [83].

2.8.1.1. Osmotic Blistering

A coating which has soluble salts at the interface can form areas of concentrated salt solution. This area has a decrease in water level and so will pull water from the environment through the coating. The osmotic pressure formed causes the coating to blister (See Fig. 21). The force exerted is in the range between 2500 and 3000 kPa, which is significantly higher than the forces of mechanical resistance to deformation of a coating (between 5 and 40 kPa) [85]. Further expansion of blisters

can continue if the pressure in the blister is greater than that of the atmospheric pressure [86].

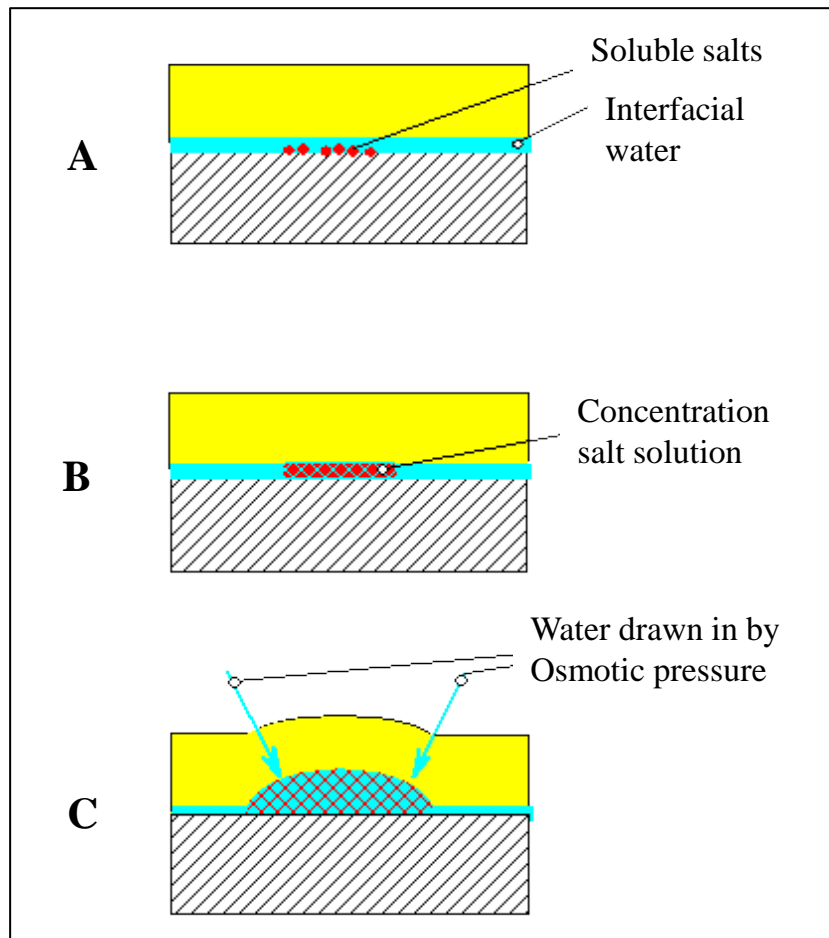


Figure 21. Schematic diagram showing an osmotic blistering process caused by contaminated substrate [42].

2.8.1.2. Anodic blistering

In a blister, there is an anodic, and cathodic region and the liquid in the blister is anodic in nature [87]. An anodic region is represented by a corroded area in the centre of the blister, initiated by chloride ions migrating through the coating at a weakness area and producing acidic conditions underneath the coating. This produces a reduction of ferric oxide on the steel to soluble ferrous state. On zinc, zinc oxide, hydroxide, and basic carbonate are formed.

2.8.1.3. Cathodic blistering

In the presence of water and oxygen, alkali ions are the by-product of the cathodic reduction reaction. It normally occurs at a damaged area of the coating and is associated with corrosion [88]. The corrosion causes the film to blister (See Fig. 22).

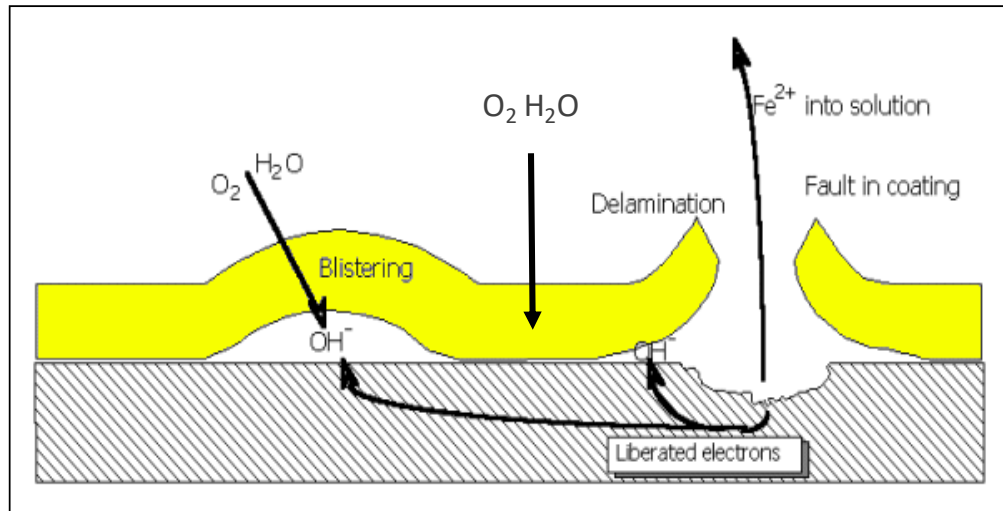


Figure 22. Schematic diagram of the blistering and delamination processes [89].

2.8.2. Delamination

There are two types of delamination that occur in organic coatings. They are cathodic and anodic delamination.

2.8.2.1. Anodic delamination

Anodic disbondment is characterised by an anode at the delamination front, where anodic undermining destroys the metal coating adhesion [88]. Filiform corrosion is the main example of an anodic delamination coating failure mechanism (See Fig. 23).

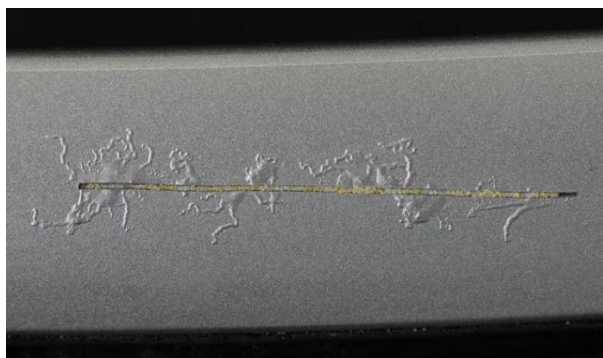


Figure 23. Photograph of filiform corrosion on a painted aluminium sample [90].

2.7.2.2. Cathodic delamination

The process is driven by the cathodic reaction, whereby the defect area underneath the coating becomes the anode and causes the dissolution of the metal and electron liberation. The electrons are consumed at the cathode site as the oxygen reduction reaction proceeds, forming alkali ions. The strong alkali condition, a pH of 10 and over [91] dissolves the interfacial bonds and causes further lifting of the paint (See Fig. 24). This can lead to corrosion products forming through to the surface of the coating.

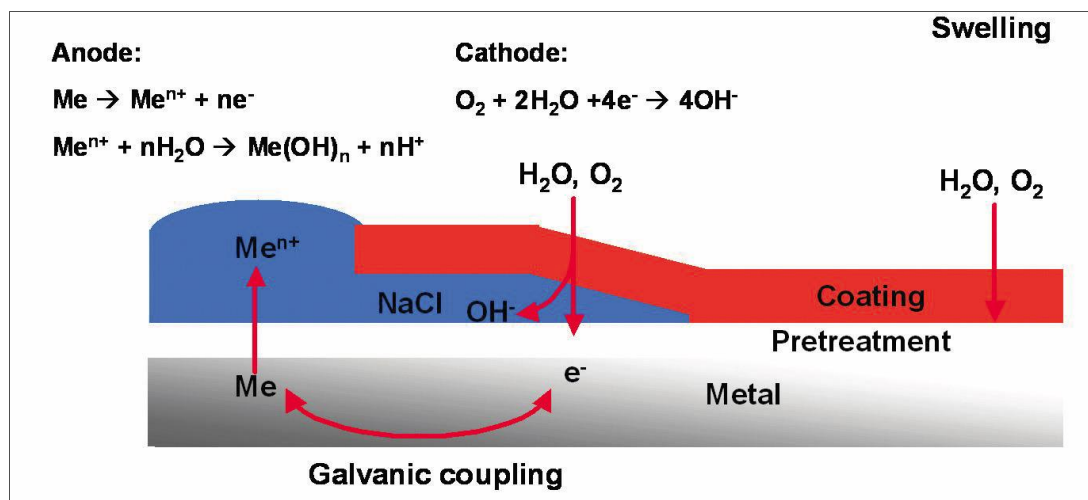


Figure 24. Schematic diagram of a cathodic delamination mechanism [91]. The anodic site is represented by the defect area on the left. The cathodic site is represented by the delaminated coating area in the middle.

2.9. Corrosion detection techniques

Corrosion of metals coated with organic coatings can be determined by a variety of techniques. Accelerated and outdoor weathering tests are commonly used by the coil coating industry to determine the corrosion performance of coil coated products. Electrochemical techniques are normally used by researchers to monitor, characterise, and determine the extent of corrosion of coated metal. For general corrosion measurements, electrochemical impedance spectroscopy (EIS) and DC electrochemical tests are commonly used. For localised corrosion measurements, scanning vibrating electrode technique (SVET), scanning Kelvin probe (SKP), scanning droplet cell (SDC) and electrochemical noise (ECN) are used.

2.9.1 Accelerated and natural weathering tests

Accelerated and outdoor weathering tests are widely used by the coil coating industry to evaluate the corrosion performance of coil coated products. Neutral salt spray (ASTM B117-09) tests are used extensively though out the industry to obtain overall corrosion resistance of coated metal.



Figure 25. Photograph of a typical salt spray chamber [92].

The coated metals are prepared and placed onto panel racks at around 90° to the rack (See Fig. 25). The panels are normally tested for 1000 hours, continuously sprayed with 50 g/l sodium chloride solution at a constant temperature of 35 °C and pH around neutral. At intervals during the test and after the test, the panels are taken out, and visually inspected for corrosion. Cyclic salt spray tests are also available in order to obtain more realistic conditions. These include prohesion and VDA (EN ISO 11997-1) [93].

Constant climate humidity (BS3900 Part F2: 1973) tests are used to assess the resistance of coatings against humid conditions (See Fig. 26). The tests are normally ran for 1000 hours at 100% relative humidity at 40 °C. At intervals during the test and after the test, the panels are taken out, and inspected for blister, corrosion products, colour, and gloss. Cyclic humidity tests are also available in order to obtain more realistic conditions.



Figure 26. Photograph of a typical humidity chamber [94]

Outdoor exposure sites such the ones in Brest, and Bohus Malmön are also used by the industry. Both locations are a C5 category site based on EN ISO 12944-2, which means that they are in a marine environment with high salt content. The classification is based on weight loss of steel and galvanised materials C1 is low, C3 is medium, and C5 is high. Bohus Malmön will be used in this project and the site is located on the South West coast of Sweden, with a typical North West European marine climate (See Figs. 24 and 25). The site belongs to the Swedish Corrosion & Metal Research Institute (KIMAB) and is classed as a C5 site for corrosivity due to the aggressive marine environment and some SO₂ pollution from a nearby factory.



Figure 27. Photograph of Bohus Malmön exposure site with exposure racks at 45° South facing.



Figure 28. Photograph of Bohus Malmön exposure site with exposure rack at 90° North facing.

2.9.2 Electrochemical Impedance Spectroscopy (EIS) [95]

2.9.2.1. EIS theory

EIS describes the response of a circuit to an alternating current (AC) or voltage as a function of frequency or time. The resistance at zero frequency in direct current (DC) circuit obeys Ohm's law ($E = IR$), where E is the potential measured in volts (V), I is the current measured in amperes (A), and R is the resistance which describes how the flow of electrons in the circuit is impeded and is measured in ohms (Ω). This is not the case when the frequency is not zero the equation now uses Z instead of R , Z represented the impedance of an AC circuit.

$$E = IZ \quad (39)$$

Impedance is now a measurement of components that impede the flow of electrons in AC circuit. The resistor, capacitor, and inductor are the impeding components.

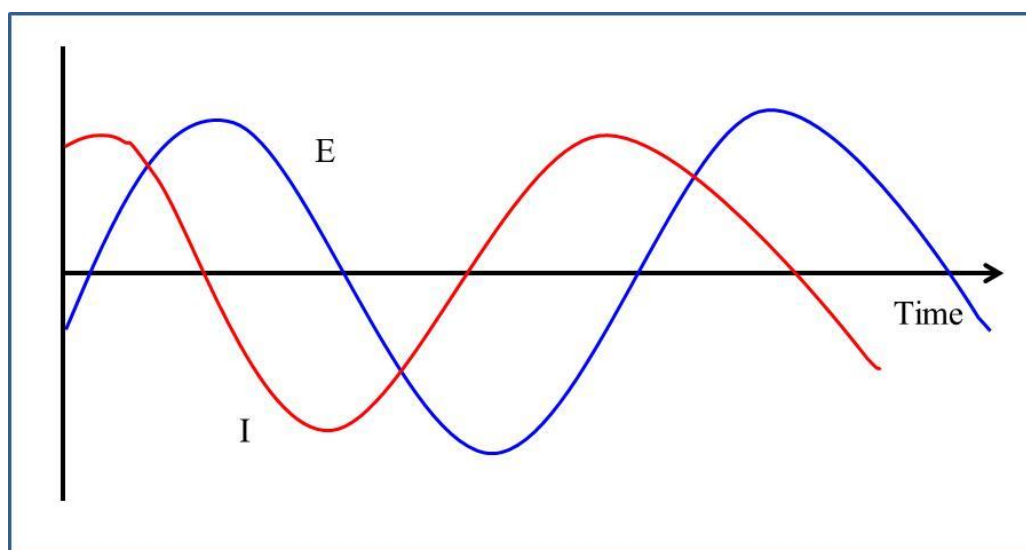


Figure 29. Schematic diagram showing the waveforms of the applied potential (E) and the response of the current in AC circuit.

Equation to describe the resulting current sine wave:

$$I(t) = A \sin (\omega t + \theta) \quad (40)$$

Where $I(t)$ is instantaneous current, A is maximum amplitude, ω is frequency in radians per second = $2\pi f$ (where f is frequency measured in Hertz), t is time and θ is phase shift in radians.

AC current (I) and voltage (E) vectors expressed as:

$$I_{\text{Total}} = I' + I''j \quad (41)$$

$$E_{\text{Total}} = E' + E'' \quad (42)$$

Where the real component is represented by I', the imaginary component is represented by I'' and j is $\sqrt{-1}$. The two components of the current are defined with respect to the voltage waveform, where the real component is in phase with the reference waveform and the imaginary component is 90 degree out of phase.

$$Z_{\text{Total}} = E' + E''j / I' + I''j \quad (43)$$

AC impedance (Z) expressed as:

$$Z_{\text{Total}} = Z' + Z''j \quad (44)$$

The absolute magnitude of the impedance ($|Z|$) and the phase angle ($\tan \theta$) can be expressed as

$$|Z| = \sqrt{Z'^2 + Z''^2} \quad (45)$$

$$\tan \theta = Z'' / Z' \quad (46)$$

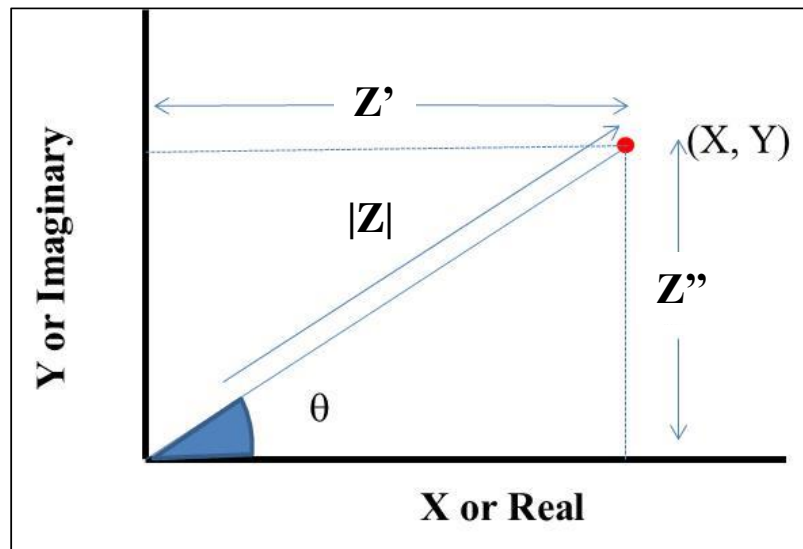


Figure 30. Schematic diagram showing a vector in terms of one (X and Y coordinates), two (angle (θ) and magnitude ($|Z|$) coordinates) and three (real (Z') and imaginary (Z'') coordinates).

Hence the impedance can now be expressed for various electrical elements, where the resistor, capacitor, and inductor have different impedance equations so that total impedance of a circuit can be determined. For elements in series, the total impedance is the vector sum of the individual impedances. For elements in parallel the admittance values are added together.

The impedance of a coating can be determined by reading and calculating from the plotted spectra. However, this is time consuming, a fitting model is used to obtain the equivalent circuit model and then the impedance. The plots give an indication of impedance (real and imaginary) component values and the phase shift behaviour as a function of frequency.

Painted metals can be expressed as electrical components of resistance, capacitance, inductive behaviour or shapes representing diffusion of reactants or products to and from the painted metal surface. It is important that the components are recognised in impedance plots so that values and models can be determined for painted metals.

2.9.2.2. Equivalent circuit models [96]

2.9.2.2.1. Equivalent circuit models of simple resistor (R), capacitor (C) connected in series.

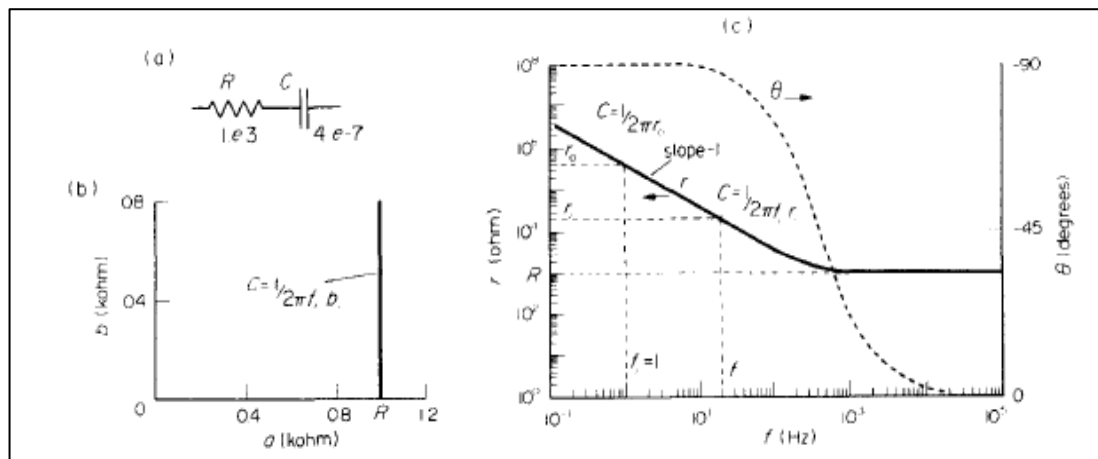


Figure 31. Schematic diagram showing an equivalent circuit containing RC in series
 (a). Nyquist (b) and Bode (c) impedance plots of this circuit.

Figure 31a shows a simple RC circuit connected in series, the components can be obtained from either the Nyquist or Bode plots (see Figs. 31b or 31c), which is illustrated in modulus impedance (solid line), and phase angles (dash line). A pure resistor has a single point on the a axis of the Nyquist plot, which is in the complex plane. For a pure capacitor, it has a vertical line at a = 0 and can be calculated by using the value of b at any frequencies (f) according to equation below.

$$C = 1/(2\pi fb) \quad (47)$$

In a Bode plot, the pure R has a straight line parallel to the log f axis which indicates that the impedance is independent of frequency and has no b value. The line then intersects at log modulus (r) axis. For a pure C, it has a straight line of slope -1 at log r, and can be determined from the modulus at any frequency where the slope of the curve is -1 (See Fig. 28c). The modulus is inversely related to frequency and the value of phase angle is -90° at all frequencies.

$$C = 1/(2\pi fr) \quad (48)$$

C can also be determined in a special case when f = 1Hz and r = r0 by using the equation in 55.

$$f=1, r = r0 = 1/(2\pi C) \quad (49)$$

The two components illustrated as a dashed line in phase angles, Bode plot show that at -90° represented a capacitor and at 0° represented a resistor.

A capacitor is made of two conducting plates separated by a non-conducting medium (dielectric). The values are dependent on the size of the plates, the distance between the plates, the properties of the dielectric medium, and is expressed as:

$$C = \epsilon_0 \epsilon_r A/d \quad (50)$$

ϵ_0 = Electrical permittivity (vacuum = 1)

ϵ_r = Relative electrical permittivity or dielectric constant (water = 80.1 F/m and organic coating = 4-8 F/m)

A = Surface area of one plate or sample (cm²)

d = distances between two plates or coating thickness (cm)

A simple RC circuit can be used to represent a metal exposed to an electrolyte and covered with an undamaged coating with a very high impedance. The coating behaviour is purely capacitive and the circuit model of the coating physical properties is shown in Fig. 32.

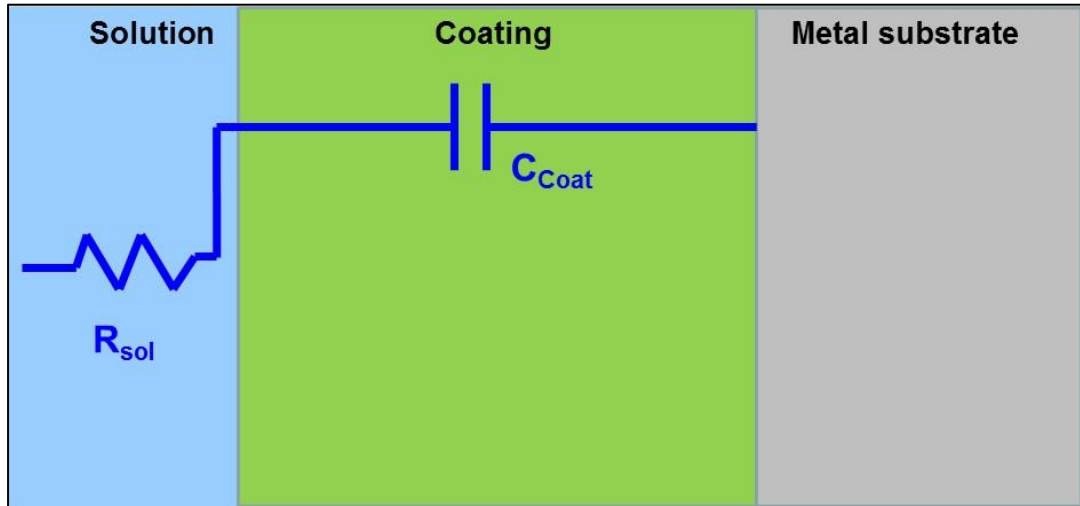


Figure 32. Schematic diagram showing coating physical properties circuit model of a perfect painted metal [97].

2.9.2.2.2. Equivalent circuit models of simple RC connected in parallel

In a simple RC circuit connected in parallel (See Fig. 33a), the Nyquist and Bode plots are different to the ones connected in series. Resistance is still determined using the Nyquist plot (See Fig. 33b) at the a axis of the end of the frequency arc shown as R and the capacitor is obtained at maximum b value by using the equation below.

$$f_{bmax} = 1/(2\pi RC) \quad (51)$$

$$C = f_{bmax} 2\pi R \quad (52)$$

In a Bode plot, the resistor is obtained from the straight line parallel to the log f axis and the intersecting the log r axis (see Fig. 30c). The capacitor is obtained by using the equation (59). The two components are illustrated as dashed line in Bode plot, phase angles show that at -90° represented a capacitor, and at 0° represented a resistor.

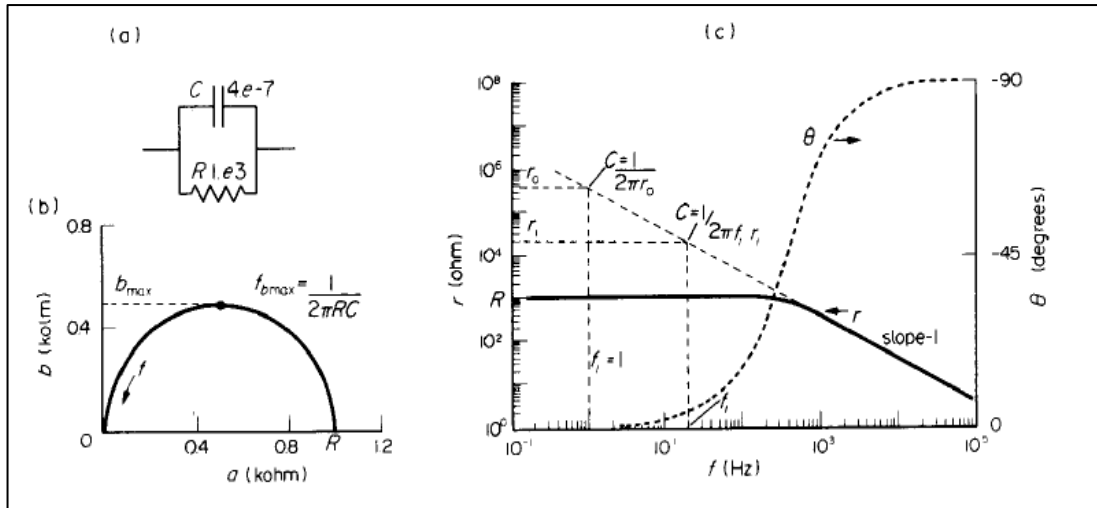


Figure 33. Schematic diagram showing an equivalent circuit containing RC in parallel (a). Nyquist (b) and Bode (c) impedance plots of this circuit.

2.9.2.2.3. Equivalent circuit models of metal/ solution interface (Randles cell)

Figure 34a shows an equivalent circuit model of the metal/ solution interface and the component values obtained from the Nyquist and Bode plots (See Figs. 34b or 34c), which is illustrated as modulus impedance (solid line) and phase angles (dashed line).

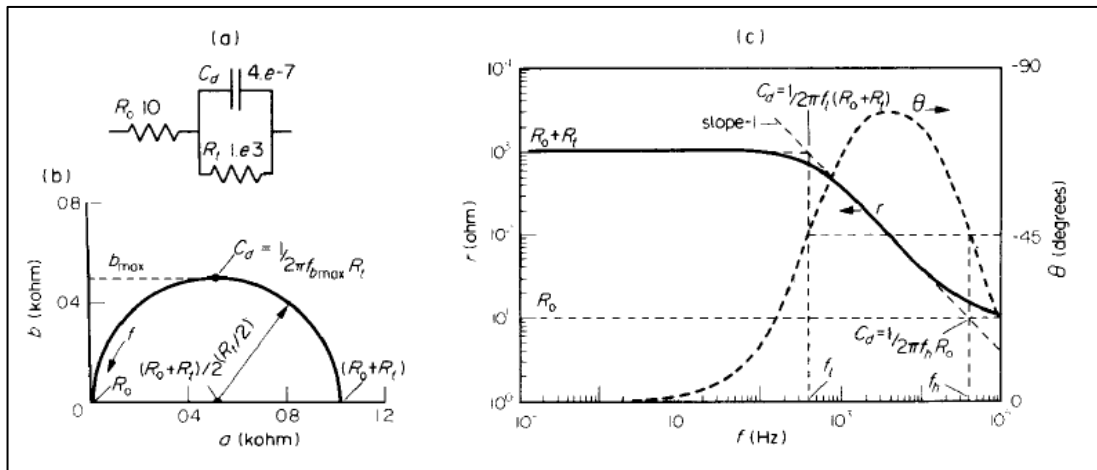


Figure 34. Schematic diagram showing an equivalent electrical circuit model of metal/ solution interface (a) and its Nyquist (b) and Bode impedance (c) plots.

The Nyquist plot shows a semicircle because the electrical components are connected in parallel. The resistance of the electrolyte solution (R_0) and surface film; R_t (metal charge transfer resistance) can be determined from the two end points of the semicircle. R_t represents the corrosion resistance of the metal in the absence of

diffusion/ adsorption processes and is obtained from $R_t + R_0 = \text{Total}$. C_d represents the electrical double layer capacitance at the metal/ solution interface and can be determined from equation (53) at maximum b value of the semicircle.

$$C_d = 1/2\pi f_{b_{\max}} R_t \quad (53)$$

The modulus, Bode plot shows that R_0 , and $R_0 + R_t$ can be determined from the two $\log r$ axis at low and high frequencies of the curve. The capacitor causes the curve to slope with a gradient of -1 between the two resistors at low and high frequencies. It can be calculated by using the equation in Fig. 34c. R_0 , and R_t are shown as dashed lines in the phase angle, Bode plot, and are represented as a dashed line approaching zero $\log r$ at low and high frequencies, in between them is the capacitive behaviour of C_d , which is rising towards -90° at intermediate frequencies.

Most paints degrade over time, water penetrates in the coating, and results in a new liquid/ metal interface with no corrosion activity. A Randles model and the circuit model of coating physical properties is used to model this behaviour (see Fig. 35).

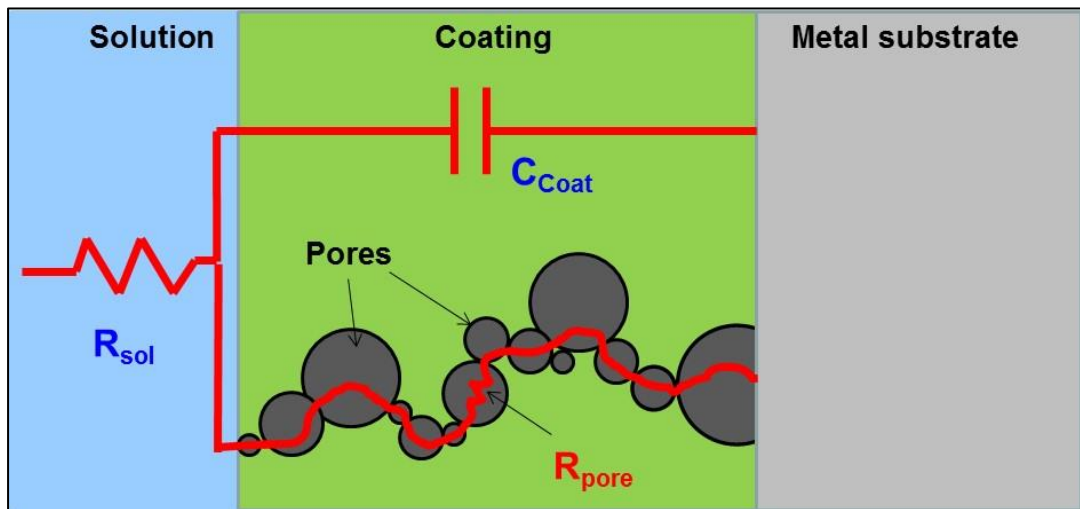


Figure 35. Schematic diagram showing coating physical properties circuit model of an intact painted metal [97].

2.9.2.2.4. Equivalent circuit models of painted metal

Mikhailovskii and co-workers first proposed an equivalent circuit model for the painted metal/ solution interface and included the paint film parameters to the circuit is shown in Fig. 37 [96] [98]. The components are:

R_0 represents the resistance of the electrolyte solution.

C_{pf} represents the capacitance of an intact film [99] and can be used to determine the water uptake of a coating in equation 54 [100].

$$X_v = \text{Volume \% H}_2\text{O} = 100 \log (C_t/C_0) / \log (80) \quad (54)$$

X_v = % of water absorbed in an organic coating

C_t = coating capacitance after some exposure time

C_0 = coating capacitance at time zero when the exposure begins

$\log 80$ = dielectric constant of water

Organic coatings do not behave as perfect capacitors. They leak over time and behave as a constant phase element expressed in equation (55).

$$Z_{CPE} = 1/C (j\omega)^{-n} \quad (55)$$

C = Capacitor (Farad)

j = imaginary unit $j = \sqrt{-1}$

ω = Angular frequency (rad s^{-1})

n = An exponent which equals 1 for an ideal capacitor. Non-ideal behaviour is <1 .

Zero represents an ideal resistor.

R_f represents the pore resistance of a film to electrolyte penetration [98] [99]. A lower resistance indicates the film has been penetrated by electrolyte and caused the film to be damaged. It can also be due to the influx of electrolyte to holes or pre-existing porous area due to inadequate crosslinking of the coating [96].

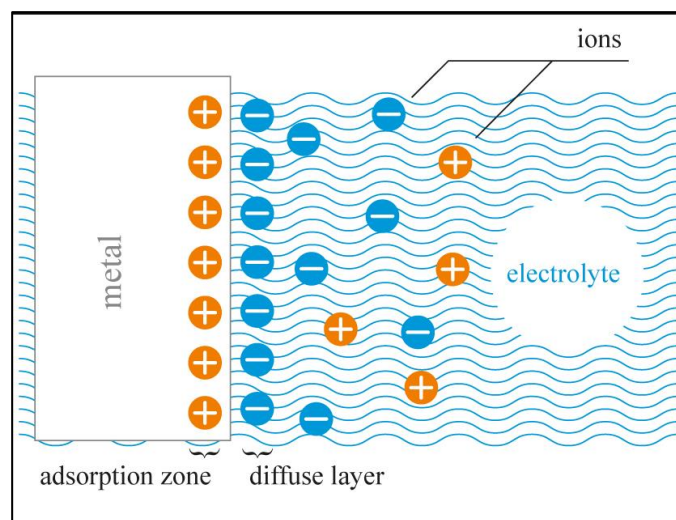


Figure 36. Schematic diagram showing an example of a double layer [101].

C_d represents the double layer capacitance of a coating. It exists at the interface between the metal and surrounding electrolyte. The ions of the double layer are formed by charge attraction to the metal surface and the charges between the two are separated (See Fig. 37). It also indicates the presence of water at the coating/ metal interface.

R_t represents the charge transfer resistance or polarisation resistance of the metal substrate to corrosion. It is inversely related to corrosion rate of the substrate and a lowering of this value indicates corrosion is occurring.

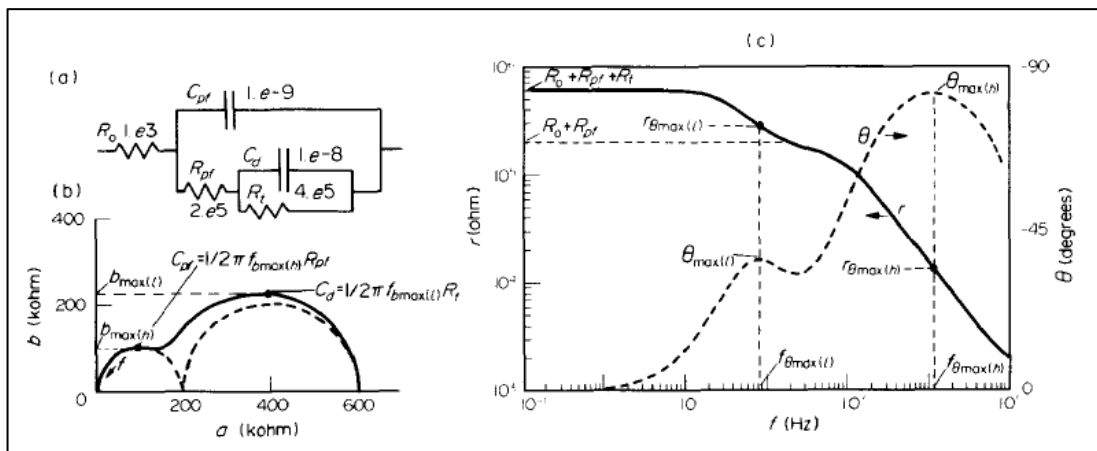


Figure 37. Schematic diagram showing an equivalent electrical circuit model of painted metal/ solution interface with distinctive separation of the paint film and metal components (a), and its Nyquist (b) and Bode impedance (c) plots.

Figure 37a shows an equivalent circuit model of painted metal/ solution interface and the component values obtained from the Nyquist and Bode plots (See Figs. 37b or 37c), which are illustrated in modulus impedance (solid line) and phase angles (dashed line). This time, the Nyquist plot is made up of two semicircles with time constants, unit in seconds for the paint film (τ_{pf}) and metal (τ_m) as expressed in equation below.

$$\tau_{pf} = R_{pf} C_{pf}; \quad \tau_m = R_t C_d \quad (56)$$

The first semicircle represents the paint film when $\tau_{pf} > \tau_m$, which in most cases occurs at higher frequencies. The second semicircle represents the metal at lower frequencies. The semicircles appear as two distinct shapes only as long as it follows the criteria below:

$$0.2 \leq (R_t / R_{pf}) \leq 5 \quad (57)$$

$$C_{pf}; \tau_m / \tau_{pf} \geq 20 \quad (58)$$

For two distinct semicircles to be apparent, equation 57 indicates that their diameters are similar to each other and the f_{bmax} values ($f_{bmax} = 1/2\pi\tau$) for each semicircle is not too close to one another as expressed in equation 58. If these two equations are not obeyed, there will be difficulty in distinguishing the two semicircles from each other, causing difficulty in determining the individual components of the equivalent circuit. This is clearly illustrated in Fig. 37, whereas Fig. 38 illustrates when the criteria is not met and separation is indistinct.

Figures 37c and 38c show the corresponding Bode plots of Figs. 37b and 38b, which contain three regions, higher frequencies represent information about the paint film and lower frequencies represents information about the metal. At the mid frequencies, a slope reduction at section of the log r curve is present and represents the separation of the semicircles in Figs. 37b and 38b. If equation 58 is not obeyed, the slope observed in Fig. 38c at $(R_0 + R_{pf})$ will not be distinguished enough to be seen in Fig. 38c. Instead a hump may be observed on the central upward slope of the Bode plot.

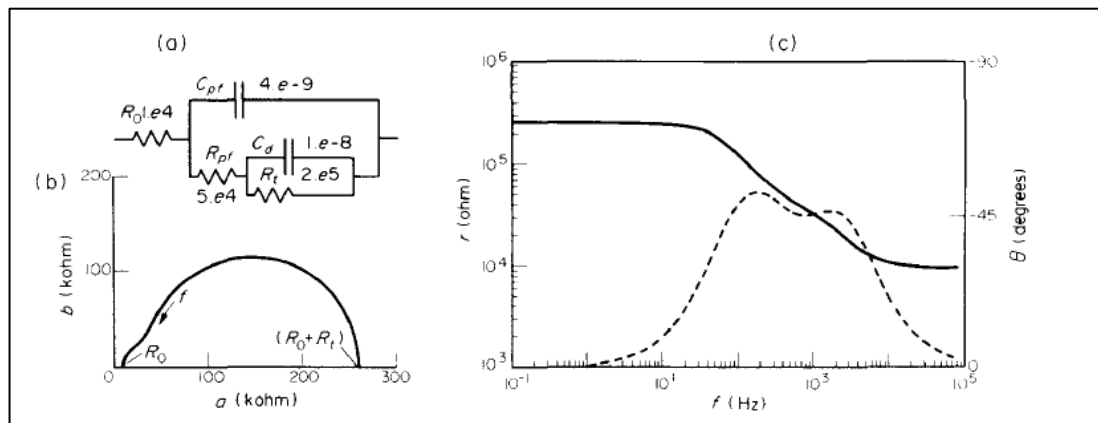


Figure 38. Schematic diagram showing an equivalent electrical circuit model of painted metal/ solution interface without distinctive separation of the paint film and metal components (a), and its Nyquist (b) and Bode impedance (c) plots.

The separation of the semicircles is clearly illustrated by the two phase angle maxima at $\theta_{max(l)}$ and $\theta_{max(h)}$ in the phase angle, Bode plot of Fig. 37c, but difficult to

obtain when they merge together in Fig 38c. However, the phase angle Bode plot is probably the most sensitive method for determining the presence of shape abnormality [96].

After some time, the new liquid/ metal interface formation causes the substrate to corrode and the circuit model of coating physical properties is used for this behaviour (See Fig. 39).

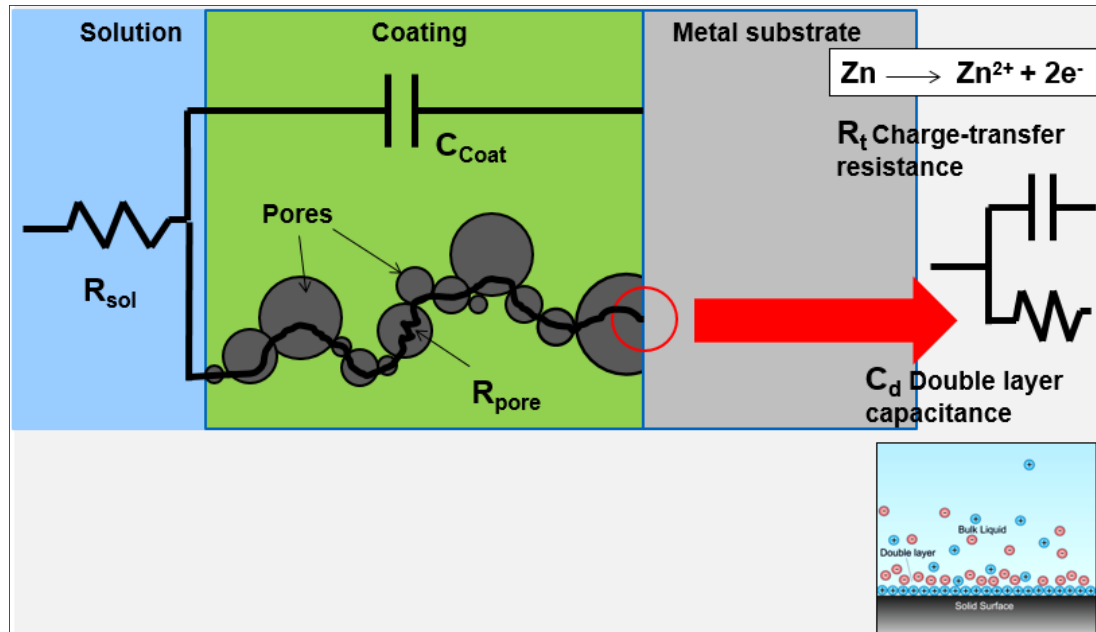


Figure 39. Schematic diagram showing coating physical properties circuit model of degraded painted metal [97]

2.9.2.2.5. Diffusion impedance

A model which includes Warburg impedance (Z_w) is normally required for a painted metal/ solution interface to represent the processes of diffusion within pores of painted film. Z_w is defined according to equation (61), connected in series with R_t but may or may not be parallel with the double layer capacitance.

$$Z_w = \sigma \omega^{-1/2} (1 - j) \quad (59)$$

σ = Warburg impedance coefficient (ohm s^{1/2})

ω = 2 π f (rad s⁻¹)

Figure 40a shows an equivalent circuit model of painted metal/ solution interface in the presence of a diffusion process and the component values obtained

from the Nyquist plot in Fig. 40b. Bode plots illustrating modulus impedance are in Fig. 40c and as phase angle in Fig. 40d. The component values are the same as in Fig. 37a and this time include Z_w , which range from 0 to 10^7 for σ values. In the Nyquist plot (Fig. 40b), the following curves are explained below.

Curve 1, where $\sigma = 0$, it is same as in Fig. 38a.

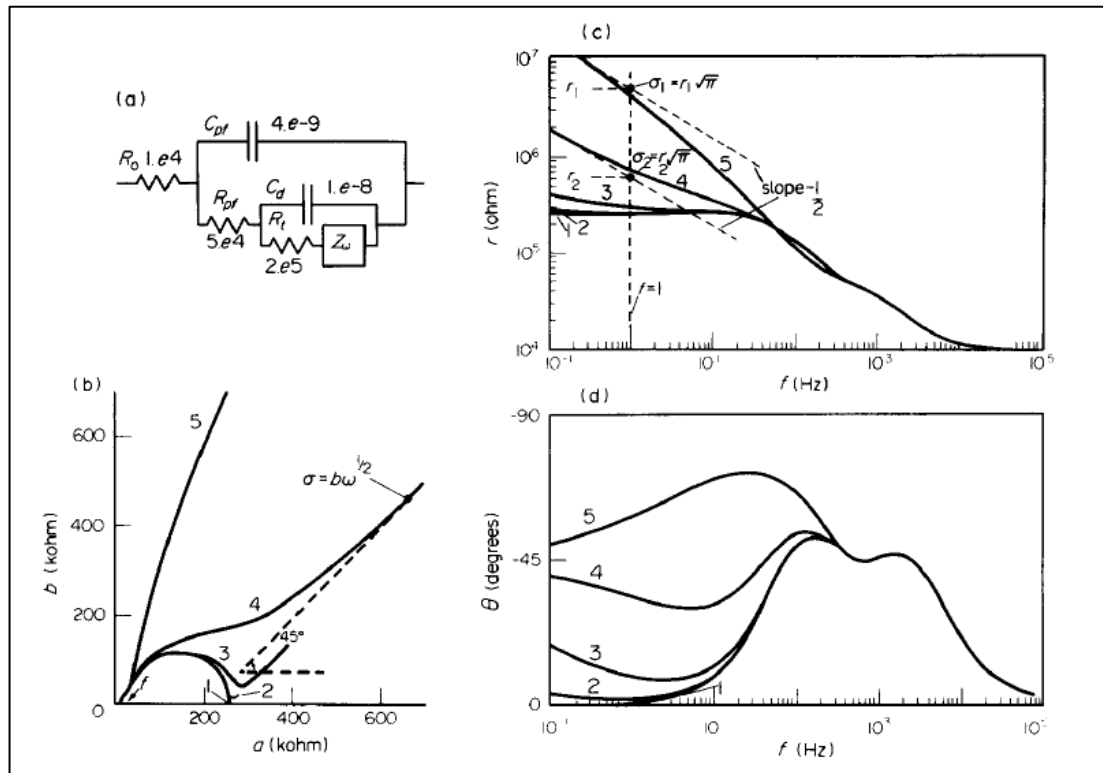


Figure 40. Schematic diagram showing an equivalent electrical circuit model of painted metal/ solution interface in the presence of diffusion (a) and the effect of varying diffusion coefficient on the curve shapes in Nyquist (b) and Bode impedance (c) plots

Curve 2, where σ has higher values than 0, at the second semicircle, a diffusion tail begins to appear at the low frequencies.

Curve 3, where σ values are similar to R_t , the diffusion tail starts to overlap the second semicircle.

Curve 4, where σ increases further, and the diffusion tail is more severe, and forms an incline at an angle of 45° to the axis at low frequencies.

Curve 5, where σ is significantly larger than R_t , the diffusion tail completely distorts the second semicircles. This occurs when the diffusion processes are slower than the metal charge transfer reaction.

Figures 40c and 40d show the corresponding Bode plots of circuit in Fig. 40a. When the $\sigma = 0$, no diffusion impedance is present, this is represented by curve 1, and the behaviour is purely resistive in Fig. 40c and the corresponding results in phase angle is a curve approaching zero in Fig. 40d. As diffusion impedance increases the spectra are no longer horizontal to the low frequencies axis resulting in curves going upwards, reaching a slope maximum of $-1/2$ for curve 4. The phase angles decrease from 0 down to -45° for increases in diffusion impedance in Fig. 40d.

If the diffusion impedance increases further and becomes significantly higher than R_t as in Fig. 40c, curve 5 at low frequencies around 0.3 Hz, a slope of $-1/2$ is formed which goes to a steeper slope at higher frequencies of up to 30 Hz. The equivalent phase angles in Fig. 40d of curve 5 then approach -45° at 0.1 Hz for low diffusion impedance.

2.9.2.3. EIS studies of coil coatings

There are number of EIS studies of coil coatings based on solventborne or waterborne systems are available to view [11] [32] [45] [71] [102] [103] [104]. However there was no research article found that is specifically about a pretreatment primer investigated by EIS. In this section a few examples of the work that has been done on coil coatings investigated by EIS are shown.

Three approaches have been used to study coatings by EIS [102]. The first approach is based on continuous submersion of architectural coatings in electrolyte solution, which ignores the real world situation. Some studies included dilution of electrolyte solution intended to simulate contaminated rain water or acid rain. This approach is one justification to use because it can accelerate coating failures to form disbondment, blistering in the undamaged areas and delamination at the edges of deliberately introduced scribe lines applied through the coating and into the substrate [32] [103] [105].

The second approach uses a modified dielectric sensor or a small device that has been dubbed a time-of-wetness sensor, which has only been tried by a few investigators. More recently, the third approach involved using a combination of EIS measurement during the exposure in salt spray chamber and QUV cabinet to simulate a real world situation [102] [106].

EIS data can be expressed as Nyquist and Bode of modulus and phase angle plots. A typical coil coating based on chromate (Cr) containing and chromate free (Cr-free) systems exposed over time can have the following spectra (See Fig. 41) [32]. Fig. 41a shows the Cr containing coil coating deteriorated over time in both modulus and phase angle Bode plots, which revealed a second time constant at the low frequency. Whereas the Cr-free coil coating shows no deterioration in the modulus Bode plot. The phase angle Bode plot is a more sensitive parameter and shows the coating is stabilising after 60 days of exposure.

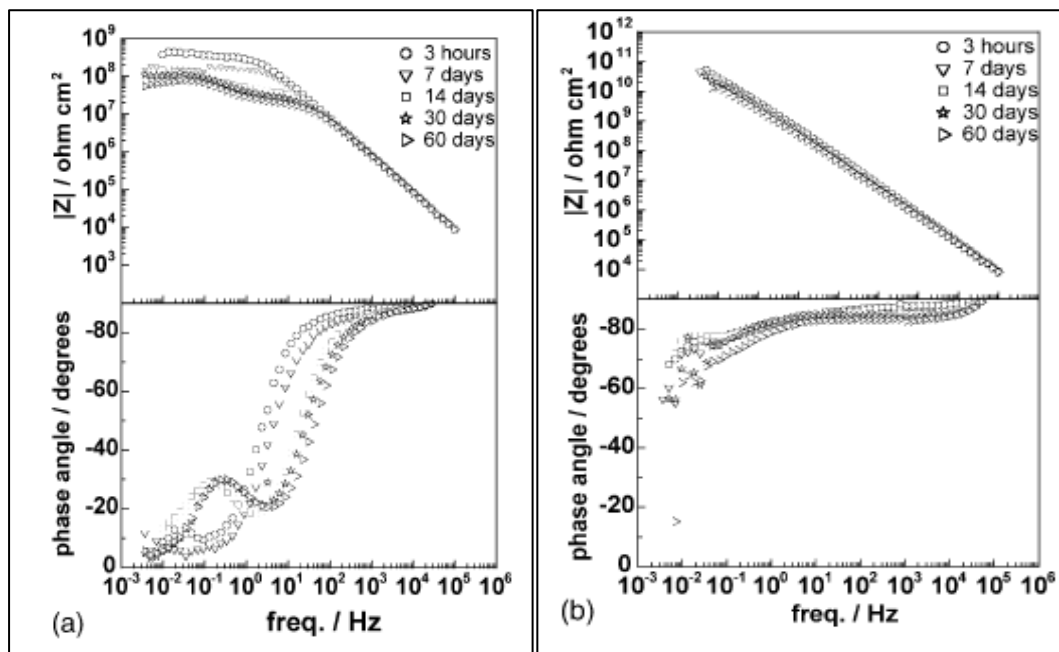


Figure 41. EIS spectra of (a) Cr containing and (b) Cr-free coil coating systems.

Another example was the work done by A. C. Bastos et al [107] where the formability of coil coatings was assessed by EIS exposure over time (See Fig. 42). Fig. 42a shows an unstrained sample exposed up to 50 days. In the modulus Bode plot the coating remained capacitive in response during the first 15 days of exposure and the resistance was above $10^{10} \Omega \text{ cm}^2$. At 21 days and beyond, the impedance decreased

significantly at the low frequency and revealed a reduction in coating protection. In the phase angle Bode plot, a second time constant appeared at the low frequencies, revealing the existence of corrosion underneath the coating at exposure times of 30 and 50 days.

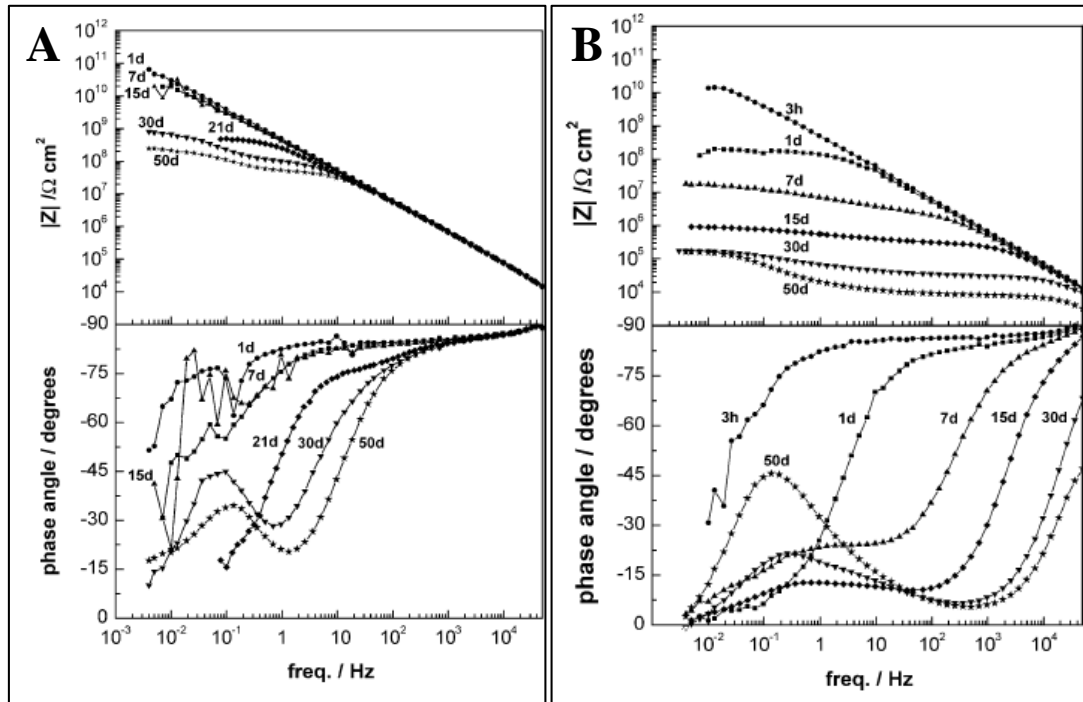


Figure 42. EIS spectra obtained for an unstrained (a) and strained (b) coil coatings exposed for 50 days.

Fig. 42b shows a strained sample with 19% uniaxial elongation exposed for 50 days. In the first stage, the coating has a capacitive response and over a short time developed into a second time constant as the total impedance of the system decreased rapidly from 3 hours onward. The impedance of the strained sample was $10^{10} \Omega \text{ cm}^2$ compared to $10^{11} \Omega \text{ cm}^2$ for the unstrained sample in the first stage of submersion. It decreased more rapidly over time and the coating resistance reached values of approximately $10^4 \Omega \text{ cm}^2$, which revealed a highly degraded coating with corrosion products.

The performance of coatings tested over time can be assessed by using approximately nine EIS data parameters, three are available from the Bode phase plot and up to six are available from the Bode modulus plot [102]. The six selected for this investigations are: (a) water uptake (X_o), (b) the total or maximum impedance ($Z_{0.1\text{Hz}}$)

which is usually measured at 0.1Hz, (c) film resistance (R_{pf}), (d) coating capacitance (Q_{pf}), (e) polarisation resistance (R_t) and (f) double layer capacitance (Q_d). The water uptake was determination using Brasher and Kingsbury equation [100]. The other five parameters were determined by using a fitting software for data analysis.

2.9.3. Focused ion beam/scanning electron microscope

Scanning electron microscopy (SEM) has been in use since 1942, described by Zworykin et al [108]. It was commercialised in 1965 and tens of thousands of SEMs are in use today [109]. The basic SEM instrument consist of a vacuum system and chamber, an electron source, an electron column, a sample stage, detectors, and a computer to run the complete instrument as illustrated in Fig. 43.

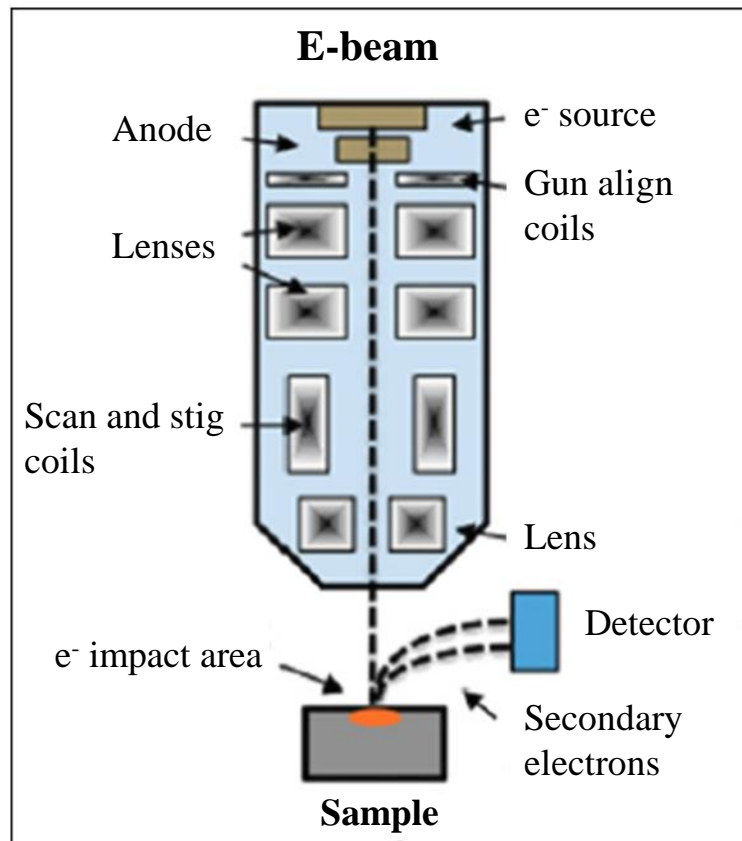


Figure 43. Schematic diagram showing typical components of a scanning electron microscope system [110].

It allows the observation of surfaces of materials by scanning them with a beam of focused electrons. The primary beam interacts with the sample and produces secondary electrons which are low energy electrons that are detected using an Everhart-Thornley detector. This is the most common imaging mode in use and it generates primarily topographical information. For imaging of contrast between areas with different chemical composition, backscattered electron detection is used which can discriminate elements of differing atomic number. High atomic number elements appear brighter than low atomic number elements due to the greater number of

backscattered electrons produced. Characteristic X-rays and other photons of various energies can also be detected [108] [109]. The images displaying the topography of the surface can range from 2D to 3D-like models at typical lateral resolution of 1-5 nm for a field emission electron source (emission of electrons induced by an electrostatic field) and 10-50 nm for a tungsten electron source (emission of electrons by a tungsten filament in a low pressure mercury gas discharge lamp) [108]. For X-rays, the typical lateral resolution is between 0.2 and 5 μ m. The resolution depends on the atomic number of the element, as well as its density, and the accelerating voltage of the SEM [108].

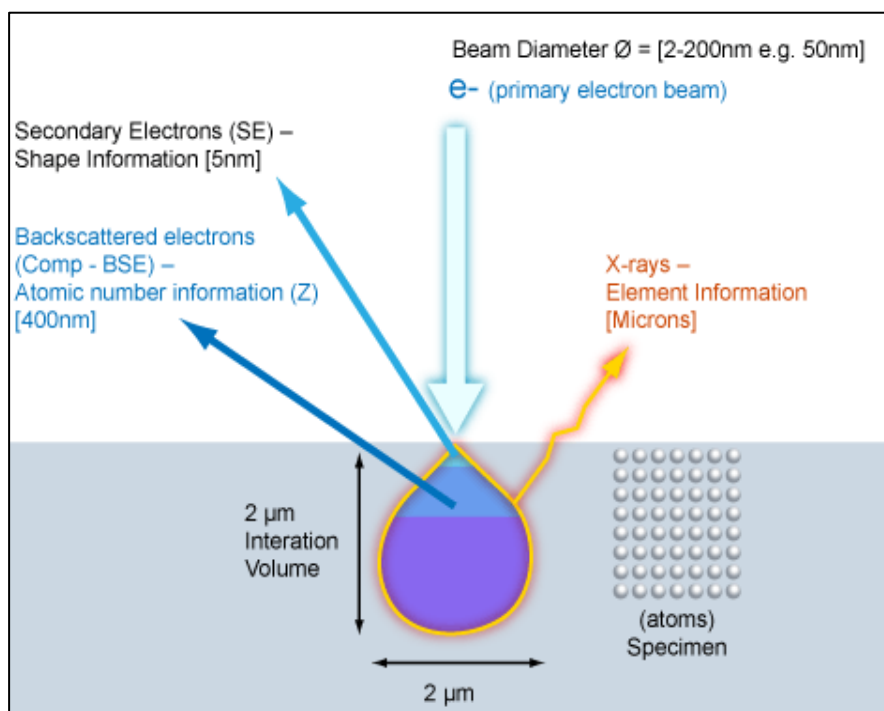


Figure 44. Schematic showing spatial resolution of SEM sources [111].

Figure 44 shows the interaction volume of an SEM. At the surface of the sample or topmost part of the interaction volume, secondary electrons are produced, and the typical spatial resolution is around 5 nm. In the top half of the interaction volume, backscattered electrons are produced, and the typical spatial resolution is around 400 nm. The whole of the interaction volume generates X-rays and the typical spatial resolution is of the order of a few micrometres.

The focused ion beam (FIB) systems have been in use since the 1970's [112]. The instrument consists of a vacuum system and chamber, a liquid metal ion source,

an ion column, a sample stage, detectors, gas delivery system, and a computer to run the complete instrument as illustrated in Fig. 45.

FIB typically use a beam of finely focused gallium (Ga^+) ions at a range of energies which allow the FIB to make a precise cut or cross-section, take an immediate image, and deposit conductive or insulating materials onto the sample surfaces [113] [114]. However, the destructive nature of ion beam (Ga^+) imaging is a major drawback. [114]. The technique is used extensively in the semiconductor industry for the fabrication of modern semiconductors and other types of electronics by imaging and nano-machining of devices [115] [116] [117].

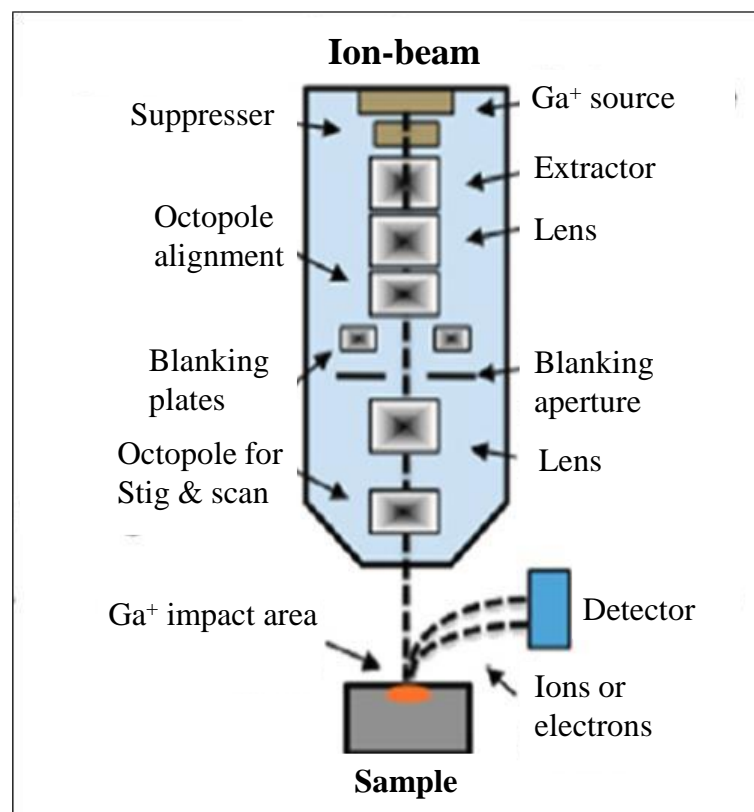


Figure 45. Schematic diagram showing typical components of a focused ion beam system [110].

These two techniques, SEM and FIB have been combined in the last twenty years and used to locate and analyse sub-surface defects. A combined system allows samples to be prepared, imaged, and analysed resulting in saved time and opening up new application areas. The ion beam is primarily used for precision milling (destructive for imaging) and electron beam for non-destructive, high resolution

imaging, and monitoring of the cross-section face while the FIB removes material, known as ‘milling’ [113]. The two beams complement each other in protective depositions, delineation of cross sections, charge reduction, and imaging information [114]. Also included is the ability to perform microanalysis of an area of interest using energy dispersive X-ray spectroscopy (EDS), which gives elemental information about the sample [113].

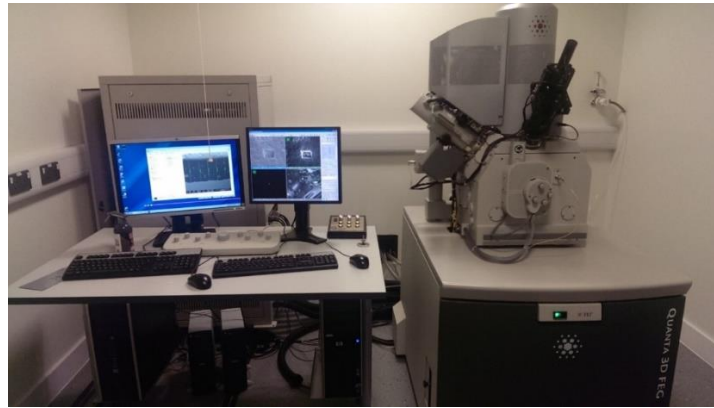


Figure 46. Photograph showing an FEI Quanta 3D FEG FIB/SEM system.

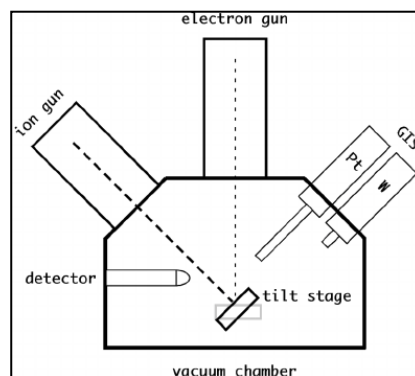


Figure 47. Schematic diagram showing a FIB/SEM system [118].

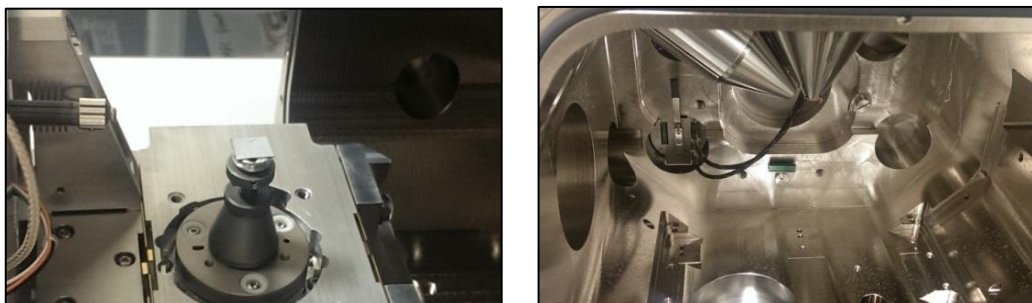


Figure 48. Photographs showing a stage with a sample (left) and chamber containing different sources (right).

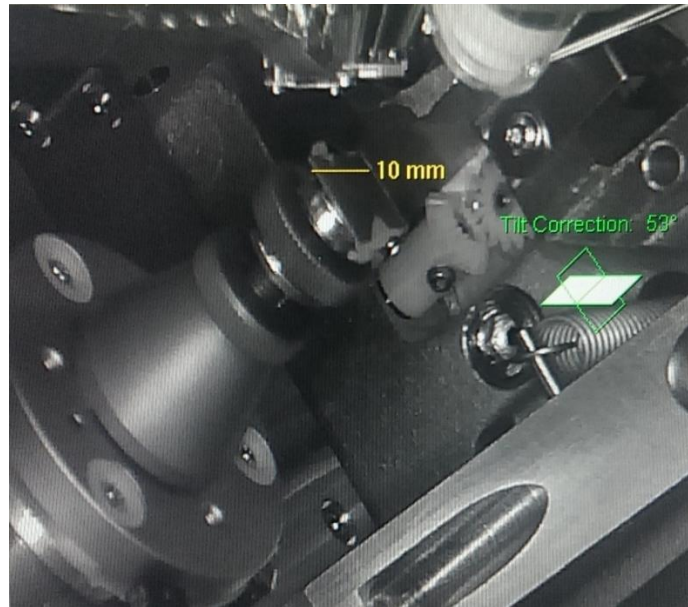


Figure 49. Photograph showing a sample tilted at 53° for milling.

FIB/SEM has the ability to reveal small voids or other fragile features without causing significant surface damage to samples as compared to conventional mechanical sectioning methods. The biggest drawbacks are that only small samples can be machined and the process is very time consuming. Other problems associated with the technique are related to charge damage and artefacts that can be generated due to striations and redeposition [114]. However, steps can be taken to minimise these problems by altering the accelerating voltage, and beam current.

Much of the published work related to FIB milling has reported the preparation of samples for transmission electron microscopy (TEM) [119] and also investigating cross-sections of different materials [120]. Typically, the work has been applied to inorganic systems. For polymeric materials, a limited number of investigations have been reported on polymer film thicknesses, the characterisation of aluminium spheres dispersed in a low density polyethylene matrix, and the damage caused to polycarbonate by FIB [117] [120] [121] [122].

FIB/SEM will be used to prepare cross-sections of corroded sample by milling, and then imaging and analysing the corrosion products.

Chapter 3. Methodology

3.1. Materials

3.1.1. Steel substrates

HDG steels supplied from Tata steels were used as substrates. The two different types of HDG steels supplied were:

- 1) Unpretreated HDG steel with a 15 μm galvanised (zinc) layer each side.
- 2) The steel supplied was already coated with a chromate-free primer. The substrate was pretreated with chromate-free 1455T conversion coating which is mainly made of phosphoric acid with titanium/ zirconium fluoro complexes and water soluble polymers.

The thicknesses of the steels were between 0.49 mm and 0.69 mm and the galvanised layer was between 15 and 20 μm . The unpretreated substrates are normally greased with oil to prevent corrosion.

3.1.2. System information

System	Substrate	Conversion coating	Primer	Topcoat
1	HDG	Cr-free pretreatment	Solvent-borne PE/Melamine primer with Cr-free anti-corrosive pigment (calcium ion exchange silica) BP 243TU	Solvent-borne PE/Melamine
2	HDG	No	Water-borne pretreatment primer clear without anti-corrosive pigment	Solvent-borne PE/Melamine
3	HDG	No	Water-borne pretreatment primer with Cr-free anti-corrosive pigment (calcium ion exchange silica)	Solvent-borne PE/Melamine
4	HDG	No	Water-borne pretreatment primer with Cr-free anti-corrosive pigment (calcium ion exchange silica) and Passivation	Solvent-borne PE/Melamine

Table 3. Information of the 4 systems.

3.1.3. Primer information

System	Primer	Composition
1	Solvent-borne PE/Melamine primer with Cr-free anti-corrosive pigment (calcium ion exchange silica) BP 243TU	Organic/others = 71.4% TiO ₂ = 17.7%; C303 = 7.4% (Ca = 0.2%) SiO ₂ = 2.0%; H ₃ PO ₄ = 0.95% S(=O) ₂ --OH = 0.25%; DBTL = 0.3%
2	Water-borne pretreatment primer clear without anti-corrosive pigment	Organic/others = 96.78% C ₂ H ₃ PO ₃ H ₂ : CH ₂ =CHCO ₂ H = 2.92% Phosphate type dispersant = 0.26% Na sulphosuccinate type wetting agent = 0.04%
3	Water-borne pretreatment primer with Cr-free anti-corrosive pigment (calcium ion exchange silica)	Organic/others = 73.7%; C303 (SiO ₂) =23.3% (Ca=0.70%) C ₂ H ₃ PO ₃ H ₂ : CH ₂ =CHCO ₂ H = 3.0%
4	Water-borne pretreatment primer with Cr-free anti-corrosive pigment (calcium ion exchange silica) and Passivation	Organic/others = 75.04% C303 (SiO ₂) =21.44% (Ca=0.64%) H ₃ PO ₄ =0.28%; H ₂ F ₆ Ti=0.24%. C ₂ H ₃ PO ₃ H ₂ : CH ₂ =CHCO ₂ H = 3.0%

Table 4. Composition of the 4 primers.

The primers of systems 2, 3, and 4 (See Table. 4) were manufactured and supplied by Beckers. Vinyl phosphonic acid/ acrylic acid copolymer formula is shown below:

Vinyl phosphonic acid: C₂H₃PO₃H₂

Acrylic acid: CH₂=CHCO₂H

3.1.4. Topcoat

The topcoat used was a polyester/ melamine crosslinked with acid catalysed reaction (372/0718) manufactured and supplied by Beckers.

3.2. Cleaning of substrate

A Waltons of Radcliffe guillotine was used to cut the untreated HDG steel to the required dimensions. It was paramount to have a clean surface before paint application whereby the oil, grease, organics, and oxides are removed from the substrates so that optimum adhesion of paints to the substrates can be achieved. To achieve this, the panels were placed into a Rotatherm cleaning tank, manufactured by

Matthes-Maschinen Industrietechnik (See Fig. 50). The panels were placed inside the cleaning tank, spray with $\leq 10 \mu\text{S}$ deionized water (DI) at 1 bar pressure for 20 seconds at a temperature of 50 °C. After cleaning, the panels were taken out of the cleaning tank, and dipped into a rinse tank containing DI water and this was repeated 3 times. A final rinse with sprayed DI water for 5 seconds was used to ensure all the cleaning solution was rinsed away. The water was blown off using a Legris air gun until completely dried surface of substrate was obtained.



Figure 50. Photograph showing a cleaning tank with DI water collection.

3.3. Paint application, panel preparation, and EIS cell constructions.

3.3.1. Paint application and panel preparation.

The pretreatment primers were applied onto the cleaned metal panels using a RDS 10 stainless steel wire rod to give a dry film thickness (DFT) of 4 μm . The panels were baked in a high efficiency R&D Bird air-circulated convection oven at a temperature of 270 °C for 10 seconds, which correlated to a peak metal temperature (PMT) of 99 °C measured by using Thermax stripes. The coated panels were quenched on a magnetic metal block and left to cool.

A polyester/melamine topcoat was applied onto the primed coated panels using a RDS 28 bar to give a DFT of around 20 μm . The panels were baked in the oven at temperature of 270 $^{\circ}\text{C}$ for 35 seconds, which correlated to a PMT of 216 $^{\circ}\text{C}$. The coated panels were quenched in a cold water bath and then dried with an air gun. The panels were then cut to required dimension and then put on tests for EIS, neutral salt spray, humidity, and outdoor exposure at Bohus Malmön, Sweden. Panels for system 2 to 4 were cut to 130 mm x 250 mm. Panels for system 1 were cut to 150 mm x 220 mm.

3.3.2. Preparation for EIS cells on panels.

The top left corner of both sides of the coated panel was sanded with a P120 coarse grit paper initially and then smoothed with a P1200 fine grit paper (See Fig. 51). It was essential to remove all of the coating so that perfect connection with the working electrode was obtained otherwise interference was observed in the EIS spectra. An acrylic tube with area of 13.85 cm^2 was placed on top on the panels and sealed with beeswax. The beeswax was melted using a hot plate and then applied by a small paint brush onto the acrylic/ panel area. This process was repeated 3 times for each panel.



Figure 51. Photograph showing a panel of system 1 with 3 cells.

3.3.3. Preparation for EIS cells on panels exposed in humidity and neutral salt spray chambers.

The top left corner of both sides of the coated panel was sanded with a P120 coarse grit paper initially and then smoothed with a P1200 fine grit paper (See Fig. 52).



Figure 52. Photographs showing system 1 panel of which one was unexposed (left) and the same one after exposure in humidity with a cell sealed with Blu Tack (right).



Figure 53. Photographs showing system 1 panels were unexposed (left) and the same one after exposure in neutral salt spray with a cell sealed with Blu Tack (right).

It was essential to remove all of the coating so that perfect connection with the working electrode was obtained. An acrylic tube with area of 13.85cm² was placed on top on the panels, marked, and sealed with Blu Tack. Blu Tack was used so that the cell can be deconstructed without causing damage to the coated panels and then returned back on exposure. Whereas beeswax will affect this. Care in construction of cells was needed to ensure perfect seal. This process was repeated twice for each panel.

3.3.4. Preparation for EIS cells on panels exposed in Bohus Malmön

The top left corner of both sides of the coated panel was sanded with a P120 coarse grit paper initially and then smoothed with a P1200 fine grit paper (See Fig. 54). It was essential to remove all of the coating so that perfect connection with the working electrode was obtained. An acrylic tube with area of 13.85 cm² was placed on top on the panels, marked, and sealed with Blu Tack. Care in construction of cells was needed to ensure perfect seal. This process was repeated twice for each panel. Two panels were prepared for each system. One panel was for South facing and the other one was for North facing, which was bend on the top left and right corners (See Fig. 54, right side). This allows the panel to hang onto a rack at 90°.



Figure 54. Photographs showing South (left) and North (right) facing panels of system 1.

3.3.5. Degree of blistering assessment

The panels exposed in accelerated and outdoor weathering were assessed for the degree of blistering using ISO 4628-2:2003 where the classification is based on the size and quantity of the blisters. The blisters size start from the smallest, 2 to the largest, 5 and the quantity start from fewest, S2 to densest, S5 (See Figs. 55 & 56 showing examples of size 2 and 5 classifications).

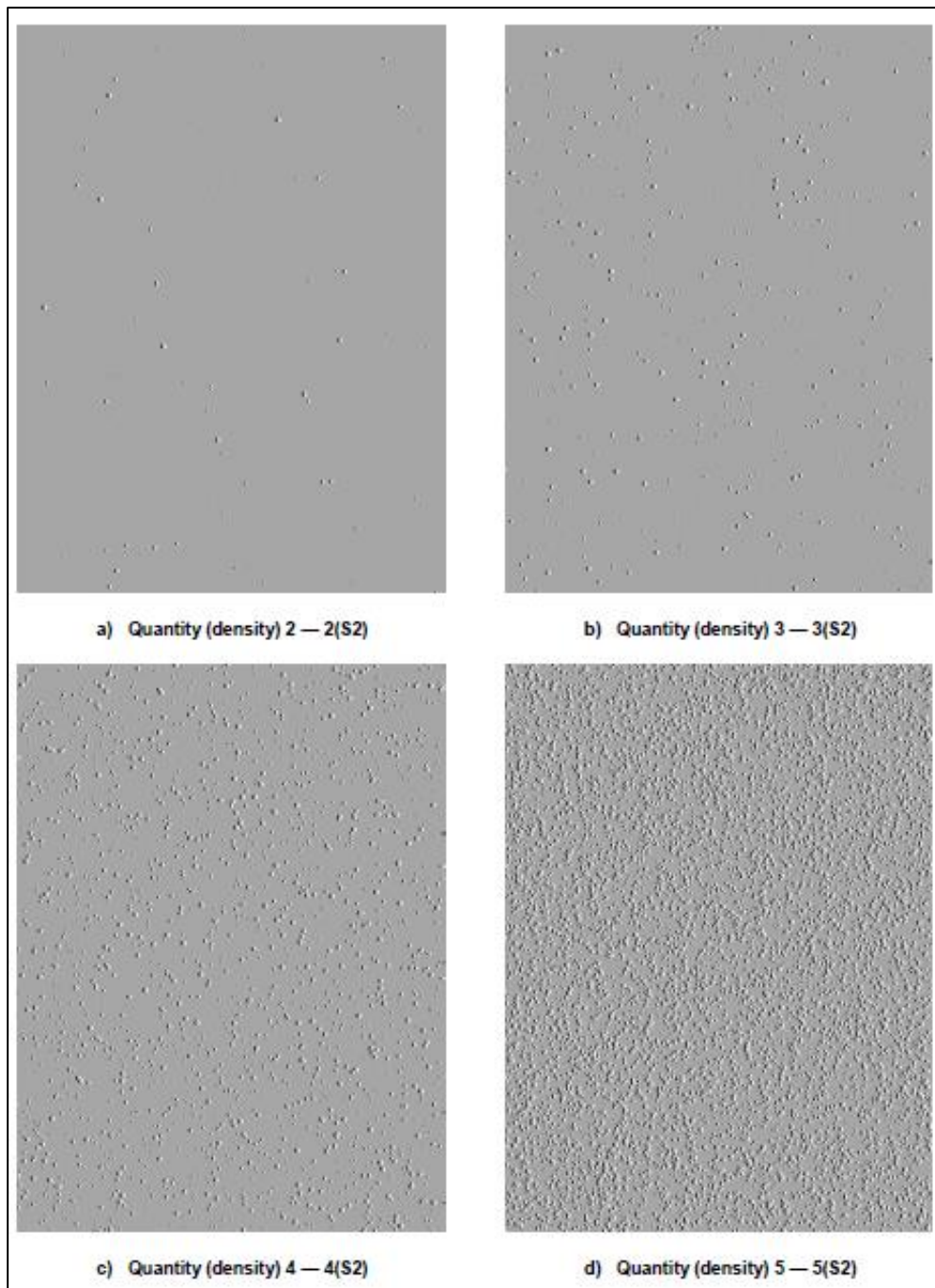


Figure 55. Illustration of blisters size 2 classification.

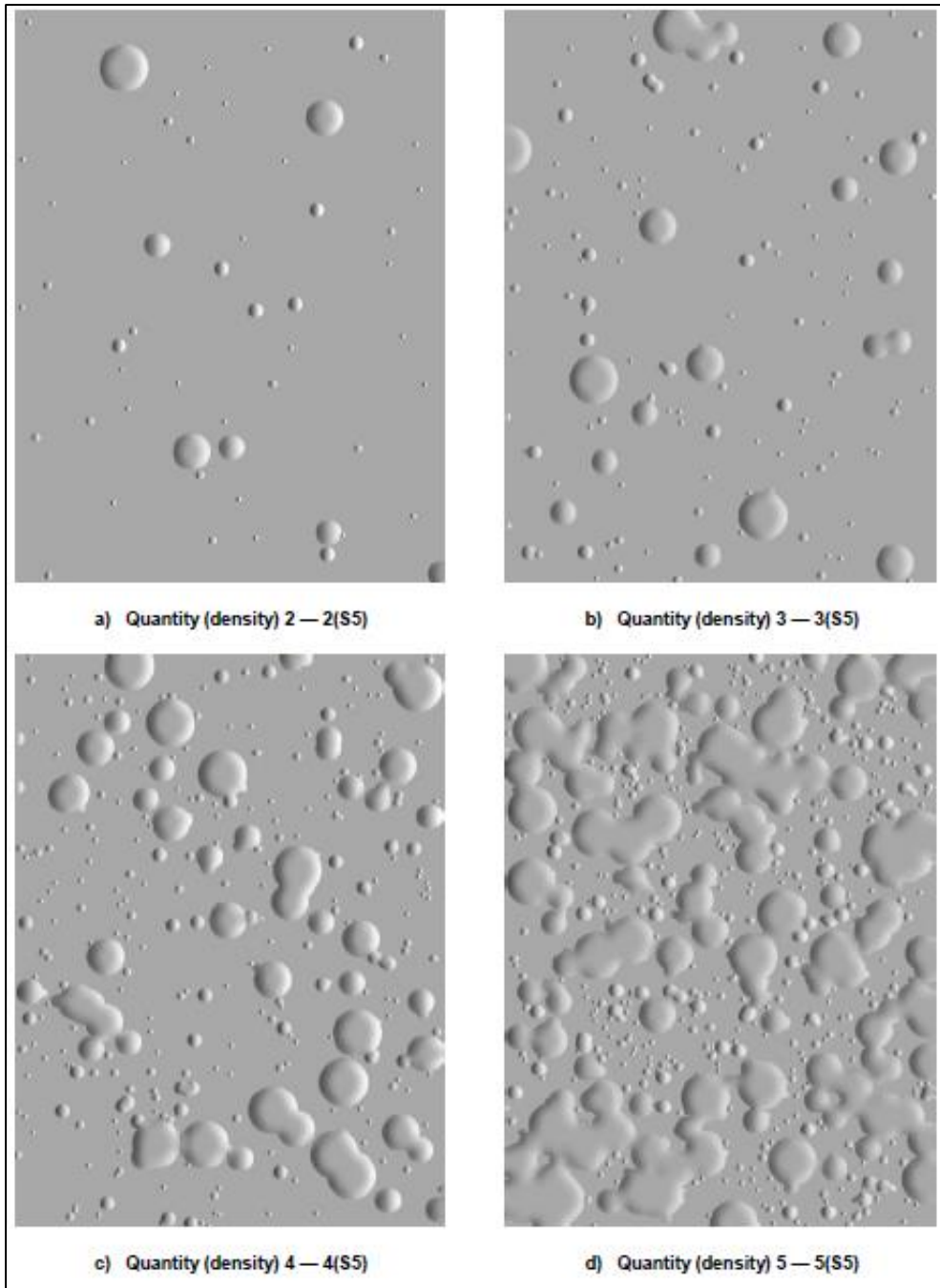


Figure 56. Illustration of blister size 5 classification.

3.4. EIS measurements of coated panels

3.4.1. EIS measurement of a dummy cell

A Princeton Applied Research dummy cell consisting of a capacitor and two resistors was measured at the start of each day of investigations to ensure that the Parstat 2273 potentiostat and the connection electrodes are working correctly. Furthermore, the procedure could detect if there was any other interference from the environment, such as electricity from the mains, and other electronic equipment.

A signal amplitude alternating voltage (AV) of 10 mV root mean square (rms) with respect to the open circuit potential (OCP) was applied to the dummy cell from the counter electrode. The perturbations were applied over a frequency range between 10 mHz to 100 kHz and the response recorded as 60 data points. The raw data expressed as Nyquist and Bode plots was compared to the results given by the manufacturer and if the results were not the same corrections were needed.



Figure 57. Photograph showing a dummy cell with connection points for the different electrodes.

3.4.2. EIS measurements of coated panels with cells.

Each cell was filled with a solution of 2.9 %w/v (0.5M) sodium chloride and then connected to a Parstat 2273 potentiostat with a lock in amplifier. A 5 minute delay was used before each measurement to allow the system to stabilise. The measurement was made using a classical three electrodes arrangement consisting of a saturated

Calomel electrode (+0.242 V vs. SHE), a platinum counter electrode, and the test sample as a working electrode (See Fig. 58).

A signal amplitude AV of 10 mV rms with respect to the open circuit potential was applied to the sample from the counter electrode. The saturated Calomel electrode and the sample substrate were used to monitor the resulting voltage response. The perturbations were applied over a frequency range between 10 mHz to 100 kHz and the response recorded as 60 data points. The raw data were expressed as Nyquist and Bode plots. EIS measurements were made at 0, 24, 48, 72, 96, 192, 240, 408, 504, 750, and 1000 hours. After EIS measurements, the cells were covered with a Parafilm M made by Bemis to prevent evaporation of the electrolyte solution.

3.4.3. EIS measurements of coated panels exposed in neutral salt spray and humidity chambers.

Each cell was filled with a solution of 2.9 % w/v (0.5M) sodium chloride and then connected to a Parstat 2273 potentiostat with a lock in amplifier. The measurement was made using a classical three electrodes arrangement consisting of a saturated calomel electrode (+0.242V vs. SHE), a platinum counter electrode, and the test sample as a working electrode.

A signal amplitude AV of 10 mV rms with respect to the open circuit potential was applied to the sample from the counter electrode. The saturated calomel electrode and the sample substrate were used to monitor the resulting voltage response. The perturbations were applied over a frequency range between 10 mHz to 100 kHz and the response recorded as 60 data points. The raw data were expressed as Nyquist and Bode plots. Also measured was the open circuit potential of each cell by using a Thander TM 531 multimeter and a Parastat 2273.

The panels were measured by EIS at the start (unexposed) and then placed back in the salt spray chamber for testing whereby the panels were sprayed continuously with 50 g/l sodium chloride solution at a constant temperature of 35 °C and pH around neutral. Before doing so, the temporary three cells were taken off the panels and the top left corners of the panels were covered with a PET film containing adhesive to

allow it to stick to the panel and stop the substrates being exposed to the testing environments. This was repeated at 24, 48, 72, 96, 192, 240, 408, 508, 750, and 1000 hours.

Panels exposed to humidity were measured and tested the same way as neutral salt spray panels. Only difference was the testing environment, whereby the panels were subjected to a continuous fog of 100 % relative humidity at 40 °C.

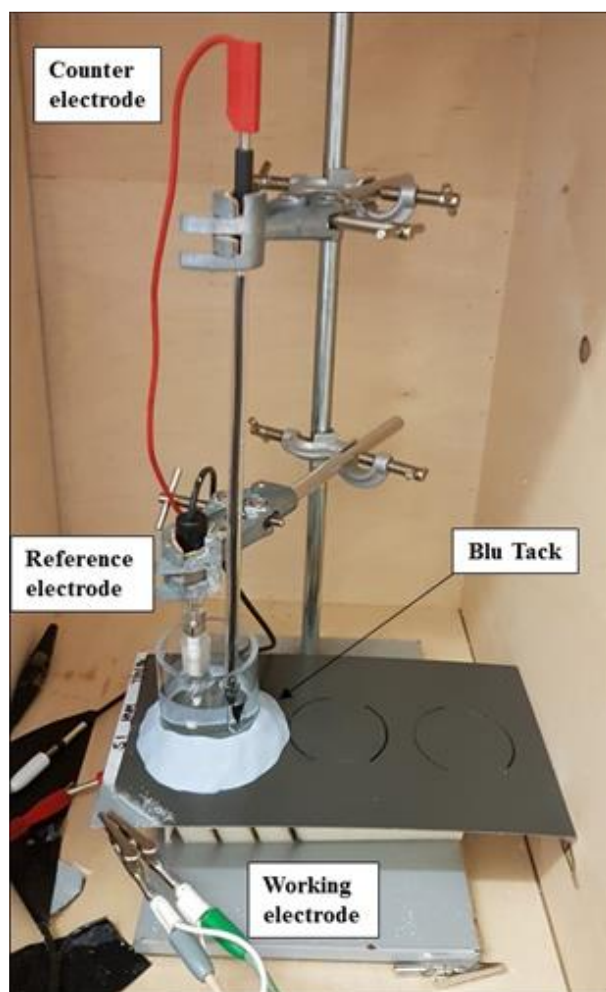


Figure 58. Photograph showing a classical three electrodes arrangement consisting of a saturated Calomel electrode (+0.242 V vs. SHE), a platinum counter electrode, and the testing sample as a working electrode.

3.4.4. EIS measurements of coated panels exposed in Bohus Malmön

The panels were measured by EIS using the same procedure as in 3.3.3. Once measured the temporary cells were taken off the panels and the top left corner of the panels were covered with a PET film containing adhesive to allow it to stick to the

panel and stop the substrate being exposed to the testing environments. The panels were then sent to Bohus Malmö for outdoor exposure, returning each year for EIS measurements. It takes about 2-3 weeks to measure, assess, and return the panels back to Bohus Malmö. A total of 2 years was exposed and measured for North and South facing panels.

3.4.5. Fitting of Nyquist and Bode spectra

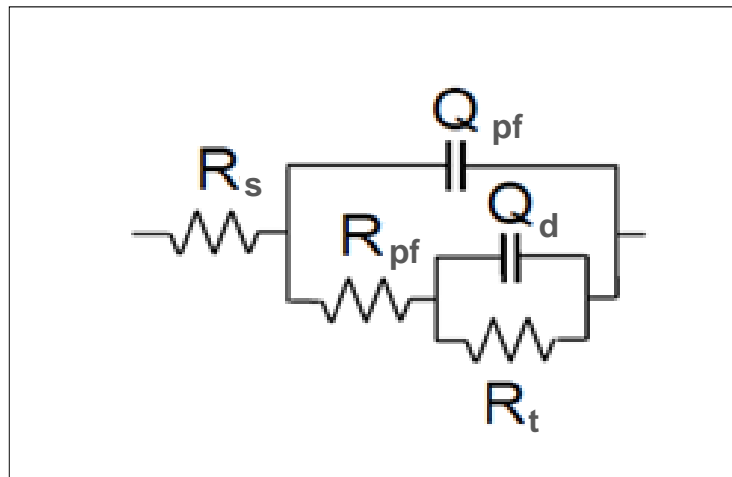


Figure 59. Schematic diagram showing an equivalent circuit model used for fitting.

[107]

ZSimpWin 3.22 fitting software was used to analyse the EIS spectra. They were fitted to an equivalent circuit model in Fig. 59 where R_s represented the solution resistance, R_{pf} represented the film resistance, R_t represented the charge transfer resistance, Q_{pf} represented the film capacitance and Q_d represented the double layer capacitance.

Organic coatings do not behave as perfect capacitor. They leak over time and produce depressed semicircles in the Nyquist plot, so in order to best fit these behaviours the capacitances are replaced with constant phase elements (Q) expressed in equation 55.

Equation 60 was used to determine the capacitance of the film. Q_{pf} was not used for water uptake determination because of the high errors obtained in the fitting model. Calculated film capacitance was used instead.

At the apex of the semicircle: $\omega_{\max} = 1/CR_f$ [123] (60)

% water uptake [100]: $X_v = 100 \log (C_m/C_{m,0}) / \log 80$ (61)

Whereby X_v = volume percent of water

C_m = measured capacitance at any time t

$C_{m,0}$ = measured capacitance at zero time

3.5. FIB/SEM

3.5.1. Development of FIB/SEM technique to observe corroded coated panels

3.5.1.1. Samples

A 0.7 mm thick sample of pre-painted HDG steel was used in this investigation. The paints (topcoat and primer) on top of the treated HDG steel are based on saturated polyester resins thermally cross-linked with melamine. The reaction between the resin and cross-linker is an acid catalysed transesterification [93]. The other components in the paints are solvents, pigments, and additives.

The sample was cut to dimensions of 10 mm x 10 mm using an Excel 2BR6 ab guillotine. One edge of the sample was then hand polished with a circular movement on MetPrep silicon carbide abrasive paper discs wetted with tap water. A P120 coarse grit paper was initially used and then fine polished with a P1200 grit paper. Polishing was needed to eliminate the damage to the pre-painted metal caused by the guillotine during cutting. The sample was then mounted onto an SEM stub using carbon cement with the topcoat facing outward and glued with Agar silver paint G3691.

3.5.1.2. FIB/SEM analysis

The mounted sample selected was based on blistered areas and was placed inside an FEI Analytical Quanta 3D FEG dual beam FIB/SEM which uses a field emission gun to produce the electron beam. Observation of the sample was performed by SEM secondary electron imaging with different accelerating voltages while maintaining the same spot size or probe setting. For higher quality imagery 10 kV was used but this had the disadvantage of damaging the coating.

Before using the FIB to remove material, it was necessary to protect the surface of the sample from stray, and out of focus Ga^+ ions. This was achieved by depositing a small platinum (Pt) rectangular shape (50 μm x 10 μm) with a thickness of 2 μm onto the surface, through the use of a gas injection system. This was carried out using an accelerating voltage of 16 kV and a beam current of 11 pA. For milling, Ga^+ ions at a tilt angle of 52° to the electron beam were employed. A beam current of 42 nA

and an accelerating voltage of 16 kV were used. In some cases, a high FIB energy (30 kV) was used to remove the material quickly.

The cross-sectioned face was then polished to produce a smooth surface and also to remove any of the Ga⁺ ions embedded in the coating during the milling process. A beam current of 7.5 nA and an accelerating voltage of 16 kV at a tilt angle of 53.5° were used. To produce an excellent finish with less curtain effects [109] (vertical broad lines), a low beam current of 1.5 nA was used, however, this took a longer time (14.5 hours). To remove the material quickly, higher beam currents were used but this tended to produce poorer finishes.

3.5.1.3. Elemental analysis

As a result of electron bombardment, emitted X-ray energies are characteristic to individual elements. Energy dispersive X-ray detector (EDS) attached to the FIB/SEM can be used to detect, analyse, and plot the characteristic X-ray energies from the sample. The technique can give both qualitative identification and quantitative elemental information from small sample volumes. The lateral resolution is typically between 0.2 and 1 µm for high atomic number elements. While low atomic number elements have a lateral resolution between 1 and 5 µm [108]. Elemental concentrations of 0.1 to 0.5% represent the limit of element detection [114]. Qualitative analysis of elemental distributions can be obtained by either using line scanning or by mapping of the area of interest. In line scanning, the electron probe is programmed to scan a line across a region of interest on the samples. When mapping, the probe rasters over the full image and records the individual X-ray photon signals as pixels on a micrograph. The pixels are shown as white on a black background in the map. A map of characteristic X-ray energies represented by pixel intensities is produced for each element of interest. The density of the pixels is associated with concentration of the elements.

EDS analysis was performed on the cross-sectioned face until at least half a million counts were obtained. The data were analysed using INCA Suite version 5.04 initially, distributed by Oxford Instruments. After initial trials, the mill shape was changed from a rectangle to an isosceles trapezoid to improve the detection of X-rays. Further improvement was achieved by changing the stage tilt and rotation angles.

3.5.2. FIB/SEM technique used to observe corroded coated panels

3.5.2.1. Sample preparation

The coated panel was punched to a diameter of 8 mm using a Roper Whitney Co. No. 5 JR hand punch (See Fig. 60). One side of the sample was then polished with a circular movement on MetPrep silicon carbide abrasive paper discs wetted with tap water. A P120 coarse grit paper was initially used and then fine polished with a P1200 grit paper. Fine polishing was needed to eliminate the damage to the pre-painted metal caused by the coarse grit paper.

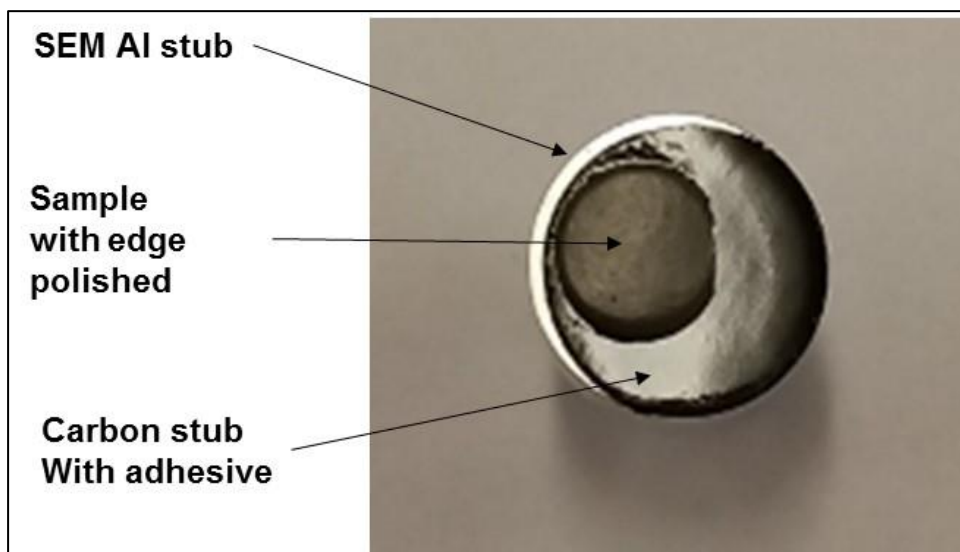


Figure 60. Photograph showing a coated HDG steel sample mounted onto an SEM stub.

3.5.2.2. FIB/SEM

The mounted sample was placed inside an FEI Analytical Quanta 3D FEG dual beam FIB/SEM which uses a field emission gun to produce the electron beam. Observation of the sample was performed by secondary electron imaging with different accelerating voltages while maintaining the same spot size or probe setting.

Before using the FIB to remove material, it was necessary to protect the surface of the sample from stray and out of focus Ga^+ ions. This was achieved by depositing a small platinum (Pt) rectangular shape ($50 \mu\text{m} \times 10 \mu\text{m}$) with a thickness of $2 \mu\text{m}$ onto the surface, through the use of a gas injection system (See Fig. 61 left). This was carried out using an accelerating voltage of 16 kV and a beam current of 11 pA. For

milling to produce a polygon shape, Ga⁺ ions at tilt angle of 52° to the electron beam were employed (See Fig. 62 left). A beam current of 42 nA and an accelerating voltage of 16 kV were used (See Fig. 62 right). In some cases a high FIB energy (30 kV) was used to remove the material quickly.

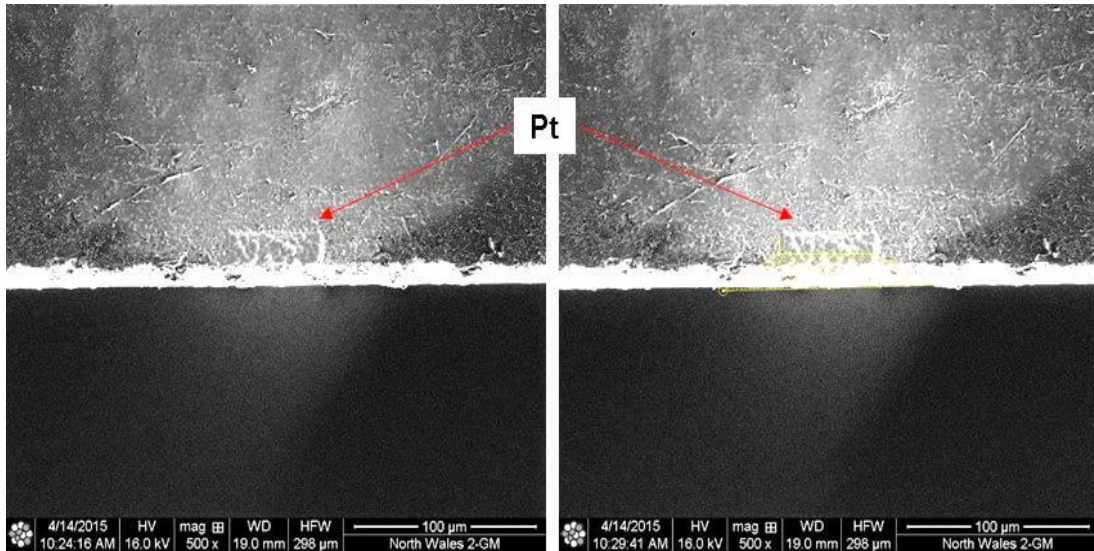


Figure 61. FIB images showing sample deposited with Pt (left) and the same sample with a polygon shape on the surface to represent the milling area shown in yellow (right).

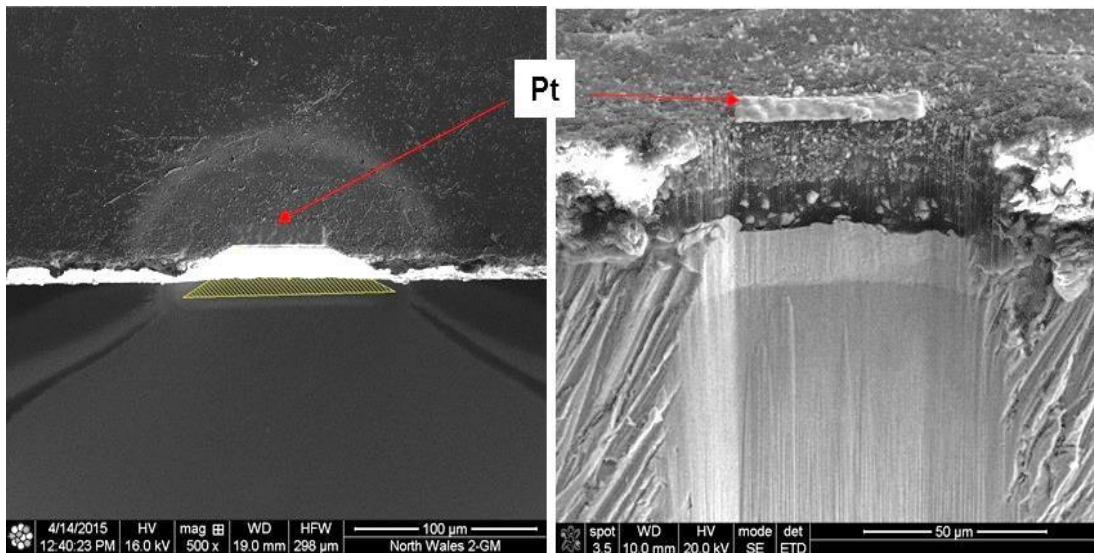


Figure 62. FIB image of sample after milling (left) and SEM image of the same sample after polishing (right).

The cross-sectioned face was then polished to produce a smooth surface and also to remove any of the Ga⁺ ions embedded in the coating during the milling process. A beam current of 7.5 nA and an accelerating voltage of 16 kV at a tilt angle of 53.5° were used. To produce an excellent finish with less curtain effects [109], a low beam current of 1.5 nA was used, however this took a longer time (14.5 hours) (See Fig. 63, right). To remove the material quickly, higher beam currents were used but this tended to produce poorer finishes.

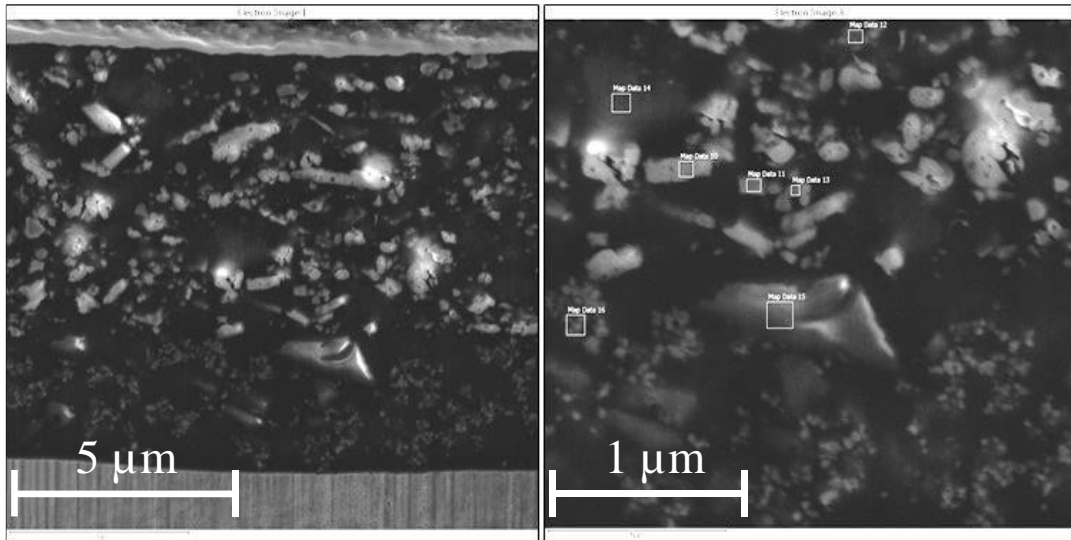


Figure 63. SEM images of main cross-sectioned area (left) and topcoat/ primer interface (right). The boxes in white represented area of EDS analysis.

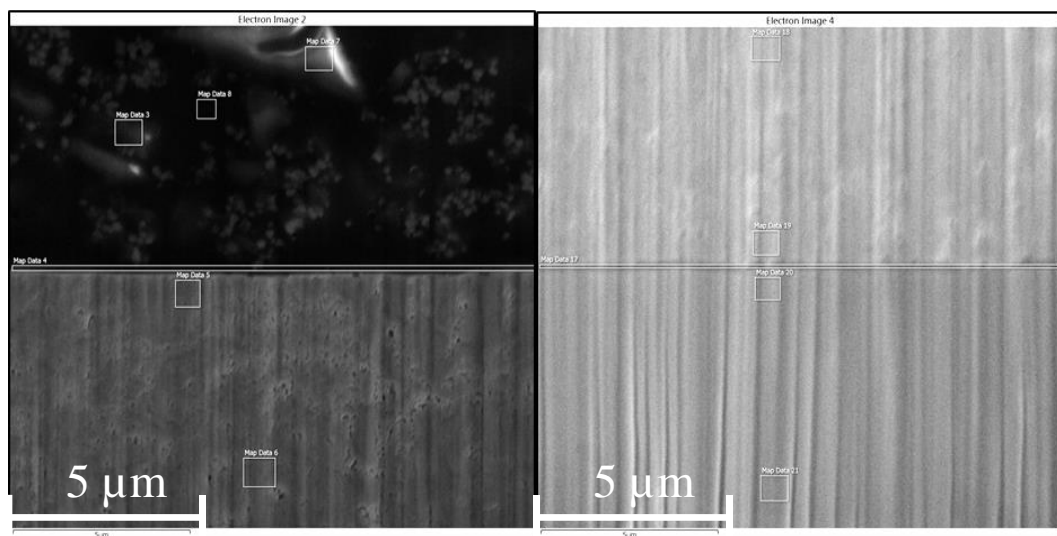


Figure 64. SEM images of primer/ zinc interface (left) and zinc/ steel interface (right). The boxes in white represented area of EDS analysis.

EDS analysis based on line scans, point & ID and mapping (See Figs. 63 & 64) was performed on the cross-sectioned face until at least half a million counts were obtained. The data were analysed using INCA Suite version 5.04 and later from 2016 onwards on Aztec version 3.1, both distributed by Oxford Instruments. The Aztec software was further updated to 3.3 in 2018. The analysis was done on the main cross section area, topcoat/ primer interface, primer/substrate interface and zinc/ steel interface. Main areas of investigation were the primer/ substrate interface.

Chapter 4. Results & discussions

4.1. EIS measurements

4.1.1. Organic coatings

Each system was measured three times to obtain an average value and the equivalent circuit models (ECM) were then used, which is shown in Figs. 65-67. The % error of the fitting to the ECM was between 3 and 10. The % RSE of the coating systems were <31% at the start of measurements and after two hours with regards to film capacitance (Q_f). However, all 4 systems showed an increase in Q_f after 2 hours, with systems 3 and 4 gave the biggest increase.

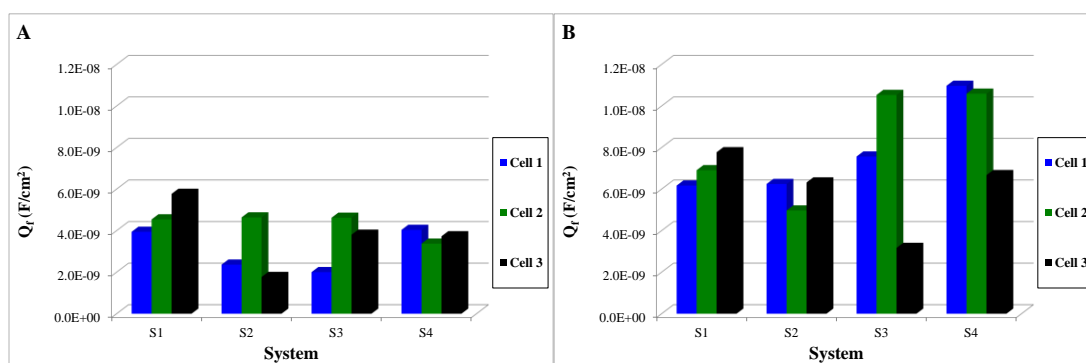


Figure 65. Q_f vs. time plots of systems measured at the start (a) and then 2 hours (b) later.

A. System	Mean Q_f	STD Error	%RSE	B. System	Mean Q_f	STD Error	%RSE
1	4.8E-09	5.4E-10	11	1	6.9E-09	4.6E-10	7
2	2.9E-09	8.7E-10	30	2	5.8E-09	4.4E-10	7
3	3.5E-09	7.7E-10	22	3	7.1E-09	2.1E-09	30
4	3.7E-09	1.9E-10	5	4	9.4E-09	1.4E-09	15

Table 5. The mean, standard error, and % RSE of Q_f component of the 4 systems at the start (a) and then 2 hours after (b).

The %RSE of the 4 systems were <100% at the start and after 2 hours with regards to film resistance (R_f). The high %RSE value was influenced by system 1, which has a very high standard deviation away from the mean.

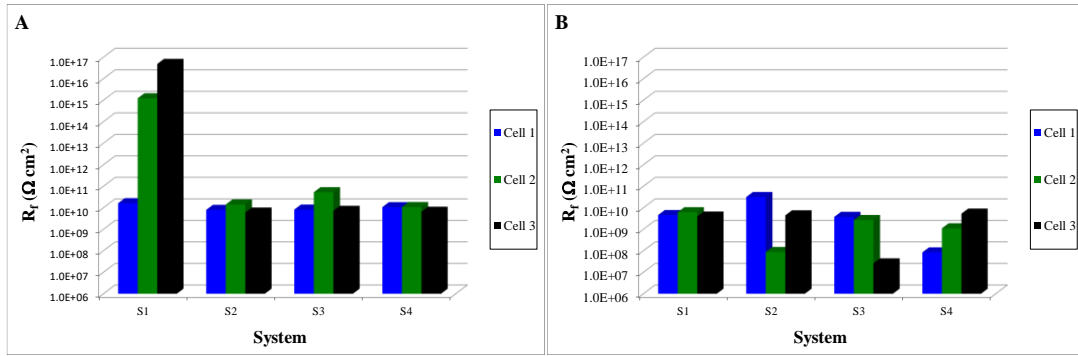


Figure 66. R_f vs. time plots of systems measured at the start (a) and 2 hours (b) later

A. System	Mean R_f	STD Error	%RSE	B. System	Mean R_f	STD Error	%RSE
1	1.70E+16	1.60E+16	61	1	4.9E+09	6.9E+08	14
2	9.30E+09	2.50E+09	26	2	1.2E+10	9.8E+09	82
3	2.30E+10	1.50E+10	66	3	2.2E+09	1.1E+09	51
4	9.30E+09	1.40E+09	15	4	2.2E+09	1.6E+09	74

Table 6. The mean, standard error, and % RSE of R_f component of the 4 systems at the start (a) and 2 hours after (b).

After 2 hours system 1 stabilised and then had the lowest %RSE. The other 3 systems increase with system 2 being the worst. There was a general decrease in the trend of R_f after 2 hours.

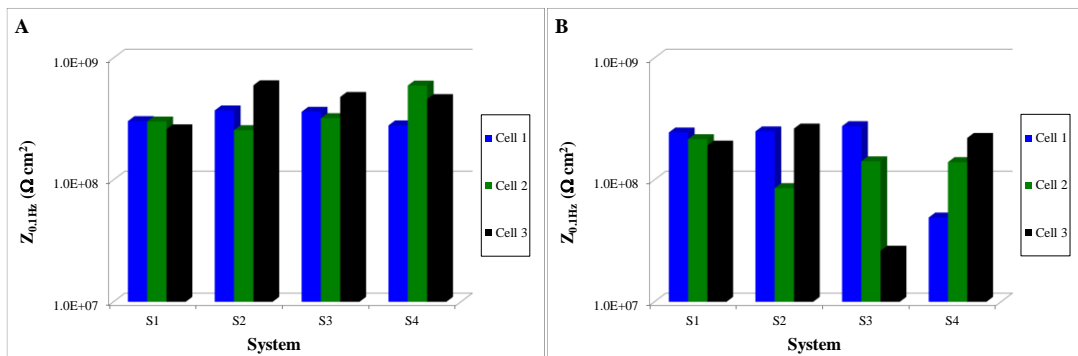


Figure 67. $Z_{0.1Hz}$ vs. time plots of systems measured at the start (a) and 2 hours (b) later.

The % RSE of the 4 systems were all <50% at the start and after 2 hours for total impedance ($Z_{0.1Hz}$), with system 1 having the least error at the start, it then increased to 7% after 2 hours. Whereas the other 3 systems have higher increase in %RSE after 2 hours, up to 49%.

A. System	Mean $Z_{0.1\text{Hz}}$	STD Error	%RSE	B. System	Mean $Z_{0.1\text{Hz}}$	STD Error	%RSE
1	2.9E+08	1.4E+07	5	1	2.2E+08	1.6E+07	7
2	4.1E+08	1.0E+08	25	2	2.0E+08	5.7E+07	29
3	3.9E+08	4.7E+07	12	3	1.5E+08	7.2E+07	49
4	4.4E+08	9.1E+07	20	4	1.4E+08	5.0E+07	36

Table 7. The mean, standard error and % RSE of $Z_{0.1\text{Hz}}$ of 4 systems at the start (a) and 2 hours after (b).

EIS measurement errors are system and component dependent, with system 1 having the lowest %RSE for Q_f and $Z_{0.1\text{Hz}}$. It had the highest %RSE for R_f at the start of the test, but after the system stabilised, it had the lowest %RSE. System 3 had the highest measurement errors and below that were systems 2 and 4 in that order.

In terms of individual components, film capacitance had the lowest average measurement error; 17% for the initial readings and 15% for readings after 2 hours. Film resistance had the highest average measurement error; 42% initial and 55% after 2 hours. The total impedance was in between the capacitances and resistances of the coatings. The measurement errors increase as system 2 to 4 degrades. This is not the case for system 1.

The work by V.S. Bonitz [124] has shown that random error in the EIS data was larger when measurements were performed with small sample areas. EIS data correlated well with reference values for larger sample area $\geq 11.4 \text{ cm}^2$. If not artefacts arising from EIS instrument and measurement protocol will be introduced. A number of recommendations by V.S. Bonitz were made to minimise EIS data variability. First, the film thickness of the coating should be as constant as possible. Second, the area of the coating is crucial, larger sample areas ($\geq 11.4 \text{ cm}^2$) are required to minimise random error in the data. Third, replicate samples of six to eight are required which is a good compromise between acceptable confidence in the results and expenditure of the time.

This work has shown similar results to those reported by V.S. Bonitz and reinforced what he recommended to do to minimise random error in the data. Only three replicates for each system were used in all EIS characterisation because of the time constraints determined by the need to measure in a day. Each sample was measured twice and the frequency range used was from 0.01 Hz to 100 kHz, which took time to complete.

4.2. Panels exposed in accelerated weathering chambers and cells

4.2.1. EIS cell

4.2.1. Open circuit potential

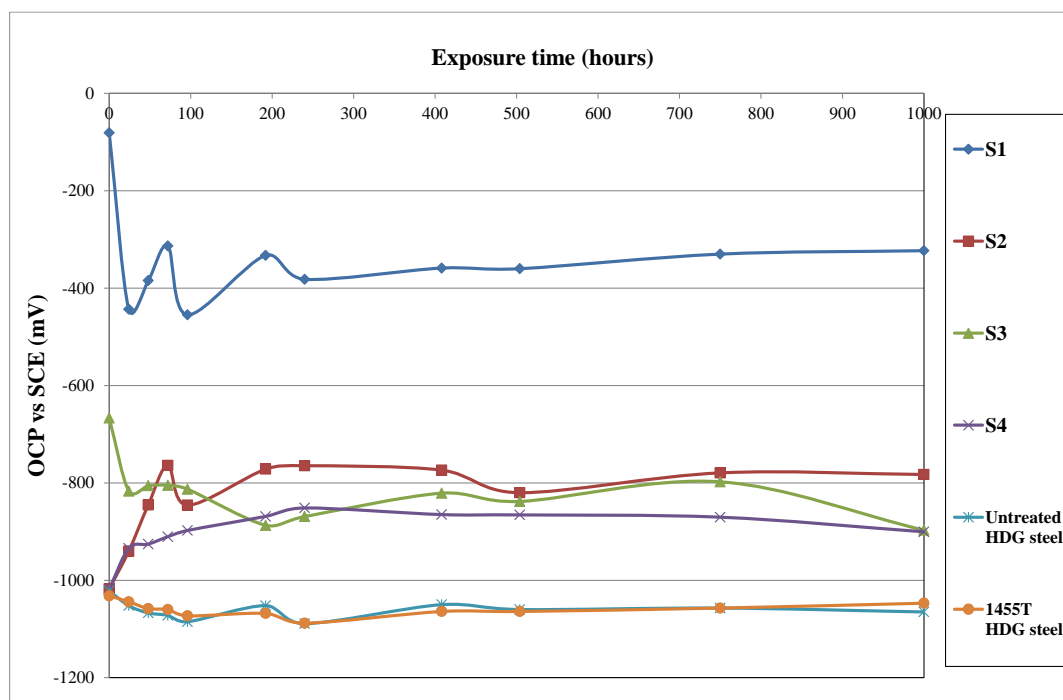


Figure 68. Open circuit potential (OCP) of 4 systems and HDG steels (untreated and pretreated with 1455T) submerged in cells over time.

The open circuit potential of each system and substrate was measured before EIS measurements were made. It was measured against the saturated calomel electrode at 0, 24, 48, 72, 96, 192, 240, 408, 500, 750 and 1000 hours in 0.5 M sodium chloride, and the data are presented in Fig. 68. The results show that the two uncoated steel substrates were the most negative in potential, followed by systems 2 and 4, and then system 3 in that order. The most positive was system 1, a commercial solvent-borne primer. The bare metals were used as a baseline value compared to the coated systems and they can't be interpreted in the same ways due to the behaviour of the organic coatings.

In the electrochemical series, the more negative the potential values are the more likely the material will corrode and this was observed for the uncoated HDG

steel substrate. The addition of a chromate-free pretreatment on the HDG steel lowered the potential to -1032 mV from -1022 mV for untreated HDG steel, hence protecting the steel by sacrificial anode. By having a coating on the steel, the potential become more positive and protects the substrate, especially for system 1, which had a potential of -81 mV compared to -1018 mV for both systems 2 and 4 at the start of the testing. System 3 had a potential of -667 mV at the start. The 3 systems were based on experimental waterborne pretreatment primers.

HDG steel substrates, system 1 and 3 generally more negative over time until reaching between 240 and 500 hours, with drifting between negative and positive potentials and then the potential stays stable to the end of the test. This may show that there was little activity present at the surface of the substrate. For systems 2 and 4, there was a general increase in positive potential from the start until reaching 240 hours whereby the systems stayed reasonably constant with one or two drops in positive behaviours on the way.

4.2.1.2. Exposed panels characterised by EIS

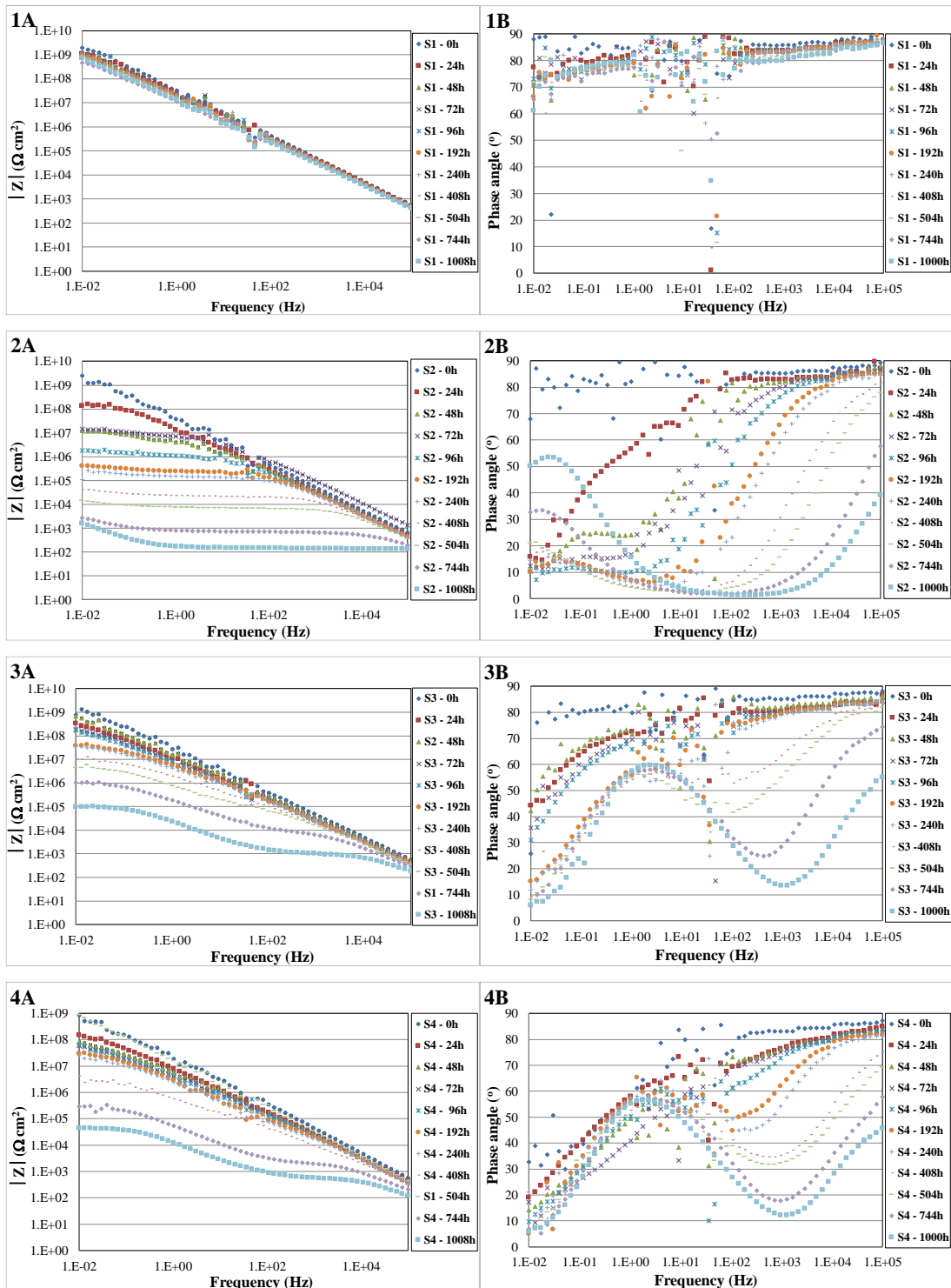


Figure 69. Bode impedance modulus (a) and phase angle (b) plots of 4 systems (labelled as 1 to 4) submerged in cells tested for 1000 hours.

After obtaining the OCP, panels were measured by EIS. Each panel was measured in 3 locations, labelled as A, B and C. The measurements were performed in alphabetical order. The EIS data shown are based on the averages of the 3 measurements for each system. They are expressed as Bode modulus impedance and phase angle plots are shown in Fig. 69. Nyquist plots were also obtained, but will not be shown because of the difficulty in showing the various low and high impedance values in one plot for the test periods. Bode phase angle plot can be used to express the same results as a Nyquist plot.

In the modulus impedance spectra, system 1 has the highest impedance and over time shows little change in value, which suggested that the coating was protecting the substrate and was the best system. System 2 is the worst and deteriorated over time, even at 48 hours, there was sign of corrosion products forming. Systems 3 and 4 have similar modulus impedance spectra to each other, they deteriorated over time and started to form corrosion products around 192 hours, but had better protection than system 2, as expected, because of containing anti-corrosive pigments in the coating.

Phase angle spectra show similar results to modulus impedance, and in addition they tell us if the systems are capacitive or resistive in response. They can also inform if there was any corrosion product forming on the substrates in the low frequency range. In all of the systems, especially at the beginning of each experiment there were high levels of interference in the spectra at around 50 Hz. There are a number of reasons why the spikes were in the spectra. They could originate from; the test environment, interference from the equipment or cable leads or signature from the coating. To prove this, EIS measurements were done in a Faraday cage to eliminate environment impact and were measured on another EIS machine to eliminate equipment and cable leads factors.

The other option was to increase the AC voltage and improved the signal strength, which caused the spikes in the spectra to disappear but the side effect of this action was an increase in the rate of redox action in the system by moving further away from the equilibrium potential and may have caused the system to corrode. The results indicated that the spikes were caused by the coating. A good performing coating (system 1) give rise to the spikes throughout the test period and a poor performing

coating did not. Systems 2 to 4 represented this quite well, especially system 2 the spikes in the spectra decreased with increases in coating deterioration over time.

System 1 was behaving as a leaking capacitor whereby the phase angle decreased from 90° to around 70° at 1000 hours. The other 3 systems deteriorated completely and the results indicated the formation of corrosion products. The phase angle of system 2 was at zero for the mid frequency range.

ZSimpWin 3.22 fitting software was used to analyse the EIS spectra. They were fitted to the different equivalent circuit models (ECM), which consisted of RC components connected in series and Randles cell. A model for painted metal/ solution interface, including paint film parameters to the circuit was used for deteriorated coatings. The ECM was first proposed Mikhailovskii and co-workers [98]. The ECM used was dependant on which EIS spectra were produced from each system. The % error of the fitting to the different ECMs were less than 20%. Most fittings were between 3 and 10%.

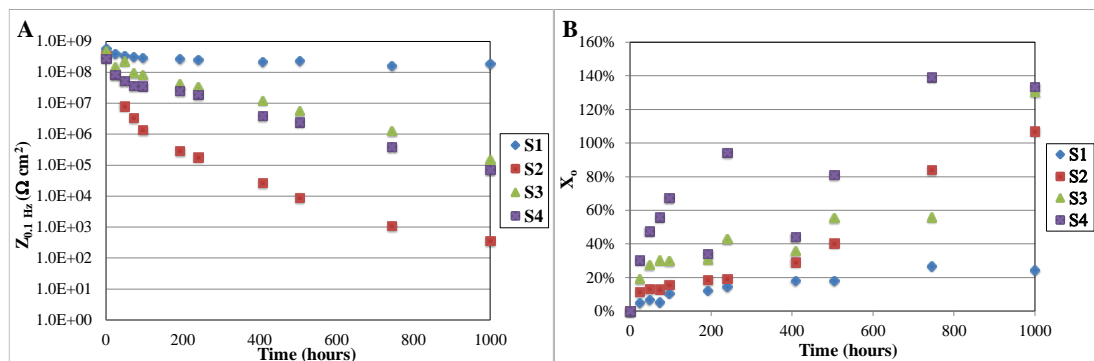


Figure 70. $Z_{0.1\text{ Hz}}$ (a) and X_c (b) vs. time plots of systems submerged in cells.

A number of researchers have used impedance at 0.1Hz to show the total impedance of a coating [97] [125] [126], a coating with $10^8 \Omega \text{ cm}^2$ or over indicates no corrosion was present underneath the film (See Fig. 70a). Between 10^6 and $10^8 \Omega \text{ cm}^2$ some corrosion is present. Below $10^6 \Omega \text{ cm}^2$ represents a large area of corrosion products. The total impedance of system 1 was above $10^8 \Omega \text{ cm}^2$ during the entire test period, staying constant, which indicates that no corrosion was underneath the film. System 2 was the worst with very sharp decreases in total impedance from the start eventually falling to around $10^2 \Omega \text{ cm}^2$ at 1000 hours. This indicates total failure in the

coating and this can be seen in the photographs taken (Fig. 73). There is little different in the performance of systems 3 and 4. It was expected that system 4 with the addition of pretreatment technology should have performed better than system 3, but this was not the case.

The results of percentage water uptake (X_o) of the 4 systems by determining the change in capacitance over time are shown in Fig. 70b. The film capacitance is controlled by the dielectric properties of the coating, which are related to the initial dielectric strength of the coating and the water uptake of that coating [100]. An increase in capacitance indicates an increase in water uptake by the coating and this could clearly be seen in the water-borne pretreatment primers (systems 2-4) compared to solvent-borne coating for system 1. Also shown was the effect of using anti-corrosive pigment (calcium exchanged silica) in system 3 and 4 compared to the unpigmented system 2, which generally has a better barrier to water than the other two systems.

No further fitting of ECM for system 1 was needed because the coating did not deteriorate much over time. It behaved as a leaky capacitor during the entire period of the test by having a small increase in capacitance. Further fitting of equivalent circuit models was needed for the other 3 systems due to the deterioration of the systems during the test, resulting in a change of ECMs.

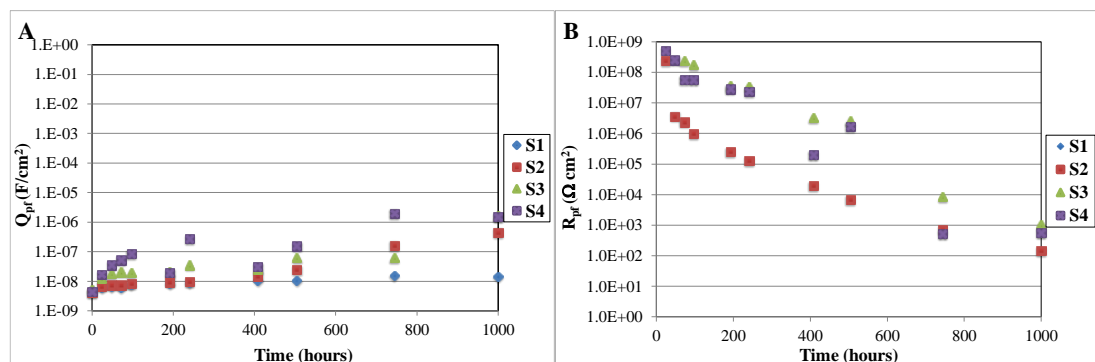


Figure 71. Q_{pf} (a) and R_{pf} (b) vs. time plots of systems submerged in cells.

The film capacitance (Q_{pf}) and resistance (R_{pf}) are shown respectively in Fig. 71a and Fig. 71b. The film capacitance was used to determine the water uptake of a coating. The film resistance represents the resistance of a film to electrolyte penetration [97]. A lower resistance indicated the film had been penetrated by

electrolyte and this caused the film to be damaged. It would also indicate the influx of electrolyte into holes or porous areas with inadequate crosslinking of the coating.

All three systems increased in capacitance over time indicating increases in water uptake. System 2 is slightly lower in capacitance compared to system 3 and 4. It may have been the result of not having anti-corrosive pigment in the coating. Pigments can behave as holes in the coating or as charged materials, by pulling electrolyte from the surface into the coating.

The film resistance of systems 3 and 4 were similar to each other during the test periods, with system 2 being slightly worse. They decreased over time and showed that after 1000 hours the 3 systems have very low resistance to electrolyte penetration, starting at $\sim 10^8 \Omega \text{ cm}^2$ and reducing to $\sim 10^3 \Omega \text{ cm}^2$ at the end of the test.

The changes in double layer capacitance, Q_d (a) and charge transfer resistance, R_t (b) of systems 2 to 4 tested over time are shown in Fig. 68. Q_d indicates the presence of water at the coating/metal interface and R_t represents the resistance of the metal substrate to corrosion [97]. It shows that systems 3 and 4 had similar performance in protecting the coating/ metal interface using an anti-corrosive pigment in the pretreatment primers. Whereas for system 2 which had no pigment in the coating, the protection at the interface was not as good as the other 2 systems. But all three systems deteriorated over time with a large number of blisters forming (See Figs. 73-76).

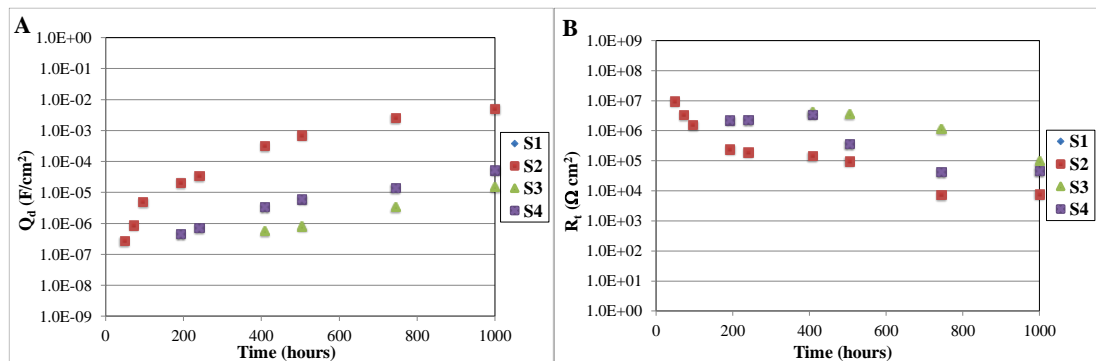


Figure 72. Q_d (a) and R_t (b) vs. time plots of systems submerged in cells.

4.2.1.3. Exposed panels assessed by visual inspection for degree of blistering

BS EN ISO 4628-2:2003 testing standard was used to assess the degree of blistering on the exposed areas. The rating of the blisters in the coatings was based on the quantity and size of the blisters. The quantity of blisters range from 2 to 5 and the blisters' sizes range from S2 to S5. This can be subjective because there are only 4 categories each for quantity and size. To express the results as graphs and be quantitative, the quantity and size of the blisters rating were multiplied by each other to give the total blister amount. Then the values were averaged for each time interval.

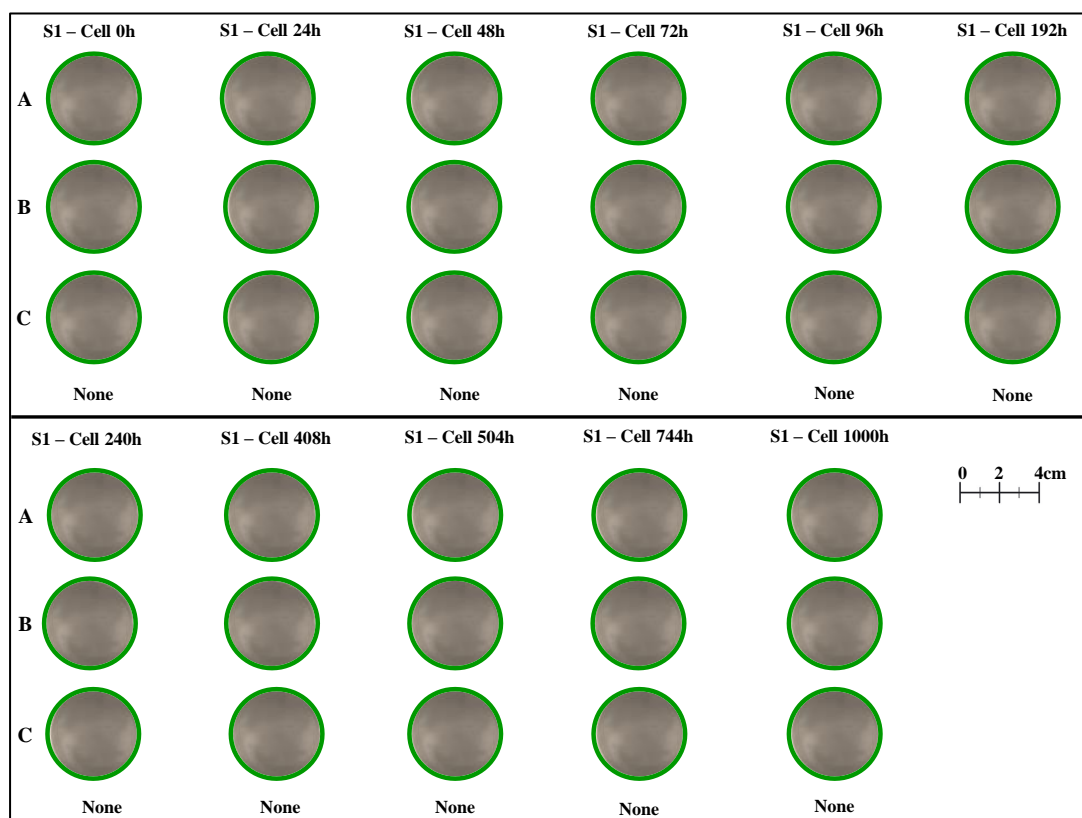


Figure 73. Photographs of triplets (a, b and c) of system 1 submerged in cells for 1000 hours.

The results of system 1 submerged in 3 cells from 0 to 1000 hours are shown in Fig. 73. The images were cropped and added together so that they can be expressed over time. It illustrates that no blisters were formed during the test. The green circles in the figures represent no blister present in the coating. If there are red circles in the figures this indicated blisters are present in the coating. The results of having no blistering in system 1 correlated with the EIS and total impedance data presented

earlier. However does this mean that there are no corrosion products underneath the film? (See Fig. 137 of exposed panels)

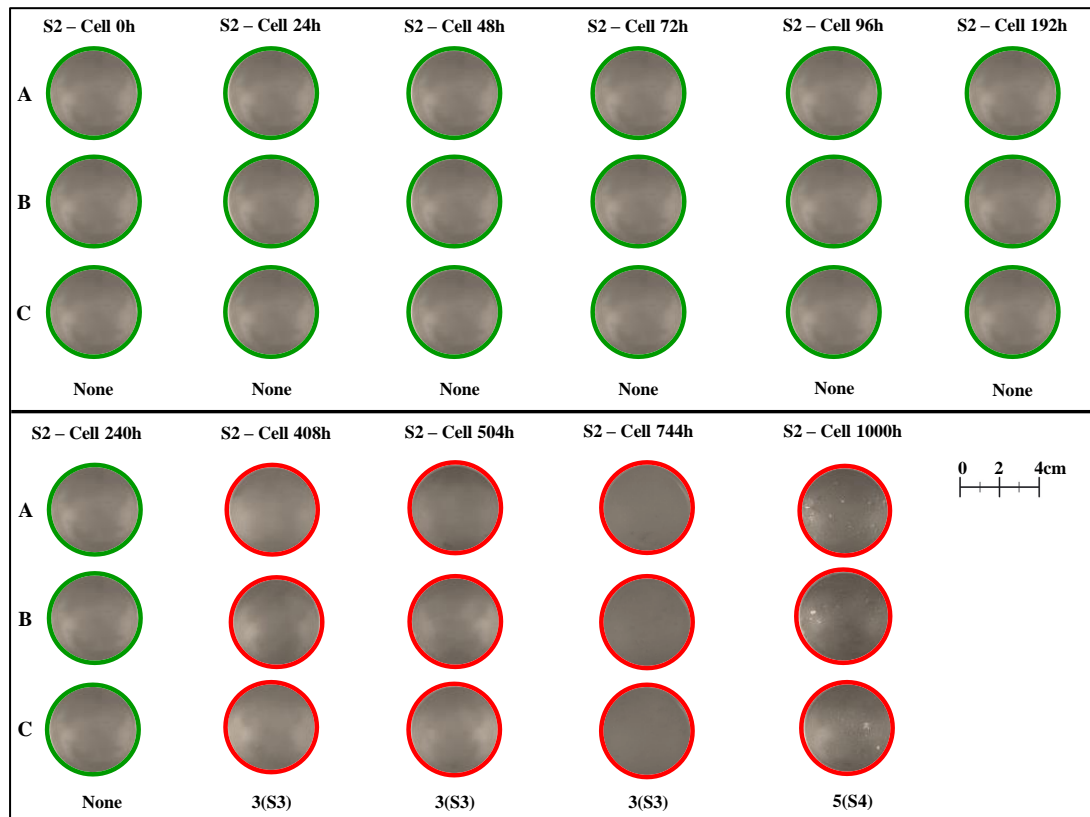


Figure 74. Photographs of triplets (a, b and c) of system 2 submerged in cells for 1000 hours.

The results of system 2 submerged in 3 cells from 0 to 1000 hours are shown in Fig. 74. No blisters were observed in the coating from 0 to 240 hours. At 408 hours of exposure, blisters were observed in the coating and eventually to the end of the test. The blister quantity and size increased over time, grown from 3(S3) to 5(S4). EIS data indicated that at 240hour corrosion started to occur and the effect of this over time caused blisters to form in the coating at 408 hours.

See Fig. 75 showings examples of enlarge photographs of system 2 submerged in a cell for 1000 hours. The images consisted of the measurements at the start, 408 h and 1000 h. It was difficult to photograph the blisters at size S2 and S3 until the blisters reached S4 and S5.

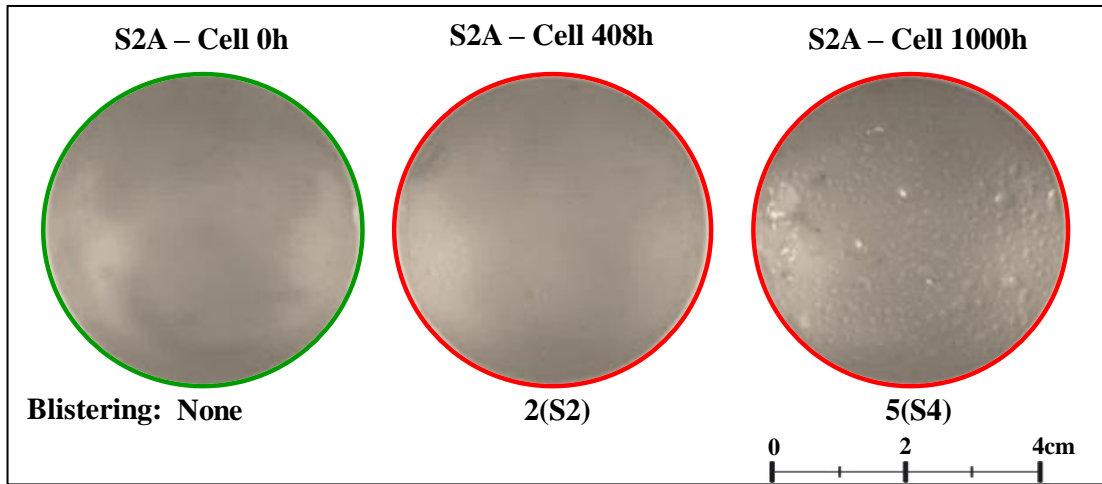


Figure 75 Enlarge photographs of S2A submerged in cell for 0, 408 and 1000 hours.

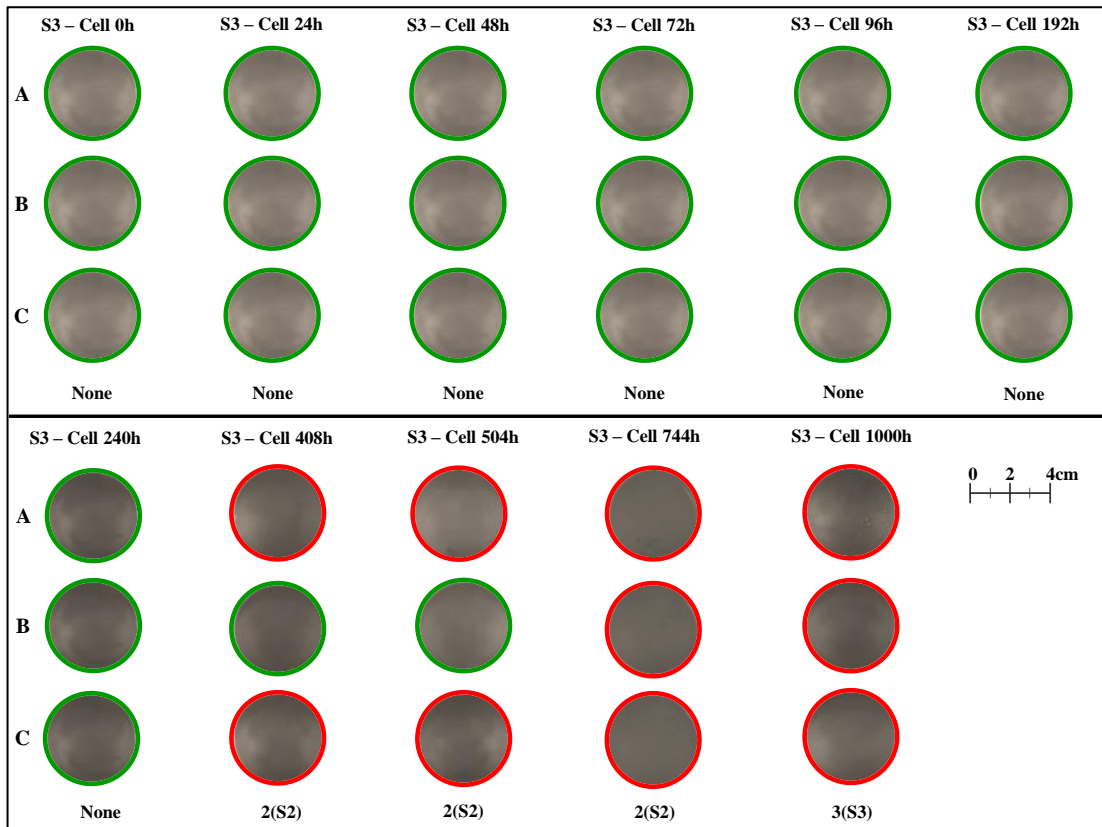


Figure 76. Photographs of triplets (a, b and c) of system 3 submerged in cells for 1000 hours

The results from system 3 submerged in 3 cells from 0 to 1000 hours are shown in Fig. 76. No blister was formed in the coating from 0 to 240 hours. At 408 hours of

exposure, blisters were formed in the coating, with cell B forming at a later time of 750 hours. The blister quantity and size both increase over time from 2(S2) to 3(S3). The blisters of system 3 were smaller than those in system 2 with fewer amounts. EIS data indicates that at 240 hours, corrosion started to occur and the effect of this over time caused the blisters to form in the coating at 408 hours.

The results from system 4 submerged in 3 cells from 0 to 1000 hours are shown in Fig. 77. No blister was formed in the coating from 0 to 240 hours. At 408 hours of exposure, blisters were observed in the coating, with cell B having blisters at a later time of 504 hours. The blister quantity and size both increase over time from 2(S2) to 4(S3). The blister size and quantity of system 4 ranked between system 3 and 2. EIS data indicated that at 240 hours, corrosion had started and the effect of this over time caused blisters to form in the coating at 408 hours.

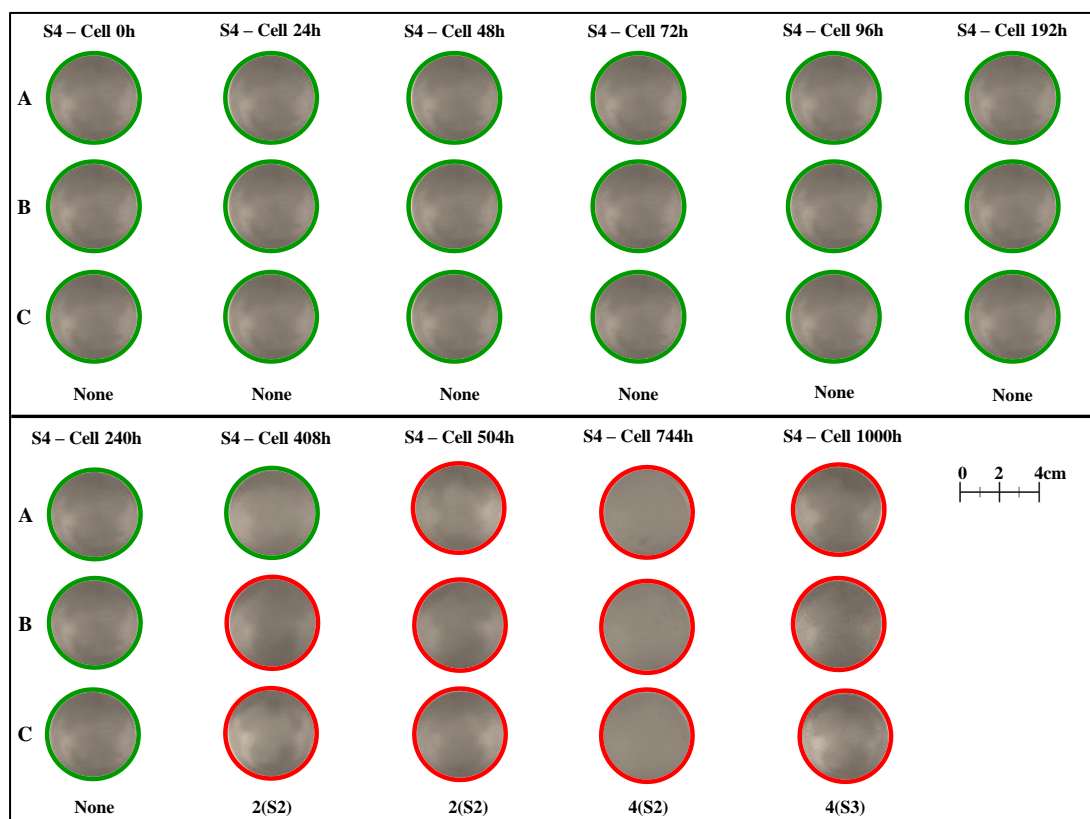


Figure 77. Photographs of triplets (a, b and c) of system 4 submerged in cell for 1000 hours.

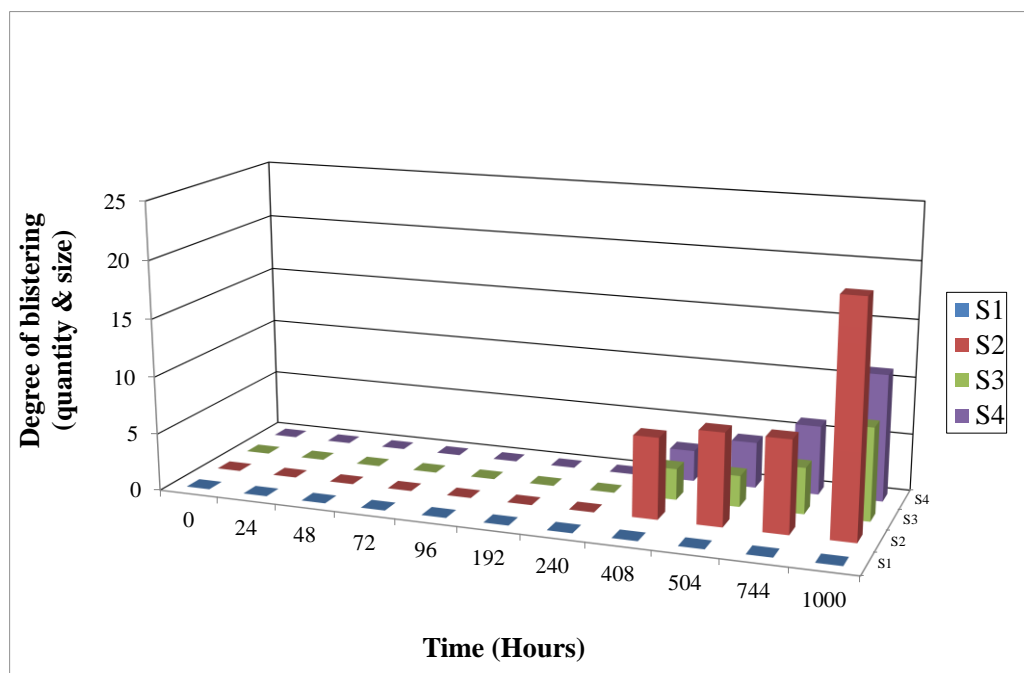


Figure 78. Degree of blistering vs. time plot of 4 systems submerged in cells for 1000 hours.

In the degree of blistering plot shown in Fig. 78, system 1, a solventborne primer clearly outperformed the other 3 systems based on experimental waterborne pretreatment primers. It has no blisters formed in the coating, whereas the other systems do, with system 2 the worst then followed by 4 and 3 in that order. All the blistering was observed at 408 hours and then increased in blisters size and amount over time. EIS data of the 3 systems show the corrosion process started at 240 hours and the effect of this at a later time was blistering.

4.2.2. Neutral salt spray test

4.2.2.1. Open circuit potential

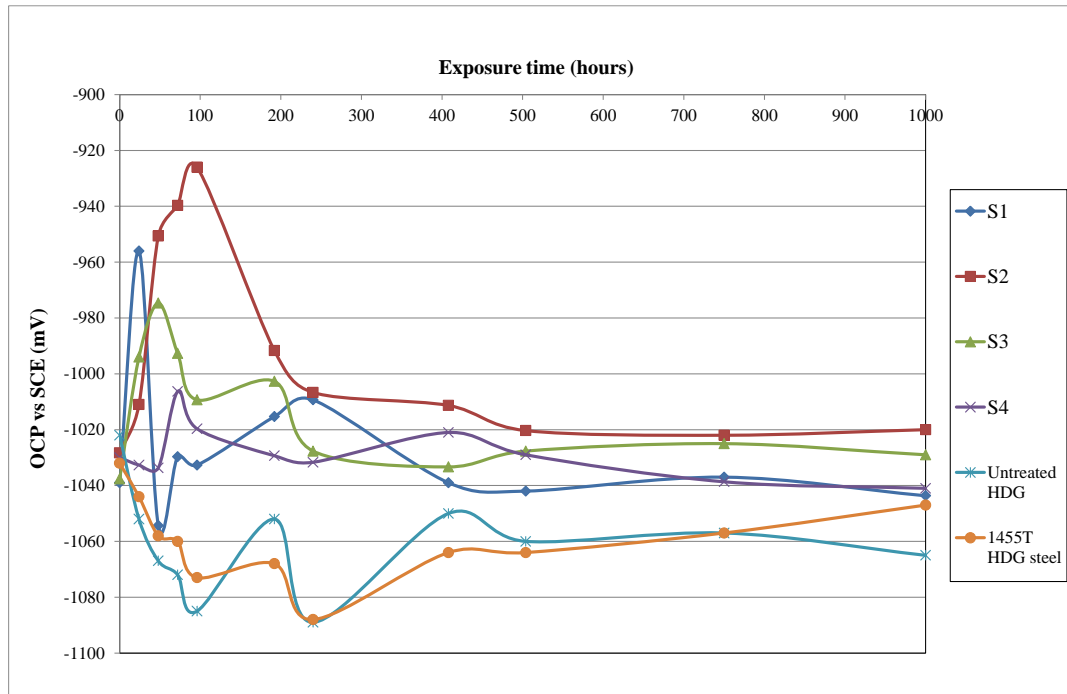


Figure 79. Open circuit potential of 4 systems tested in NSS chamber compared to HDG steels, untreated and treated with 1455T Cr-free pretreatment.

The open circuit potential of each system during NSS tests was measured and the results are represented in Fig. 79. They were compared to the measured OCP of HDG steel substrates obtained during EIS cell measurements in the previous chapter to act as baseline readings. The data shows system 1 and 3 had the highest negative potential at the initial measurement, then followed by 1455T treated HDG steel, system 4, system 2 and untreated HDG steel in that order.

As the systems were exposed in the NSS chamber over time, these systems generally increased in positive potential in the first 2-4 measurements period. Then the systems drifted from positive and negative in potential until reaching 500 hours when the potential started to stabilise. They continue this path until reaching 1000 hours of exposure where the OCP results show no distinction between good and bad systems.

4.2.2.2. Panels exposed in NSS chamber and characterised by EIS

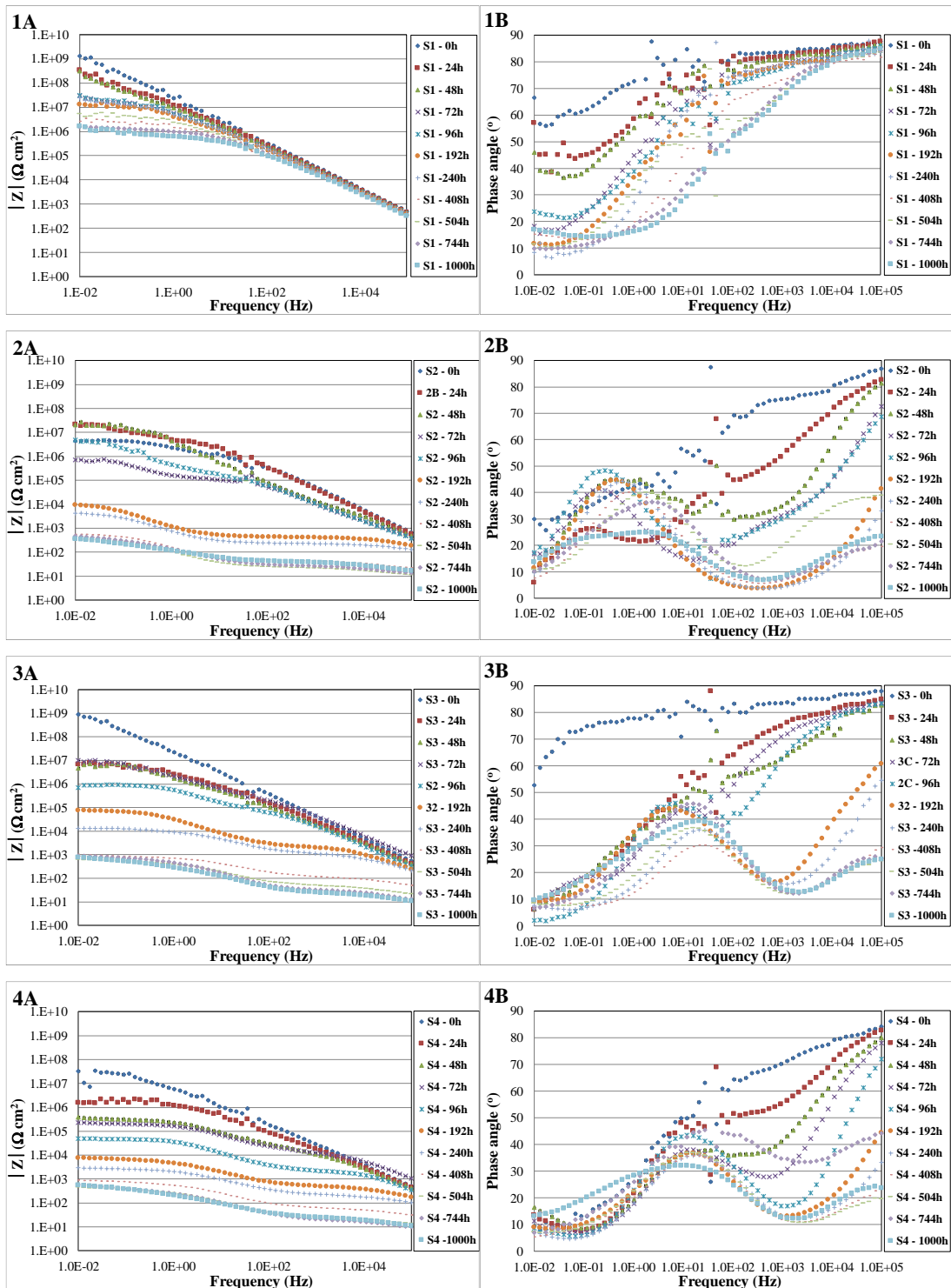


Figure 80. Bode impedance modulus (a) and phase angle (b) plots of 4 systems (labelled as 1 to 4) tested in a neutral salt spray chamber over time.

The results of impedance modulus spectra are shown in Fig. 80. System 1 had the highest impedance and showed some deterioration after 72 hours of exposure. After 1000 hours of exposure the impedance modulus was still high, around $10^6 \Omega \text{ cm}^2$, which indicated that the coating was still protecting the substrate with little or no corrosion product nor blisters present. System 2 is the worst even at the beginning of the exposure, deterioration was already there and resulted in the formation of corrosion products after 24 hours. At the end of the test system 2 reached an impedance value of $<10^3 \Omega \text{ cm}^2$, which was similar to systems 3 and 4.

Systems 3 and 4 had similar impedance modulus spectra after 1000 hours of exposure. System 3 started to corrode at 192 hours and system 4 started slightly earlier at 96 hours. At the beginning of the test, system 3 had slightly better impedance for several time periods of measurements than system 4. At the end of the test, they deteriorated to around $10^3 \Omega \text{ cm}^2$, which was similar in value to system 2.

The results show that NSS is a very aggressive test compared to EIS cells and that is why the commercial system, impedance modulus $|Z|$ value decreased from the start, $\sim 10^9 \Omega \text{ cm}^2$ to $\sim 10^6 \Omega \text{ cm}^2$ after 1000 hours with no blister forming in the coating (See Fig. 84). NSS test conditions were not the same as those used in the cells, the salt solution concentration is 5 %w/v compared to 2.9 %w/v respectively. The test temperature of NSS is 35 °C compared to ~ 21 °C for EIS cells. The higher temperature has two effects on the test conditions, one it can increase the rate of redox reaction and two, being at the same temperature as the topcoat Tg it is easier for salt solution to penetrate through the coating, into the substrate and caused corrosion. At 21 °C, the test temperature is below the coating Tg, the coating will be stiff and limit the migration of salt solution to the substrate and caused less corrosion.

The phase angle spectra show similar results to impedance modulus and in addition they indicate if the systems are forming any corrosion products at the substrates. Systems 2 to 4, all have corrosion products forming at the coatings/substrates interfaces, which are represented by a second cycle in the spectra at mid frequency. System 1 showed some sign of corrosion activity near the end of the test.

In all of the systems, especially at the beginning there were spikes in the spectra at around 50 Hz. Again this shows the signal to noise ratio is high and indicates how good coatings are in protecting the steel. A good performing coating (system 1) will have the spikes throughout the test period and a poor performing coating will not. Systems 2 to 4 represented this quite well.

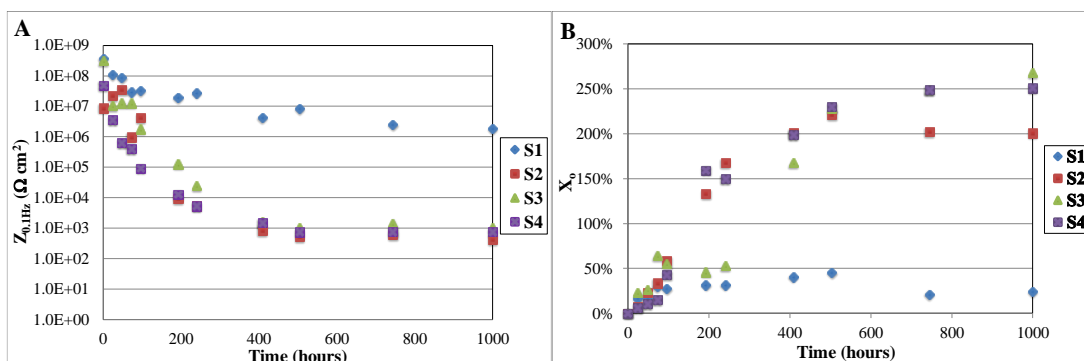


Figure 81. $Z_{0.1\text{Hz}}$ (a) and X_o (b) vs. time plots of systems exposed in NSS chamber.

The total impedance of system 1 is above $10^6 \Omega \text{ cm}^2$ during the entire period of the test and this indicates that no or very little corrosion product formed underneath the film (See Fig. 81a). Systems 2 to 4 have similar $Z_{0.1\text{Hz}}$ to each other but system 2 is slightly worse with a very sharp decreases in total impedance from the start and then progresses to around $10^3 \Omega \text{ cm}^2$ at 1000 hours, which indicates total failure of the coating and this can be seen in the photographs taken (See Figs. 84-87).

The results are the same at the end of the tests for the 3 systems, even the anti-corrosive pigments that were incorporated in systems 3 and 4, $Z_{0.1\text{Hz}}$ did not improve the values. It only helped during the first 200 hours of testing.

The results for percentage water uptake of the 4 systems determined by the change in capacitance over time are shown in Fig. 81b. An increase in capacitance indicates an increase in water uptake by the coating and this could clearly be seen in the water-borne pretreatment primers of systems 2 to 4 compared to the solvent-borne primer of system 1. System 1 only increases by 50% compared to the 200-250% increases for systems 2 to 4, with system 2 having the lowest % water uptake. The % water uptake was also much higher in NSS chamber compared to EIS due to the higher temperature used in the test.

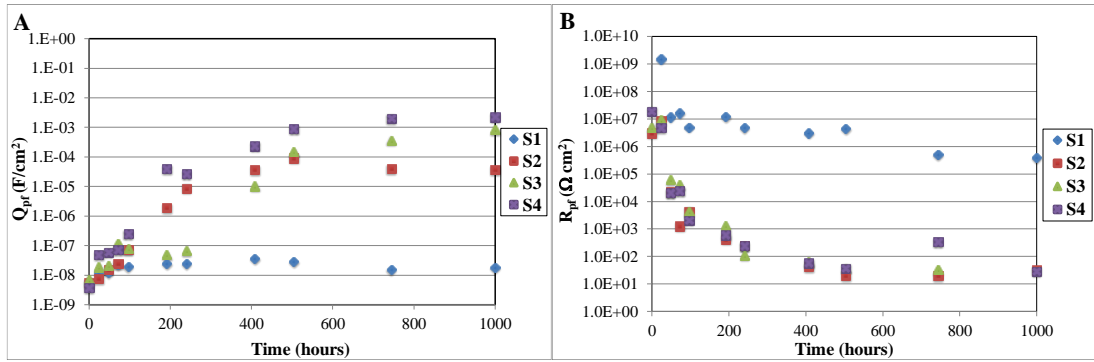


Figure 82. Q_{pf} (a) and R_{pf} (b) vs. time plots of systems exposed in NSS chamber.

The results of film capacitance, Q_{pf} (a) and film resistance, R_{pf} (b) of the 4 systems are shown in Fig. 82. It shows that system 1 had the lowest increase in film capacitance over time and resulted in the lowest percentage water uptake out of the 4 systems. Systems 2, 3 and 4 have similar trend in Q_{pf} performance over time with system 2 having the lowest increase out of the 3 systems, followed by system 3. The worst in this test was system 4.

The film resistance of system 1 was the highest, but deteriorated over time and then decreased to as low as $\sim 10^6 \Omega \text{ cm}^2$. Systems 2, 3 and 4 have similar film resistance and the trends in the plots were also similar. They decreased to $< 10^2 \Omega \text{ cm}^2$ at 1000 hours and having so low film resistance indicates there is no protection from the coating to stop electrolyte penetrating through into the coating/ metal interface.

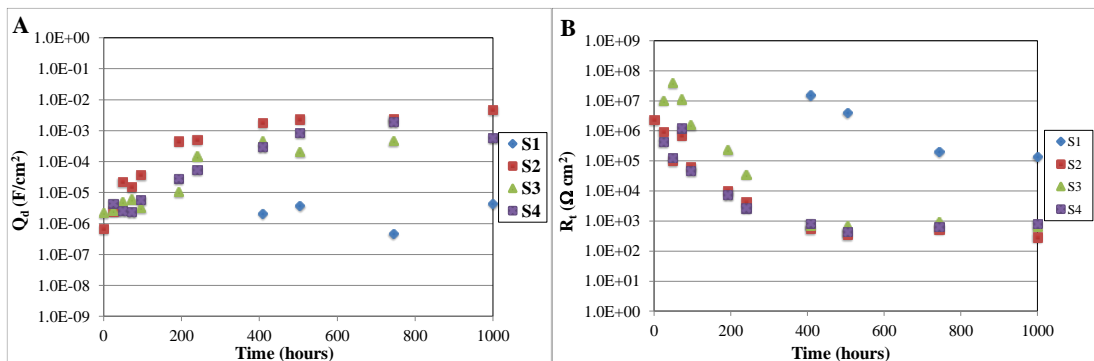


Figure 83. Q_d (a) and R_t (b) vs. time plots of systems exposed in NSS chamber.

The results of double layer capacitance, Q_d (a) and charge transfer resistance, R_t (b) of the 4 systems are shown in Fig. 83. It shows that system 1 had the lowest increase in double layer capacitance over time compared to the other 3 systems, which

indicates that although some water was present at the coating/metal interface, the coating was performing well. Systems 2, 3 and 4 have similar trends in Q_d performance over time with system 2 slightly worse than system 3 and 4 which were similar in value.

The charge transfer resistance of system 1 was the highest, but deteriorated over time and then decreased to as low as $\sim 10^5 \Omega \text{ cm}^2$. Systems 2, 3 and 4 have similar R_t and the trends in the plots were also similar. They decreased to $< 10^3 \Omega \text{ cm}^2$ at 1000 hours and having so low R_t indicated no resistance to corrosion. Even those having anti-corrosive pigments (systems 3 and 4) did not help to improve R_t . System 2 has no pigment in the coating; the protection at the interface was as good as the other 2 systems. It also shows that having pretreatment technology in system 4 did not help to improve the resistance to corrosion.

4.2.2.3. Exposed panels in NSS assessed by visual inspection for degree of blistering

The results of system 1 exposed in the NSS chamber for 1000 hours are shown in Fig. 84. There were no blisters formed during the test period in the 3 circle areas labelled as A to C.



Figure 84. Photographs of panels with 3 areas (a, b and c) of EIS measurements. System 1 was exposed in NSS chamber for 1000 hours and measured by EIS.

The results of not having blistering in system 1 correlated quite well with the EIS and total impedance data presented earlier, which indicated a small presence of corrosion product. Cell images also supported this whereby blisters were formed sometime after the corrosion products were detected by EIS measurements.

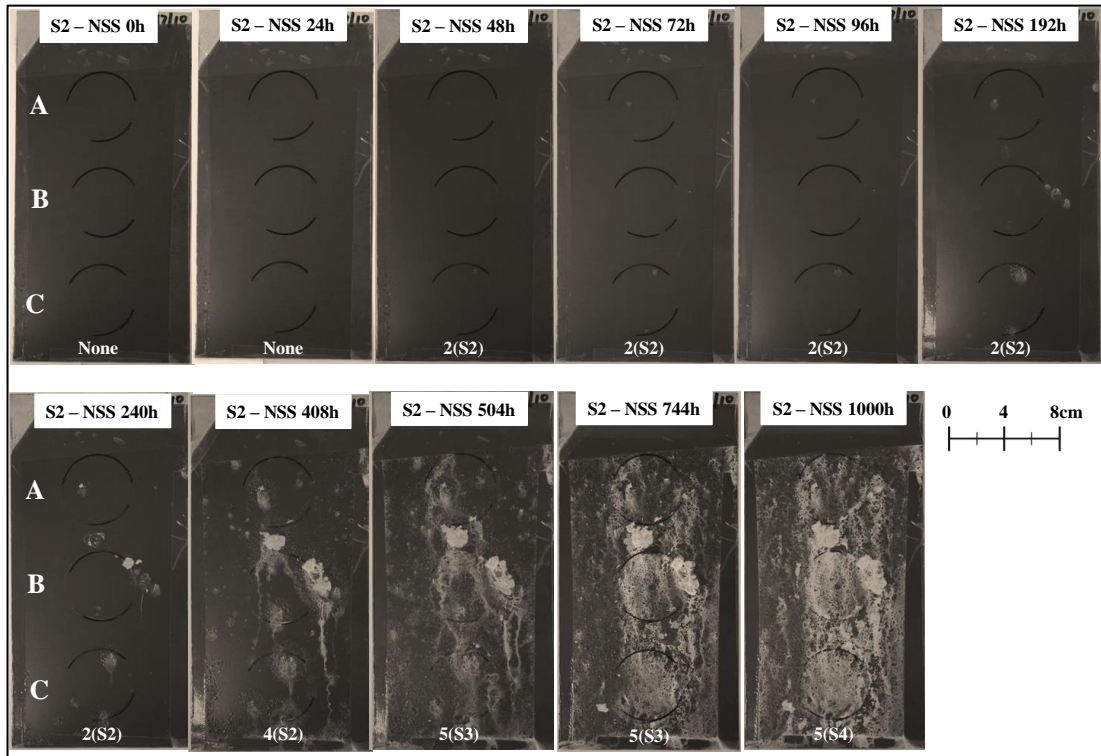


Figure 85. Photographs of panels with 3 areas (a, b and c) of EIS measurements. System 2 was exposed in NSS chamber for 1000 hours and measured by EIS.

The results of system 2 exposed in NSS chamber for 1000 hours are shown in Fig. 85. Blisters, 2(S2) was observed at 48 hours in the 3 black circle areas and then over time increased in number and size to 5(S4) at 1000 hours. The image also shows a large amount of corrosion products represented by white areas on the surface of the coated panel from 408 hours onward to 1000 hours (See Fig. 85). EIS data indicates that at 24 hours, corrosion products were detected and the effect of this caused the blisters to form in the coating at 48 hours.

The results of system 3 exposed in NSS chamber for 1000 hours are shown in Fig. 86. No blister was observed until 240 hours of exposure. Blisters, 2(S2) were formed in the 3 black circle areas and then over time increase in number and size to 5(S5) at 1000 hours. The image also shows a small amount of corrosion product,

represented by white areas on the surface of the coated panel from 408 hours onward to 1000 hours (See Fig. 86). The blisters size of system 3 were larger than system 2 with similar number of blisters. EIS data indicates that at 192 hours corrosion products were present and the effect of this over time caused blisters to form in the coating at 240 hours.

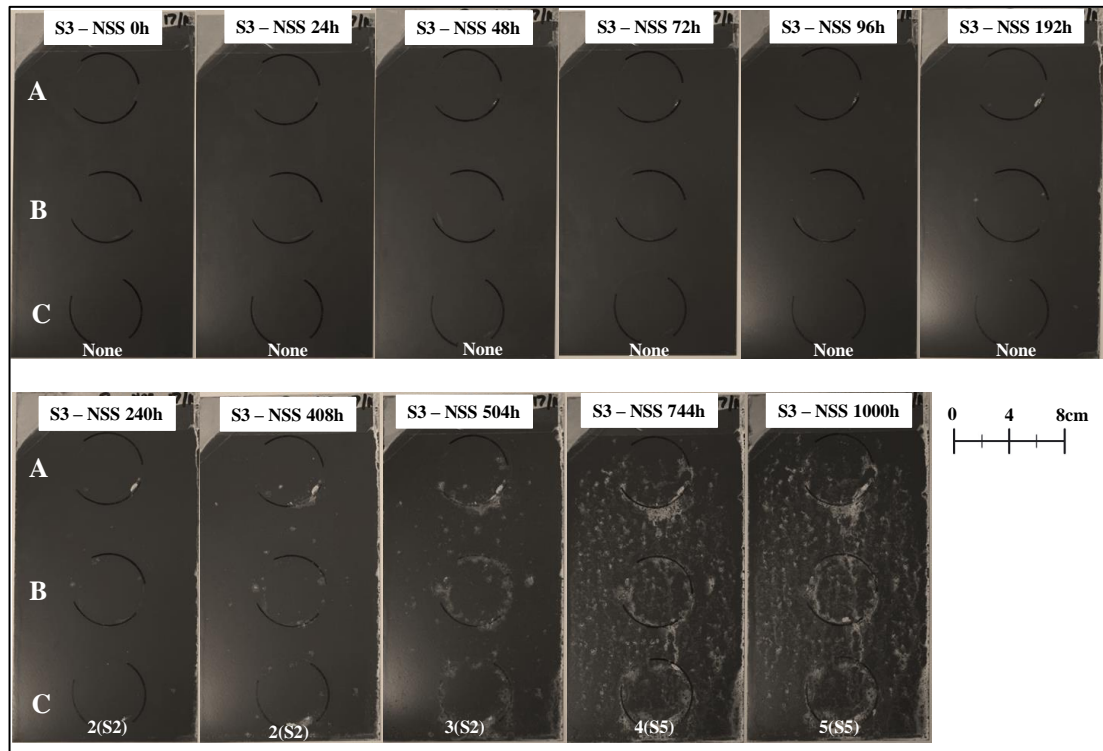


Figure 86. Photographs of panels with 3 areas (a, b and c) of EIS measurements. System 3 was exposed in NSS chamber for 1000 hours and measured by EIS.

The results of system 4 exposed in NSS chamber for 1000 hours are shown in Fig. 87. No blister was observed until 240 hours of exposure was reached. Blisters, 2(S2) were formed in the 3 black circle areas and then over time increased in number and size to 5(S5) at 1000 hours. The images also show a small amount of corrosion products, represented by white areas on the surface of the coated panel, starting at 408 hours and then gets worst at 1000 hours (See Fig. 87). The blister quantity and size of system 4 were similar to system 3, but larger than system 2 with similar number of blisters. EIS data indicates that at 192 hours corrosion products are present and the effect of this over time caused blisters to form in the coating at 240 hours.

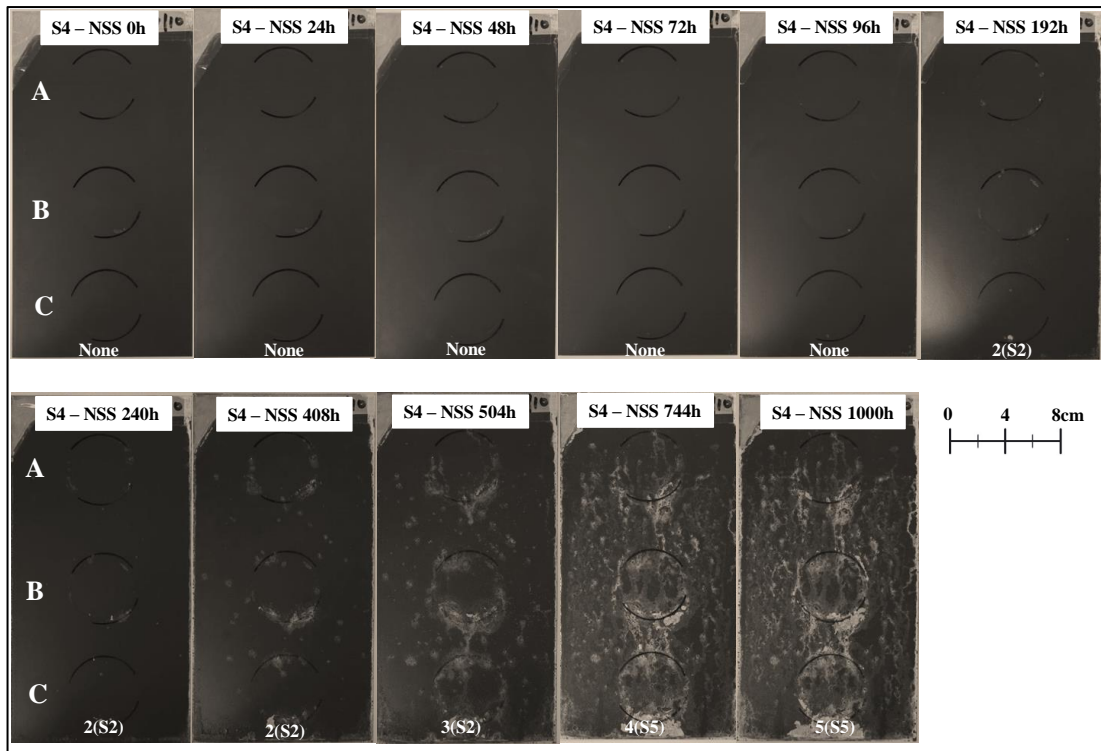


Figure 87. Photographs of panels with 3 areas (a, b and c) of EIS measurements. System 4 was exposed in NSS chamber for 1000 hours and measured by EIS.

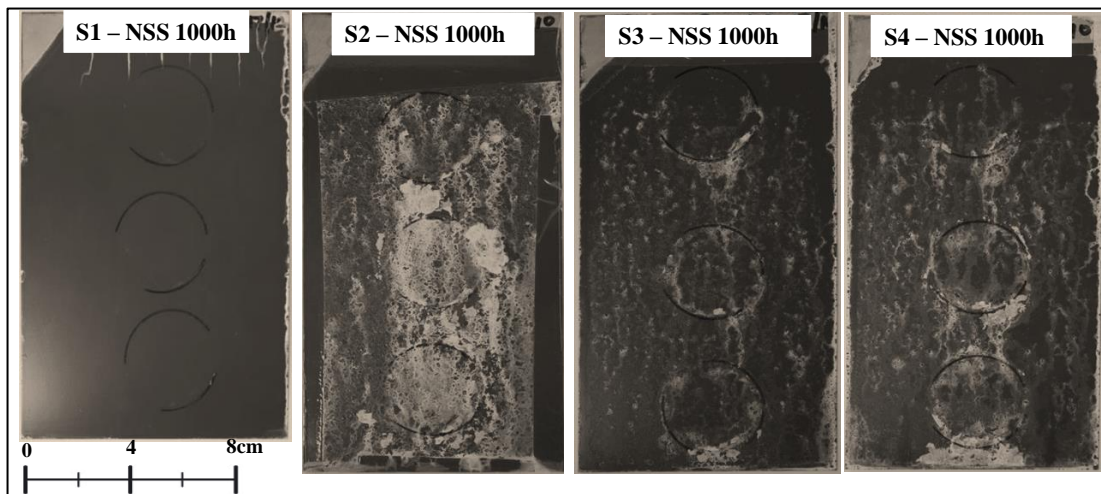


Figure 88. Photographs of System 1 to 4 after 1000 hours of exposure in NSS.

A summary of systems 1 to 4 exposed in NSS after 1000 hours is shown in Fig. 88. It clearly shows that a solventborne primer clearly outperformed the other 3 systems based on waterborne pretreatment primers. It has no blisters formed in the coating, whereas the other 3 systems do, with system 2 looking the worst, then followed by systems 3 and 4. However when assessed by degree of blistering, system

3 and 4 were the worst, system 2 was slightly better based of the scoring used (See Fig. 89). The reason for the lower scoring was due to the smaller blister size formed in system 2 compared to system 3 or 4, which were larger.

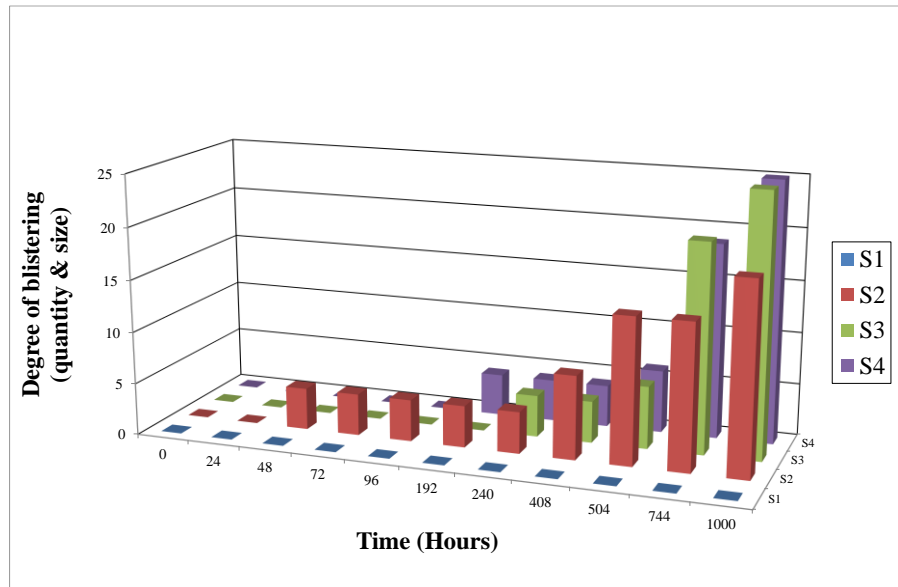


Figure 89. Degree of blistering vs. time plot of 4 systems exposed in NSS cabinet for 1000 hours.

4.2.3. Humidity test

4.2.3.1. Open circuit potential

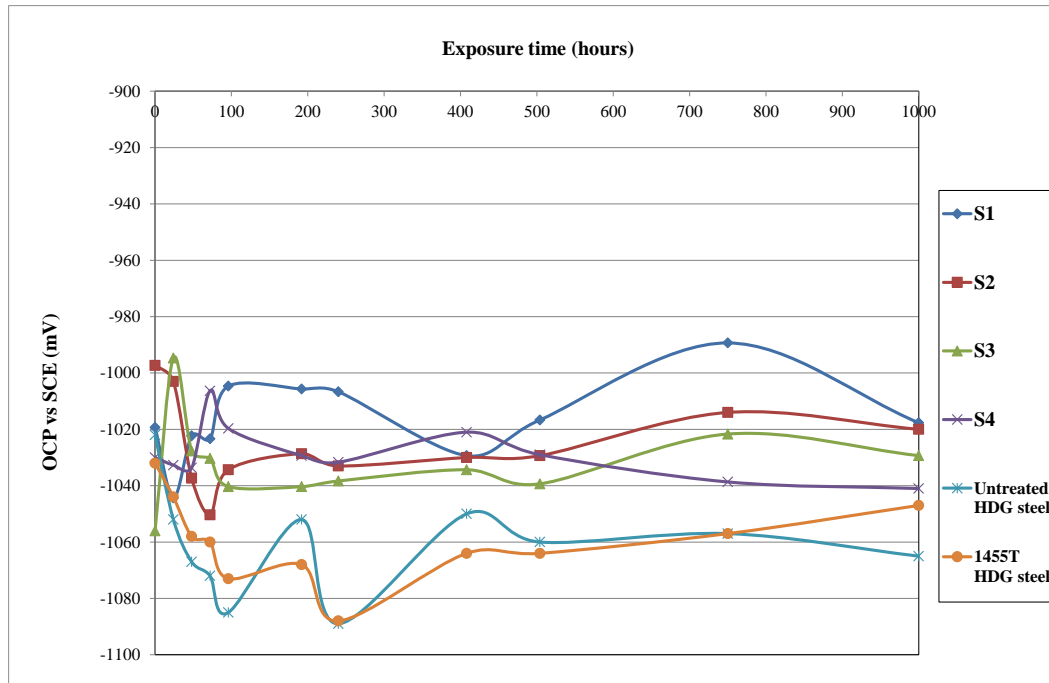


Figure 90. Open circuit potential of 4 systems tested in NSS over compared to HDG steels.

The open circuit potential of each system during humidity testing was measured and the results are presented in Fig. 90. They were compared to the measured OCP of HDG steel substrates obtained during EIS cell measurements in the previous chapter acting as baseline readings. The data showed system 3 had the most negative potential at the initial measurement, and then followed by 1455T treated HDG steel, system 4, untreated HDG steel and system 1 in that order. The most positive potential was system 2 which had no anti-corrosive pigment.

As the systems were exposed in the humidity chamber over time, the potential of these systems increased or decreased for the first 2-3 readings and then went into cycles of either positive or negative in behaviour until the end of the test. The rank of potential values of the 4 systems tested in humidity chamber is the same as obtained in EIS cells.

4.2.3.2. Panels exposed in humidity chamber and characterised by EIS

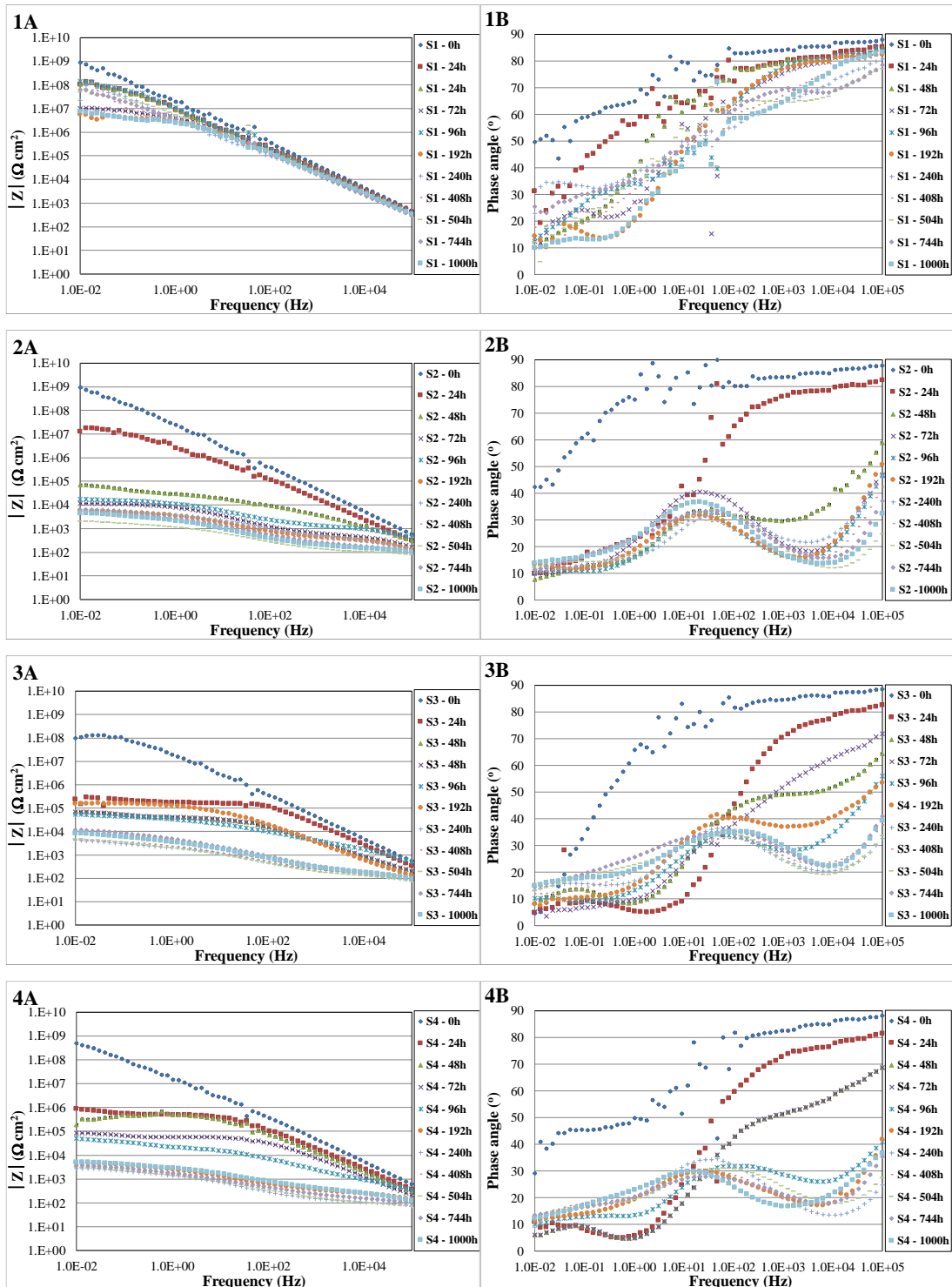


Figure 91. Bode impedance modulus (a) and phase angle (b) plots of 4 systems (labelled as 1 to 4) tested in a humidity chamber over time.

The spectra of impedance modulus for the 4 systems are shown in Fig. 91. System 1 has the highest impedance and over time shows some deterioration after 192 hours of exposure. After 1000 hours of exposure the modulus impedance was still high, around $10^7 \Omega \text{ cm}^2$ which indicated that the coating was still protecting the substrate with little or no corrosion products and blisters present. Systems 2, 3 and 4 have similar modulus impedance spectra throughout the period of the test. They start to deteriorate after 24 hours with systems 3 and 4 decreasing dramatically to $<10^6 \Omega \text{ cm}^2$ whereas system 2 stayed at $\sim 10^7 \Omega \text{ cm}^2$. At 48 hours all three systems decreased to $\sim 10^5 \Omega \text{ cm}^2$ and then progressed to $\sim 10^4 \Omega \text{ cm}^2$ at the end of the test.

The results show that humidity test is more aggressive than EIS cells but slightly less aggressive than NSS. Even the benchmark system showed some deterioration in impedance modulus value going as low as $<10^7 \Omega \text{ cm}^2$ with no blister forming in the coating (See Fig. 88). Humidity is a different test to the other two tests, no salt solution is used; only 100% relative humidity at 40 °C is used. The higher temperature and water are the key parameters to induce the corrosion process.

The phase angle spectra complement the results of impedance modulus, and in addition it can indicate the presence of corrosion products in the system. Systems 2 to 4, all have corrosion products forming at the substrates, which are represented by a second cycles in the spectra at mid frequency range. Both systems 3 and 4 have corrosion products at 24 hours compared to system 2, which have no anti-corrosive pigment, performed slightly better at 48 hours. System 1 shows some sign of corrosion activity near the end of the test.

In all of the systems, especially at the beginning there was interference in the spectra at around 50 Hz. Again this shows the signal to noise ratio is high and indicates how good a coating is in protecting the steel. A good performing coating, in this case system 1, will have high interference at the beginning and then over time less so throughout the test period. A poor performing coating will not, in this case the interference finished at 24 hours for the other 3 systems. Systems 2 to 4 represented this quite well (See Fig. 91b).

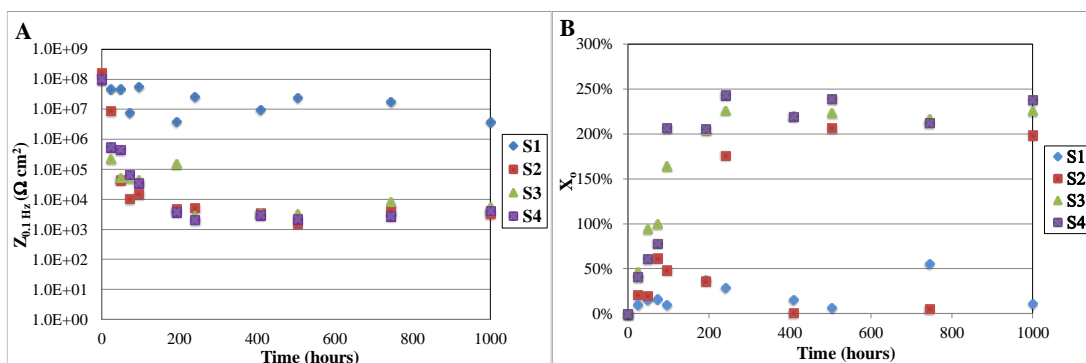


Figure 92. $Z_{0.1\text{Hz}}$ (a) and X_c (b) vs. time plots of systems exposed in humidity chamber.

The total impedance of system 1 is above $10^6 \Omega \text{ cm}^2$ during the entire period of the test (See Fig. 92a), and this indicates that no or very little corrosion product formed underneath the film. Systems 2 to 4 have similar performances over time and the sharpest decrease in total impedance was found in the first 192 hours of exposure, values dropping from $10^8 \Omega \text{ cm}^2$ at the start to $<10^4 \Omega \text{ cm}^2$ during time period between 240 and 1000 hours. This indicates that the coatings will not protect the steel. However, this is not the case when viewing the photographs of exposed panels (See Fig. 95-98). The total impedance performance between the three systems was similar to each other. Addition of anti-corrosive pigments into systems 3 and 4 did not improve the performance. System 2 contains no pigment.

The percentage water uptake of the 4 systems were determined by the change in capacitance over time are shown in Fig. 92b. An increase in capacitance indicates an increase in water uptake by the coating and this could clearly be seen in the waterborne pretreatment primers (Systems 2-4) compared to solvent-borne primer of system 1. System 1 increased by around 50% compared to between 200 and 250% for systems 2 to 4, with system 2 having the lowest amount of water uptake out of the 3 systems. The percentage water uptake calculated for humidity test is similar to NSS but not to EIS cells. This is probably due to the similar testing temperatures used by the 2 tests. EIS cell testing temperature was a lot lower than the other 2 tests, 21 °C compared to 35-40 °C.

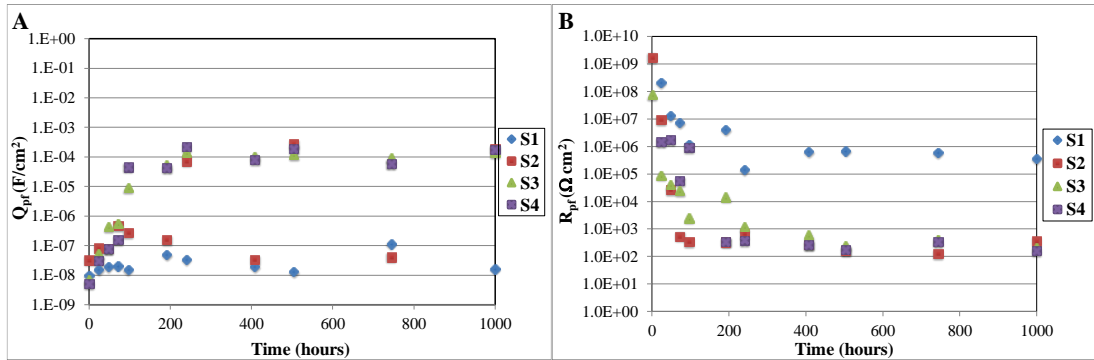


Figure 93. Q_{pf} (a) and R_{pf} (b) vs. time plots of systems exposed in humidity chamber.

The results for the film capacitance, Q_{pf} (a) and film resistance, R_{pf} (b) of the 4 systems are shown in Fig. 93. It shows that system 1 has the lowest increase in film capacitance over time and this is why the percentage water uptake was the lowest out of the 4 systems. Systems 2, 3 and 4 have similar trend in Q_{pf} performance over time with system 2 having a more dramatic decrease at 408 and 750 hours. This may be the results of when the sample was taken out and measured by EIS.

The film resistance of system 1 is the highest, but deteriorates over time to $\sim 10^6 \Omega \text{ cm}^2$ at 408 hours and stays reasonably constant until the end of the test to $\sim 10^5 \Omega \text{ cm}^2$. Systems 2, 3 and 4 have similar film resistance throughout the test with the biggest decrease between 0 and 200 hours, and the trends in the plots were also similar. They decrease to $< 10^2 \Omega \text{ cm}^2$ at 1000 hours and having so low film resistance indicates no protection from the coating to stop electrolyte penetrating through into the coating/metal interface.

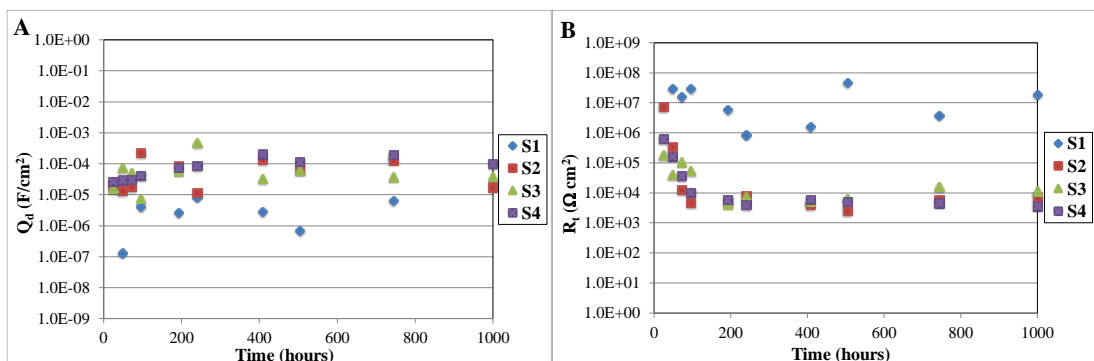


Figure 94. Q_d (a) and R_i (b) vs. time plots of systems exposed in humidity chamber

The results of double layer capacitance (a) and charge transfer resistance (b) of the 4 systems are shown in Fig. 94. It shows that system 1 had the lowest increase in double layer capacitance over time compared to the other 3 systems, but it does indicate some water was present at the coating/metal interface. Systems 2, 3 and 4 had similar trends in Q_d performance over time. System 2 was marginally better than systems 3 and 4 with system 4 being the worst.

The charge transfer resistance of system 1 was the highest, but deteriorated over time to a minimum of $\sim 10^6 \Omega \text{ cm}^2$ and then increased to $\sim 10^7 \Omega \text{ cm}^2$ at the end of the test. This may be the effect of having anti-corrosive pigment leaching into the substrate. The R_t of systems 2, 3 and 4 decreased dramatically in the first 200 hours and then stayed reasonably constant to the end of the test. The plots had similar R_t trends, decreasing to $<10^4 \Omega \text{ cm}^2$ at 1000 hours. Having so low an R_t indicates little resistance to corrosion. Also the presence of anti-corrosive pigment in systems 3 and 4 did not improve R_t value compared to system 2 with no pigment. The R_t trend of the 3 systems tested in humidity were similar to that of NSS when tested to 1000 hours, with only slightly high value of $<10^4 \Omega \text{ cm}^2$ compared to $<10^3 \Omega \text{ cm}^2$ respectively.

4.2.3.3. Exposed panels in humidity assessed by visual inspection

The results of system 1 exposed in the humidity chamber for 1000 hours are shown in Fig. 88. There were no blisters formed during the test period in the 3 black circle areas labelled as A to C. The result of not having blistering in system 1 correlated quite well with the EIS and total impedance data presented earlier, which indicated a little or no corrosion product present. Blistering was always found to form a period of time after corrosion product was detected.

There were small amounts of white marks around area A due to the damage caused by the acrylic tube used during the construction of the cell for EIS measurements. It may also be due to the high testing temperature used in humidity, which can soften the topcoat making it easier to damage using the acrylic tube during the construction of cells for EIS measurements.

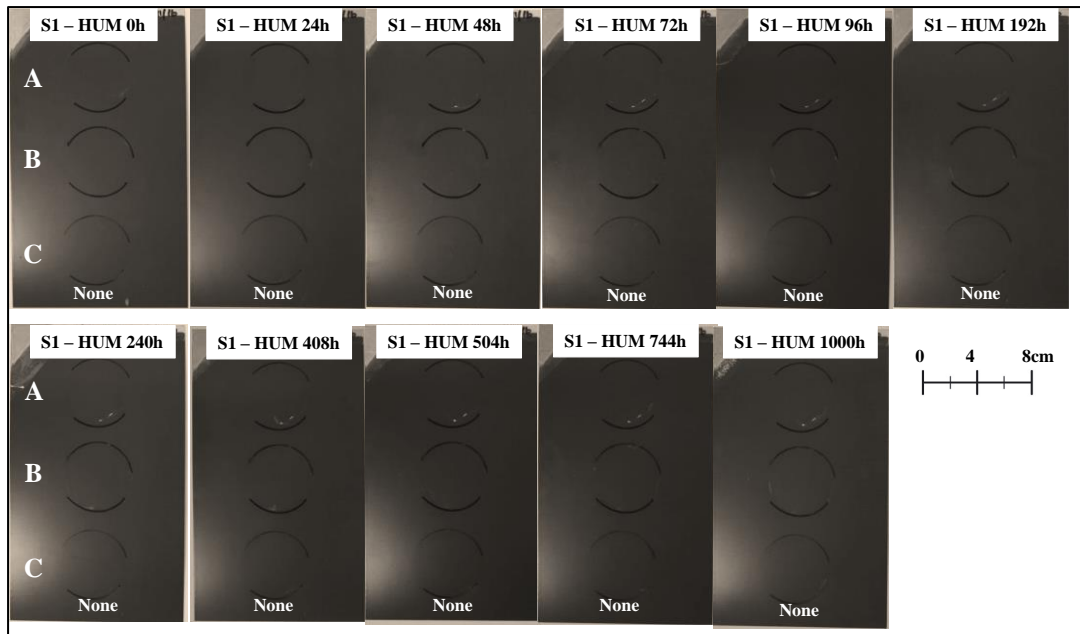


Figure 95. Photographs of panels with 3 areas (a, b and c) of EIS measurements. System 1 was exposed in humidity chamber for 1000 hours and measured by EIS.

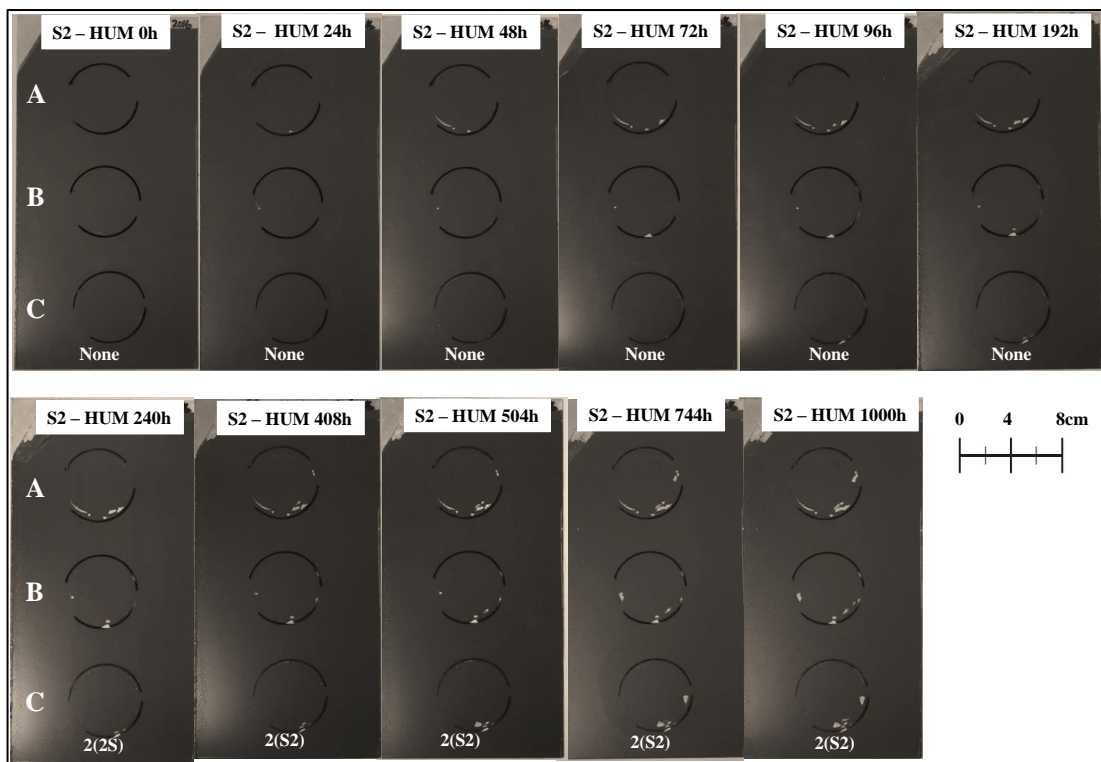


Figure 96. Photographs of panels with 3 areas (a, b and c) of EIS measurements. System 2 was exposed in humidity chamber for 1000 hours and measured by EIS.

The results of system 2 exposed in humidity chamber for 1000 hours are shown in Fig. 96. Blisters, 2(S2) are formed in the coating at 240 hours in the 3 circle areas and then show no increase in number or size of the blisters. Visually, the S2 blisters could be with human eyes but could not be observed in the photographs that were taken due to the blisters size been in between 1 and 2 mm diameter.

There were corroded areas on the panels, represented by white marks around the 3 circle areas, due to the damage caused by the acrylic tube used during the construction and de-construction of the cell during EIS measurements. In addition, the high testing temperature does not helped, it can soften the coating and damage easier when placing acrylic tubes of it. The blister results correlated quite well with the ECM data, which indicated that after 240 hours, no change in performance would occur.

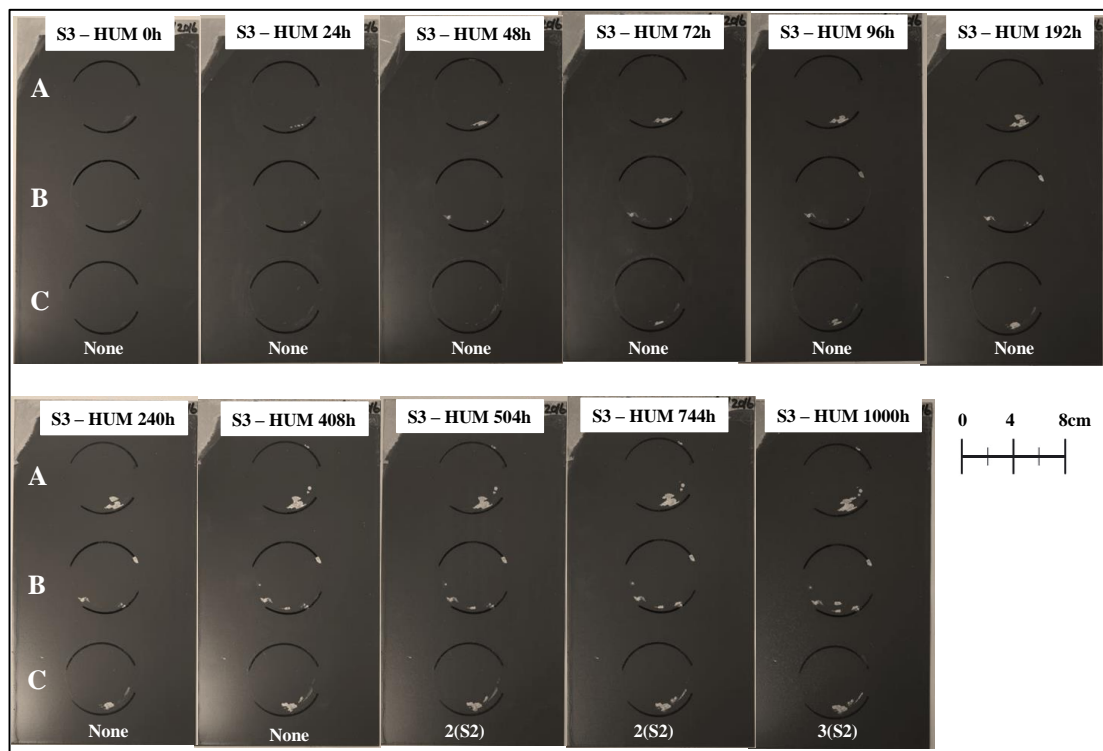


Figure 97. Photographs of panels with 3 areas (a, b and c) of EIS measurements. System 3 was exposed in humidity chamber for 1000 hours and measured by EIS.

The results of system 3 exposed in humidity chamber for 1000 hours are shown in Fig. 97. For the first 408 hours there were no blisters formed in the coating. At 500 hours blisters, 2(S2) were observed and they gradually increased in quantity to 3(S2) at 1000 hours. The white marks around the 3 circle areas were due to the damage

caused by the acrylic tube used during the construction of the cell for EIS measurements.

The blister results correlated quite well with the ECM data which indicated that after 500 hours, no significant change in performance would occur.

The results of system 4 exposed in humidity chamber for 1000 hours are shown in Fig. 98. Blisters, 2(S2) were formed at 240 hours in the 3 black circle areas and then stayed the same size and quantity over time to 1000 hours. The white marks around the 3 circle areas were due to the damage caused by the acrylic tube used during the construction of the cell for EIS measurements.

The blister results correlated quite well with the ECM data which indicated that after 240 hours, no change in performance would occur and this effect on blistering can be seen in Fig. 91



Figure 98. Photographs of panels with 3 areas (a, b and c) of EIS measurements. System 4 was exposed in humidity chamber for 1000 hours and measured by EIS.

The results of assessing the degree of blistering for the 4 systems are shown in Fig. 99. It shows humidity is the least aggressive of the 3 accelerated tests when evaluating blisters. System 1, a solvent-borne primer clearly outperformed the other 3 systems based on water-borne pretreatment primers. It had no blisters formed in the coating, whereas the others 3 system did. In fact, they all presented with the same results after 1000 hours of exposure. System 3 was delayed by 250 hours in formation of blisters compared to system 2 and 4, both of which were observed at 240 hours.

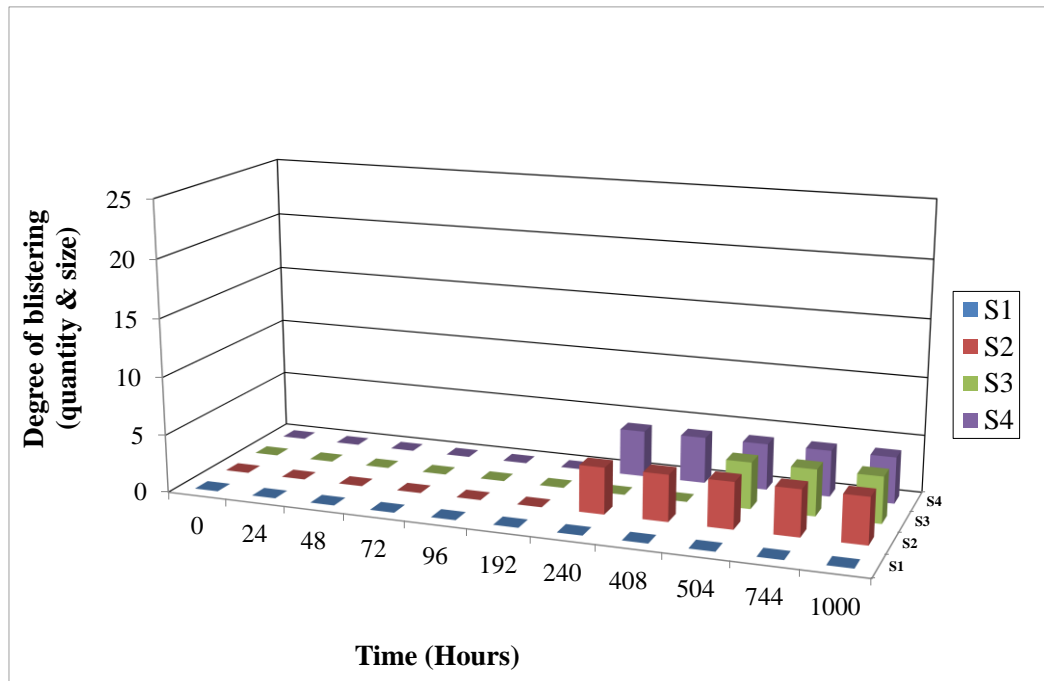


Figure 99. Degree of blistering vs. time plot of 4 systems exposed in a humidity cabinet for 1000 hours.

4.3. Panels exposed in outdoor weathering

4.3.1. North facing panels characterised by EIS

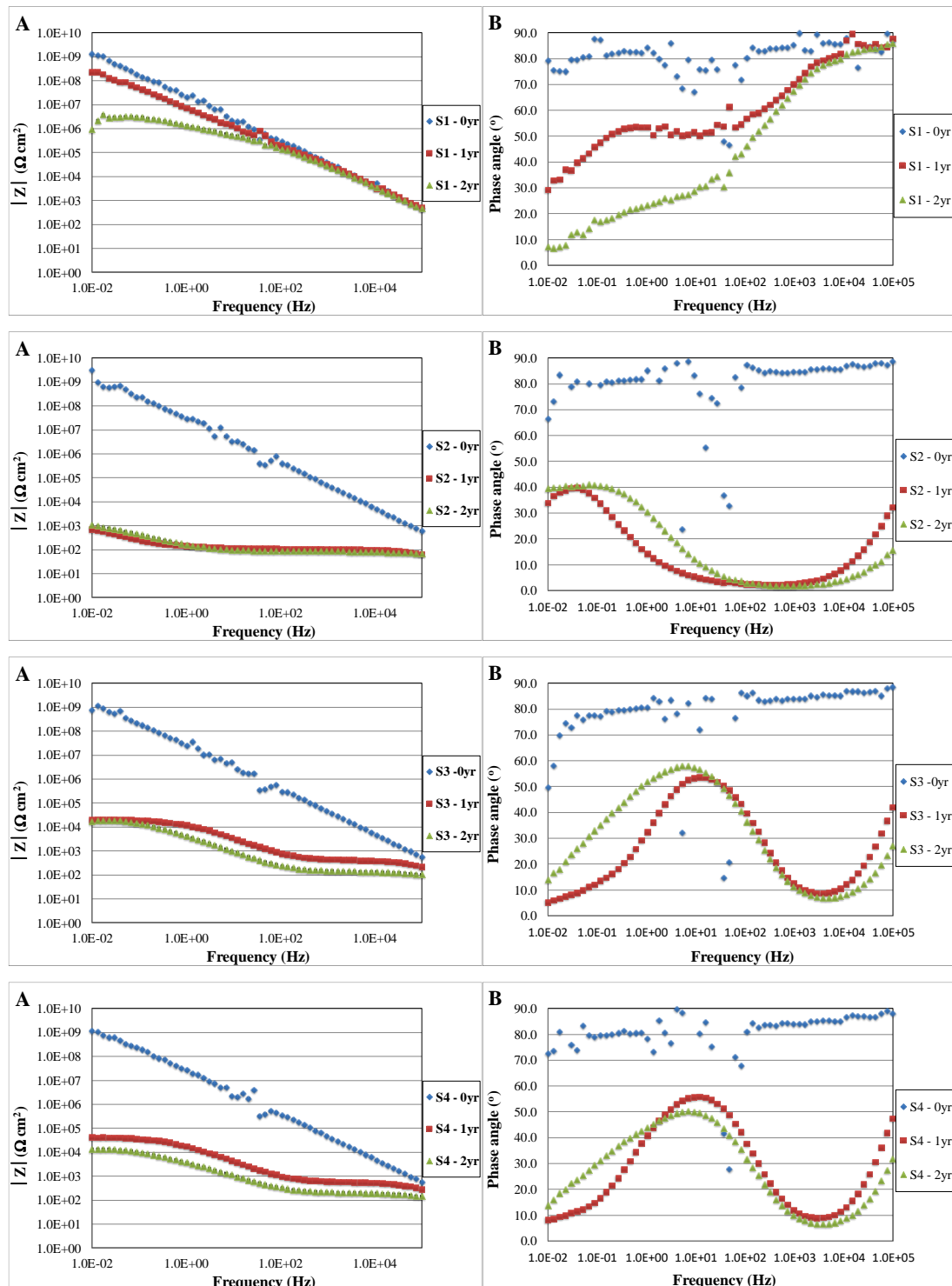


Figure 100. Bode impedance modulus (a) & phase angle (b) plots of 4 systems (labelled as S1, S2, S3 and S4) exposed at 90° North facing in Bohus Malmön for 2 years.

The spectra of impedance modulus for the 4 systems exposed in Bohus Malmön, 90° North facing are shown in Fig. 100. System 1 had the highest impedance and over time showing a small deterioration after 1 year. After 2 years, the coating impedance decreased to $\sim 10^6 \Omega \text{ cm}^2$, which indicated that the coating was still protecting the substrate with some corrosion products and blisters present. Systems 2, 3 and 4 have similar modulus impedance spectra at the start of the test. They deteriorated at a similar rate with systems 3 and 4 ($\sim 10^4 \Omega \text{ cm}^2$) only slightly better than system 2 ($\sim 10^3 \Omega \text{ cm}^2$).

The phase angle spectra complemented the results of modulus impedance, and in addition, it indicated whether or not the systems were forming corrosion products at the substrates. System 1 shows a small deterioration from zero to 2 years, but there is no sign of a 2 cycle formation, which indicates no corrosion products are present. Systems 2 to 4, all have corrosion products forming at the substrates, which are represented by a second cycle in the spectra at mid frequency range.

In all of the systems, especially at the beginning, there were interferences in the spectra at around 50Hz. Again, this shows the signal to noise ratio is high and indicates how good a coating is in protecting the steel. A good performing coating, in the case of system 1 did have interference at the beginning and after 1 year of exposure, but did not have after 2 years of exposure. For poor performing coatings (systems 2, 3 and 4) the interferences in the signal only occurred at the beginning of the test.

4.3.2. North facing panels assessed by visual inspection for degree of blistering

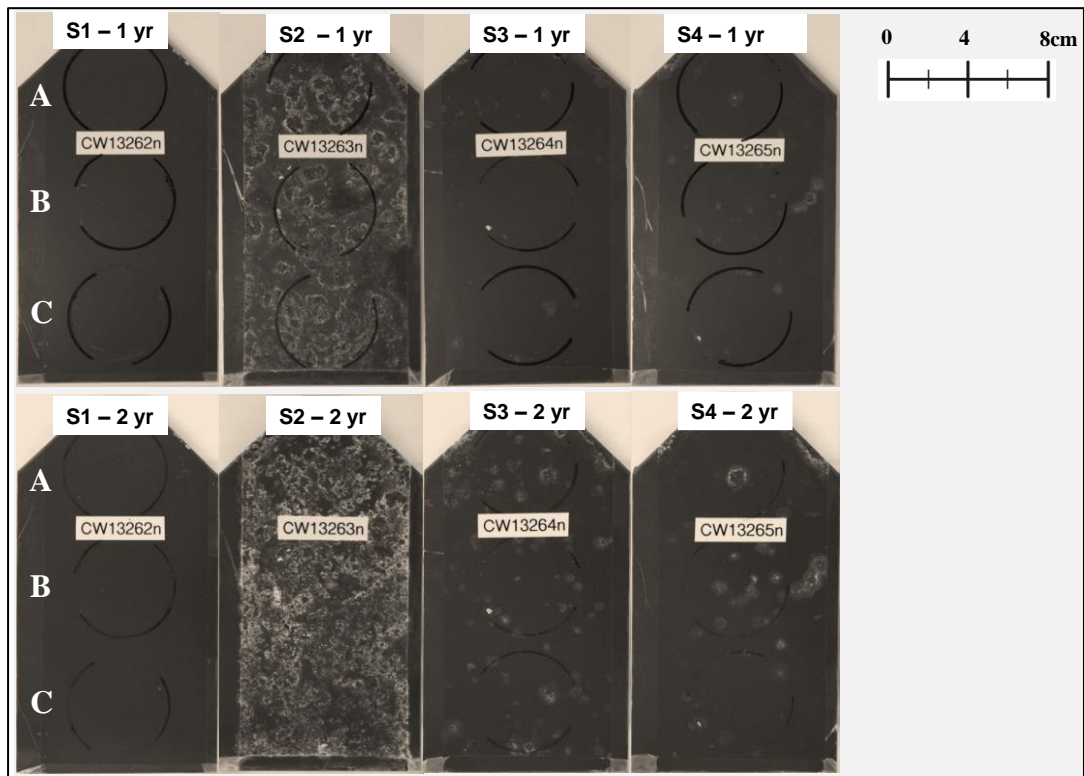


Figure 101. Photographs of panels of 4 systems exposed at 90° North facing in Bohus Malmön for 2 years.

The photographs of panels of the 4 systems exposed at 90° North facing in Bohus Malmön for 2 years are shown in Fig. 101. System 1 is the best with no blistering for the first year and in the second year, only a few blisters were present, 2(S2). System 2 was the worst even after one year. It just shows how important it is to have anti-corrosive pigment in the primer when tested outdoor. This is not the case for system 2 when exposed in accelerated tests; it had performed similarly to systems 3 and 4. Corrosion products can be seen all over the panel of system 2.

Systems 3 and 4 had similar blister size (S3) to each other with system 4 (quantity = 2) marginally better than system 3 (quantity = 3) after 2 years for number of blisters. Again, some corrosion products can be seen on the blistered area of the panels of these two systems, but not as much as system 2, which was assessed as 5 (4S).

The results of blistering in the 4 systems correlated quite well with the EIS and total impedance data presented earlier, which indicates a small to large presence of corrosion product. Blistering was found to form sometime after corrosion product was detected.

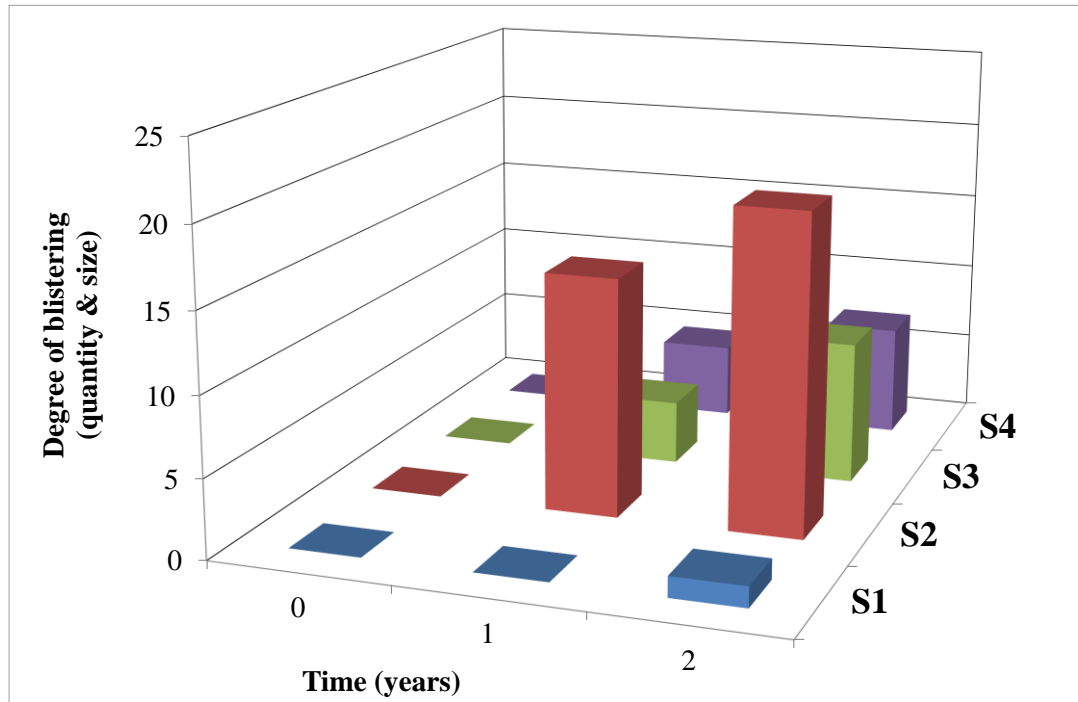


Figure 102. Degree of blistering vs. time plot of 4 systems exposed at 90° North facing in Bohus Malmö for 2 years.

The degree of blistering on the panels of the 4 systems exposed at 90° North facing in Bohus Malmö for 2 years are shown in Fig. 102. It clearly demonstrated that system 1 is the best, system 2 is the worst and in between them are systems 3 and 4 with no significant differences in performance.

4.3.3. South facing panels characterised by EIS

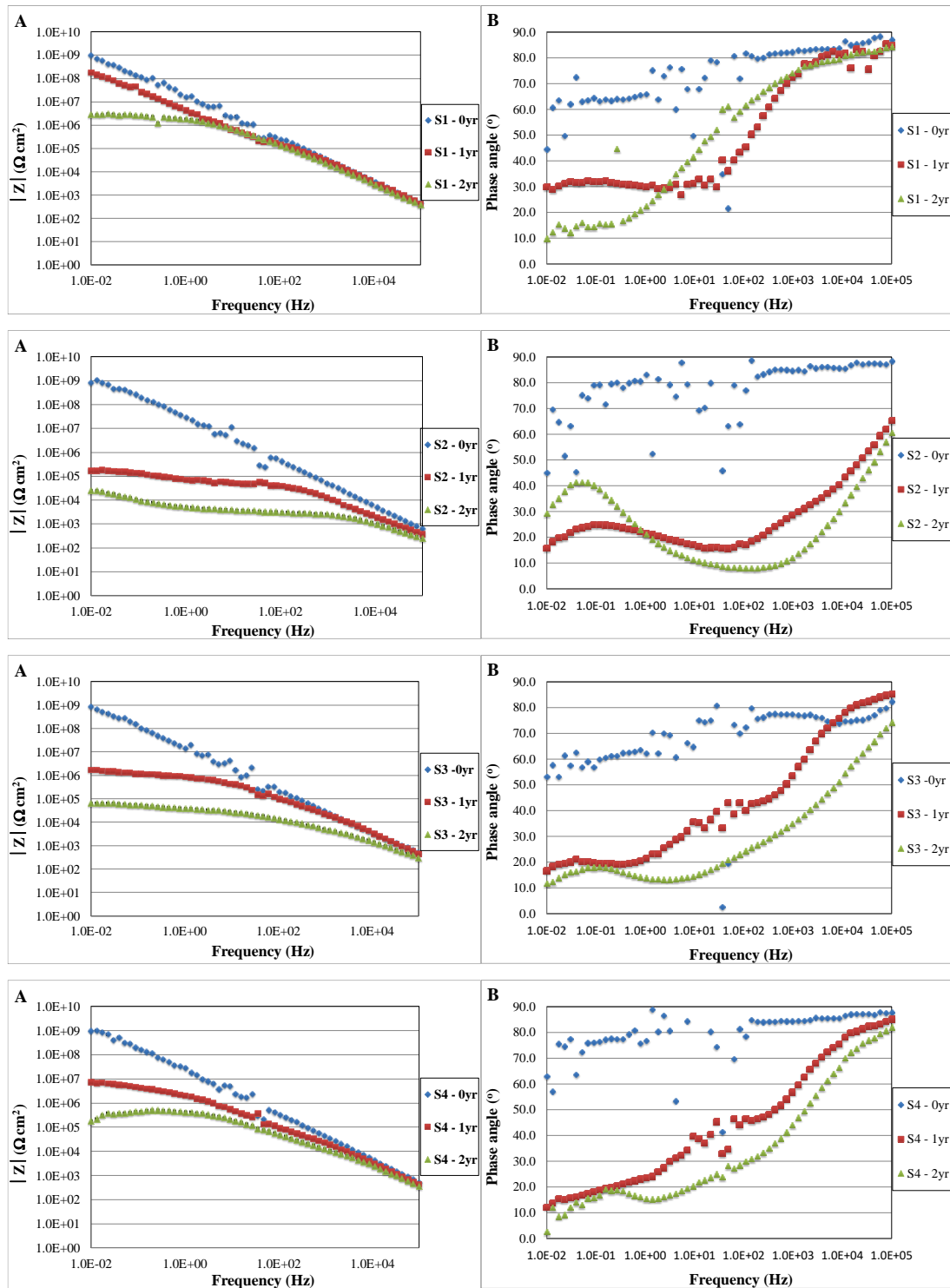


Figure 103. Bode impedance modulus (a) and phase angle (b) plots of 4 systems (labelled as S1, S2, S3 and S4) exposed at 45° South facing in Bohus Malmön for 2 years.

The spectra of impedance modulus for the 4 systems exposed in Bohus Malmö, 45° South facing, are shown in Fig. 103. System 1 has the highest impedance and over time shows a small deterioration after 1 year. After 2 years the coating impedance decreased to $\sim 10^6 \Omega \text{ cm}^2$ which indicates that the coating was still protecting the substrate with some corrosion products and blisters presented. It is difficult to explain why similar results are observed on panel exposed in South facing compared to North facing. Previous experience has shown that North facing was more aggressive environment than South facing due to more time in wet condition and salt deposited on the panels.

Systems 2, 3 and 4 have similar impedance modulus spectra at the start of the test. This time around, in a less aggressive environment, the 3 systems deteriorated at similar rate with system 4 ($\sim 10^5 \Omega \text{ cm}^2$) marginally better than system 3 ($< 10^5 \Omega \text{ cm}^2$) and system 2 the worst at $\sim 10^4 \Omega \text{ cm}^2$.

The phase angle spectra complemented the results of modulus impedance, and in addition indicated whether or not the systems were forming corrosion products at the substrates. System 1 shows a small deterioration from 0 to 2 years, but no sign of second cycles, which indicates no corrosion product is presented. Systems 2 to 4 all show corrosion products forming at the substrates, which are represented by second cycles in the spectra at mid frequency range.

4.3.4. South facing panels assessed by visual inspection for degree of blistering

The photographs of panels of the 4 systems exposed at 45° South facing in Bohus Malmö for 2 years are shown in Fig. 104 and the results of the assessment are shown as a plot in Fig. 98. System 1 is the best with no blistering for the first year and in the second year, only a few number of blisters are presented, 2(S2). System 2 is the worst even after one year. Again it just shows how important it is to have anti-corrosive pigment in the pretreatment primer when tested outdoors. This is not the case for system 2 when exposed to accelerated tests, it had similar performance to systems 3 and 4. Systems 3 and 4 had similar results of blistering to each other with system 4 marginally better than system 3 after 2 years.

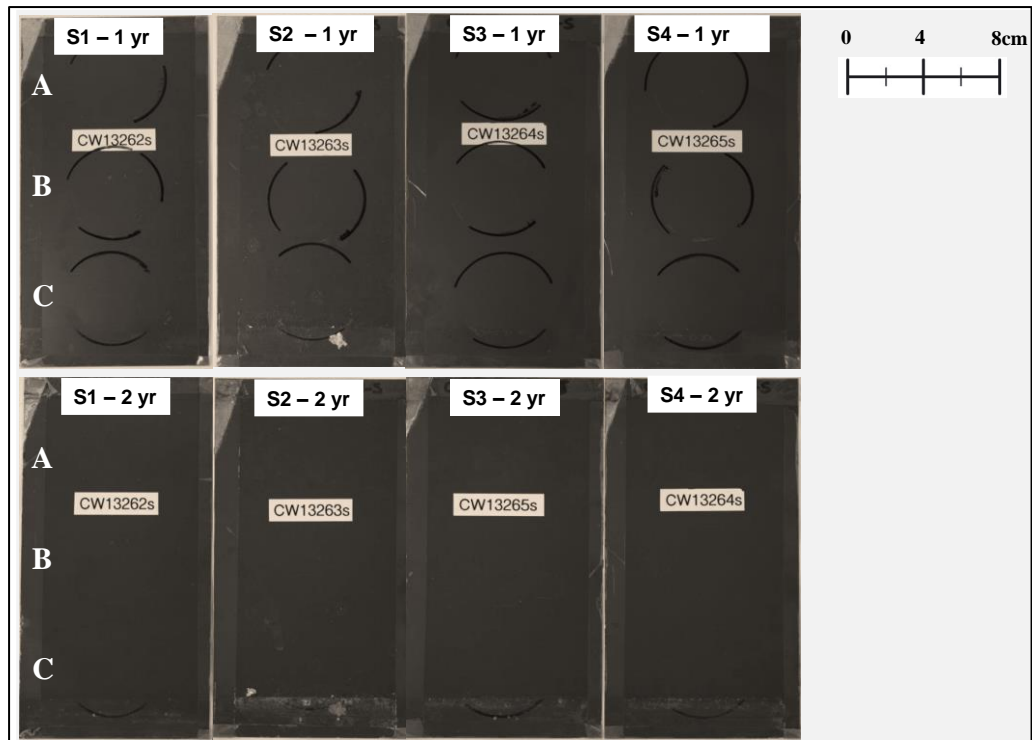


Figure 104. Photographs of panels of the 4 systems exposed at 45° South facing in Bohus Malmön for 2 years.

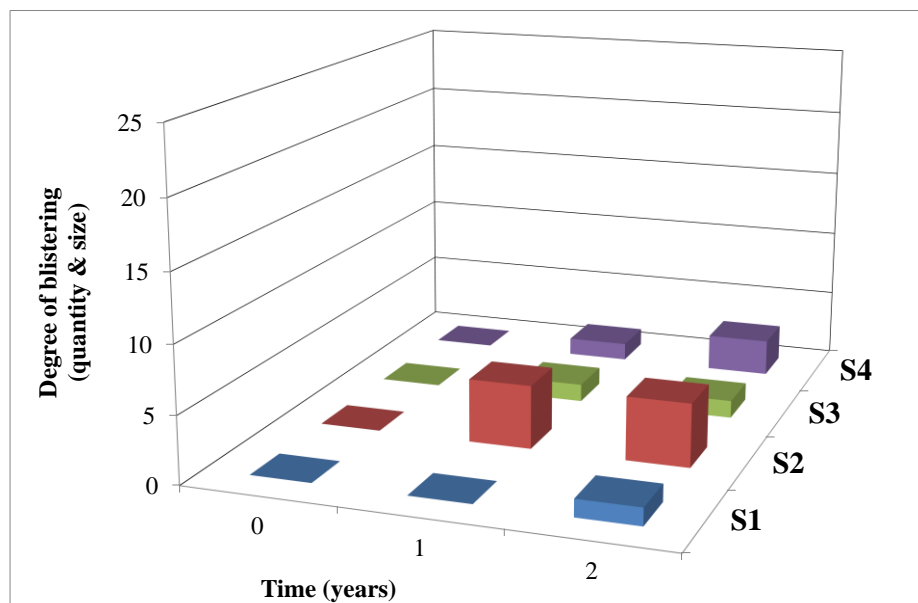


Figure 105. Degree of blistering vs. time plot of 4 systems exposed at 45° South facing in Bohus Malmön for 2 years.

4.3.5. ECM of North & South facing panels exposed in Bohus Malmön.

Total impedance results of the 4 systems exposed at North and South facing in Bohus Malmön (BM) are shown in Fig. 106. It shows that system 1 has similar performance at both locations and the panels deteriorated similarly over time. Whereas the other 3 systems show that North facing panels deteriorated more than panels facing South, indicating the North has a more aggressive environment than the South. But the ranking of the performance was similar for North and South facing panels.

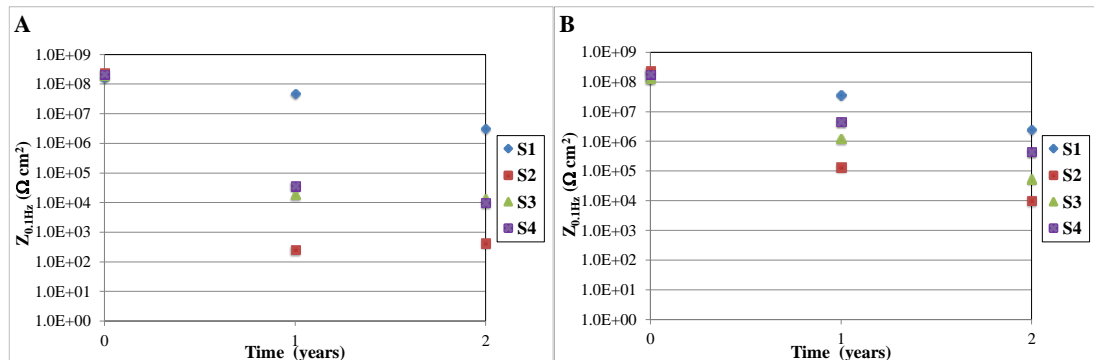


Figure 106. $Z_{0.1\text{Hz}}$ vs. time plots of 4 systems exposed at 90° North (a) and 45° South (b) facing in Bohus Malmön for 2 years.

Percentage water uptake results of the 4 systems exposed at North and South facing in BM are shown in Fig. 107. It shows that panels located North have a greater increase in percentage water uptake than panels located South.

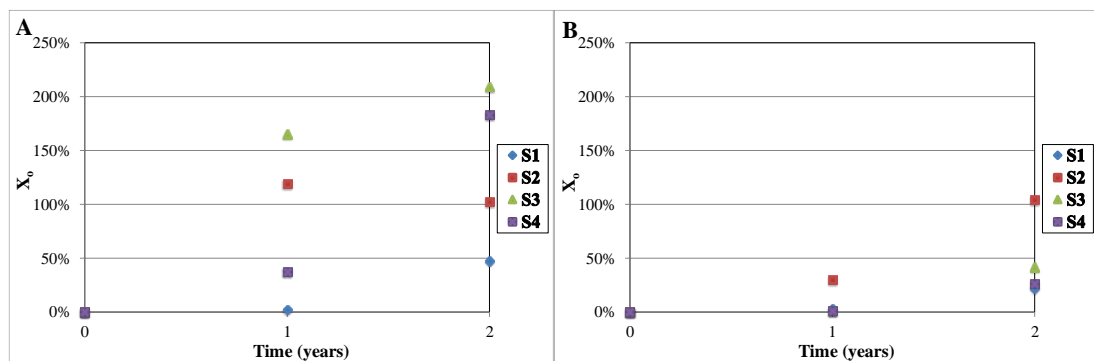


Figure 107. X_0 vs. time plots of 4 systems exposed at 90° North (a) and 45° South (b) facing in Bohus Malmön for 2 years.

This correlated quite well with the experience Beckers has had in exposing panels in Bohus Malmön for over 30 years [37]. The only exception is system 1 which, had

similar percentage water uptake for North and South facing panels. The results may be different if the system 1 is exposed for longer period of time.

The film capacitance results of the 4 systems exposed at North and South facing in BM are shown in Fig. 108. It shows that panels positioned North have a greater increase in Q_f than panels positioned South. This correlated quite well with the experience Beckers has had in exposing panels in Bohus Malmön. The only exception was system 1, which has similar percentage water uptake for both North and South facing panels.

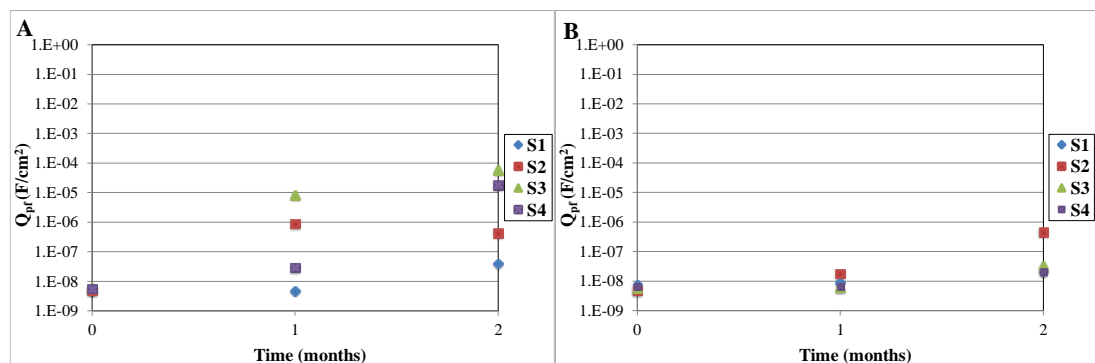


Figure 108. Q_{pf} vs. time plots of 4 systems exposed at 90° North (a) and 45° South (b) facing in Bohus Malmön for 2 years.

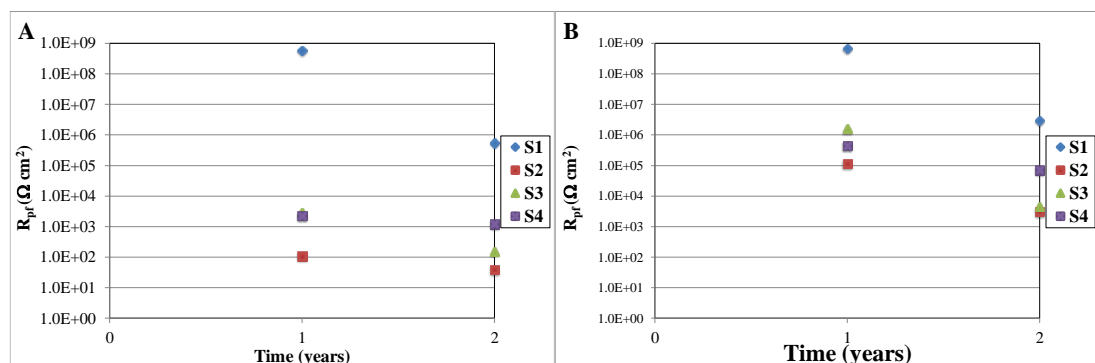


Figure 109. R_{pf} vs. time plots of 4 systems exposed at 90° North (a) and 45° South (b) facing in Bohus Malmön for 2 years.

The film resistance results of 4 systems exposed at North and South facing in BM are shown in Fig. 109. It shows that system 1 is the best system in North and South and has similar values in both locations. In the North, system 4 is next; follow by system 3 and system 2 the worst in that order. In the South, system 4 is next,

followed by system 3 and the worst is system 2. The 3 systems have higher R_f for the South than the North which indicates the coatings were still protecting in the South, but not doing so quite as well in the North location.

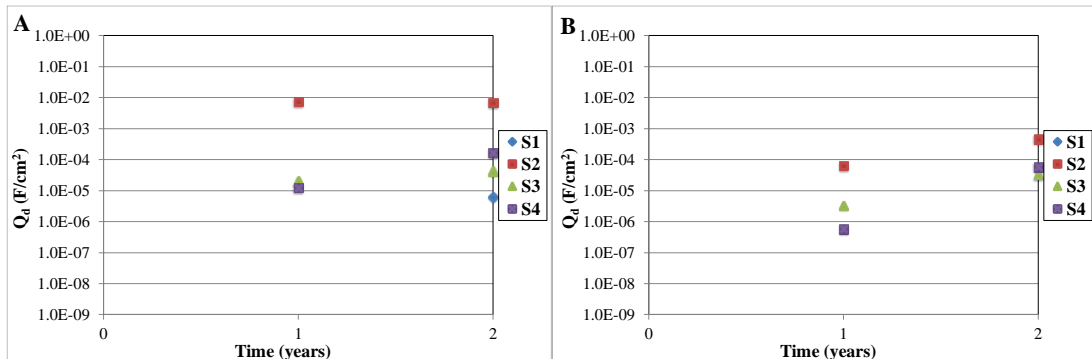


Figure 110. Q_d vs. time plot of 4 systems exposed at 90° North (a) and 45° South (b) facing in Bohus Malmön for 2 years.

The double layer capacitance results of the 4 systems exposed at North and South facing in BM are shown in Fig. 110. Once more, it shows that system 1 is the best in North and South locations. System 3 is next, followed by system 4 and the worst is system 2.

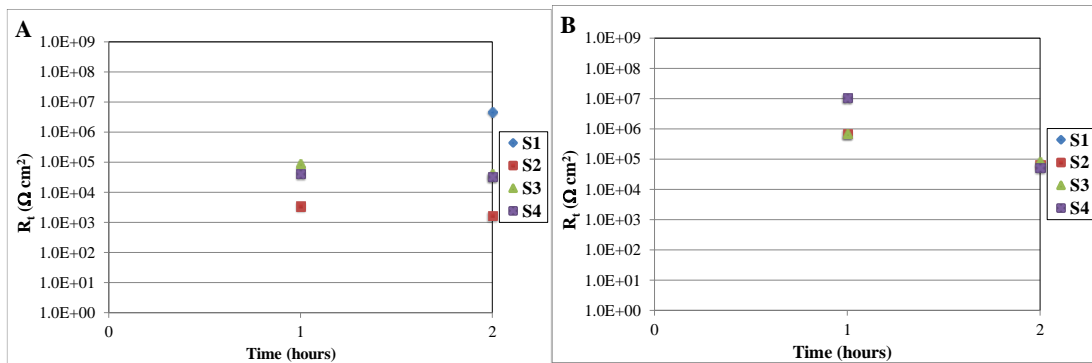


Figure 111. R_t vs. time plot of 4 systems exposed at 90° North (a) and 45° South (b) facing in Bohus Malmön for 2 years.

Charge transfer resistance results of the 4 systems exposed at North and South facing in BM are shown in Fig. 111. Predictably, it shows that system 1 is the best and the worst are the 3 systems based on the waterborne pretreatment primers. South facing panels for the 3 systems deteriorated less than North facing panels, as you would expect.

4.4. Summary of accelerated and outdoor weathering tests

Test		System 1	System 2	System 3	System 4
Cell – 1000h	EIS ($Z_{0.1, Hz}$)	1.8×10^8	4.3×10^2	1.0×10^3	7.5×10^2
	Degree of blistering	None	5(S4)	3(S3)	4(S3)
NSS – 1000h	EIS ($Z_{0.1, Hz}$)	1.9×10^8	7.2×10^2	1.5×10^5	7.2×10^4
	Degree of blistering	None	5(S4)	5(S5)	5(S5)
Humidity – 1000h	EIS ($Z_{0.1, Hz}$)	3.7×10^6	3.4×10^2	5.9×10^3	4×10^3
	Degree of blistering	None	2(S2)	3(S2)	2(S2)
BM-N – 2 years	EIS ($Z_{0.1, Hz}$)	2.6×10^6	1.0×10^3	5.4×10^4	4.4×10^5
	Degree of blistering	2(S2)	5(S4)	3(S3)	3(S2)
BM-S – 2 years	EIS ($Z_{0.1, Hz}$)	3.0×10^6	4.4×10^2	4.4×10^5	9.9×10^3
	Degree of blistering	2(S2)	4(S2)	2(S2)	3(S2)

Table 8. Summary of accelerated and outdoor weathering tests characterised by EIS and assessed by degree of blistering.

The results of four systems tested for 1000 hours in a cell, NSS, humidity and 2 years in BM-N and BM-S are shown in Table 8. The EIS results were based on the total impedance of the coating system. The degree of blistering results were assessed by using ISO 4628-2:2003. The results show that system 1 was the best in all tests with little or no deterioration. System 2 was the worst in all tests. System 3 and 4 were similar in all tests with no significant improvement between the two systems.

It was very difficult to distinguish which test deteriorated the most when comparing them to the four systems. If the tests were compared to individual system, then for system 1, cell and NSS were the least severe and the most aggressive tests were humidity, BM-N and BM-S. For system 2, been so poor in performance in all tests, there was no significant difference in the results of the tests. For system, 3 and 4 the least severe tests were NSS and BM-S and the most aggressive tests were cell, humidity and BM-S.

4.5. Development of FIB/SEM technique to observe corroded coated panels

The ultimate goal was to optimise the technique so that pigment dispersion, interfacial properties and changes occurring after exposure could be studied. EDS analysis was included in this study to investigate the chemical composition inside the coatings. Only the topcoat side of the pre-painted product was investigated, as this is the surface normally exposed to the environment. This investigation constituted part of a larger project assessing corrosion performance of organic primers.

4.5.1. Results and discussion

There is a lot of information available on sample preparation for SEM analysis [109] [113] [127] [128] [129] [130] [131] but few details of good practice of sample preparation for analysis of cross-sections of organic coating using FIB/SEM [117] [121]. The following sections show how an effective procedure was developed, using examples from various trials to demonstrate some of the issues encountered. To illustrate this, a schematic summary of the development process is shown in Fig. 112 which, outlines the logical order of the steps used to develop the milling process so that an effective EDS analysis of the sample can be produced.

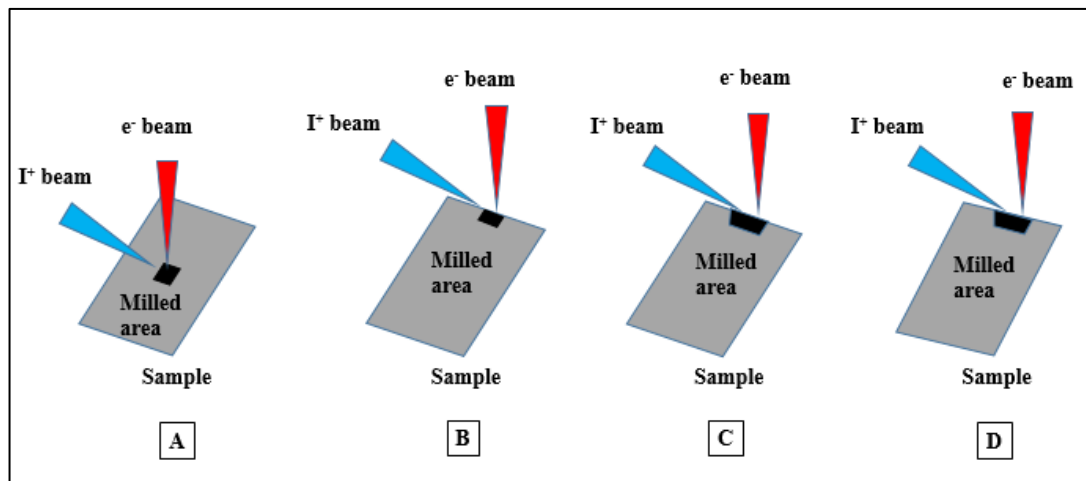


Figure 112. Schematic representation of sample position and beam geometry [121].

Sample stage at 52° so that the ion beam is 90° to the top surface of the sample (a).

The milled area is at the centre of the sample. The milled area (b) is moved to the edge of the sample and polished to improve X-ray detection (c) The milled shape is modified to an isosceles trapezoid to further improved X-ray detection. Increase in the

tilt and rotation angles added additional (d) improvement in X-ray detection and resulted in no shadowing effect.

4.5.1.1. Milling at centre of sample

During the initial experiments, milling was started at the centre rather than the edge because of the possible damage caused during the sample cutting process.

Figure 113a shows a secondary electron SEM image of a milled area of pre-painted metal at the centre of the sample. It can be seen that the milling process produces a poor finish for the cross-section, with no distinction between the coating and substrate, demonstrating why further material removal at lower beam current ('polishing') is necessary for good imaging of the cross-section.

Figure 113b shows a secondary electron SEM image of the same cross-section in Fig. 113a after polishing. Both the HDG steel and coatings containing pigments can now be observed. The combined coatings (topcoat and primer) have a thickness of approximately 35 μm .

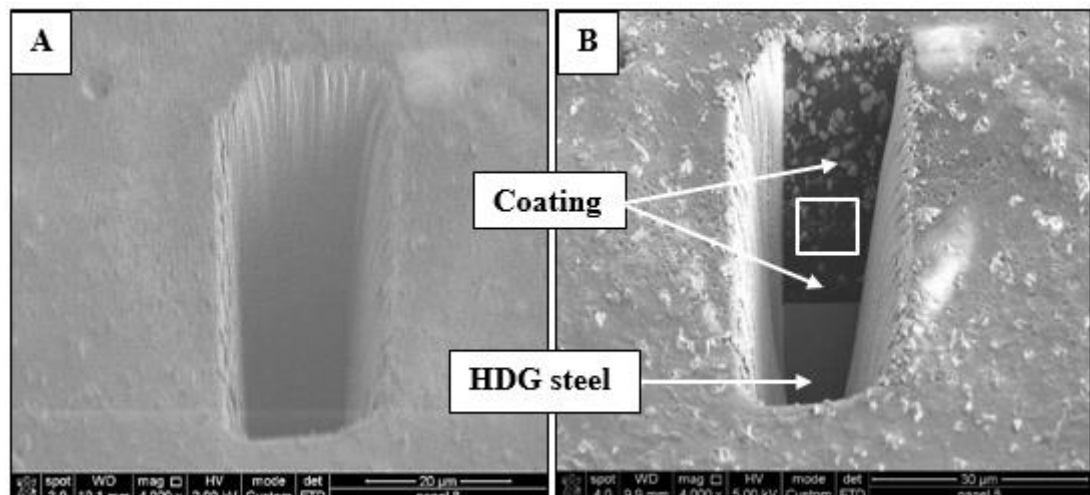


Figure 113. Secondary electron SEM images of milled (a) and polished areas (b) at the centre of sample. The red box indicates the area where EDS elemental mapping was performed (See Fig. 117 for results)

EDS analysis was carried out on the cross-sectioned area of this sample. Figure 114 shows EDS mapping of carbon in the cross-sectioned and highlights the problem with producing a cross-sectioned from the centre. The grey and white pixels indicate the presence of carbon, therefore bright regions represent carbon rich areas, while

black areas indicate an absence of X-ray detection. This was caused by the coating wall obstructing the X-ray signal, thus creating a shadowing effect (1) graphically illustrated in Fig. 114. Other elements were also mapped (not shown here) and showed similar results.

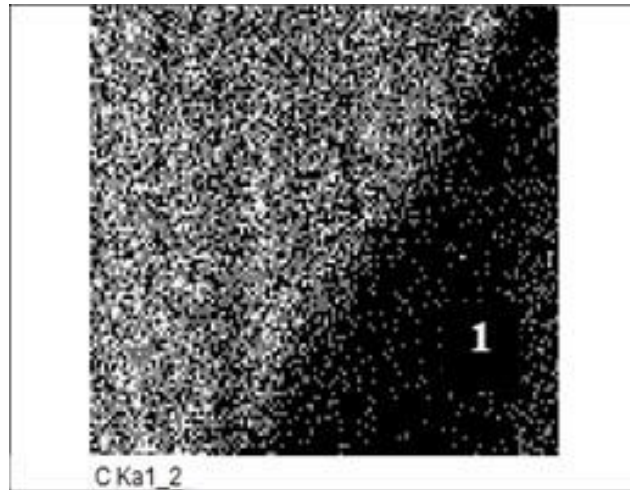


Figure 114 EDS element map for carbon after polishing. Cross-section taken from sample centre. Illustration showing shadowing effect caused by the wall of the milled area.

Due to the poor detection of X-rays from the centre of the sample, the FIB milled cross-section was moved to the edge of the sample.

4.5.1.2. Milling at edge of sample without sample preparation

Figure 115a shows a secondary electron SEM image of milled area (1) at edge of the sample without preparation. It clearly shows that the coating has been damaged through the use of a guillotine. Even after milling back from the edge with the FIB, tears in the coating (2) can be observed in the cross-section area. Also apparent was a charge build-up in the coating (5).

Figure 115b shows the backscattered electron SEM image of the milled area (1). The dark area represents low atomic number element (organic coating) and the lighter area represents the high atomic element (HDG steel). The contrast in the HDG steel revealing the steel (4) and zinc layer (3) is more apparent in the backscatter electron image.

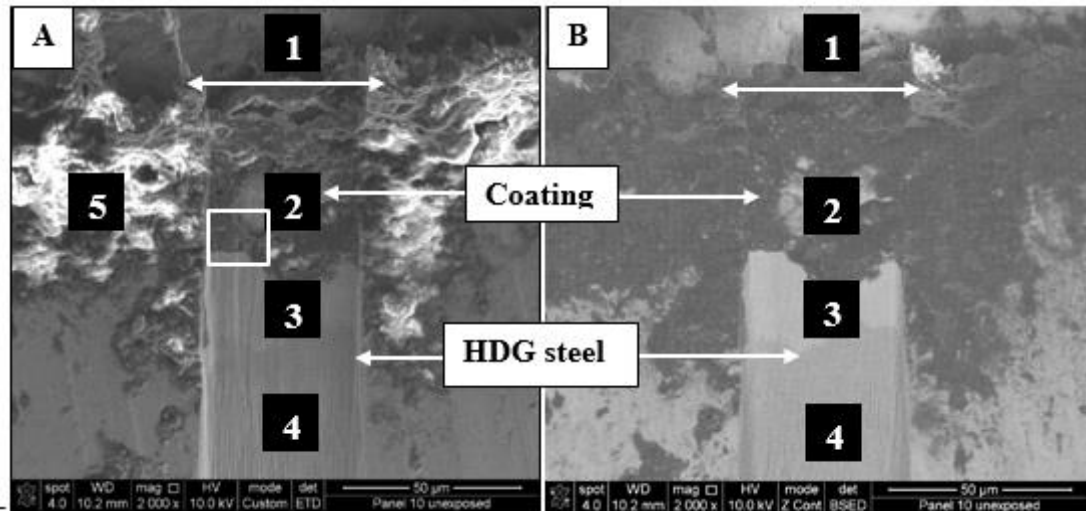


Figure 115. Secondary electron SEM image of milled area (a). Backscattered electron (BSED) SEM image of milled area (b). Number annotations are described in the text. The white box indicates the area where EDS elemental mapping was performed. (See Fig. 119 for results)

Although the location of the cross-section was moved to the edge of the sample, poor elemental composition data was once again obtained from EDS analysis. Figure 116 shows only half the map area for carbon which represents the organic part of the coating was detected (1). Same effect that was seen previously in Fig. 114.

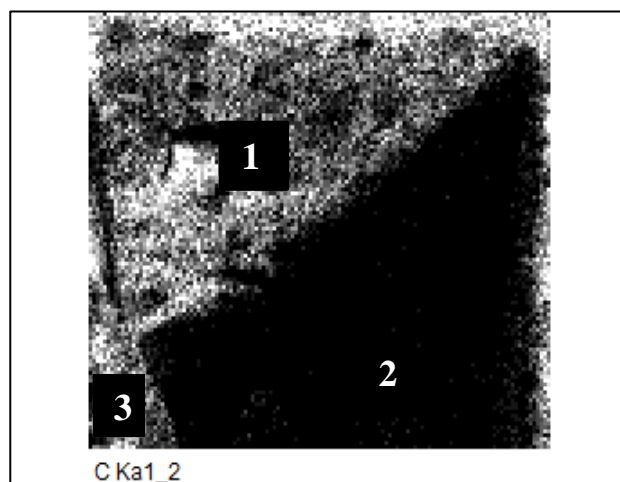


Figure 116. EDS element map for carbon. Cross-section taken at sample edge. Illustration highlights the shadowing effect caused by the wall of the milled area (annotation 2).

As the micrographs in Fig. 116 show, further refinement of the technique was needed due to the damage caused to the coating when the panel was guillotined. The method adopted was to hand polish the same edge with coarse and fine grit papers to remove the damaged area. The other option would have been to mill deeper into the sample until no damage to the coating can be seen but this would take longer using FIB than hand polishing.

An additional improvement was to change the mill shape from a rectangle to an isosceles trapezoid to improve the X-ray detection by removing material blocking X-rays from the detector path, which reduces the shadowing effect shown in Figs. 114 and 116.

4.5.1.3. Milling performed at the polished sample edge with modified milling shape

Figure 117 images show the top down view of ion beam (a) and electron beam (b) is interacting at a different angle as well as detector angle. Figure 117a shows a Ga^+ ion FIB image taken from the edge of the sample which was going to be milled using an isosceles trapezoid shape shown in white (1). Also visible in the FIB image is a strip of deposited Pt (2), which was used to protect the surface from stray, out of focus ions and give a smoother surface after milling [121].

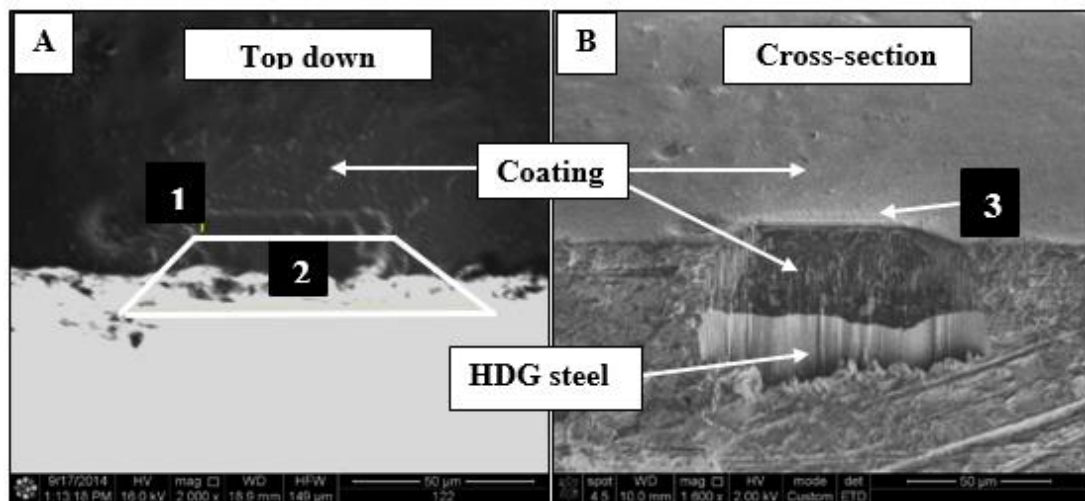


Figure 117. Ga^+ ion FIB image of edge of sample before milling (a). White annotation indicates milling location. Secondary electron SEM image of first milled area without polishing (b).

Figure 117b shows a secondary electron SEM image of the first milled area and it can be seen that there is no apparent damage to the surface of the coating. The Pt layer had protected the coating and all that remained of the Pt was a thin strip on the surface of the coating (3). The image also shows that at the edge of the sample, there was no damage to the coating itself. This demonstrates the benefit of hand polishing the edge of the sample with abrasive paper before milling.

Figure 118a shows the Ga⁺ ion FIB image of edge of the sample after the first mill (1), also visible in the image is a deposited layer of Pt (2). It clearly shows that further material removal was required in front of the milled area (3). An isosceles trapezoid milling area shown in white (4) was used to remove this unnecessary material.

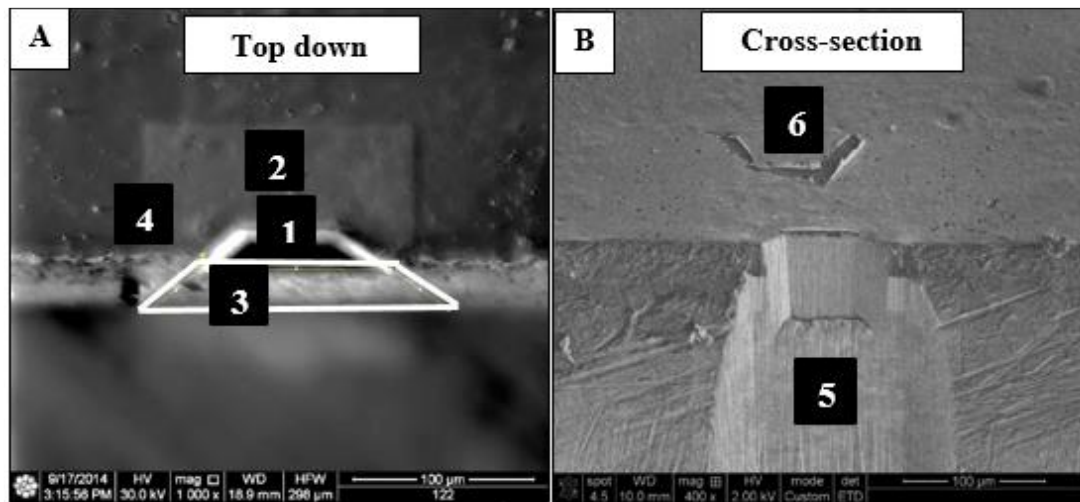


Figure 118. Ga⁺ ion FIB image of edge of sample after first mill (a). White annotation indicates milling location. Secondary electron SEM image of cross-sectioned area after second mill (b).

Figure 118b shows a secondary electron image of cross-section area after second mill with no material in front of the cross-section (5) but with some damage (6) on the surface of the coating. This was the result of milling at a high accelerating voltage to remove the edge material quickly.

Figure 119a shows a secondary electron SEM image of second milled area after polishing. The topcoat, primer and HDG steel can be observed together with a thin line of Pt deposited on top of the coating. In the topcoat and primer, pigments and inorganic materials can be observed.

Figure 119b shows a backscattered SEM image of the second milled area after polishing. The contrast in the image clearly shows the different materials in the pre-painted metal product. Lighter shades represent materials with higher atomic mass. The organic materials, associated with elements having lower atomic mass, are represented by darker areas. The thin, bright line on top of the coating is the protective Pt strip. The HDG steel again shows two distinct layers, which represent zinc and steel. It is also possible in these micrographs to distinguish the primer and topcoat layers, as indicated by the annotations in Fig. 119.

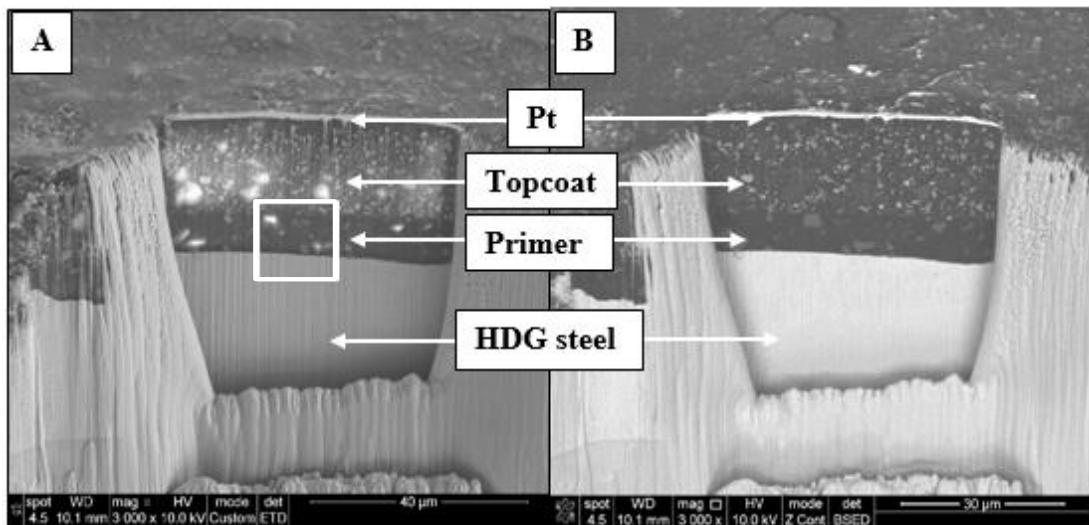


Figure 119. Secondary electron (a) and backscattered SEM (b) images of cross-sectioned area after polishing. The red box indicates the area where EDS elemental mapping was performed (See Fig. 120-124 for results)

Figure 120 shows the topcoat, primer and the zinc layer of the HDG steel. Again, it is possible to differentiate visually between the primer and topcoat. A charge build (1) up was also evident in the primer area due to the nature of the pigment used. The main focus was to analyse the primer and its surroundings, including the zinc and topcoat.

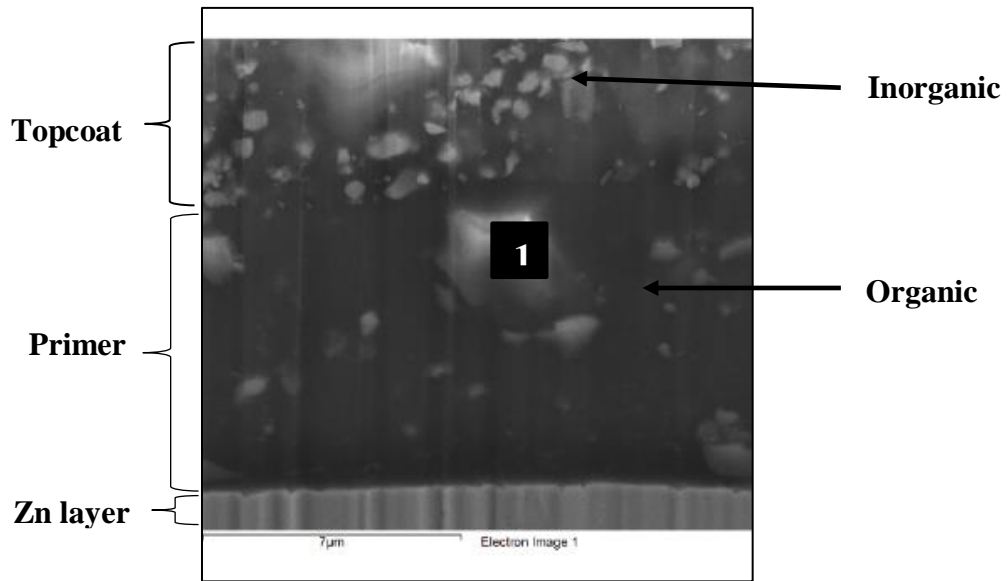


Figure 120. Secondary electron SEM image of polished area that was mapped using EDS analysis (See Fig. 124 for EDS analysis method development and Fig. 125 for all elements identified in this cross-section).

Figure 120 shows the improvement in mapping quality of cross section area of sample by changing the stage tilt and rotation angle. This improves the detection of X-rays from the substance and reduces the shadow effect apparent in Fig.114 and Fig. 116.

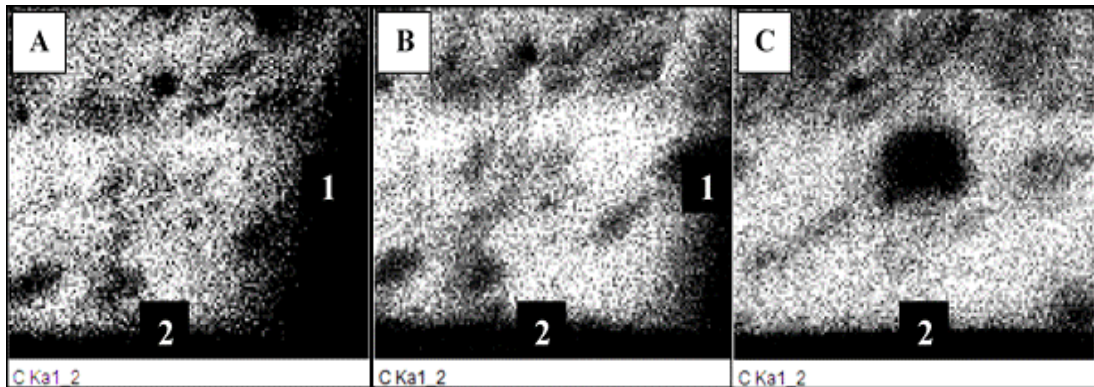


Figure 121. EDS carbon element maps acquired from area shown in Fig. 120 at 53.5° tilt (A), 60° tilt (B) and 60° tilt and -9° rotation (C). Illustrations show how the shadowing effect (marked 1 on map) was eliminated by changing the tilt and rotation.

The light areas represent areas where carbon was detected. The dark areas in the carbon map represent no detection of carbon and are associated with other inorganic elements. The shadowing apparent in Fig. 114 and 116 is still visible in Fig. 121a (marked 1 on map), though it can be seen that changing, the shape of the milled area to a trapezoid has reduced the effect. Increasing the tilt angle to 60° further improved the ability to obtain elemental data from the bottom right hand corner of the cross-section (See Fig. 121b). However, detection of X-rays from all areas of the cross-section, shown in Fig. 115c, achieved by additionally rotating the stage to -9°. The dark area at the bottom of the images represents zinc (2) and can be supported from Fig. 122.

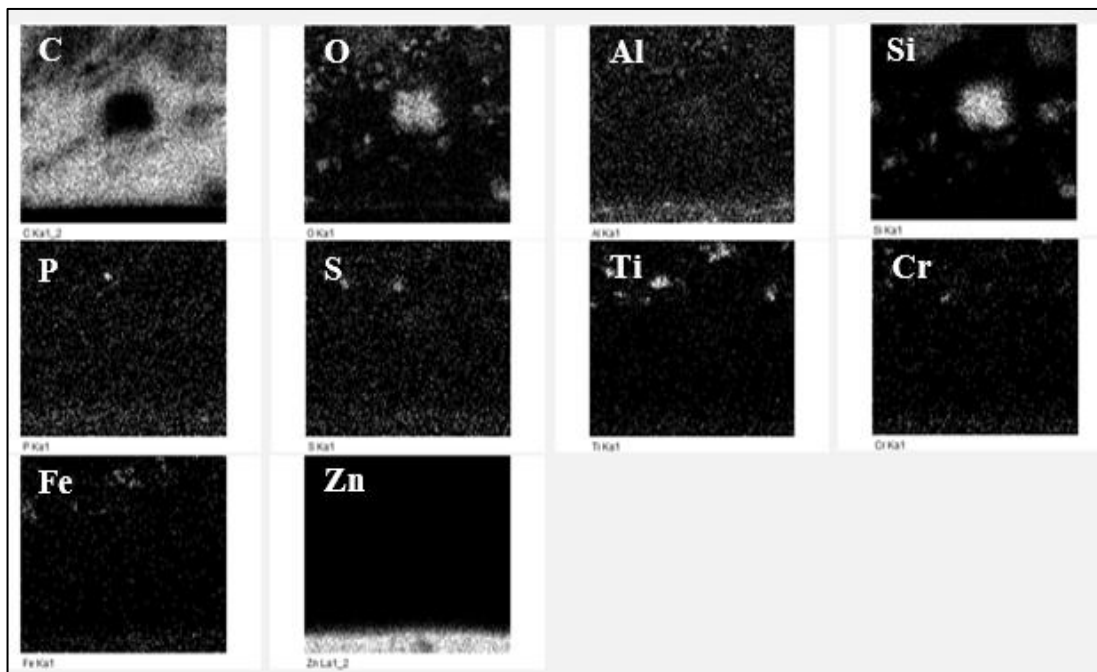


Figure 122. EDS maps for elements identified in the cross-section shown in Fig. 121c. Differences between topcoat, primer and substrate can be observed.

Figure 122 shows all the elemental maps of the area seen in figure 124c using 60° tilt and -9° rotation to analyse that section. Each map represents an individual element. Light areas represent the presence element in the element map. The elemental maps correspond to the cross-section image in Fig. 120 (See next page showing explanation of the analysis).

Figure 123 shows the spectrum of the area seen in figure 121c. The total number of counts obtained for this spectrum was 550,000 and when zoom in at 10,146 counts full scale, elements of different atomic weight can be identified from their photon energy (keV) values.

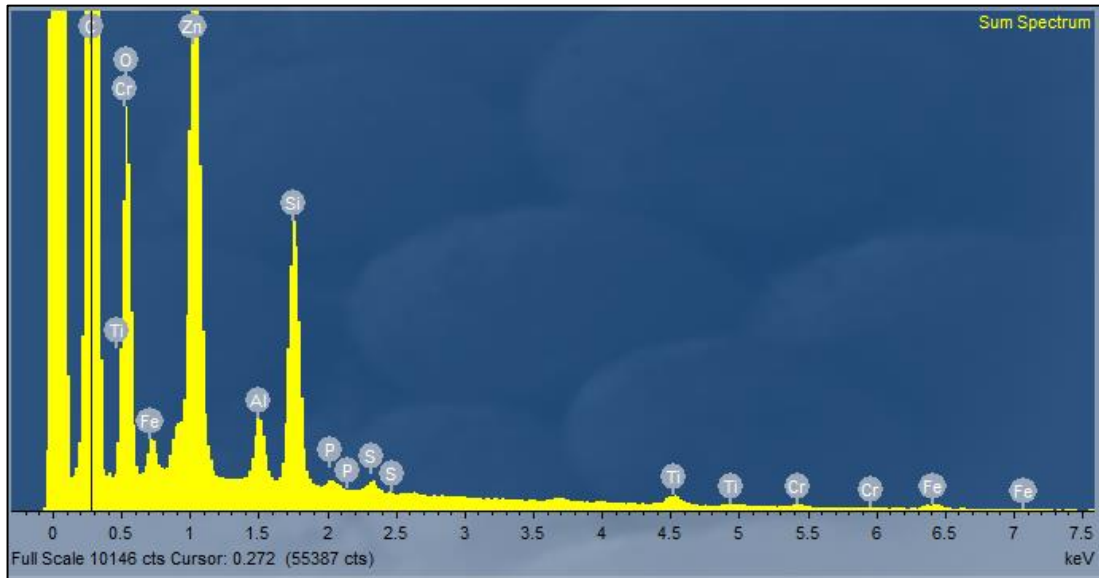


Figure 123. EDS spectrum of a sample in Fig. 121c.

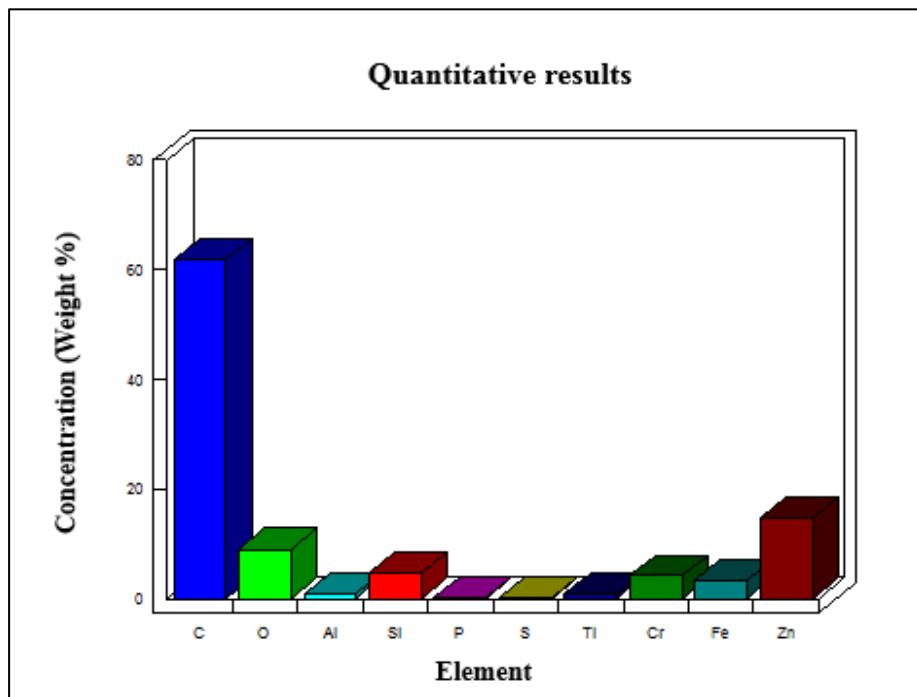


Figure 124. Semi-quantitative elemental results of sample in Fig. 121c. The statistical error, sigma quoted is less than 0.5 for all elements.

Figure 124 shows the quantitative results obtained from the cross-section in Fig. 121c, which includes the topcoat, primer and substrate. The elements in the coating are Al, O, Si, S, Ti, Cr and Fe. These are derived from the inorganic pigments and the matting agent (additive used to control the gloss of coatings) that were used. The HDG steel is represented by element Zn, Fe, Al and O. Mapping of these elements, also supports this. Although the topcoat, primer and substrate can be identified using EDS mapping, no conclusive results were obtained indicating the presence of the pretreatment layer. Although Ti and P should be found in chromate-free pretreatments [93] [132] [133], the maps were not able to show a concentration of these elements between the zinc layer and the primer (See Fig. 124).

4.5.5. Summary

FIB/SEM is an effective technique to study organic coating applied to metal substrates. In-situ cross-sectioning can provide secondary and backscatter electron images revealing the pigment dispersion within a coating, the interfacial properties, changes occurring after exposure, the thickness of the coating and presence of defects.

The technique has the ability to reveal small voids or other fragile features without causing damage to samples compared to conventional mechanical polishing methods, providing an optimum set of process parameters are determined [114]. But it has its drawbacks: The technique can only cut or mill small areas and the process is very time consuming [114]. Other problems associated with the technique are related to charge damage and artefacts which, can be generated due to striations and redeposition [114].

However via careful development and optimisation of the technique it is possible to obtain representative elemental data. It was found that optimal results were obtained by milling an isosceles at the edge of the sample. Hand polishing before milling was also found to be necessary when samples were prepared by guillotining. Finally the tilt and rotation of the stage were changed for further improvement in X-ray detection using a tilt angle of 60° and rotation angle of -9° .

EDS analysis allows mapping of the elements distributed in the coating and also the quantification of those elements in the coating. The results obtained in this study corresponded to the formulation of the pre-painted metal product.

4.6. Panels investigated by FIB/SEM analysis

4.6.1. Unexposed panels

This section will concentrate on unexposed panels of the 4 systems. Each unexposed system was cross-sectioned in two locations. They were milled and then polished to allow imaging and analysis of cross-sectioned area. Mapping and line scans were used to analyse the majority of the cross-sectioned areas.

4.6.1.1. Unexposed panel of system 1 (Solventborne primer with anti-corrosive pigment)

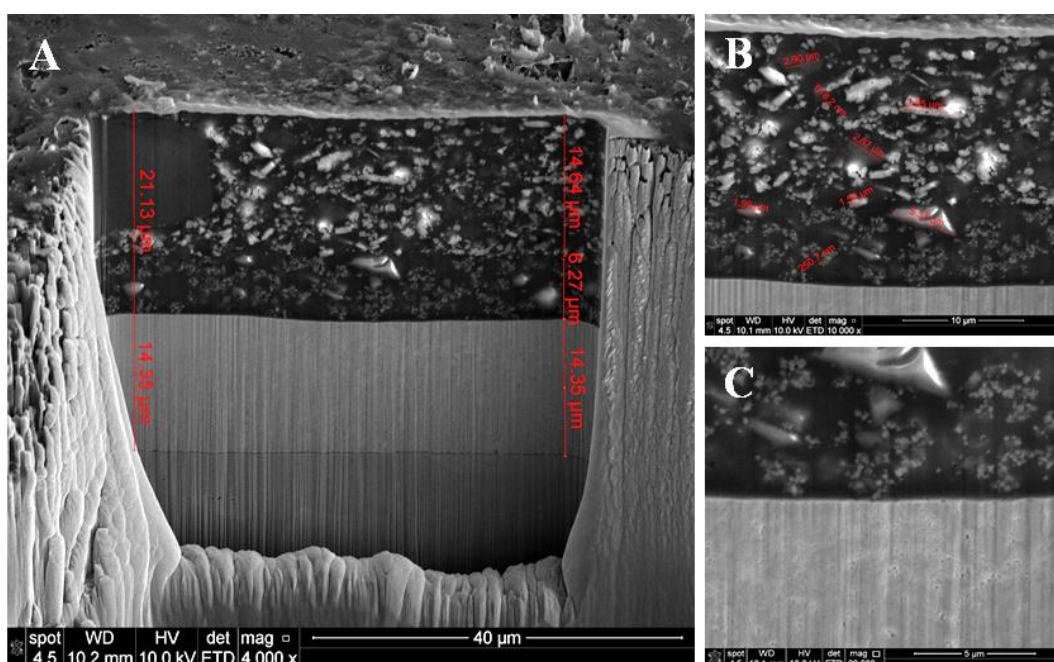


Figure 125. Secondary electron SEM images of an unexposed panel of system 1, area 1. Cross-sectioned area (A), topcoat/ primer/ zinc interface (B) and primer/ zinc interface (C).

The results of milling and polishing of system 1, a benchmark solvent-borne product are shown in Fig. 125. It shows the cross-sectioned area of system 1 (Fig. 125a) containing the topcoat, primer, zinc and steel. On top of the cross-sectioned area is Pt, which is used to protect the surface of the sample from stray and out of focus Ga^+ ions. The film thickness of the topcoat is 14.6 μm , the primer is 6.3 μm thick and the zinc layer is 14.4 μm thick. The film thickness of the topcoat is quite low. It should have been between 18 and 22 micrometres, which is normally used for precoated steel

so that optimum corrosion and durability performances are achieved. Fig. 125b shows the topcoat, primer and the zinc layer of the HDG steel. It shows the different pigments that were used in the coatings, together with the measurements of the particles shown in red. Fig. 125c shows the primer and zinc cross-sectioned area. It also revealed that pigment particles are not touching the zinc layer and zinc has different phases. Another example of a cross-sectioned area of an unexposed system 1 can be seen in appendix IV (See Fig. 181).

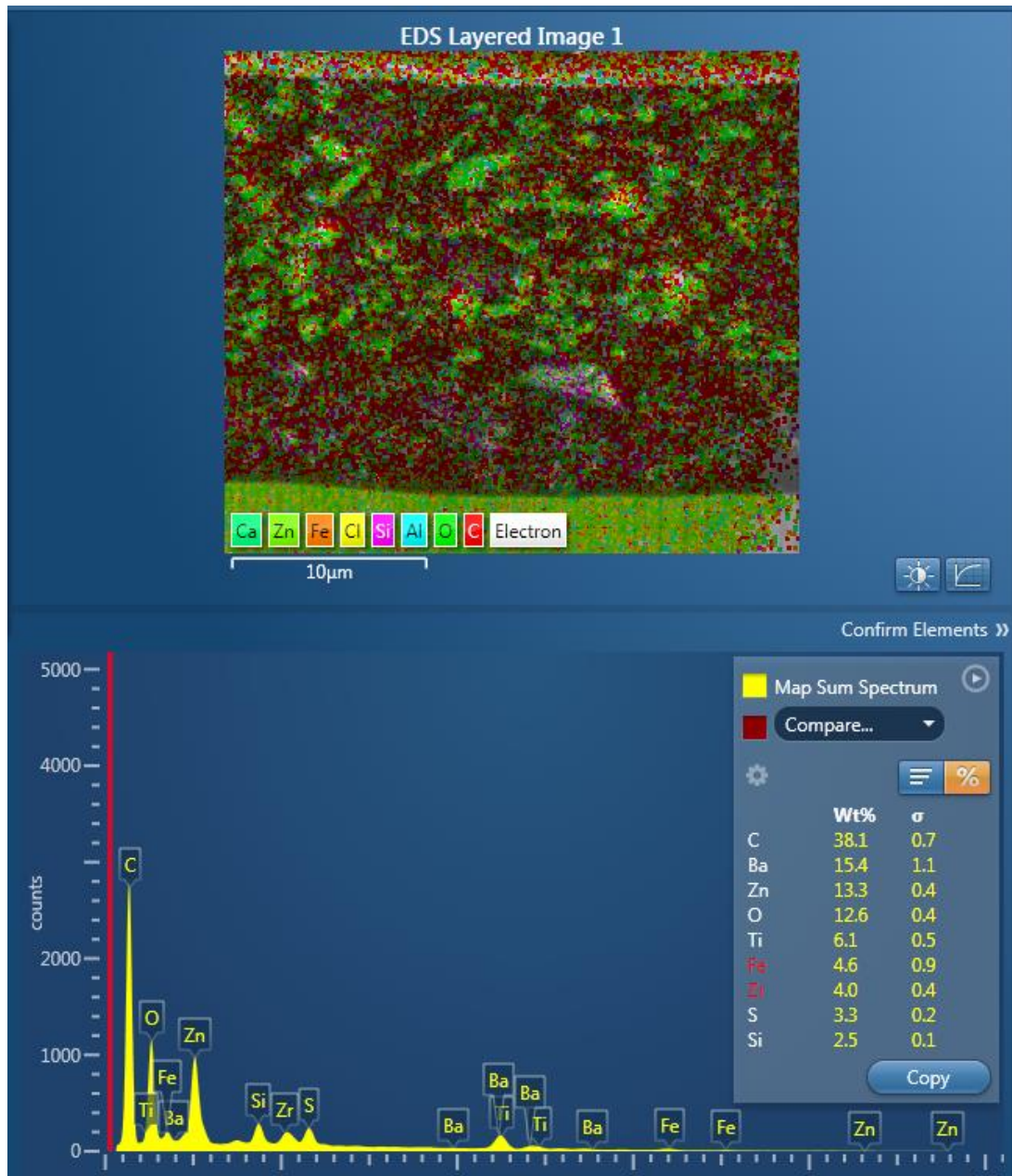


Figure 126. EDS spectra and mapping results of an unexposed panel of system 1 analysed from Fig. 125b.

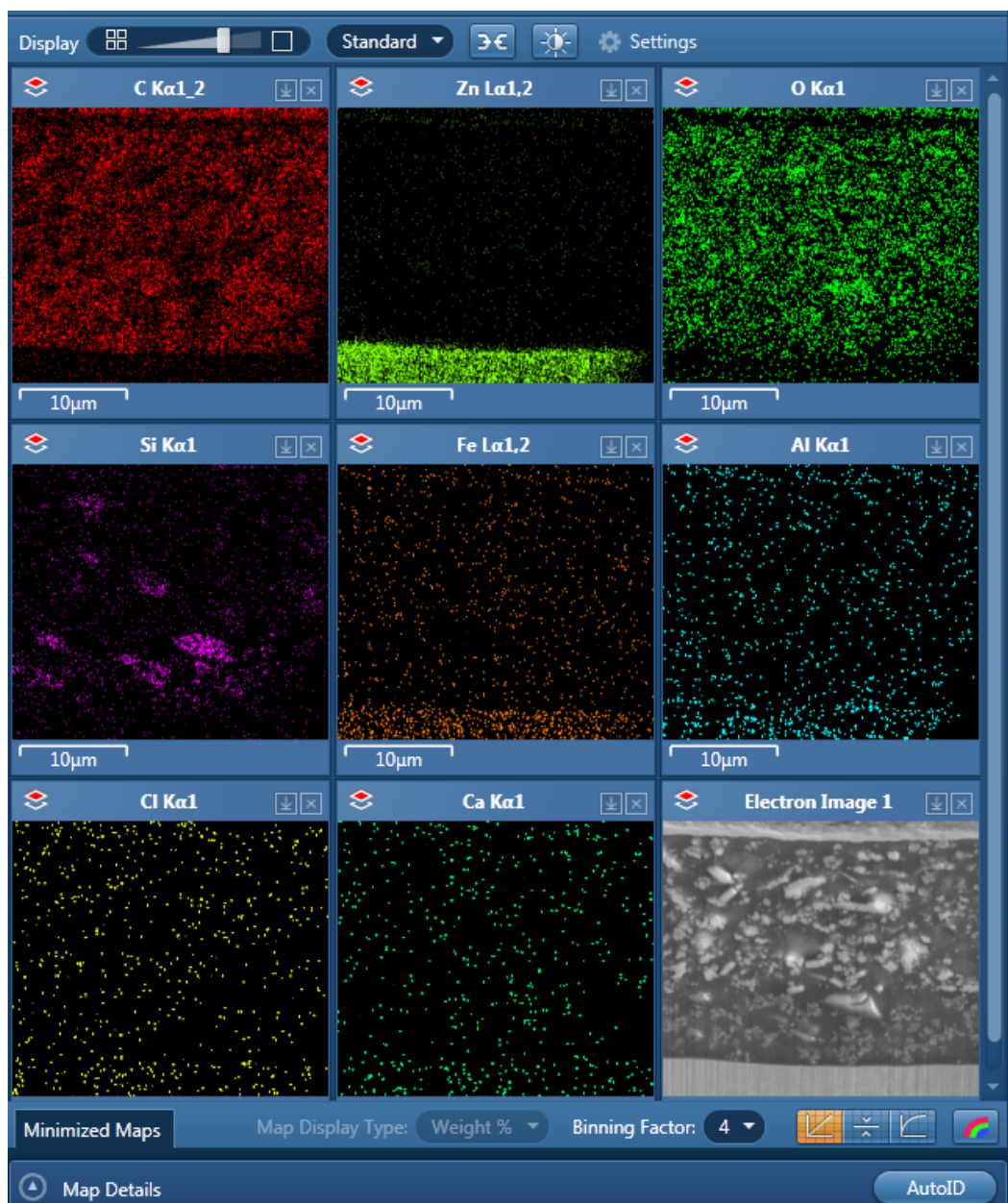


Figure 127. EDS mapping results of individual elements of an unexposed panel of system 1 analysed from Fig. 125b.

The results of elemental mapping of area of Fig.125b are shown in Figs. 126 & 127. Each map represents an individual element (See Fig. 127). Colour areas represent the element in the map. Also included is the spectrum of the area that was mapped (See Fig. 126). The total number of counts obtained for this spectrum was at least 250,000 and the elements of different atomic number were identified from their photon energy (keV) values.

The quantitative results obtained from the cross-sectioned of unexposed system 1 in Fig. 135b, which includes the topcoat, primer and zinc layer. The elements in the coating were C, Ba, O, Si, Zr, S and Ti. These were derived from the inorganic pigments and the matting agent (additive used to control the gloss of the coating) that were used. The HDG steel is represented by elements Zn, Fe and O. Although the topcoat, primer and substrate can be identified using EDS, no conclusive results were obtained indicating the presence of the pretreatment layer. The maps were not able to show a concentration of these elements (F, Ti and Zr) between the zinc layer and the primer.

4.6.1.2. Unexposed panel of system 2 (Waterborne pretreatment primer with no anti-corrosive pigment)

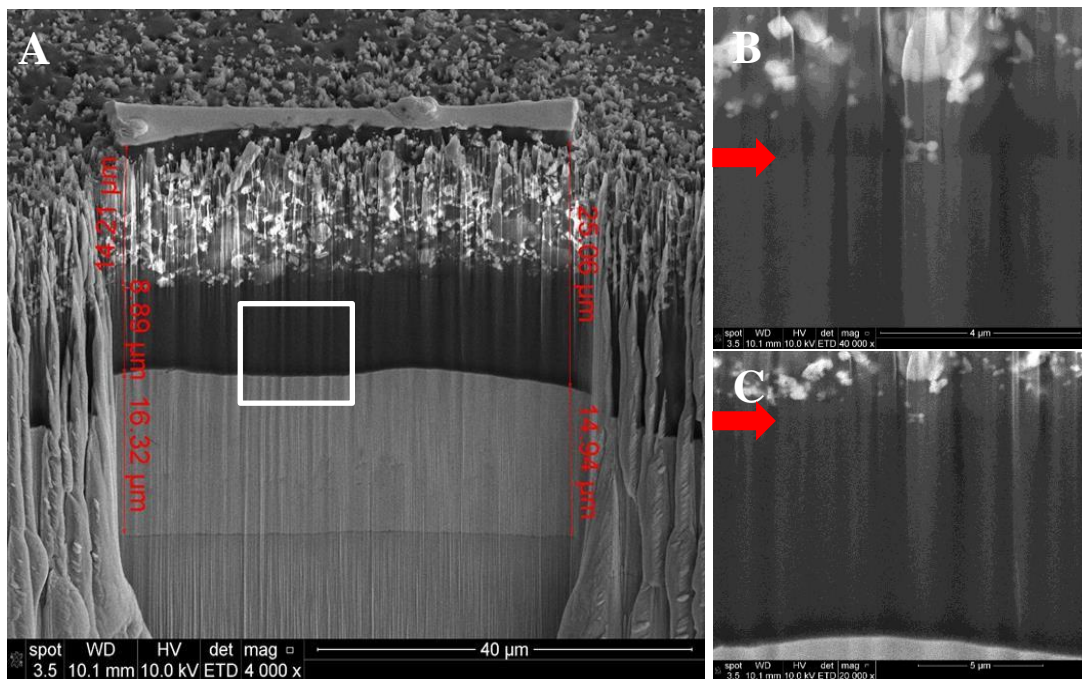


Figure 128. Secondary electron SEM images of an unexposed panel of system 2.

Cross-sectioned area (A), topcoat/ primer/ zinc interface (B) and primer/ zinc interface (C). Red arrows represent the phase difference between topcoat and primer.

A white square shows area of EDS analysis.

The results of milling and polishing of system 2, an experimental water-borne pretreatment primer containing no anti-corrosive pigment, are shown in Fig. 128. It shows the cross-sectioned area of system 2 (See Fig. 128a) containing the topcoat,

primer, zinc layer and steel. The film thickness of the topcoat is 14.2 μm , the primer thickness is 8.8 μm and the zinc layer is 16.3 μm thickness. Again the topcoat is lower than what is normally required. Fig. 128b show topcoat, primer and a red arrow, which indicates the phase difference separation between the topcoat and primer. This may be caused by the topcoat being solventborne and pretreatment primer being waterborne. It shows there is no pigment in the pretreatment primer layer. Fig. 128c shows the topcoat, primer and zinc. It also revealed that there is a phase difference between the topcoat and pretreatment primer. The white square was area analysed by EDS analysis (See Figs. 129 and 130). Another example of a cross-sectioned area of an unexposed system 2 can be seen in appendix IV (See Fig. 182).

Fig. 129 shows the pretreatment primer and zinc area, which is mapped, and the results are shown in Fig. 130. Figure 130 shows the quantitative results obtained from the cross-sectioned in Fig. 129, which includes the pretreatment primer and zinc interface.

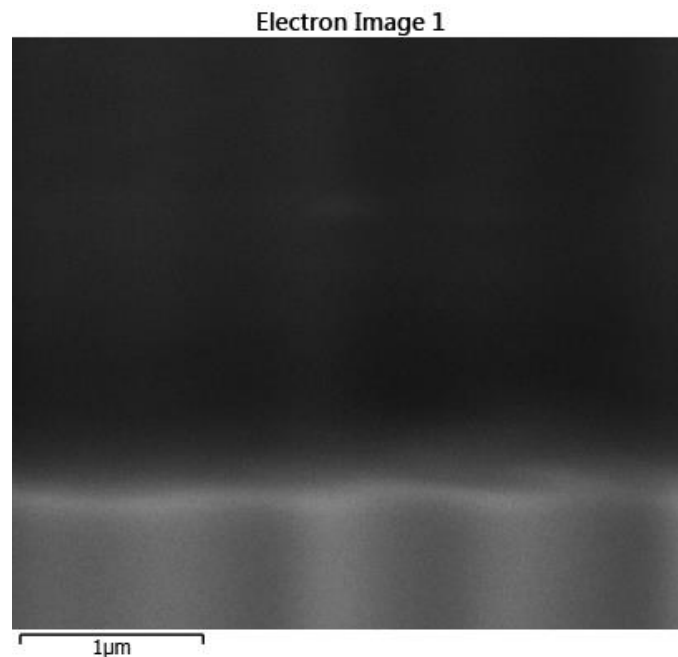


Figure 129. Secondary electron SEM image of an unexposed panel of system 2 that was mapped.

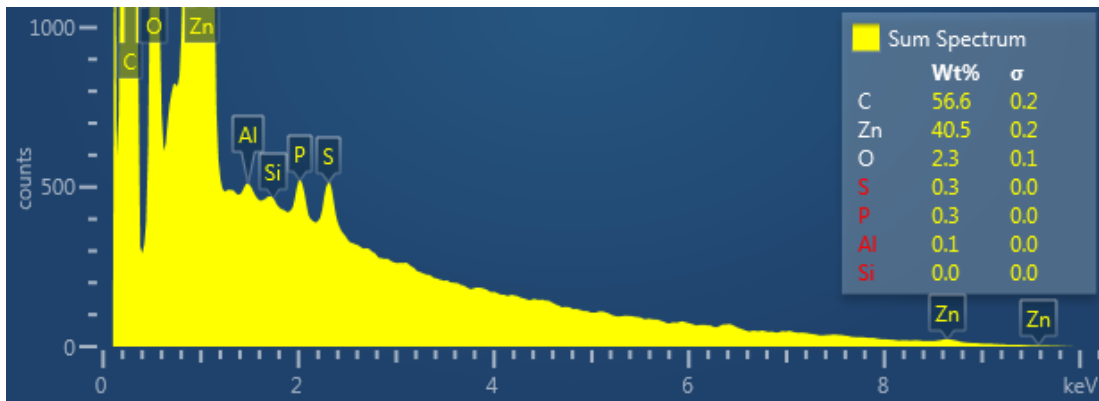


Figure 130. EDS spectrum of an unexposed panel of system 2 in Fig. 128.

The elements in the coating are C, O, S and P. These are derived from the adhesion promoter and surfactants that are used. The zinc layer is represented by element Zn and Al which is added to the zinc to improve the adhesion of the zinc to the steel hence aiding flexibility.

4.6.1.3. Unexposed panel of system 3 (Waterborne pretreatment primer with anti-corrosive pigment)

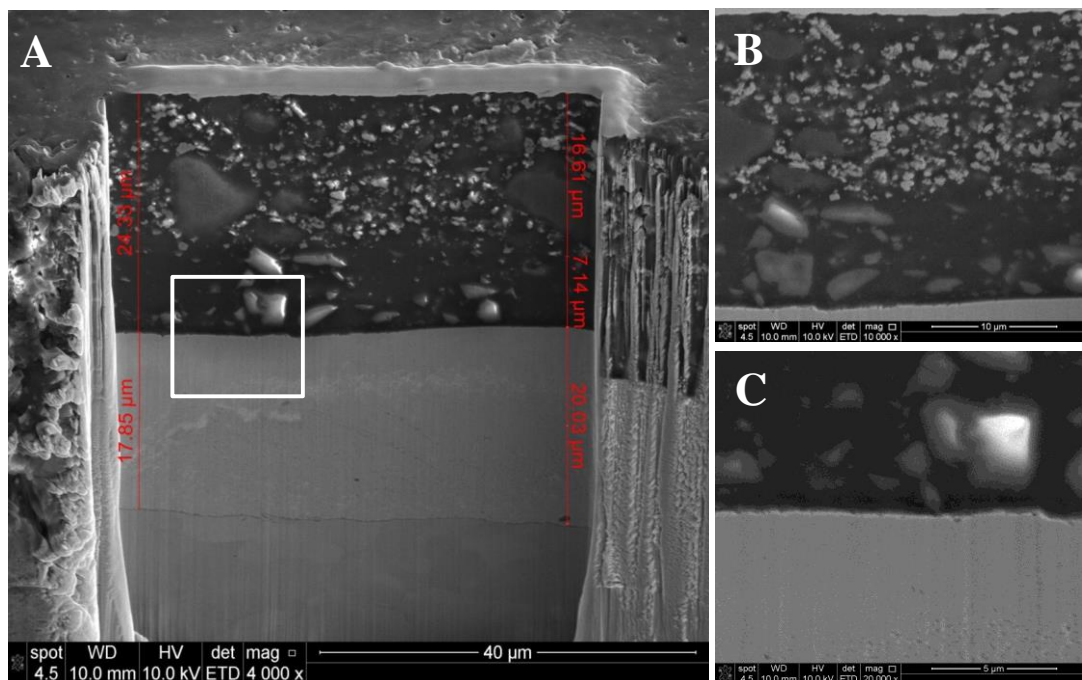


Figure 131. Secondary electron SEM images of an unexposed panel of system 3, area 2. Cross-sectioned area (a), topcoat/ primer/ zinc area (b) and primer/ zinc area (c). A white square shows area of EDS analysis.

The results of milling and polishing of system 3, an experimental water-borne pretreatment primer containing anti-corrosive pigment are shown in Fig. 131. It shows the cross-sectioned area of system 3 (See Fig. 131a) containing the topcoat, pretreatment primer, zinc layer and steel. The film thickness of the topcoat is 16.6 μm , the primer is 7.1 μm and the zinc layer is between 17.9 and 20 μm . This time the topcoat thickness was slightly lower than what is required. The white box represents an area that was mapped. Fig. 131b shows the topcoat, primer and zinc layer. It is difficult to see if there is a phase difference between the two coatings.

Fig. 131c shows the pretreatment primer and zinc interface. It also revealed that there were anti-corrosive pigments present in the coating as was expected. The white squares are areas that were analysed by EDS analysis (See Figs. 132 and 133). Another example of a cross-sectioned area of an unexposed system 3 can be seen in the appendix IV (See Fig. 182), which shows a phase difference between the solvent-borne topcoat and water-borne pretreatment primer.

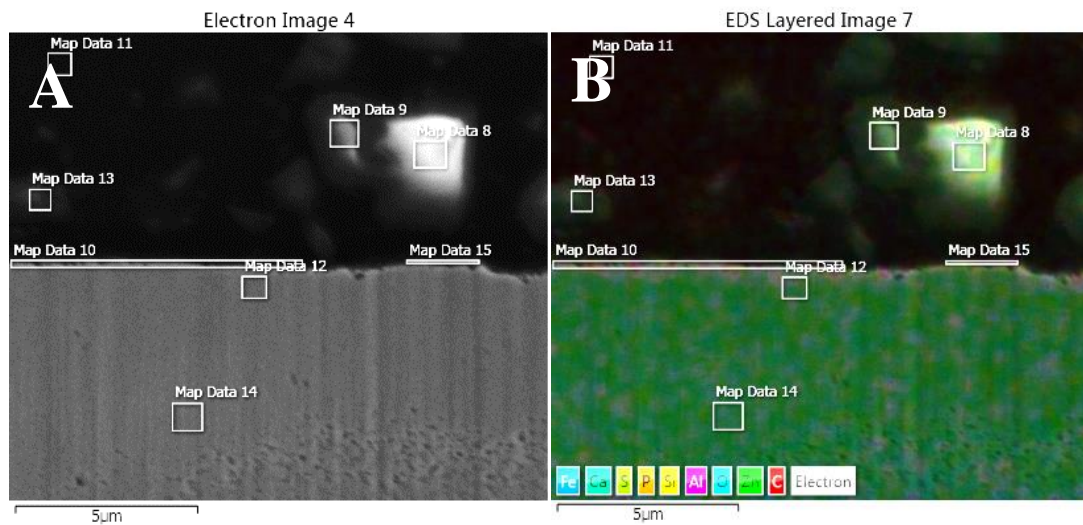


Figure 132. Secondary electron SEM image (a) and the results of EDS mapping (b) of an unexposed panel of system 3 from Fig. 131A.

Fig. 132 shows the secondary electron SEM image of a pretreatment primer and zinc cross-sectioned area (a) and the mapping results of that area (b). Also included are the elements detected in the map and areas that were mapped. The results of the mapping are shown in Fig. 133 as spectra.

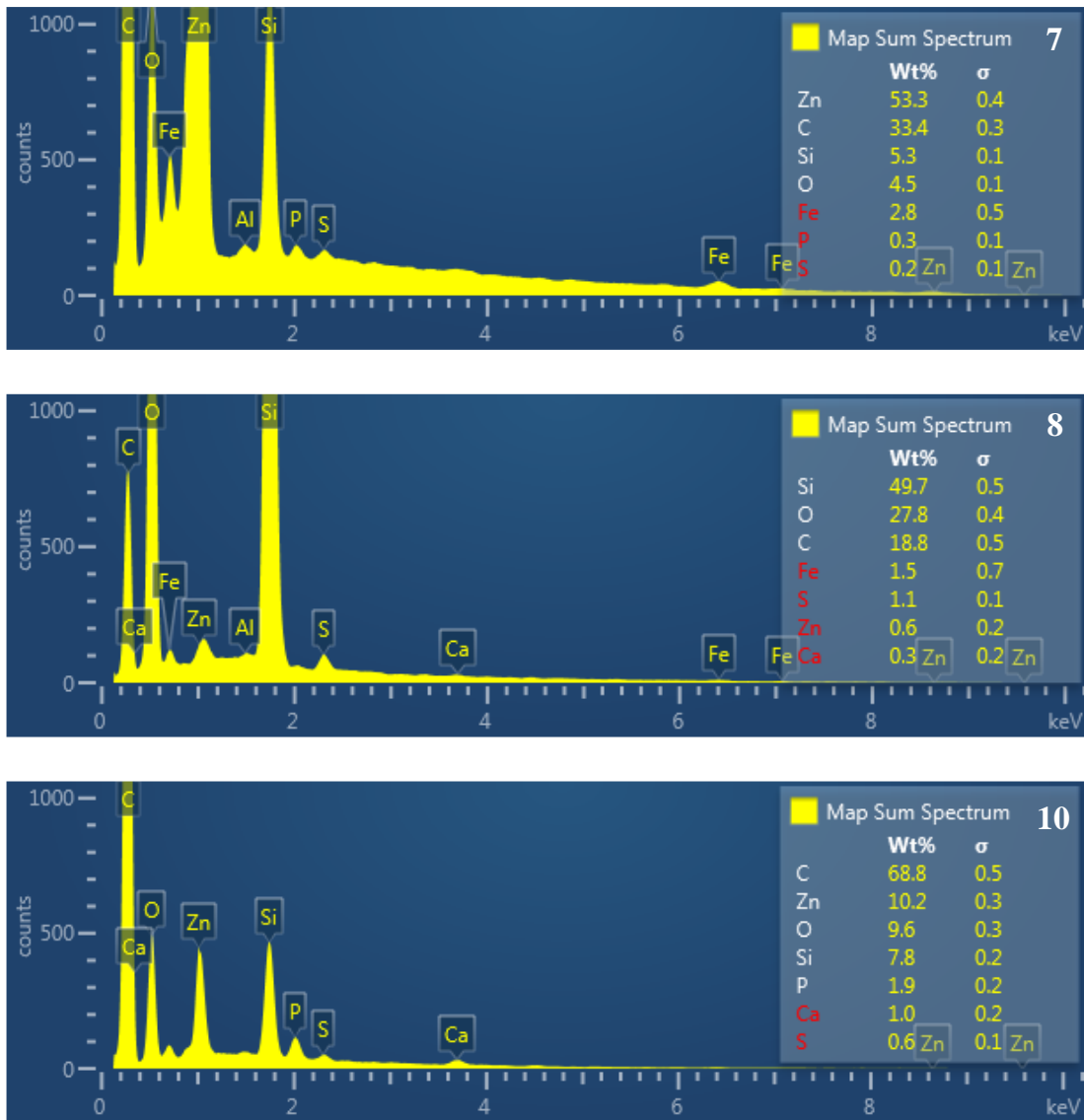


Figure 133. EDS spectra of an unexposed panel of system 3 from Fig. 132 with 3 areas of analysis.

Map 7 shows the quantitative results obtained from Fig. 132, which includes the pretreatment primer and zinc area. The elements in the coating are C, O, Si, P and S. The results were the same as in system 2, except that this time Si was detected, which represented the anti-corrosive pigment (calcium ion exchange silica) used in this formulation. The zinc layer is represented by element Zn and Fe.

Map 8 shows the quantitative results obtained from calcium ion exchange silica pigment in Fig. 132. The elements in the pigment were Si and Ca and this were expected. The other elements are from the pretreatment and substrate.

Map 10 shows the quantitative results obtained from pretreatment primer/zinc interface in Fig. 132. The elements in the interface were Zn, C, O, Si, P, S and Ca and the results were expected. The Ca element may be detected at the interface or from the pigment nearby. It was difficult to confirm whether the detected Ca came from. It may be from the interface of pretreatment primer/ zinc or from surrounding calcium silicate pigments.

4.6.1.4. Unexposed panel of system 4 (Waterborne pretreatment primer with anti-corrosive pigment and pretreatment technology)

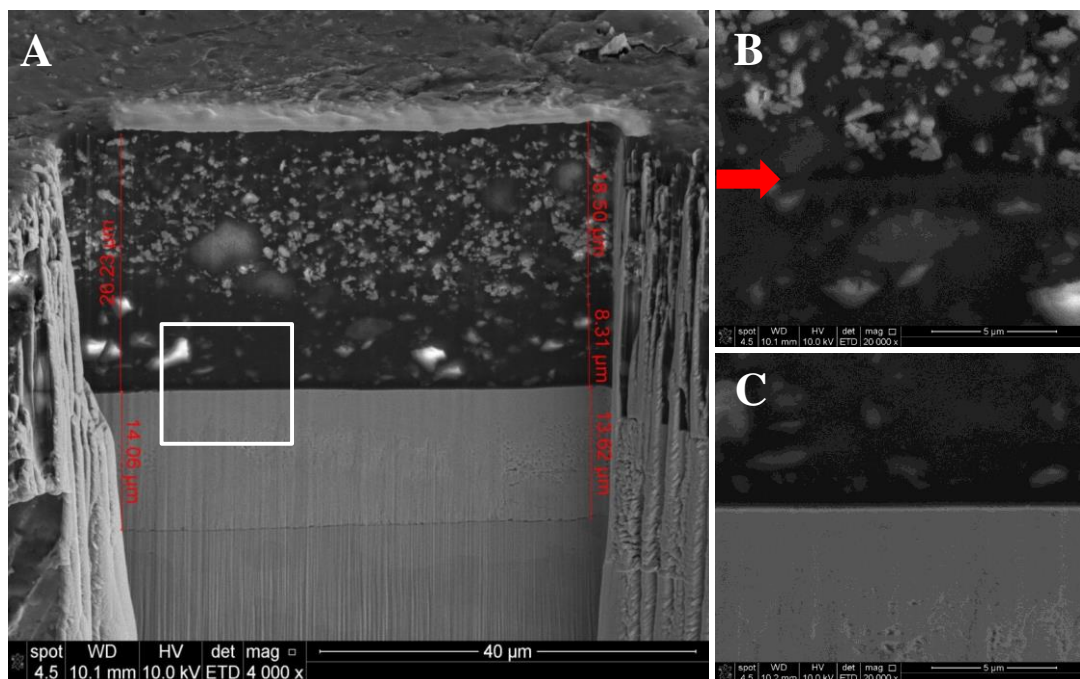


Figure 134. Secondary electron SEM images of an unexposed panel of system 4, area 2. Cross-sectioned area (a), topcoat/ primer/ zinc area (b) and primer/ zinc area (c). A red arrow represents the phase difference between the topcoat and primer. A white square shows area of EDS analysis.

The results of milling and polishing of system 4, an experimental water-borne pretreatment primer containing anti-corrosive pigment and pretreatment technology are shown in Fig. 136. It shows the cross-sectioned area of system 4 (Fig. 134a) containing the topcoat, pretreatment primer, zinc and steel. The film thickness of the topcoat is 18.5 μm , the primer is 8.3 μm and the zinc layer is between 13.6 and 14.1 μm . This time the film thickness of the topcoat was within what is required. Fig. 134b show

the topcoat, primer and a red arrow, indicating the presence of a phase difference between the topcoat and primer. This may be caused by the topcoat being solvent-borne and pretreatment primer being water-borne.

Fig. 134c shows the pretreatment primer and zinc cross-sectioned area. It also revealed that there are calcium silicate pigments present in the coating and the difference phases in the zinc was expected. Another example of a cross-sectioned area of an unexposed system 4 can be seen in the appendix IV (See Fig. 184).

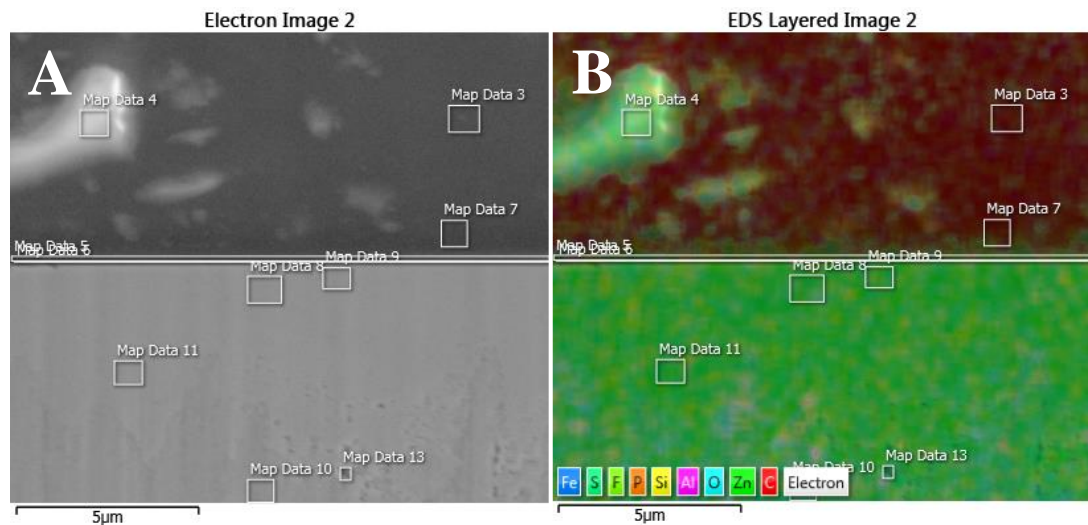
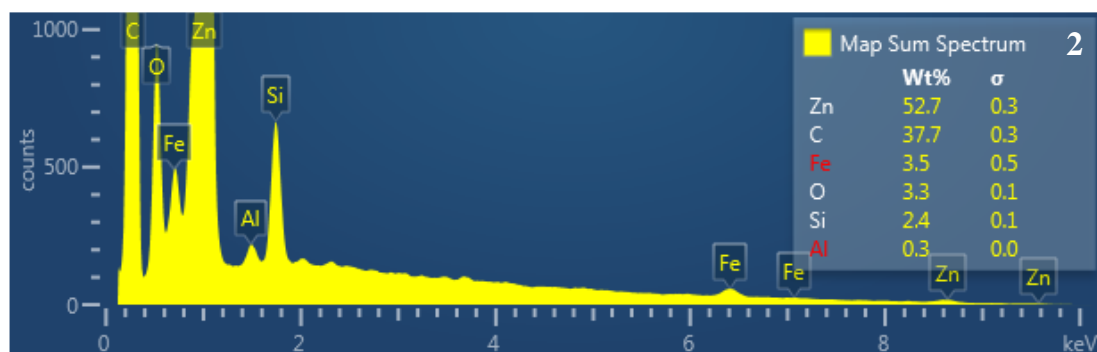


Figure 135. Secondary electron SEM image (a) and the results of EDS mapping (b) of an unexposed panel of system 4 from Fig. 136a.

Fig. 135 shows the secondary electron SEM image of a pretreatment primer and zinc cross-section area (a) and the mapping results of that area (b). Also included are the elements detected in the map and the different areas going to be mapped. The results of the mapping are shown in Fig. 136 as spectra.



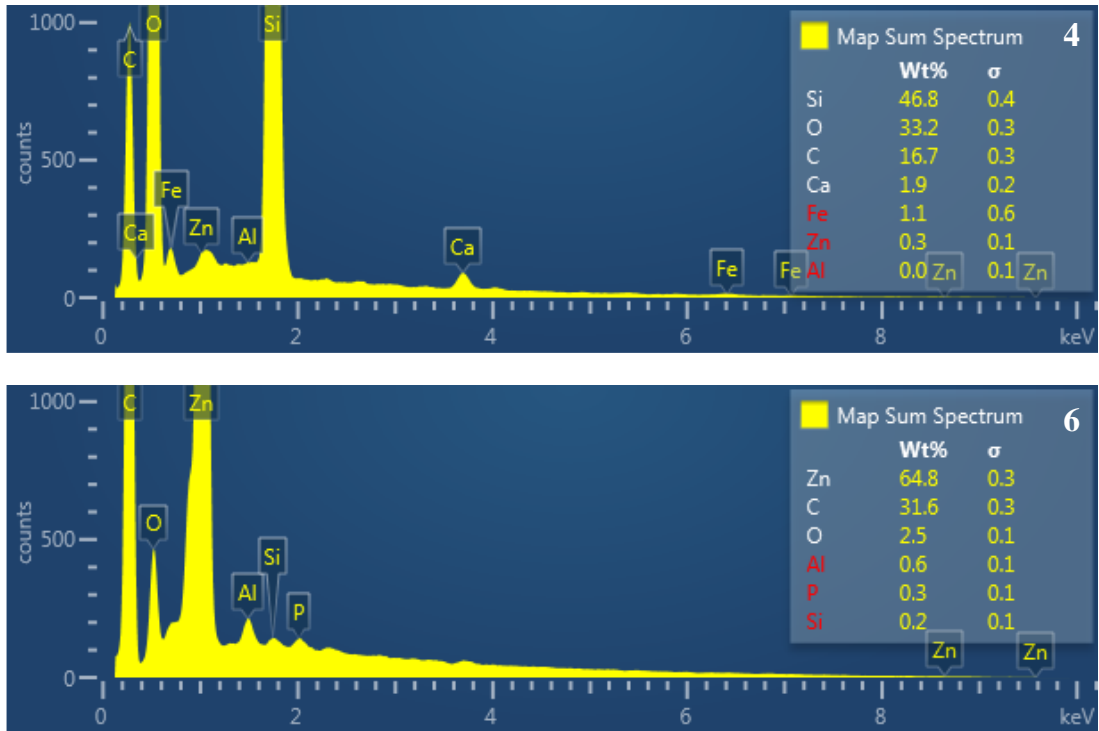


Figure 136. EDS spectra of an unexposed panel of system 4 from Fig. 137 with 3 locations of analysis.

Map 2 shows the quantitative results obtained from Fig. 135, which consisted of a pretreatment primer and zinc. The elements in the coating were C, O and Si. The results were similar to system 3 without the detection of P and S. The zinc layer is represented by element Zn, Fe and Al.

Map 4 shows the quantitative results obtained from calcium silicate pigment in Fig. 135. The elements in the pigment were Si and Ca and this was expected. The other elements were from the surrounding pretreatment primer and substrate.

Map 6 shows the quantitative results obtained from pretreatment primer/ zinc interface in Fig. 135. The elements detected in the interface were Zn, C, O, Al, P and Si. There is no Ca detected.

4.6.2. Exposed panels

This section will concentrate on exposed panels of the 4 systems. Each exposed system at different time intervals (0, 192, 408 and 1000 hours) was cross-section in one or more locations. The time intervals used are based on OCP and impedance results. Only one example will be shown for each time interval for each system. The rest of the images and analysis will be in appendix V (See Fig. 185-96). The exposed panels were milled and then polished to allow imaging and analysis of cross-sectioned area. Mapping and line scans were used to analyse for the majority of the cross-sectioned areas.

4.6.2.1. Exposed panels of system 1 (Solvent-borne primer with anti-corrosive pigment)

4.6.2.1.1. System 1 submerged in a cell from 0 to 1000 hours.

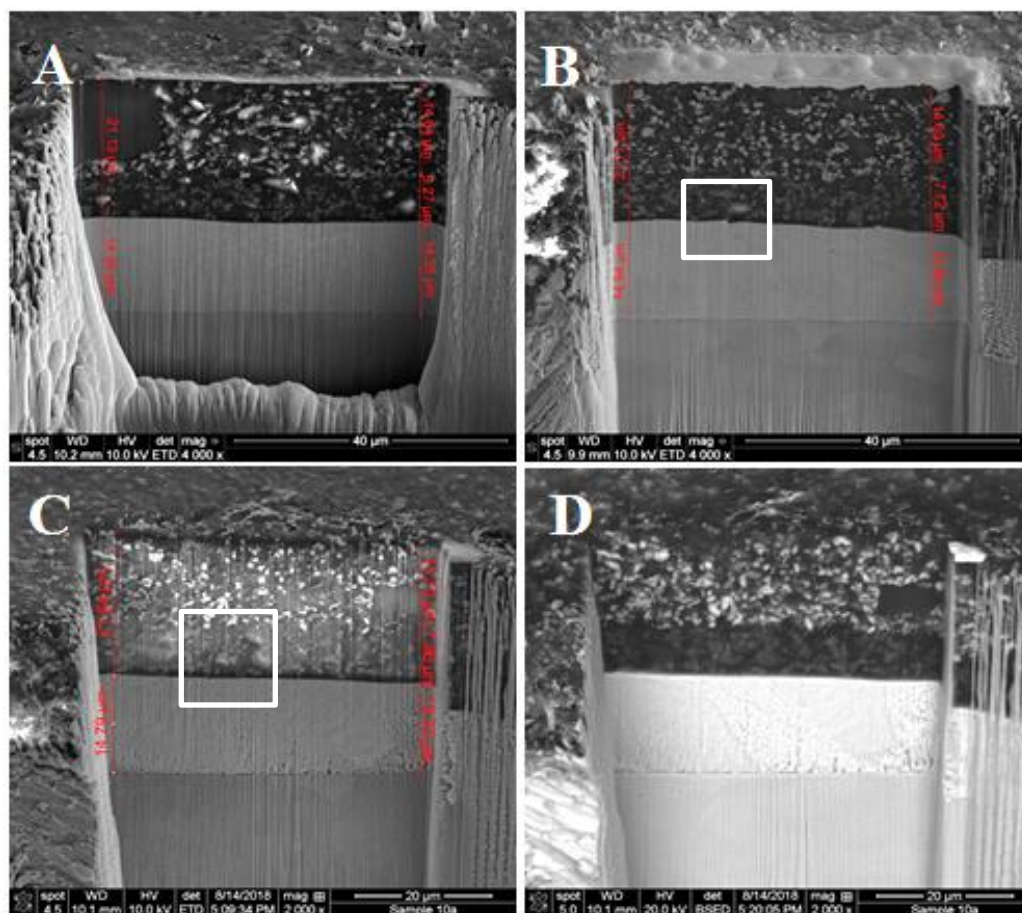


Figure 137. Secondary electron & backscattered electron SEM images of unexposed and exposed panels of system 1 submerged in a cell for 0 hr (A), 408 hrs (B) and 1000 hrs, SE (C) and BSED (D) images. White squares show area of EDS analysis.

The results of milling and polishing of system 1 submerged at 0 (A), 408 (B) and 1000 hours (C & D) are shown in Fig. 137. There is no change, damage or defect in the cross-sectioned area exposed over time when viewed under secondary electron mode. In BSED images, the dark area represents low atomic number element (organic coating) and the lighter and brighter area represents the high atomic element (HDG steel). The contrast in the HDG steel revealing the steel and zinc layer is more apparent in BSED image. It also shows that the surface of the zinc layer was different to Fig. 137d. In the next few sections, the results of system 1 submerged in a cell for 408 and 1000 hours will be revealed and explained.

4.6.2.1.2. System 1 submerged in a cell for 408 hours.

The results of submerging system 1 in a cell for 408 hours are shown in Fig. 137 and 138. Figure 138 shows the secondary electron SEM image of a primer and zinc cross-sectioned area (a) and the mapping results of that area (b). Also included are the elements detected in the map and the areas that were mapped. The results of the mapping are shown in Fig. 139 as spectra.

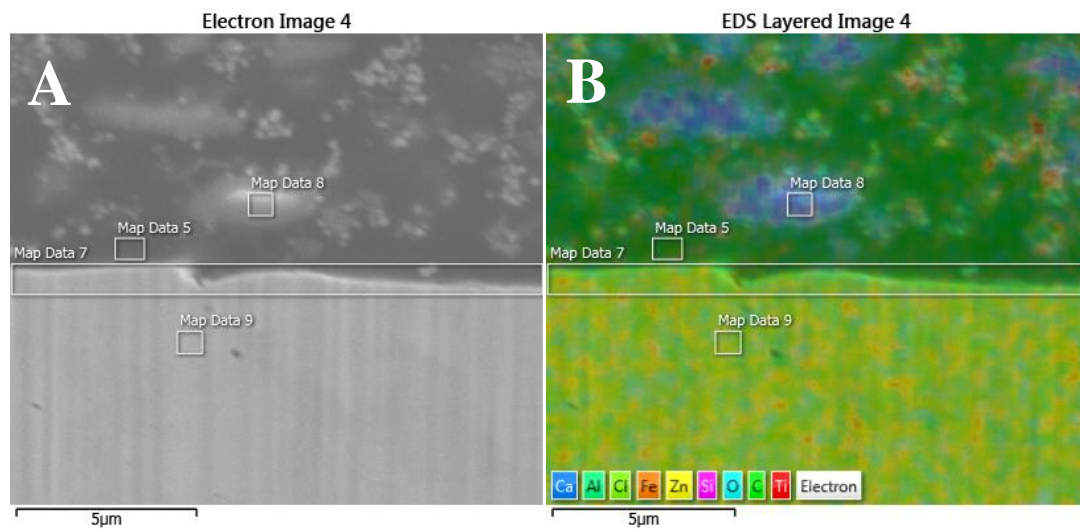


Figure 138. Secondary electron SEM image (a) and the results of EDS mapping (b) of an exposed panel of system 1 submerged in a cell for 408 hours from Fig. 137b.

Map 4 shows the quantitative results obtained from Fig. 138, which consisted of a primer and zinc. The elements in the coating are C, O, Ti and Si. The results are

similar to the unexposed panel. The zinc layer is represented by element Zn, Fe and Al.

Map 7 shows the quantitative results obtained from the primer and zinc interface in Fig. 138. The elements in the primer were C, O, Ti, Si and P. The other elements were from the substrate. There was no sign of any NaCl electrolyte present in the coating.

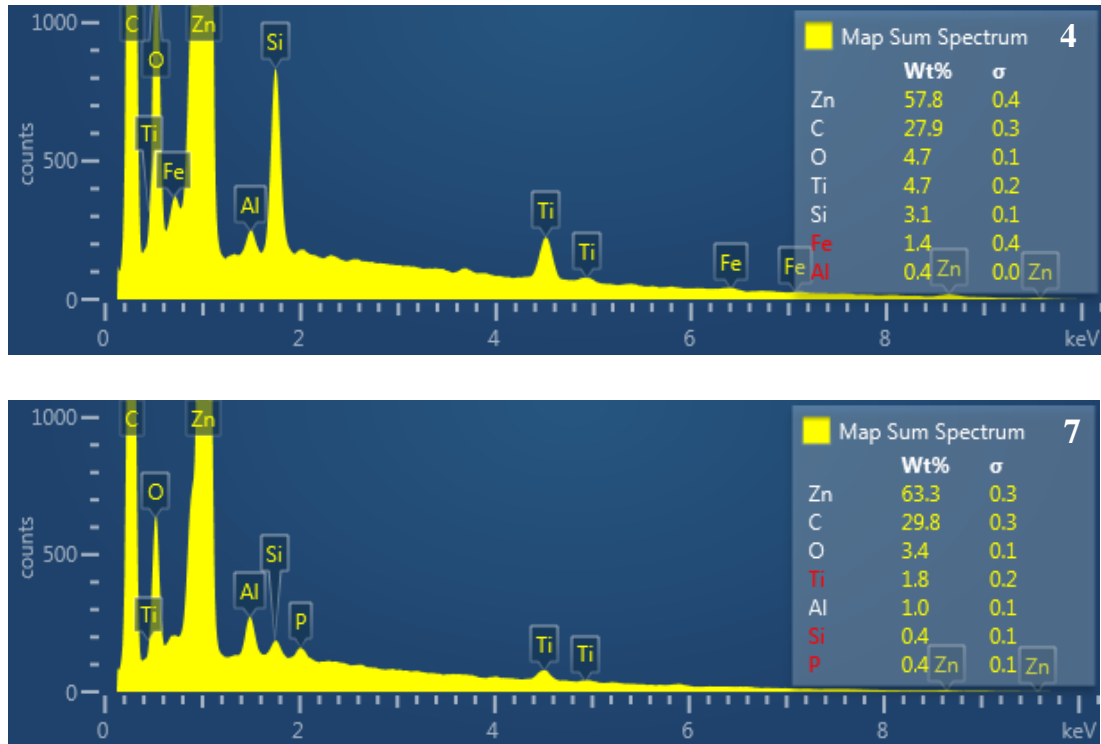


Figure 139. EDS spectra of an exposed panel of system 1 submerged in a cell 408 hours from Fig. 138 with 2 areas of analysis.

4.6.2.1.3. System 1 submerged in a cell for 1000hours.

The results of submerging system 1 in a cell for 1000 hours are shown in Fig. 137c and 140. Figure 140 shows the secondary electron SEM image of a primer and zinc cross-sectioned area and the area going to be analysed by point & ID analysis. The results of the mapping are shown in Fig. 141 as spectra.

Spectrum 3 shows the quantitative results obtained from Fig. 140, which was analysed in the primer. The elements in the coating were C, O, Ti, Si and Cl. The result shows 0.2% chlorine is in the primer at 1000 hours and not at the start or 408 hours. The zinc layer is represented by element Zn, Fe and Al.

Spectrum 4 shows the quantitative results obtained from the primer and zinc interface in Fig. 140. The elements in the primer were C, O and Si. The other elements (Zn, Fe and Al) were from the substrate.

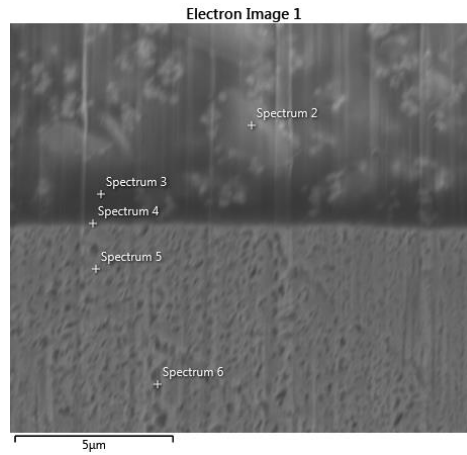


Figure 140. Secondary electron SEM image of an exposed panel of system 1 submerged in a cell for 1000 hours.

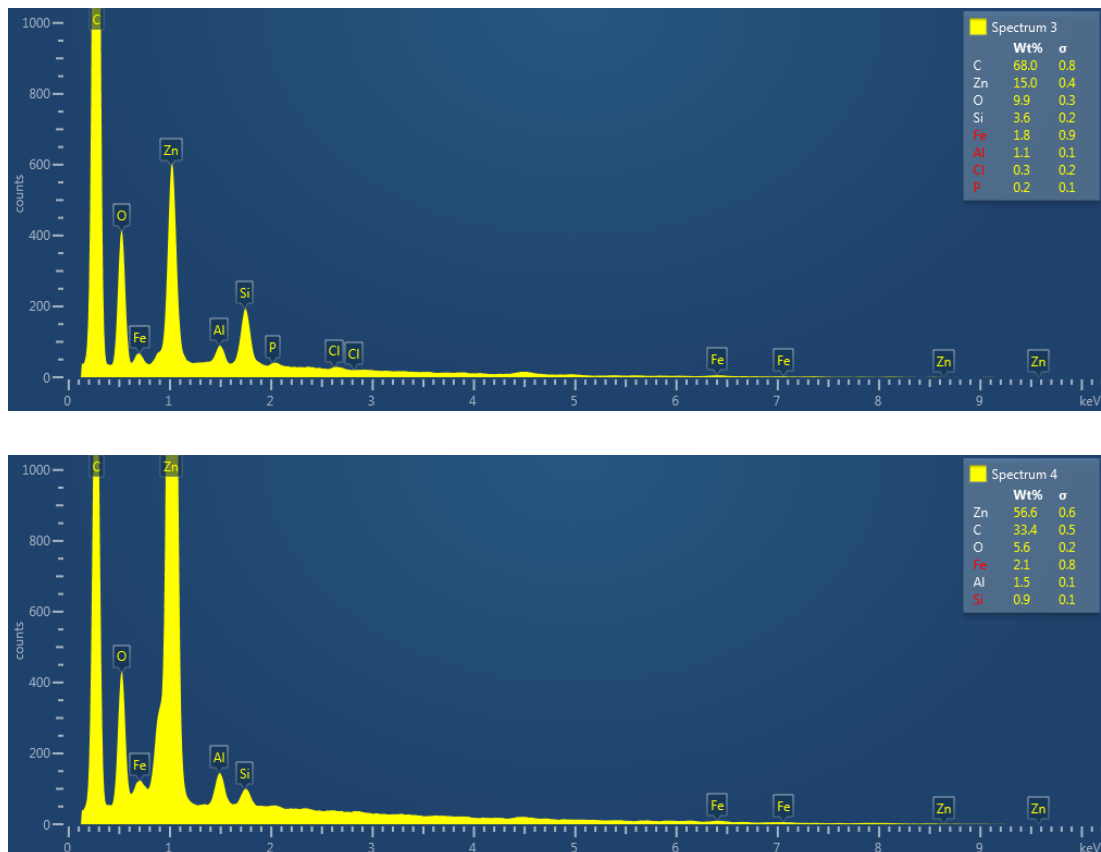


Figure 141. EDS spectra of an exposed panel of system1 submerged in a cell for 1000 hours. Spectrum 3 and 4 are the results of areas located in Fig. 140.

4.6.2.2. Exposed panels of System 2 (Waterborne pretreatment primer with no anti-corrosive pigment)

4.6.2.2.1. System 2 submerged in a cell from 0 to 1000 hours.

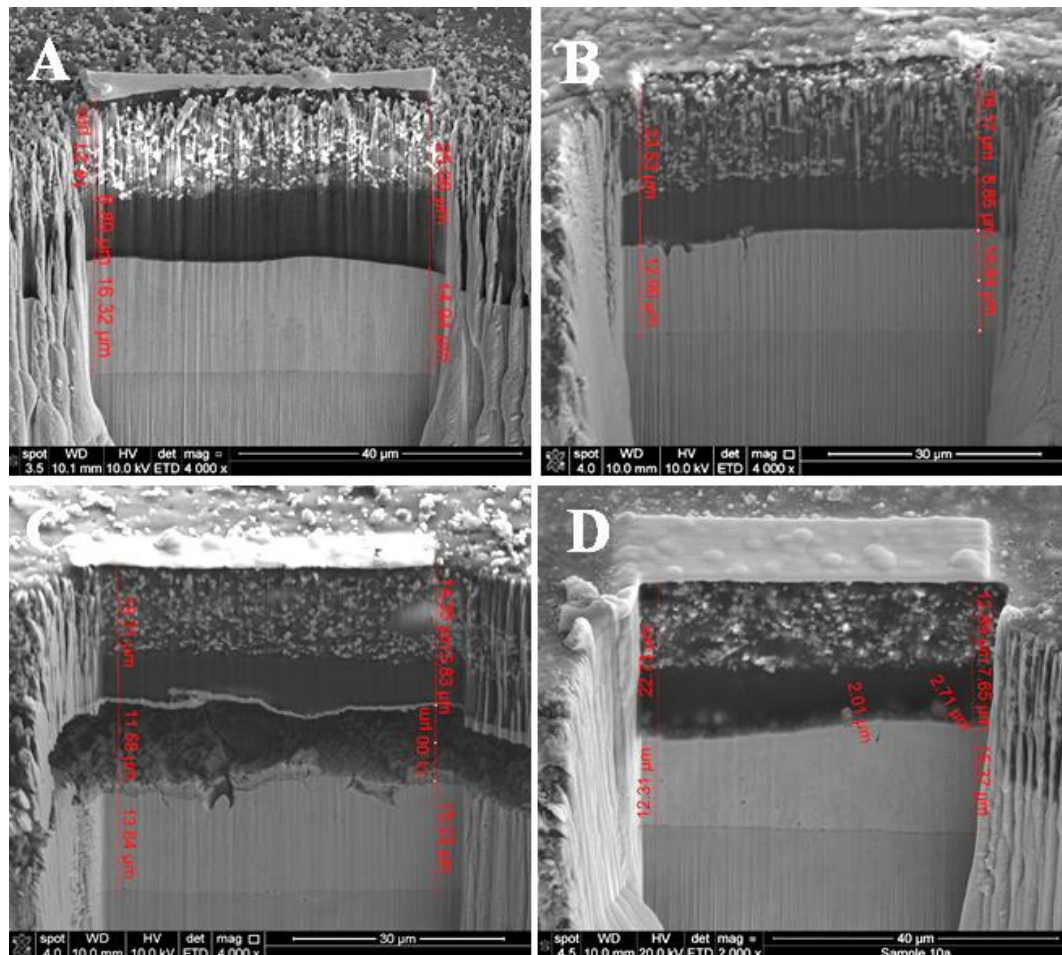


Figure 142. Secondary electron SEM images of unexposed and exposed panels of system 2 submerged in a cell for 0 hr (A), 192 hrs (B), 408 hrs (C) and 1000 hrs (D).

The results of milling and polishing of system 2 submerged at 0 (A), 192 (B), 408 (C) and 1000 (D) hours are shown in Fig. 142. The investigation started at blister areas first and then moved to areas with no deterioration, which was difficult to find on coated panel that has been exposed for 1000 hours. There was no material at the primer/ zinc interface at the start, but after 192 hours, there were materials present. At 408 hours delamination of a blister is observed and investigated. At 1000 hours, blisters are present all over the panel, but it was not cross-sectioned. Only an area with no blistering were cross-sectioned to see whether there are any corrosion products

present and the results are shown in Fig. 146d. It shows that there is corrosion product along the zinc layer. In the next few sections, the results of system 2 submerged in a cell for 192, 408 and 1000 hours will be revealed and explained.

4.6.2.2.2. System 2 submerged in a cell for 192 hours.

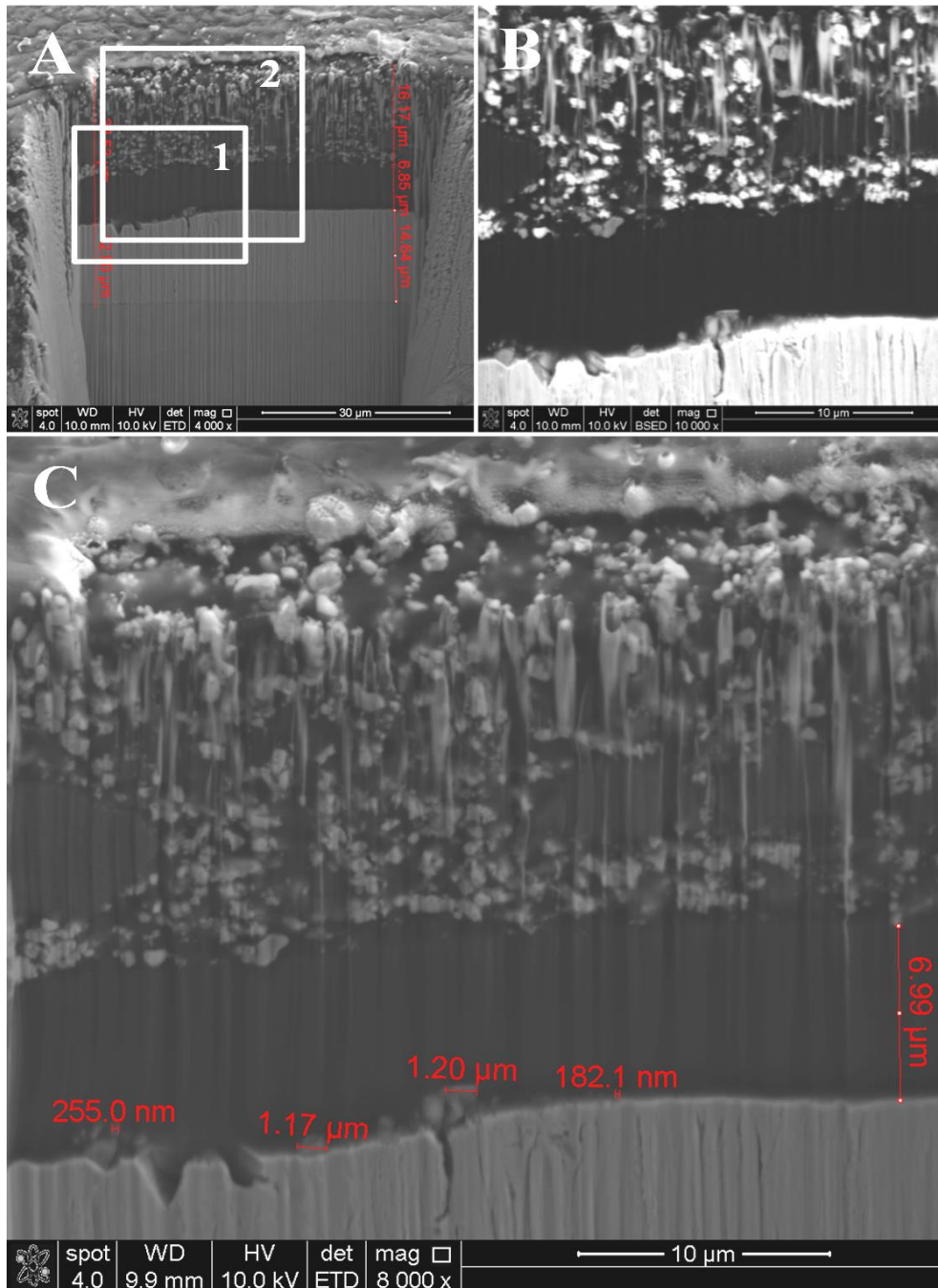


Figure 143. Secondary (a & c) & backscattered (b) electron images of an exposed panel of system 2 submerged in a cell for 192 hours. Cross-sectioned area with 2 white squares (a) zoom in area 1 (b) and zoom in area 2 (c).

The results of submerging system 2 in a cell for 192 hours are shown in Fig. 143. Figure 143a shows the cross-sectioned area of system 2 and the 2 white boxes are areas where EDS analysis will be measured. Figure 143b shows the cross-sectioned area of topcoat, pretreatment primer and zinc in BSED imaging mode. It clearly shows that the corrosion products (light grey) formed on top on the zinc layer are not pure zinc (white). Figure 143c shows the cross-sectioned area of topcoat, pretreatment primer and zinc in secondary electron imaging mode. Included in the image are the measurements of the corrosion products formed on top on the zinc layer, ranging from 182 nm to 1200 nm.

Area 1 in Fig. 143a was analysed and the secondary electron SEM image is shown in Fig. 144 together with points on the image where EDS analysis are going to be analysed. One of the results (spectrum 3) is shown in Fig. 145, which shows that there was no chloride present. However, zinc or iron can be oxidised to form corrosion products from elements found in the analysis. The materials found are not pure zinc as supported by BSED image. They are mixture of oxide/ hydroxide ferrous with Zn [2] [8]. Area 2 in Fig. 143b analysis results are shown in the appendix IV.

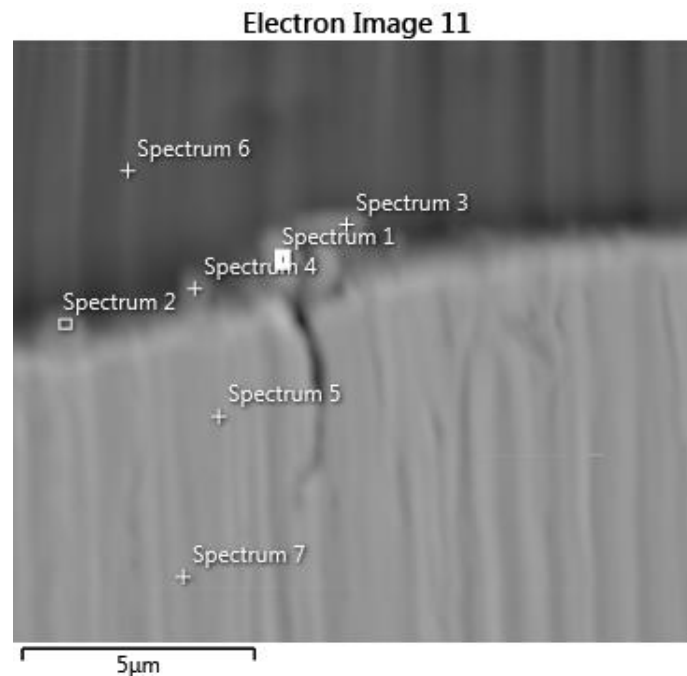


Figure 144. Secondary electron SEM image (image 11) of the areas that were analysed. The result is shown in Fig. 147.

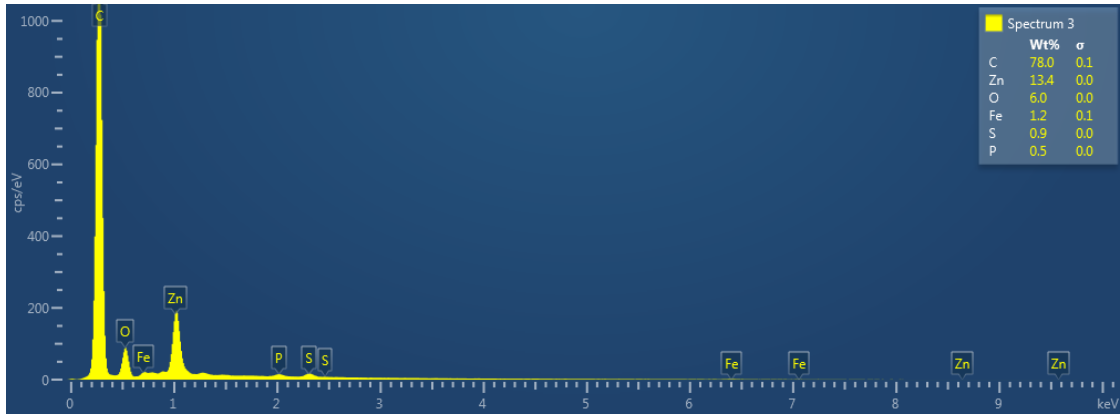


Figure 145. EDS spectrum of an exposed panel of system 2 submerged in a cell for 192 hours.

4.6.2.2.3. System 2 submerged in a cell for 408 hours, area A.

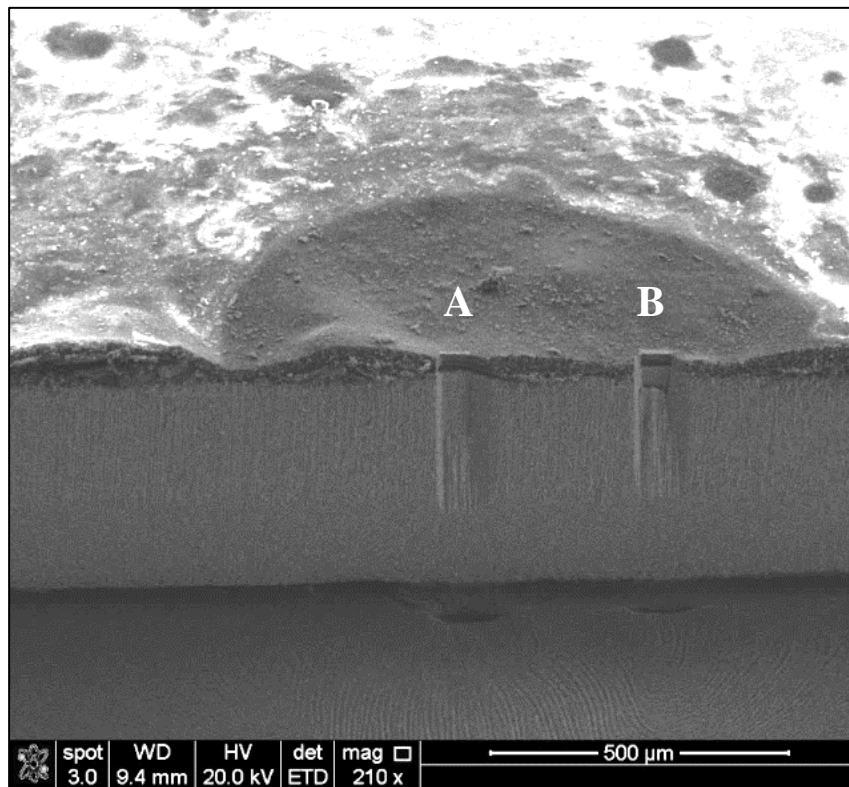


Figure 146. A panel of system 2 submerged in a cell for 408 hours.

The results of submerging system 2 in a cell for 408 hours are shown in Fig. 146. It shows at the edge of the panel, there are a couple of blisters present. Two milled

and polished areas were constructed on this section. The cross-sectioned areas are from the edge of a blister (a) and ~150 μm away from the blister (b). The two cross-sections were imaged and analysed by EDS analysis as shown in the next section.

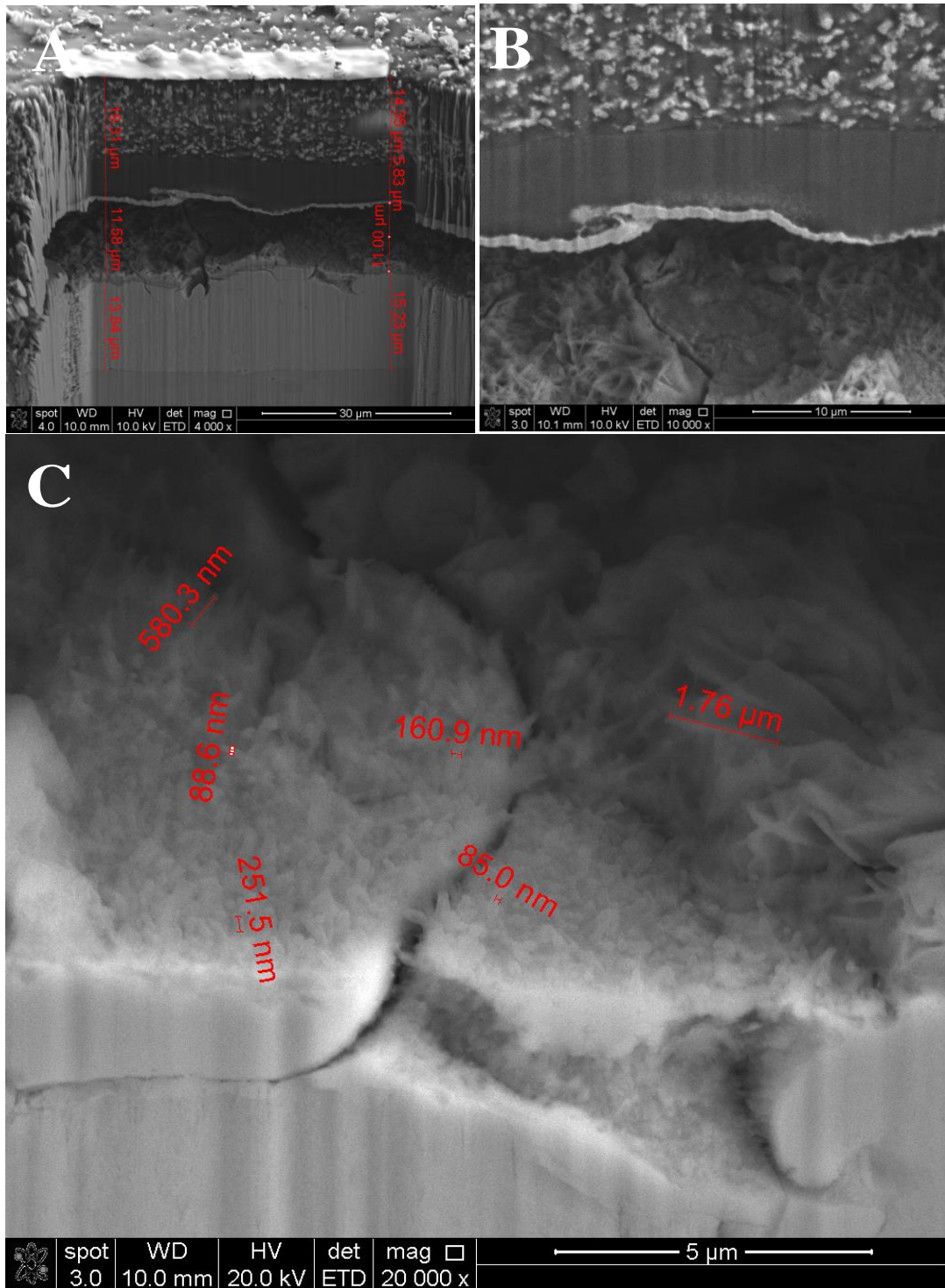


Figure 147. Secondary electron SEM images of a cross-section at edge of a blister, located in Fig. 146a.

The results of cross-sectioning at edge of a blister are shown in Figure 147. It shows that the pretreatment primer is still adhered to the zinc but together they have been separated from the main zinc layer with a gap of around 11 micrometres in depth (See Fig. 147a). Figure 147b shows that there is a phase difference between topcoat and pretreatment primer and corrosion products are forming in the pretreatment primer layer. Figure 147c shows the growth of corrosion product crystals on top on the zinc layer. The width of these crystal like structures range from 85 to 250 nm.

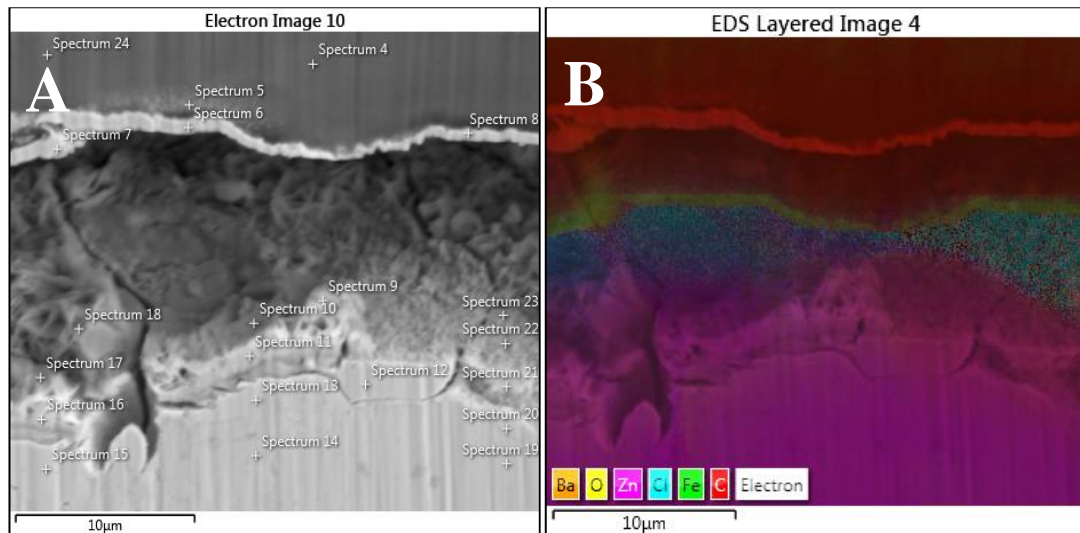


Figure 148. Secondary electron SEM image (a) and the results of EDS mapping (b) of a cross-sectioned area.

Figure 148 shows the area that will be analysed by EDS analysis and the results of the mapping (Fig. 148b). The map shows the different elements found in that area and is represented by the various colours in that map. Chlorine was detected in the middle of the map which is represented by the turquoise colour. The other elements of Ba, O, Zn, Fe and C are there to represent the coating and substrate.

The mapping results of Fig. 148b are shown in map spectrum. It shows that 2.3% chlorine was detected in the corroded area. The coating and substrate are represented by the other elements found in the analysis.

Point & ID analysis was performed on Fig. 148a. It represented areas where point & ID were done. The results are shown in spectrum 9 from Fig.149, which shows that 6.7% chlorine is detected in point 9.

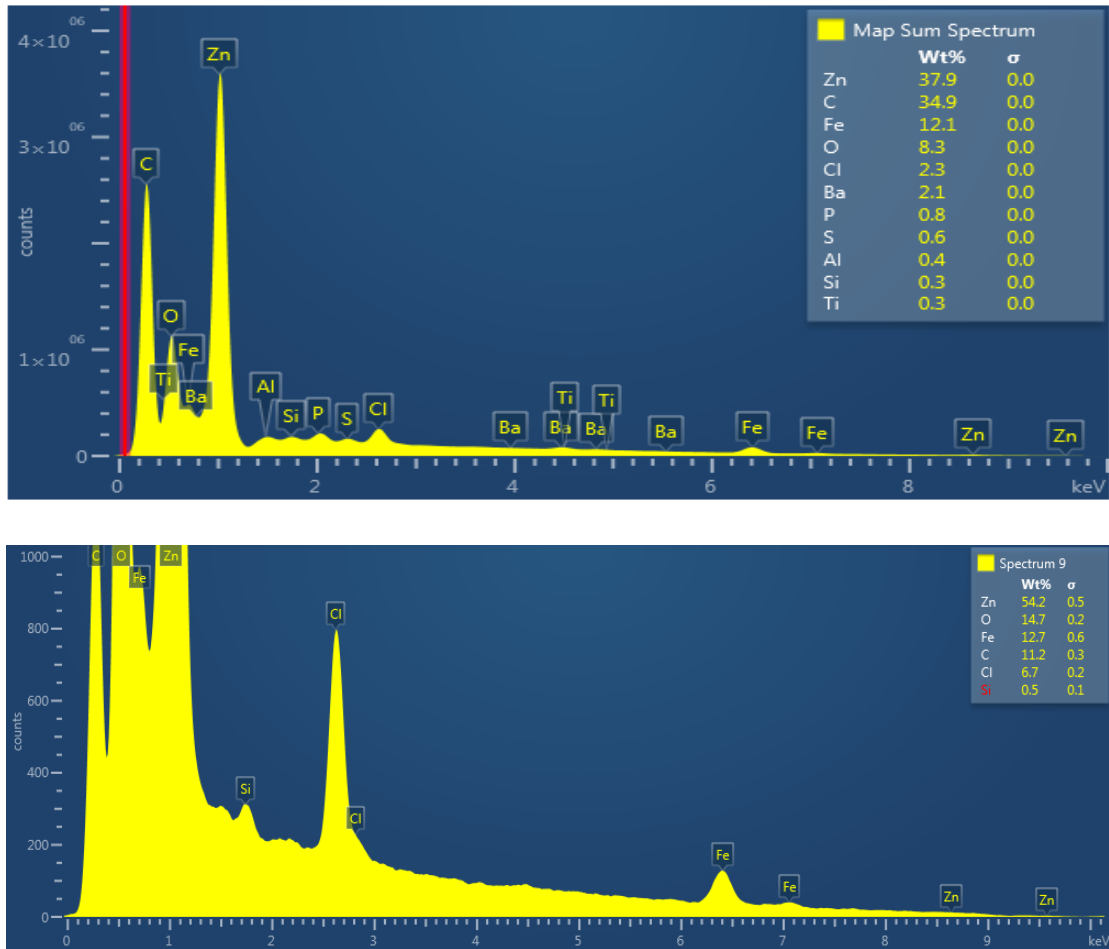


Figure 149. EDS spectra (map and spectrum 9) of Fig. 148.

4.6.2.2.4. System 2 submerged in a cell for 408 hours, area B.

The results of cross-sectioning $\sim 150 \mu\text{m}$ away from a blister are shown in Figure 150. Figure 150a shows that the pretreatment primer and zinc are still intact with no sign of corrosion present. When zoomed in as shown in Fig. 150b, corrosion products were observed at the damaged zinc area. Further magnification of 40,000 times revealed the presence of corrosion products formed on top of the zinc layer as shown in Fig. 152c. The sizes of these corrosion product range between 47 and 343 nm. Also included in the image is the oxidation of the zinc layer when compared to an unexposed panel.

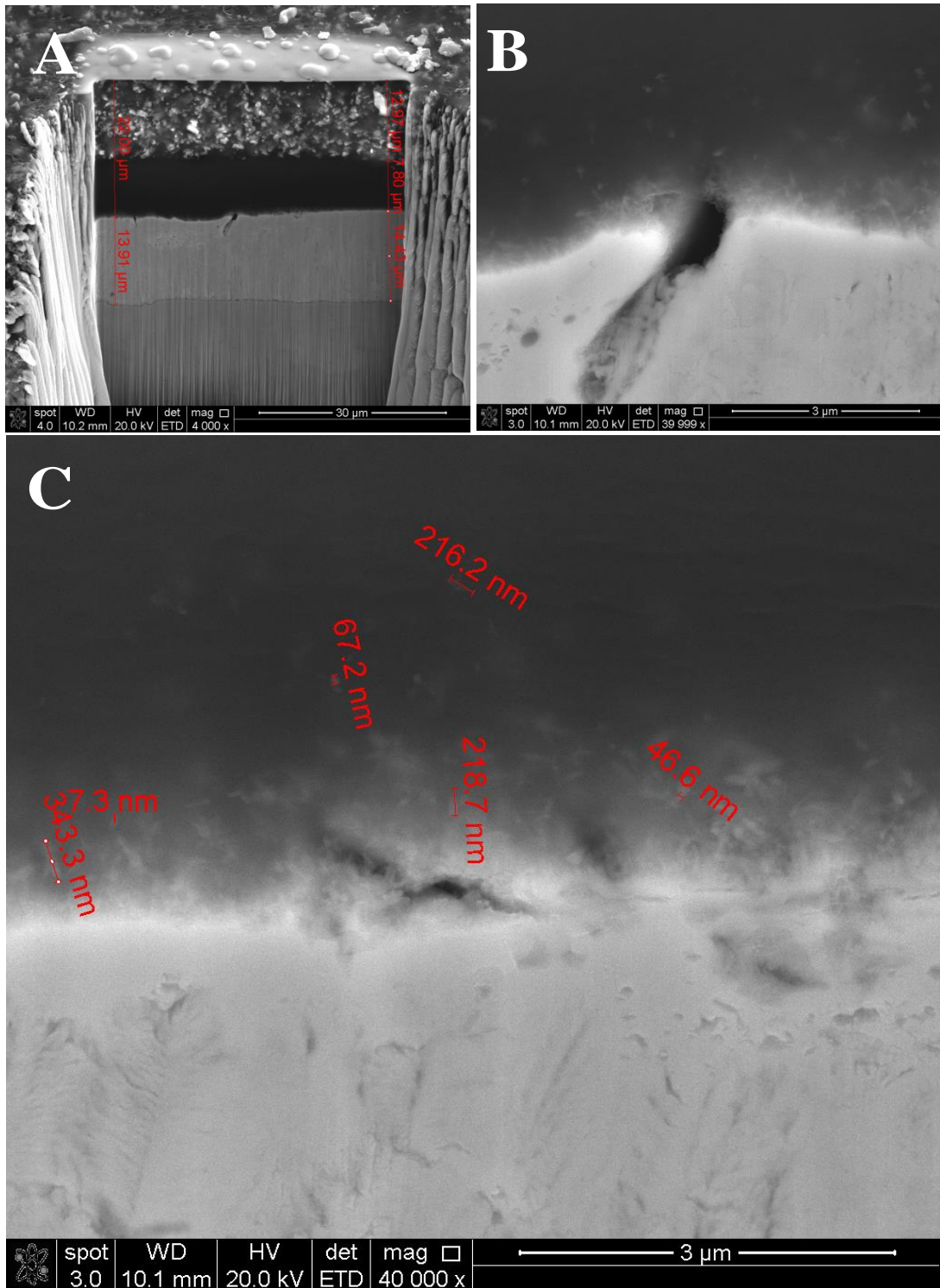


Figure 150. Secondary electron SEM images of a cross-section area closed to a blister, located in Fig. 146b. Cross-sectioned area (A), defected area in the zinc layer (B) and primer/zinc interface (C)

The results of EDS analysis of Fig. 150b are shown in Fig. 151 and 152. It shows a small trace of chlorine present at the zinc layer, but the corrosion products formed will be mainly based on oxides or hydroxides, which are difficult to distinguish using this technique. The pretreatment primer and substrate are represented by the other elements found.

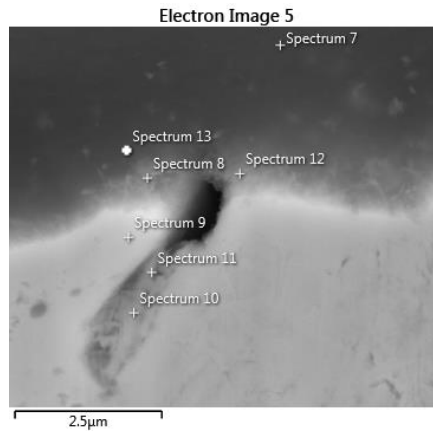


Figure 151. Secondary electron SEM image of areas going to be analysed using point & ID EDS analysis.

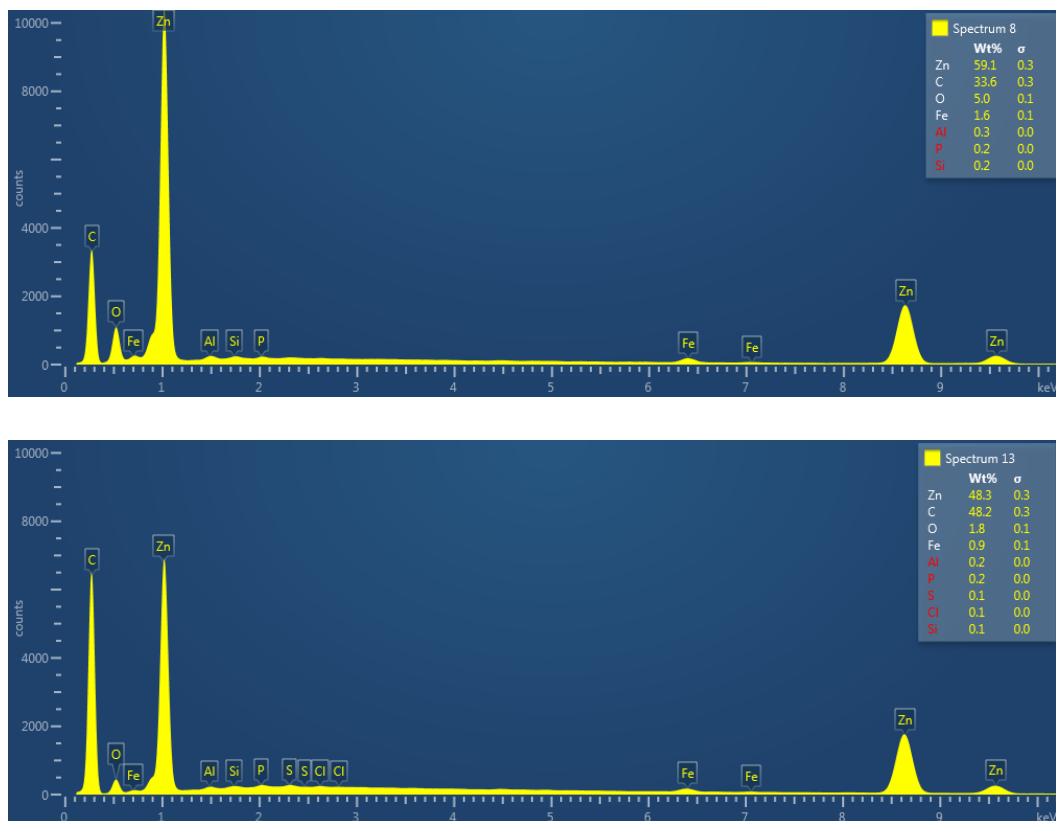


Figure 152. EDS spectra of areas 8 and 13 in Fig. 151.

4.6.2.2.5. System 2 submerged in a cell for 1000 hours.

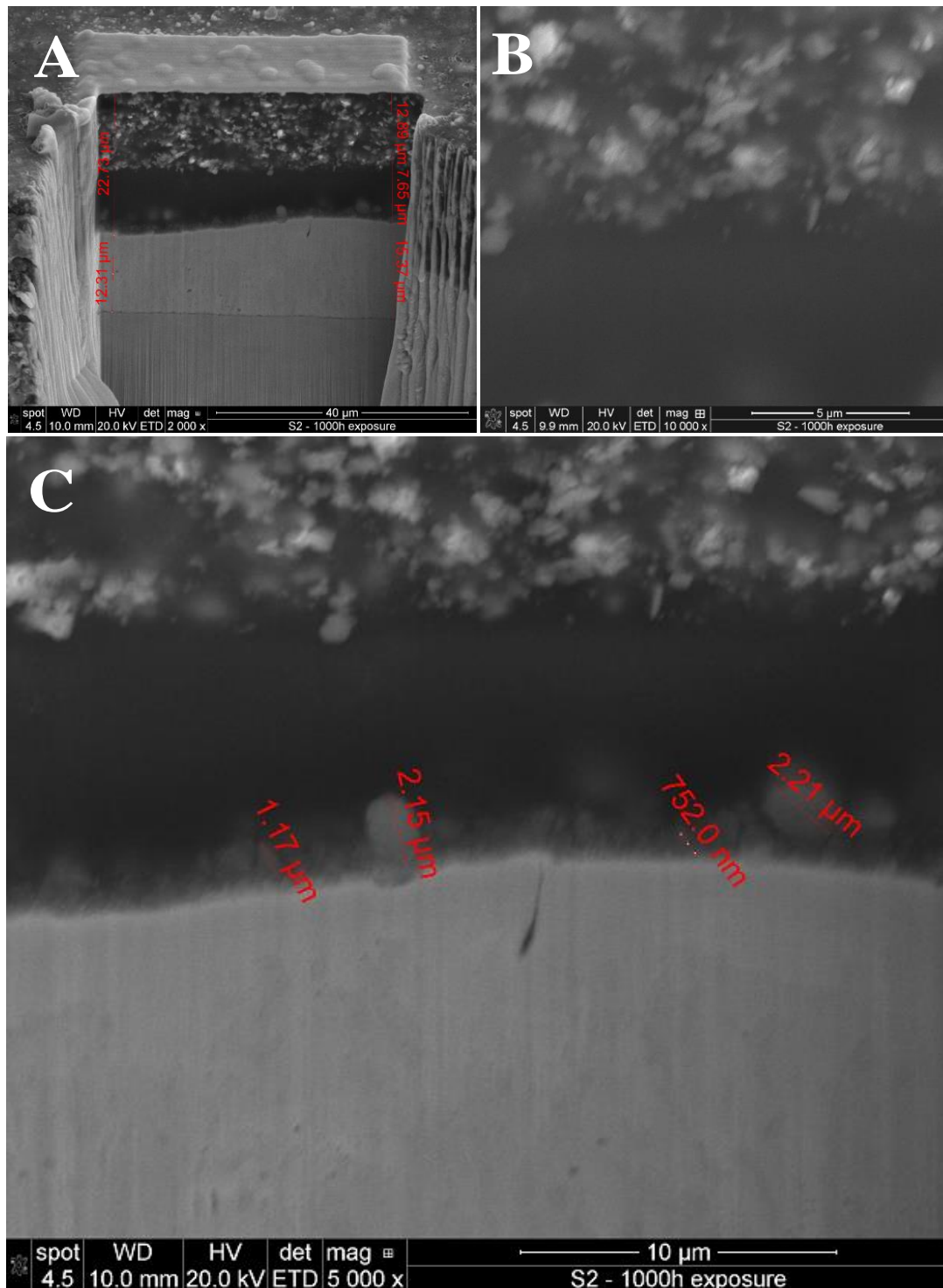


Figure 153. Secondary electron SEM image of an exposed panel of system 2 submerged in a cell for 1000 hours. Cross-section of milled area (A), topcoat/ primer area (B) and topcoat/ primer/ zinc area (C).

A number of areas could be cross-sectioned to show how severe the corrosion can be after 1000 hours of exposure. However, the results have already been investigated and reported at 408 hours when blisters were formed. The interesting results will be what the cross-sections reveal when areas of the panel are un-blistered and have good appearance with no damage area. The results of the cross-section of an undamaged area is shown in Fig. 153 and the image quality is not as good as previous samples. SEM image quality depends on a number of factors, the main factor is sample interactions with the electrons and that is why 2 or 3 cross-section areas are needed for each sample.

The cross-sectioned area of Fig. 153a shows the topcoat, pretreatment primer and zinc was still intact with each other, with signs of corrosion products present on the zinc layer. Figure 153b shows the topcoat and pretreatment primer with no sign of phase difference separation as observed in previous investigations. However, it may be due to the poor quality of the image obtained. Further magnification of 5,000 times revealed the presence of corrosion products formed on top of the zinc layer as shown in Fig. 153c. It enables the corrosion products formed on top of the zinc layer to be measured and the size of the corrosion products range between 750 nm and 2210 nm. Included in the image is the presence of oxidation of the zinc layer when compared to an unexposed panel.

4.6.2.3. Exposed panels of system 3 (Waterborne pretreatment primer with anti-corrosive pigment)

4.6.2.3.1. System 3 submerged in a cell from 0 to 1000 hours.

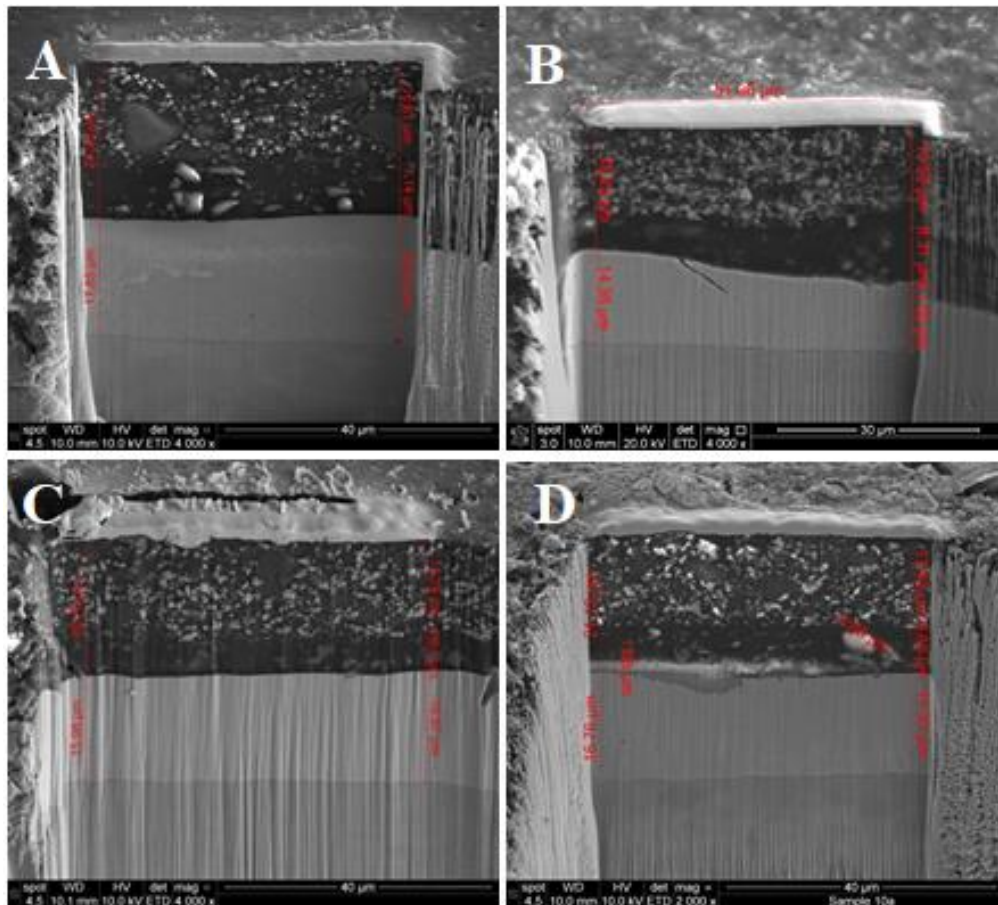


Figure 154. Secondary electron SEM images of unexposed and exposed panels of system 3 submerged in a cell for 0 hr (A), 192 hrs (B), 408 hrs (C) and 1000 hrs (D).

The results of milling and polishing of system 3 submerged at 0 (A), 192 (B), 408 (C) and 1000 (D) hours are shown in Fig. 156. It shows there are small changes in the primer/ zinc interface at 192 (B) and 408 (C) hours with one or two areas of corrosion products forming. At 1000 hours (D), further growth in corrosion products at the primer/ zinc interface is observed and they covered the length of the cross-sectioned area.

In the next few sections, the results of system 3 submerged in a cell for 192, 408 and 1000 hours will be revealed and explained.

4.6.2.3.2. System 3 submerged in a cell for 192 hours.

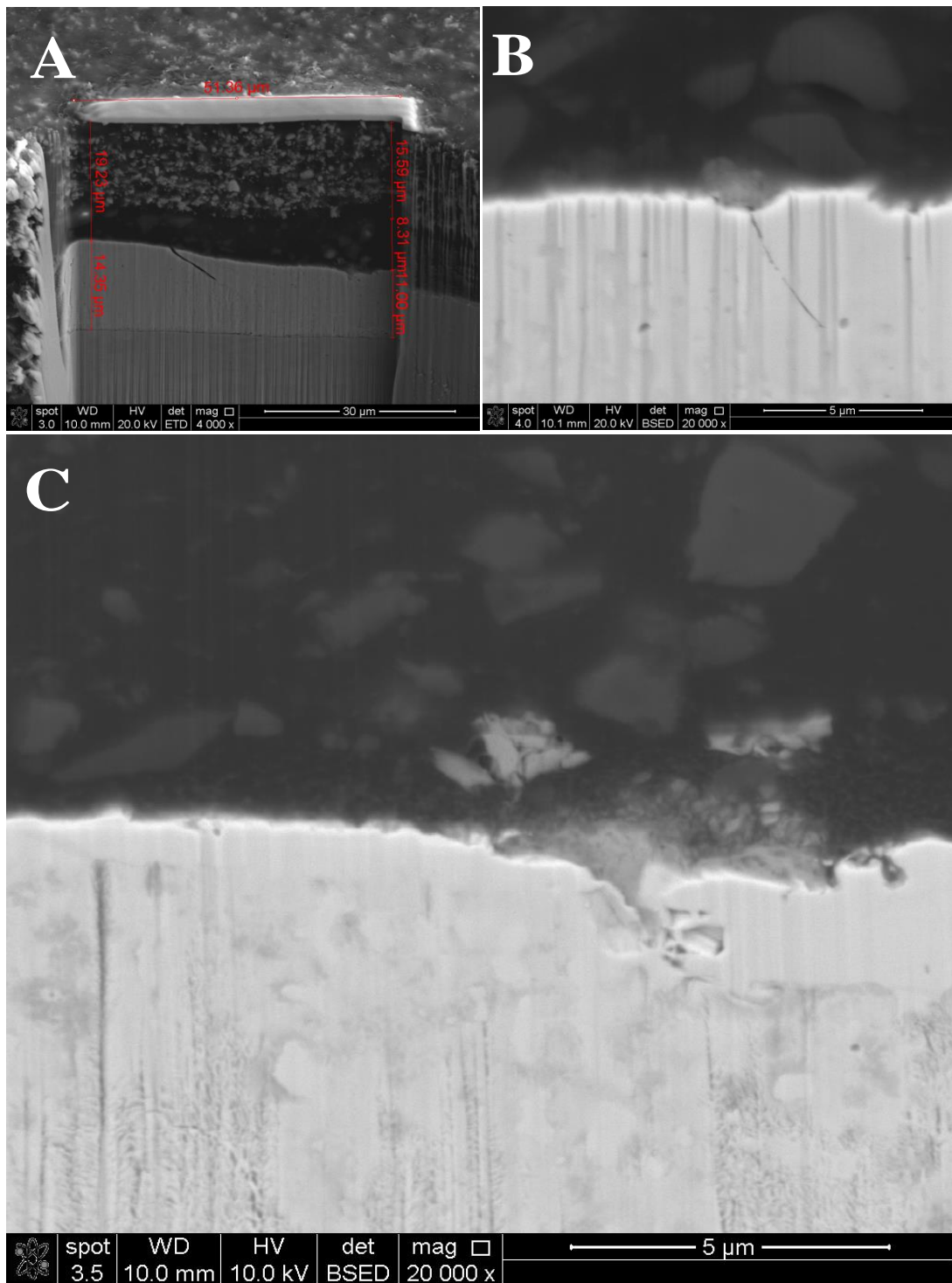


Figure 155. Secondary (A) & backscattered electron (B & C) SEM images of an exposed panel of system 3 submerged in a cell for 192 hours. Cross-section of milled area (A), primer/ zinc interface (B) and another example of primer/ zinc interface (C).

The results of cross-sectioning a panel of system 3 submerged in a cell for 192 hours are shown in Fig. 155. Figure 155a shows the cross-sectioned area of the topcoat, pretreatment primer, zinc and steel. There is a small amount of corrosion product presented at the primer/ zinc interface. Further magnification of 20,000 times using BSED mode reveals and proves the presence of a corrosion product formed on top of the zinc layer as shown in Fig. 155b. The result is supported by the colour difference of the corrosion product compared to zinc and calcium ion exchange silica pigment.

Figure 155c also shows this effect but in a different location in the cross-sectioned area. In this region, an oxidation process is seen in the zinc layer supported by comparing with an unexposed panel. The different shades of white presented in the zinc are a good indication of oxidation.

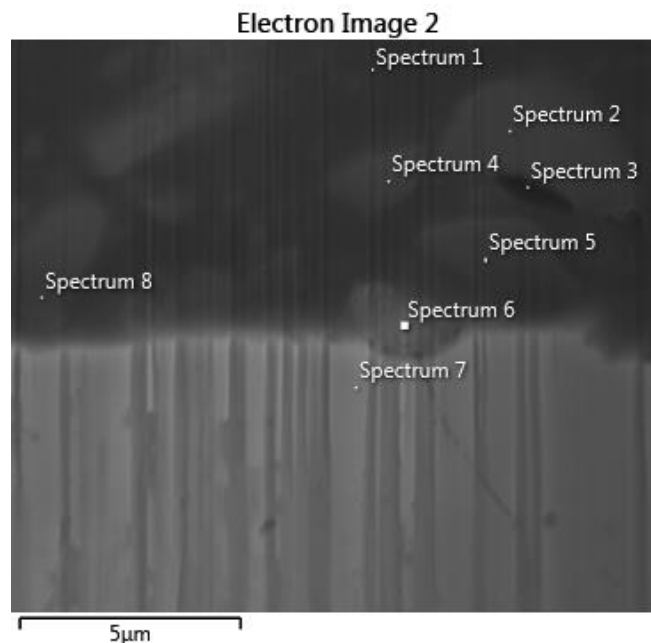


Figure 156. Secondary electron SEM image of areas was analysed using point & ID EDS analysis.

The results of EDS analysis of Fig. 156 are shown in Fig. 157. It detected small traces of chlorine presence in spectrum 6, which indicated that at 192 hours chlorine had diffused to the coating/ zinc interface. The corrosion products formed were mainly based on mixture of oxide/ hydroxides and are difficult to distinguish by EDS technique. The pretreatment primer and substrate are represented by the other elements found. Spectrum 5 shows the presence of Ca, which is associated with calcium ion

exchange anti-corrosive pigment. The other elements are from the coating and substrate.

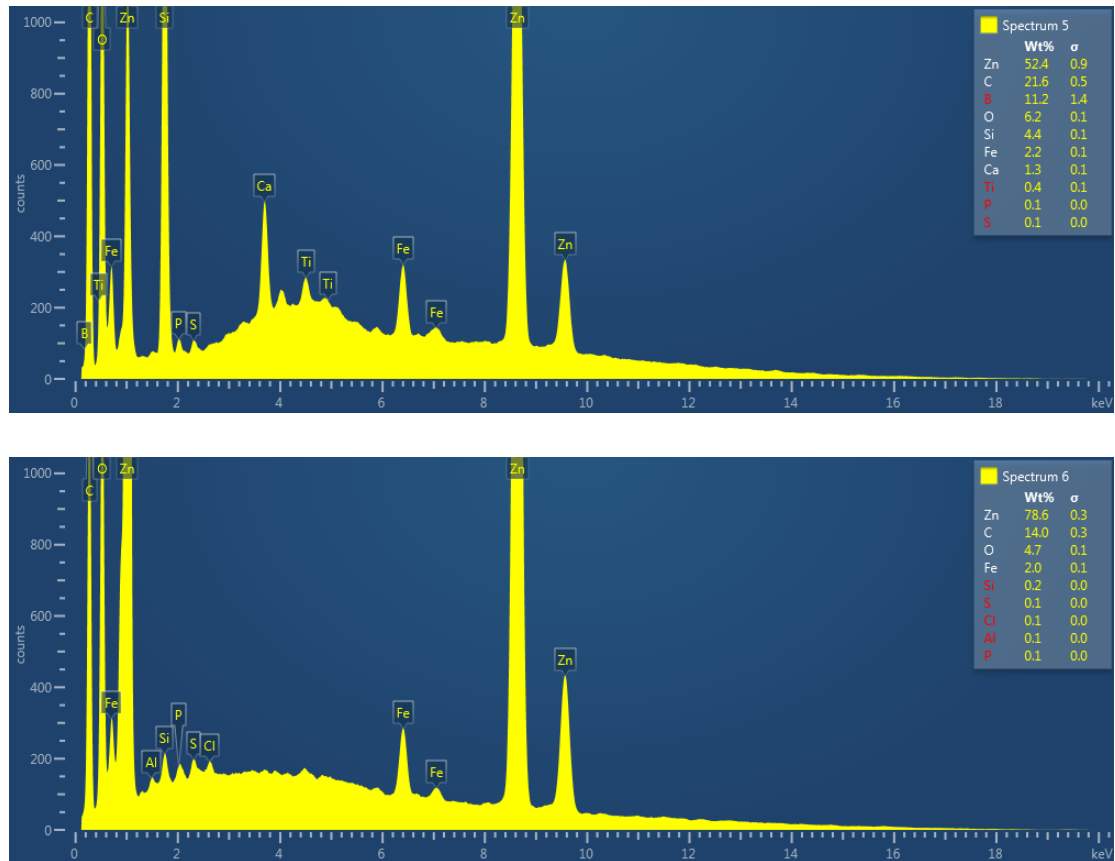


Figure 157. EDS spectra of spectrum 5 and 6 in Fig. 156.

4.6.2.3.3. System 3 submerged in a cell for 408 hours.

The results of cross-sectioning a panel of system 3 submerged in a cell for 408 are shown in Figure 158. Figure 158a shows the cross-sectioned area of the topcoat, pretreatment primer, zinc and steel. There is small amount of corrosion product presented at the primer/ zinc interface. Further magnification of 20,000 times using BSED mode reveals the corrosion product is $\sim 2.5 \mu\text{m}$ in size as shown in Fig. 158b. The result is supported by the colour difference of the corrosion product compared to zinc and calcium silicate pigment.

Figure 160c shows the secondary electron SEM image of Fig. 158b. It reveals the corrosion product surface is breaking up and the zinc layer has small areas of damage.

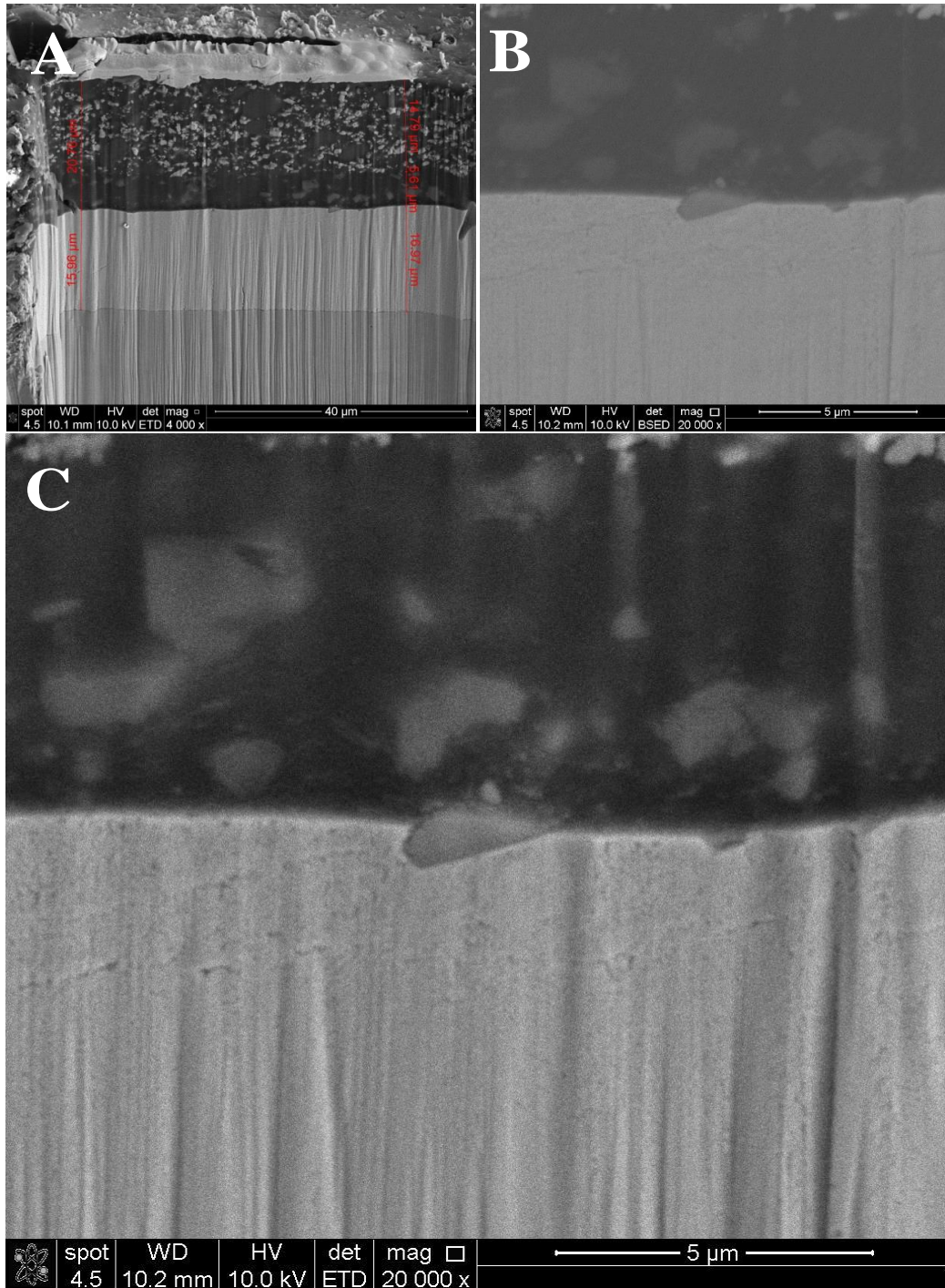


Figure 158. Secondary (A & C) & BSED (B) SEM images of an exposed panel of system 3 submerged in a cell for 408hrs. Cross-section of milled area (A), BSED image of primer/ zinc area (B) and SE image of primer/ zinc area (C).

Figure 159 shows the area that will be analysed by EDS analysis (a) and the results of the mapping (b). The map shows the different elements found in that area and is represented by the various colours in that map. No chlorine is detected in the map possibly due to small concentration of <0.1% presented in the map area. The other elements of C, O, Zn, Fe, Si and Al are there to represent the coating and substrate.

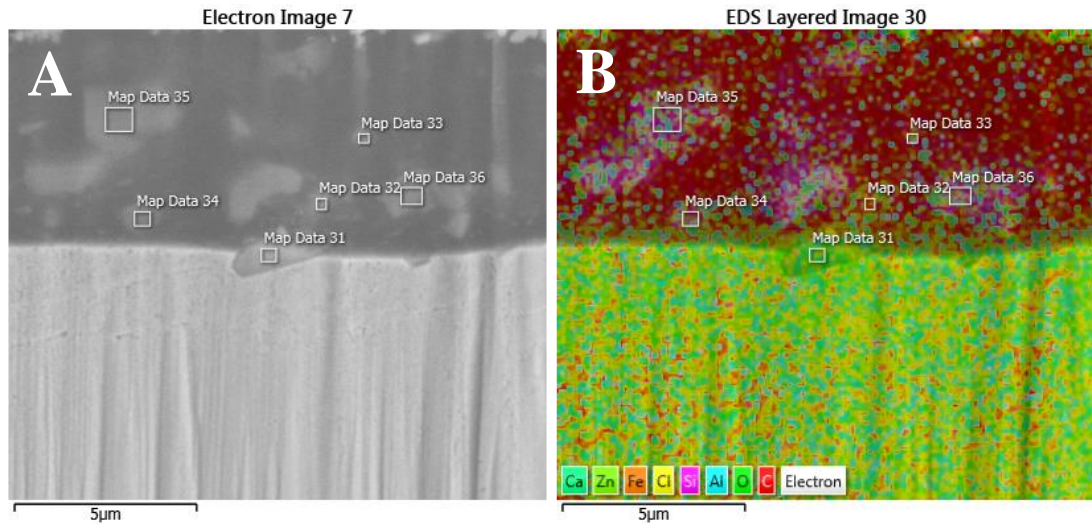


Figure 159. Secondary electron SEM image (left) and the results of EDS mapping (right).

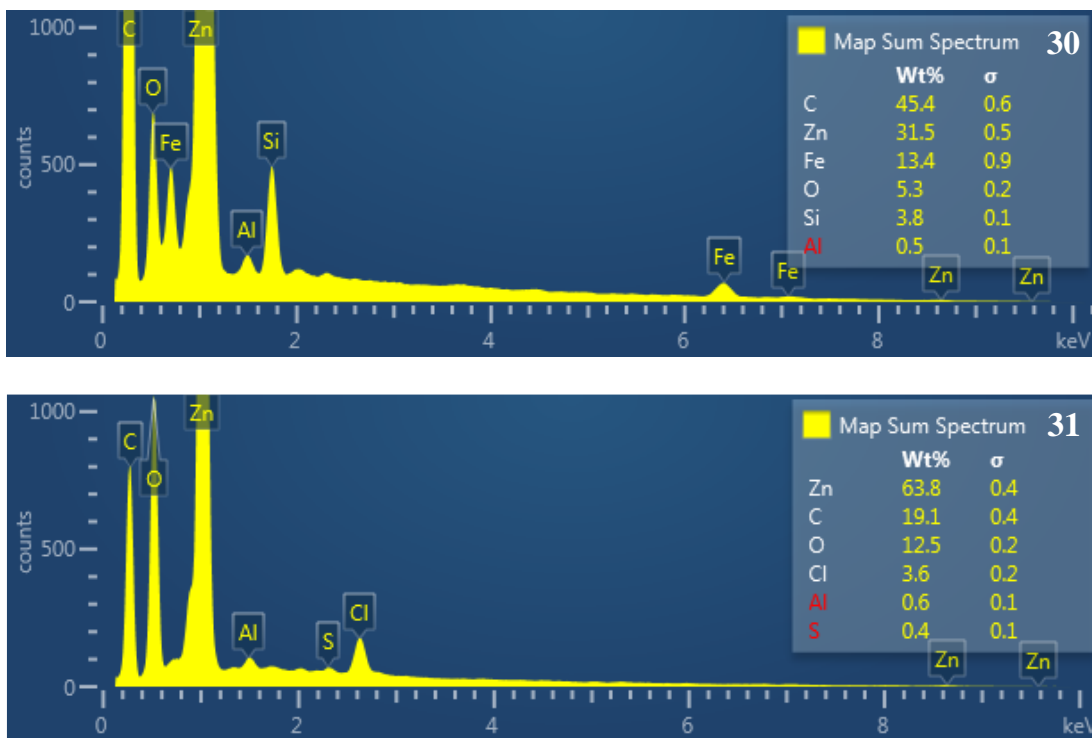


Figure 160. EDS spectra of maps 30 and 31 from Fig. 161.

The mapping results of Fig. 160 right are shown in map 30. It shows that no chlorine was detected in that area. The coating and substrate are represented by the other elements found in the analysis.

Point & ID analysis was performed on the left image of Fig. 159. The results are shown in spectrum 31 from Fig.160, which shows that 3.6% chlorine is detected in the corrosion product. The other elements are related to the coating and substrate.

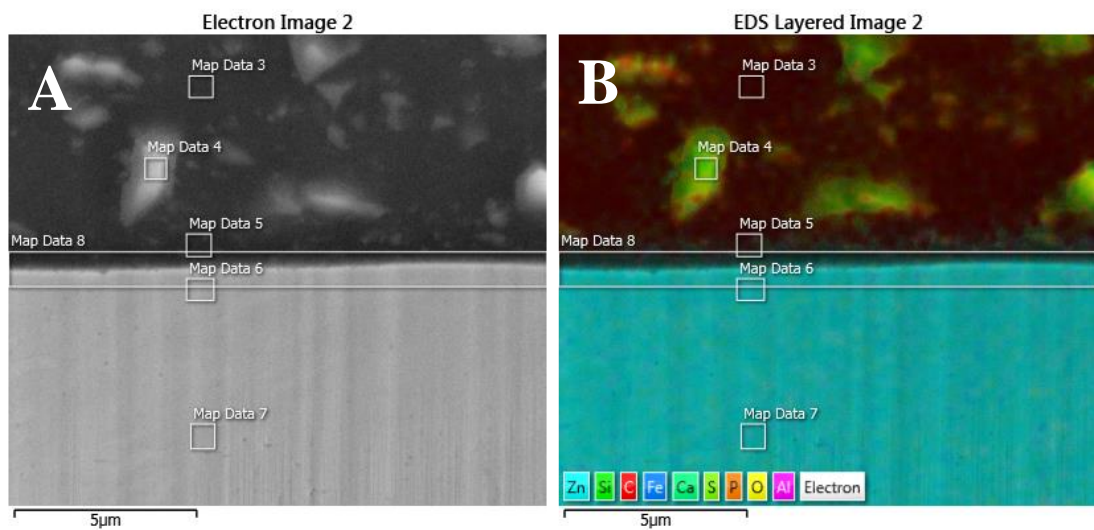
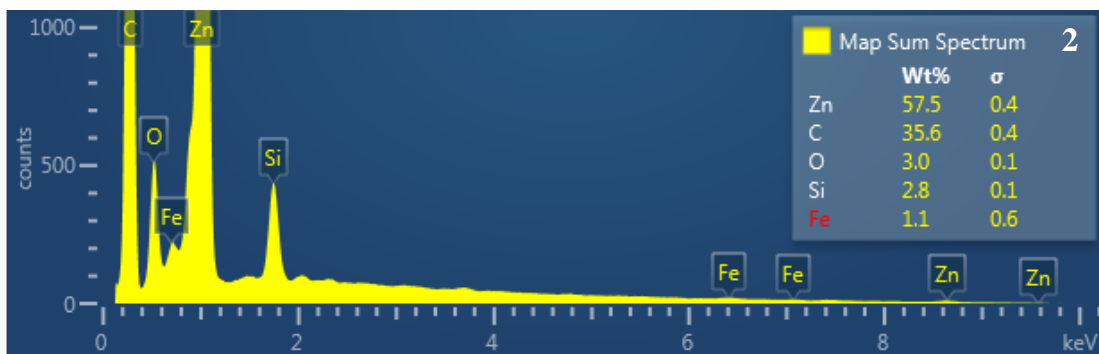


Figure 161. Secondary electron SEM image (a) and the results of EDS mapping (b).



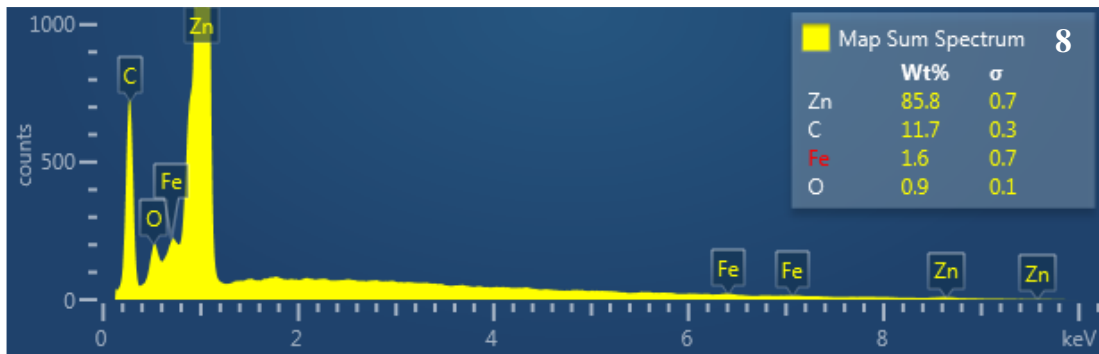


Figure 162. EDS spectra of maps 2 and 8 from Fig. 163.

Further EDS analysis were done at the primer / zinc interface to see whether Si or Ca can be detected so proving the use of anti-corrosive pigment role. Figure 161 shows the area that was analysed by EDS analysis (a) and the results of the mapping (b). The map shows the different elements found in that area and are represented by the various colours in that map.

Spectrum 2 shows the EDS mapping resulting of Fig. 161b. The coating is represented by element C, O, and Si. The substrate is represented by element Zn, Fe and O.

Spectrum 8 shows the quantitative values for those elements. The spectrum shows there was no Si or Ca presented at the primer/ zinc interface, hence no protection for the steel.

4.6.2.3.4. System 3 submerged in a cell for 1000 hours.

The results of submerging system 3 in a cell for 1000 hours are shown in Fig. 163. Figure 163a shows the secondary electron SEM image of the topcoat, pretreatment primer, zinc and steel cross-sectioned area. At the pretreatment primer and zinc interface there is large area of corrosion product formation. Also observed are the different phases in the zinc and steel.

Figure 163b shows the secondary electron SEM image of the topcoat, and pretreatment primer. Due to the poor quality of the image, it was difficult to observe the phase difference between the two coatings normally seen in previous images.

Figure 163c shows the higher magnification of pretreatment primer and zinc region. It shows in details of the corrosion products that are formed at the interface.

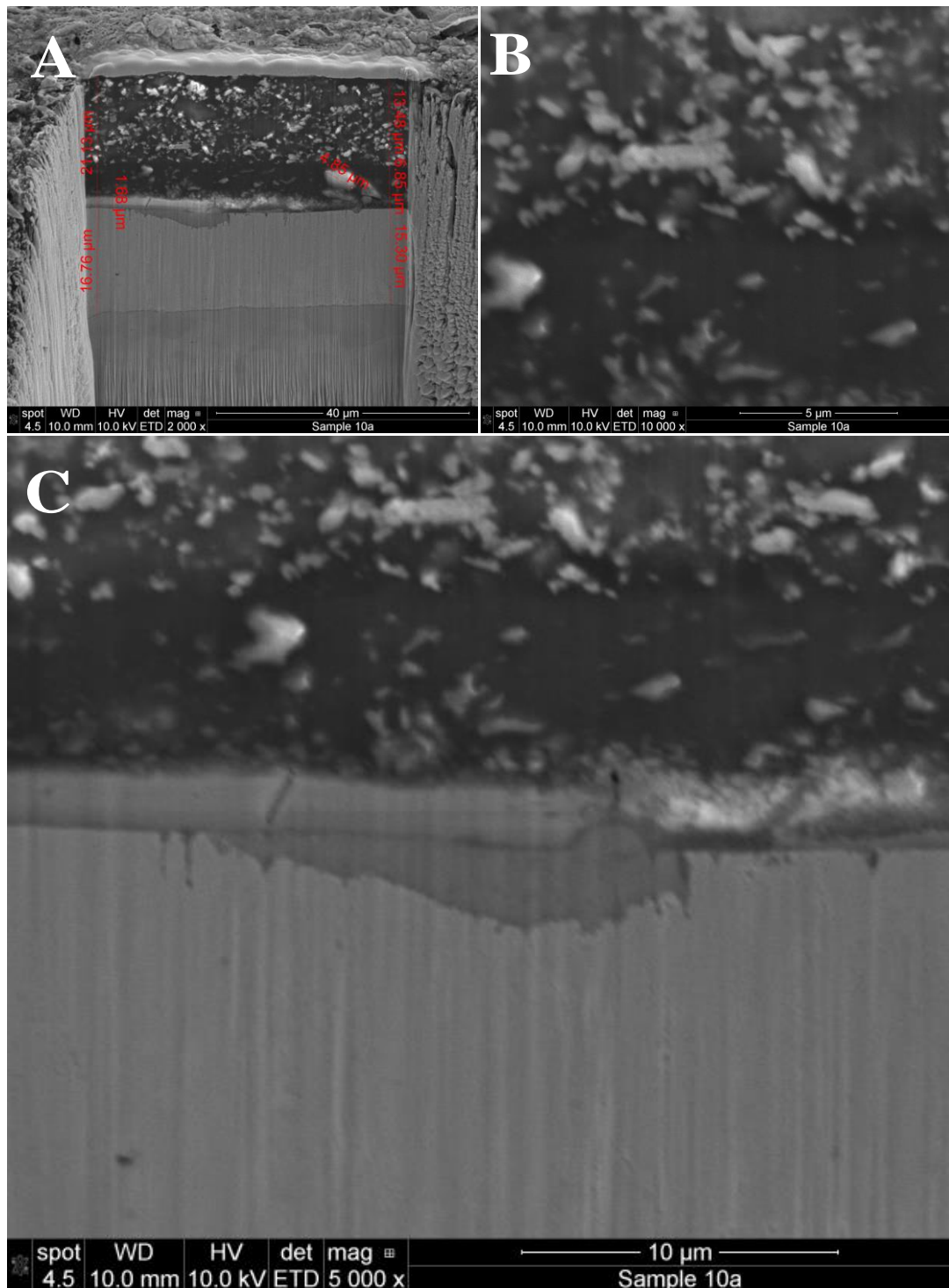


Figure 163. Secondary electron SEM images of an exposed panel of system 3 submerged in a cell for 1000hrs. Cross-section of milled area (A), topcoat/ primer interface (B) and primer/ zinc interface (C).

The thickness of the corrosion product layer is between 2 and 3 μm. Also revealed from the image is the marking of the zinc layer with the corrosion products.

Is this the effect of milling or polishing or actual leaching of corrosion product into the zinc layer?

EDS mapping and line scans of the pretreatment primer/ zinc areas were analysed and the results are shown in fig. 164-165.

Figure 164 shows the results of EDS mapping of fig. 163c. In the figure, an elemental map is presented (top left) together with the elements (right) of that map represented by the different colours of that element. The coating is represented by elements C, O, Si, P, Ba and Ca. The substrate is represented by element Zn, Fe, and Al. The corrosion product is represented by element chlorine and 2.1% was found. The spectrum shown at the bottom left of Fig.166 shows the quantity of each element that was detected.

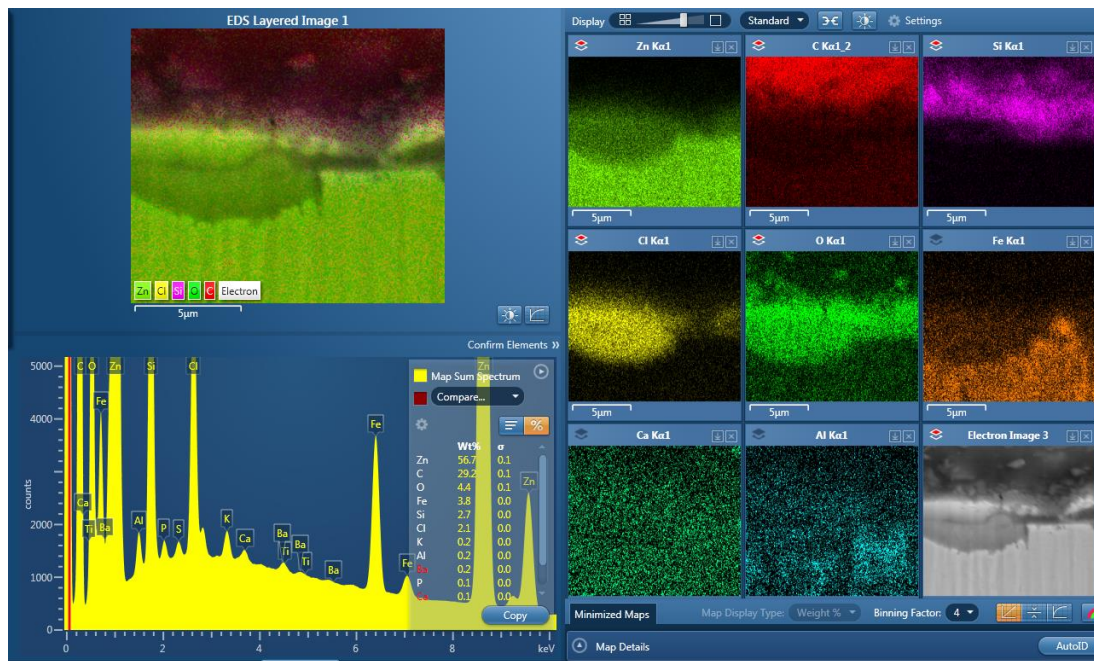


Figure 164. EDS mapping results of area of primer and zinc region in Fig. 163.

Further EDS analysis were done using line scan method on the interface of the pretreatment primer and zinc are shown in Fig. 165. It supports the results in Fig. 164 and also shows that at the interface, 5.3% of chlorine was detected.

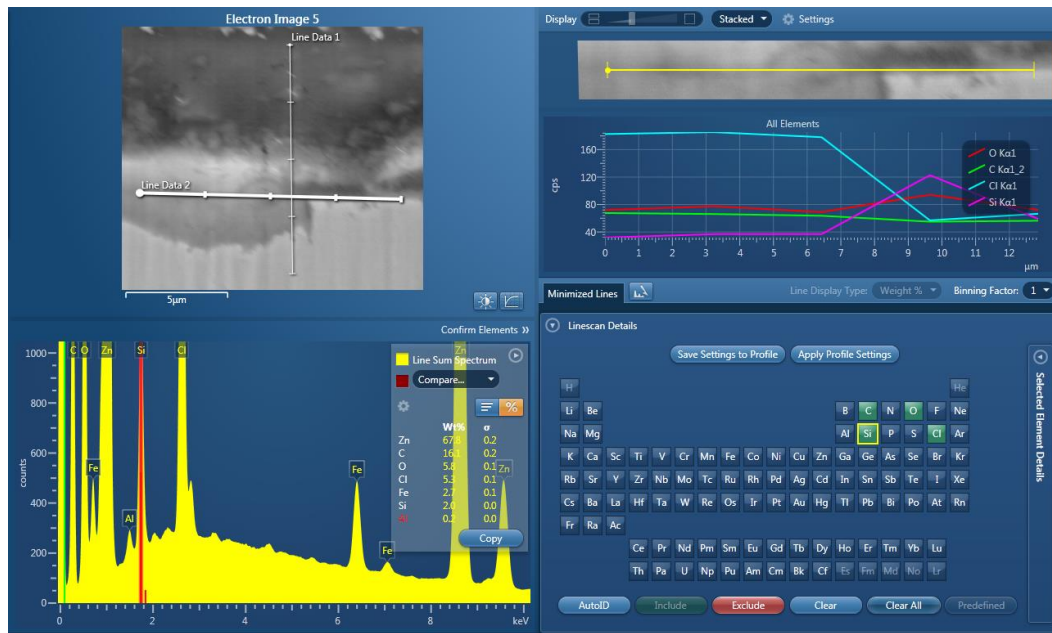


Figure 165. EDS line scan results of area of primer/ zinc interface in Fig. 163.

4.6.2.4. Exposed panels of system 4 (Waterborne pretreatment primer with anti-corrosive pigment and pretreatment technology)

4.6.2.4.1. System 4 submerged in a cell from 0 to 1000 hours.

The results of milling and polishing of system 4 submerged at 0 (a), 192 (b), 408 (c) and 1000 (d) hours are shown in Fig. 168. It shows there was no or little change in the primer/ zinc interface at 192 (b) and 408 (c) hours with one or two areas of corrosion products forming. At 1000 hours (d), further growth in corrosion products and delamination at the primer/ zinc interface is observed. It covers the length of the cross-sectioned area (~50 μm length).

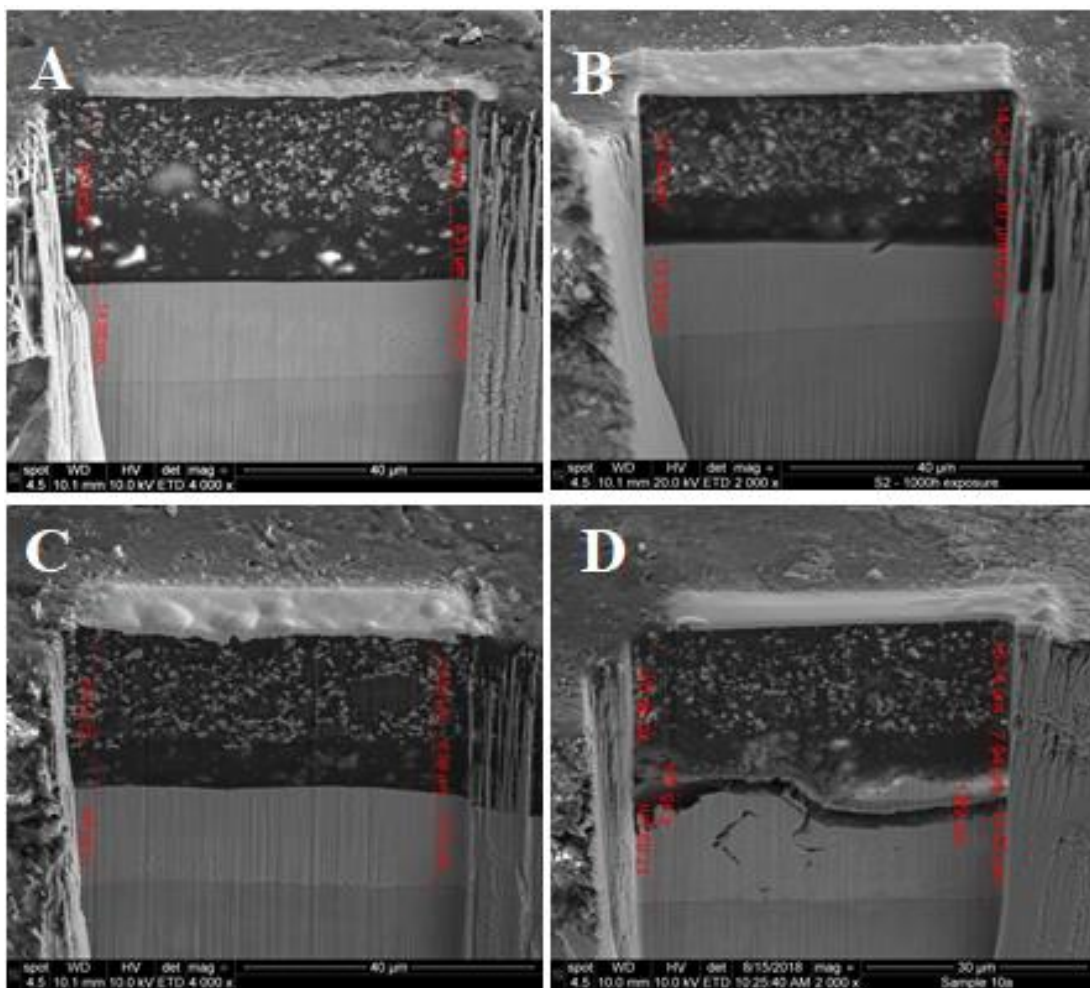


Figure 166. Secondary electron SEM images of unexposed and exposed panels of system 4 submerged in a cell for 0 hr (A), 192 hrs (B), 408 hrs (C) and 1000 hrs (D).

In the next few sections, the results of system 4 submerged in a cell for 192, 408 and 1000 hours will be revealed and explained.

4.6.2.4.2. System 4 submerged in a cell for 192 hours.

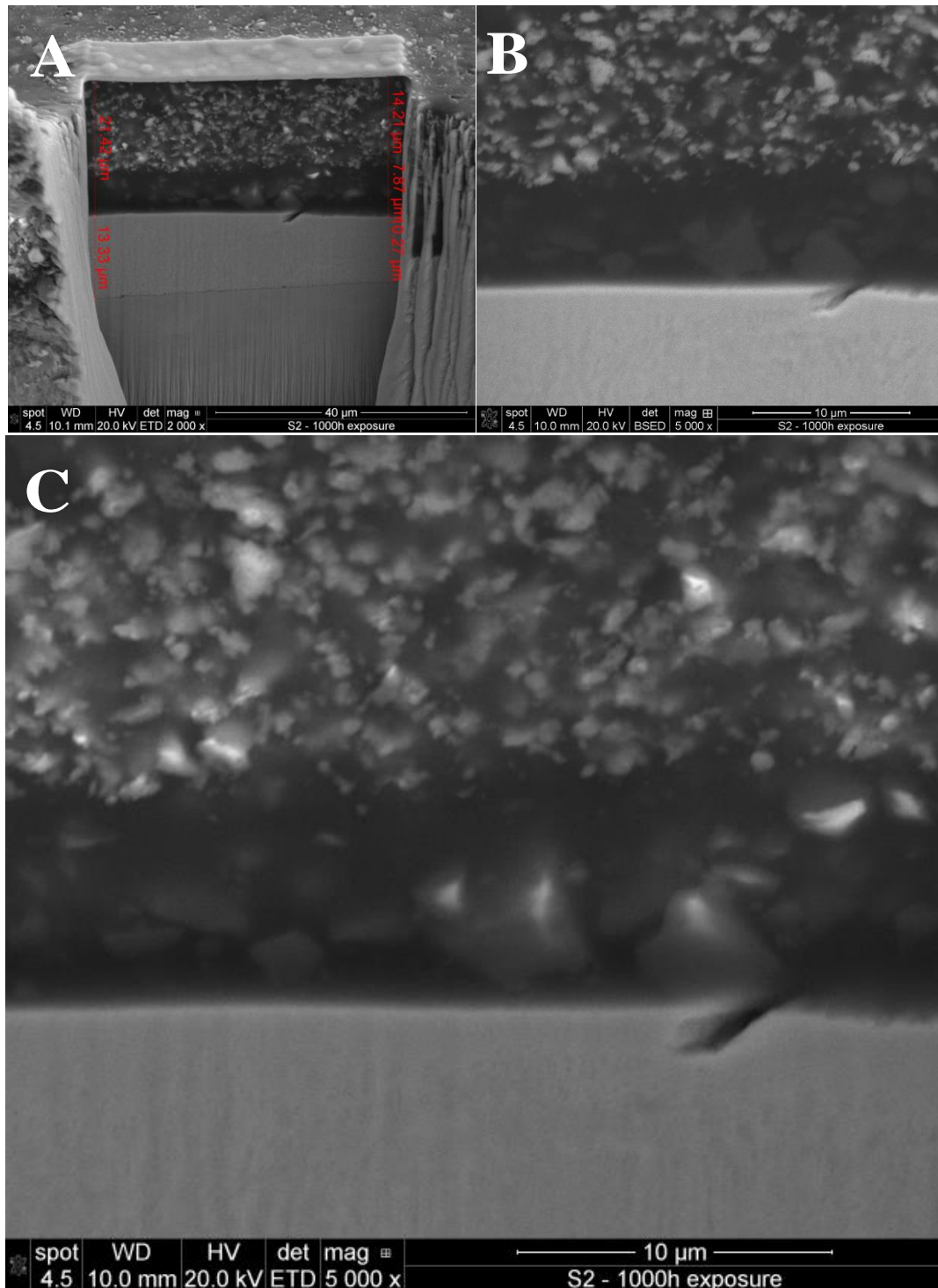


Figure 167. Secondary (a & c) & backscattered (b) electron SEM images of an exposed panel of system 4 submerged in a cell for 192 hrs. Cross-section of milled area (a), topcoat/ primer/ zinc area (b) and topcoat/ primer/ zinc area (c).

The results of submerging system 4 in a cell for 192 hours are shown in Fig. 167. Figure 167a shows the cross-sectioned area of the topcoat, pretreatment primer, zinc and steel. There is no sign of damage or corrosion product on top of the zinc layer. Figure 167b shows the cross-sectioned area in BSED imaging mode. It shows the topcoat, pretreatment primer and zinc layer. There is no sign of oxidation process in the zinc layer. Figure 169c shows the cross-sectioned area of topcoat, pretreatment primer and zinc in secondary electron imaging mode. No analysis were done on this sample due to poor sample interactions with EDS technique.

4.6.2.4.3. System 4 submerged in a cell for 408 hours.

The results of submerging system 4 in a cell for 408 hours are shown in Fig. 168. Figure 168a shows the cross-sectioned area of the topcoat, pretreatment primer, zinc and steel. At first inspection, there is no sign of deterioration at the pretreatment primer/ zinc layer. Further inspection reveals one corrosion product on top of the zinc layer.

Figure 168b shows the cross-sectioned area in BSED imaging mode. It shows the pretreatment primer and zinc layer, in between them is the corrosion product. The dark area represents the low atomic number (organic coating) and the lighter and brighter represents the high atomic element (zinc layer). The corrosion product colour is between the two colours and is not the same as calcium silicate pigment.

Figure 168c shows the cross-sectioned area of pretreatment primer and zinc in secondary electron imaging mode of Fig. 168b. It clearly shows there are corrosion products at the pretreatment primer/ zinc interface. Mapping of this area by EDS proved the imaging is correct.

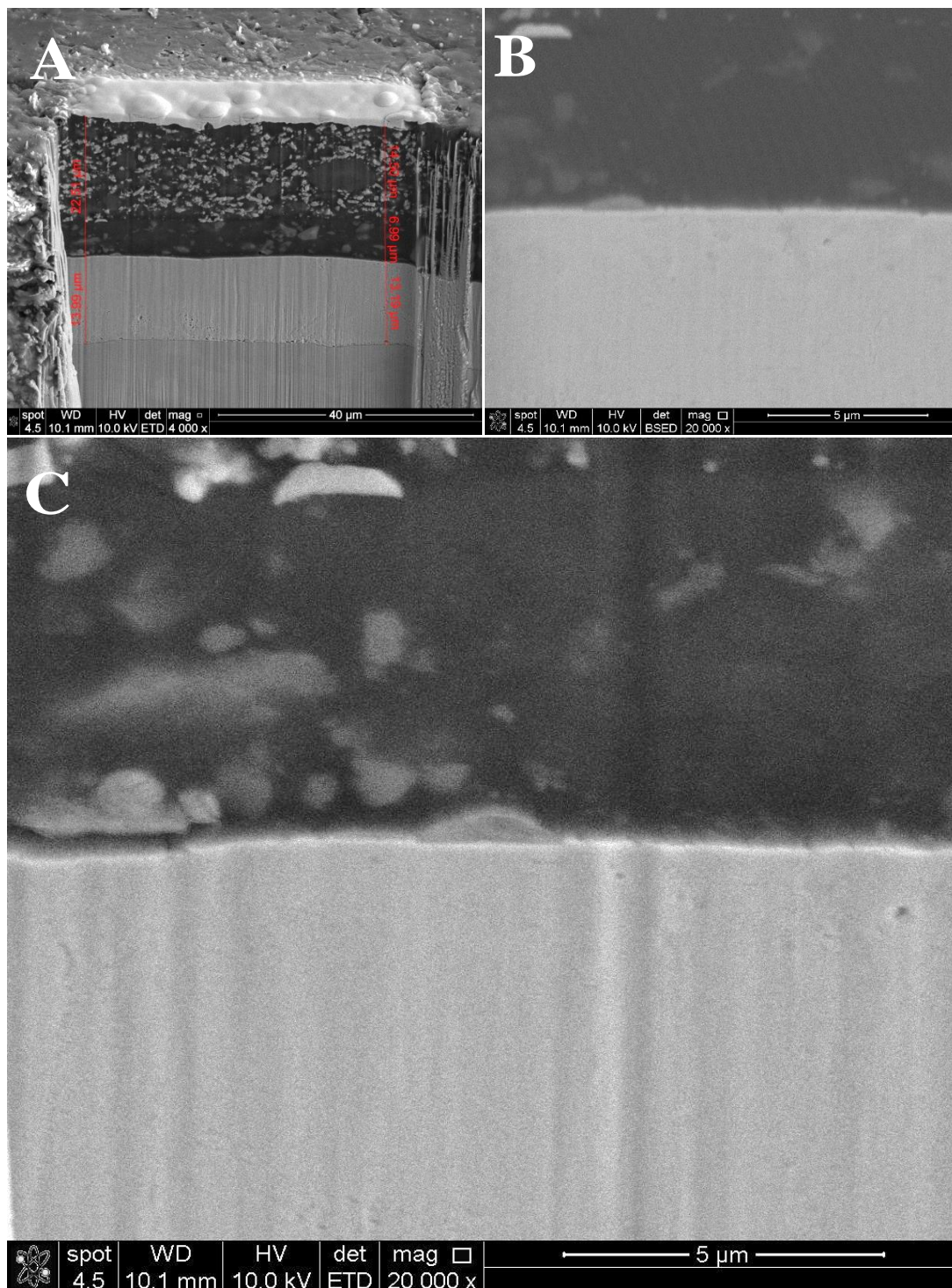


Figure 168. Secondary (A & C) & backscattered (B) electron SEM images of an exposed panel of system 4 submerged in a cell for 408hrs. Cross-section of milled area (A), primer/ zinc interface (B) and primer/ zinc interface (C).

Figure 169 shows the area that was analysed by EDS analysis and the results of the mapping (See Fig. 169a). The map shows the different elements found in that area and is represented by the various colours in that map. No chlorine is detected in the map. The other elements of Zn, C, Fe, O, Si and Al are there to represent the coating and substrate.

The mapping results of Fig. 168b are shown in spectrum 1. It shows that no chlorine was detected in that area. The coating and substrate are presented by the other elements found in the analysis.

EDS analysis were performed on a number of locations in Fig. 169. Only two interesting spectra will be shown. Spectrum 2 shows the present of 0.4% chlorine in the corrosion product. Spectrum 3 shows the present of 0.4% silicon and no calcium at the pretreatment primer/ zinc interface.

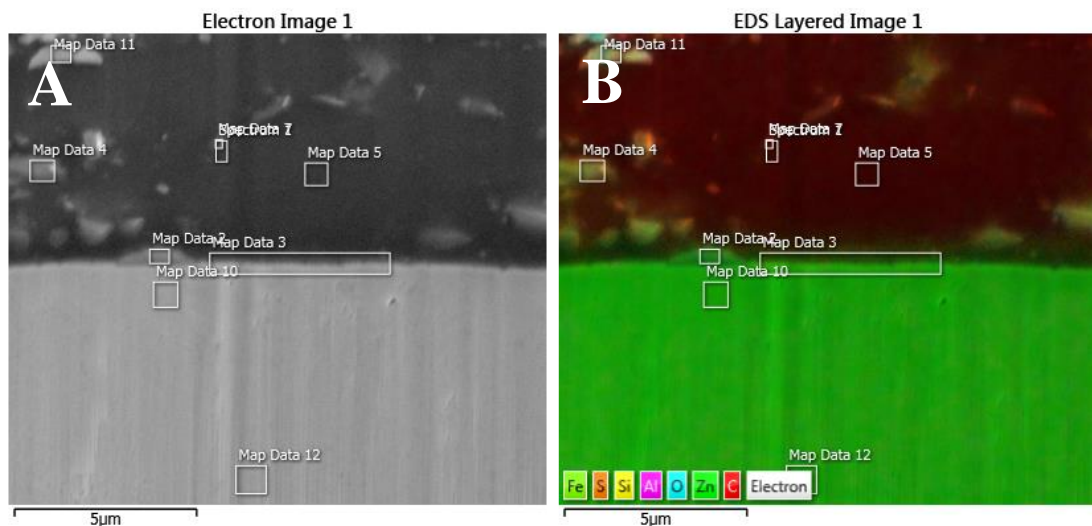


Figure 169. Secondary electron SEM image (A) and the results of EDS mapping (B) of that image.



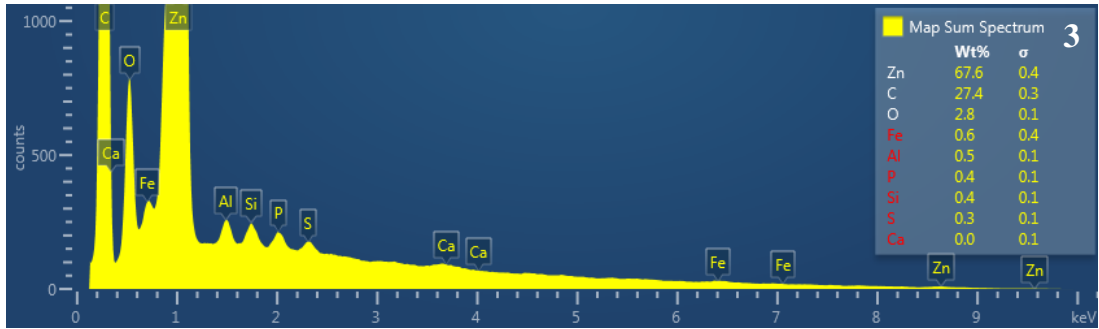
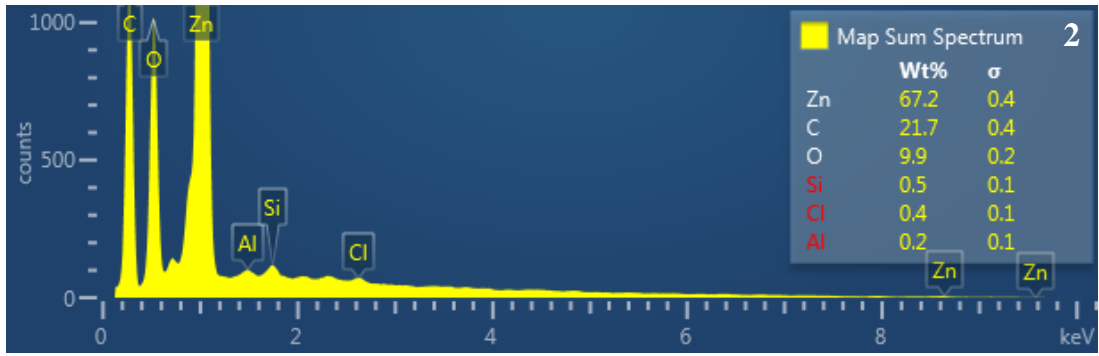


Figure 170. EDS spectra of maps 1, 2, and 3 from Fig. 169.

4.6.2.4.4. System 4 submerged in a cell for 1000 hours.

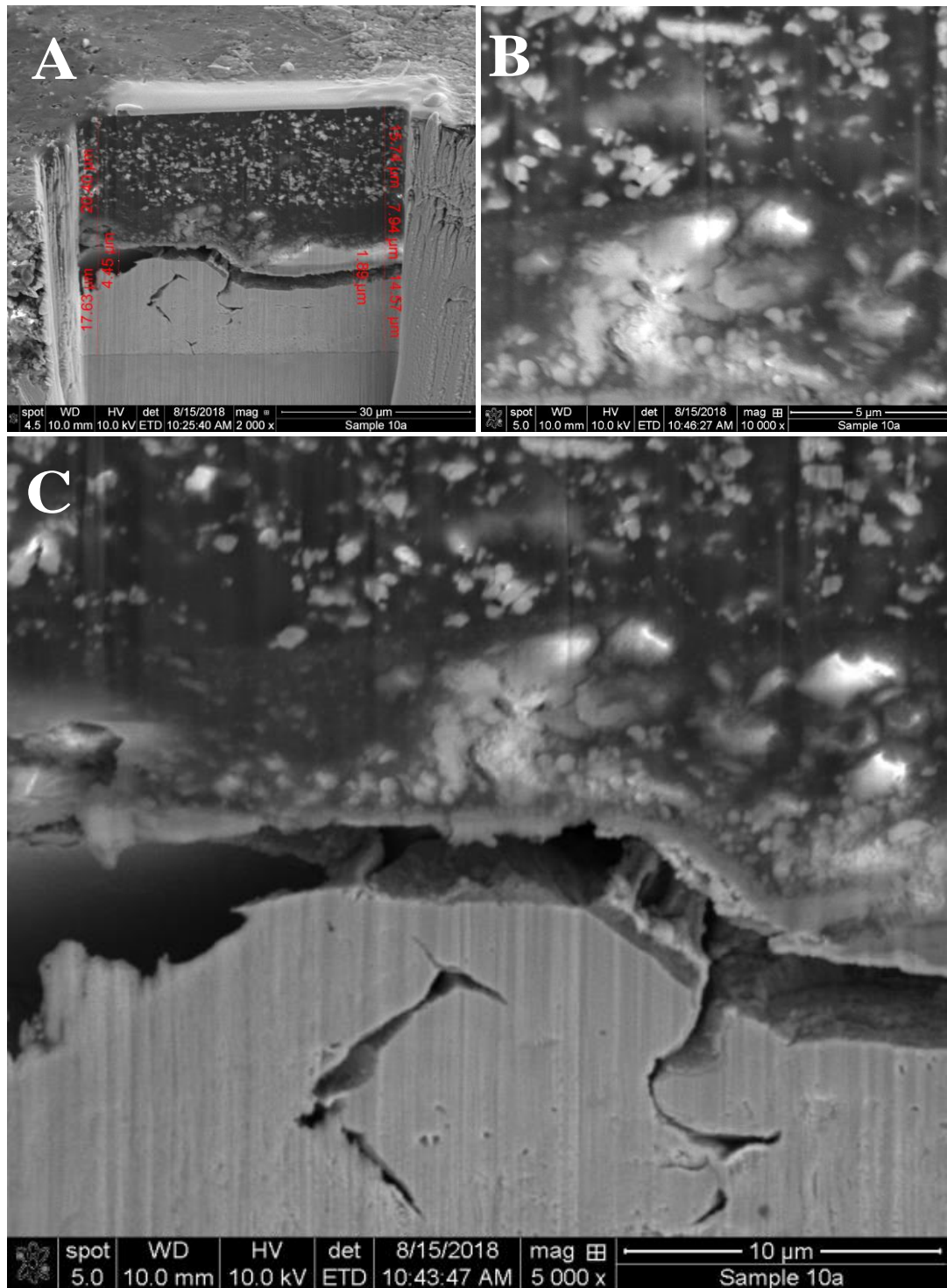


Figure 171. Secondary electron SEM images of an exposed panel of system 4 submerged in a cell for 1000 hrs. Cross-section of delaminated area (a), topcoat/primer interface (b) and delamination of zinc interface (c).

The results of submerging system 4 in a cell for 1000 hours are shown in Fig. 171. Figure 171a shows the secondary electron SEM image of the topcoat, pretreatment primer, zinc and steel cross-sectioned area. A separation of 2-5 μm depth is observed in the zinc layer. The other part of the zinc, the pretreatment primer is still adhered to the topcoat. Corrosion products are also in the pretreatment primer.

Figure 171b shows the secondary electron SEM image of the topcoat, and pretreatment primer. Due to the good quality of the image, a phase difference between the two coatings is revealed.

Figure 171c shows the higher magnification of the topcoat, pretreatment primer and zinc region than in Fig. 171a. It shows more in details of the zinc layer, separation in the zinc layer and corrosion products forming in the pretreatment primer.

Mapping and point & ID are used to analyse Figs. 171c and 173 and the results are shown in fig. 172 and 174.

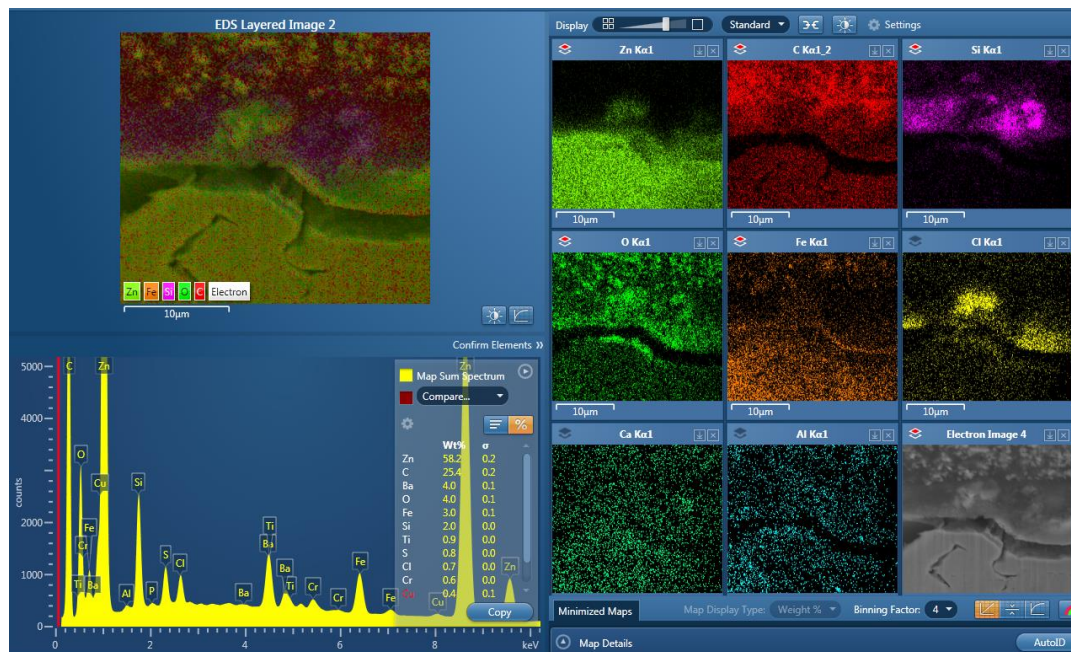


Figure 172. EDS mapping results of delaminated area.

The results of EDS mapping of Fig. 171c are shown in Fig. 172. In the figure, an elemental map is presented (top left) together with the elements (right) of that map represented by the different colours of that element. The coating is represented by element C, O, Si, and Ca. The substrate is represented by elements Zn, Fe, and Al. Not

all the elements are represented in the map, only elements that are important in revealing corrosion products. The corrosion products represented by element chlorine (yellow) and is found across the pretreatment primer and small amount in the zinc layer (See Fig.172). The spectrum shown at the bottom left of Fig.172 shows the quantity of each element that is detected. It detected 0.7% chlorine in the map.

Further EDS analysis of that region (See Fig. 173) was done by point & ID and the results are shown in spectrum 14. It shows the corrosion product contains 7.5% chlorine. The other elements are related to the coating and substrate.

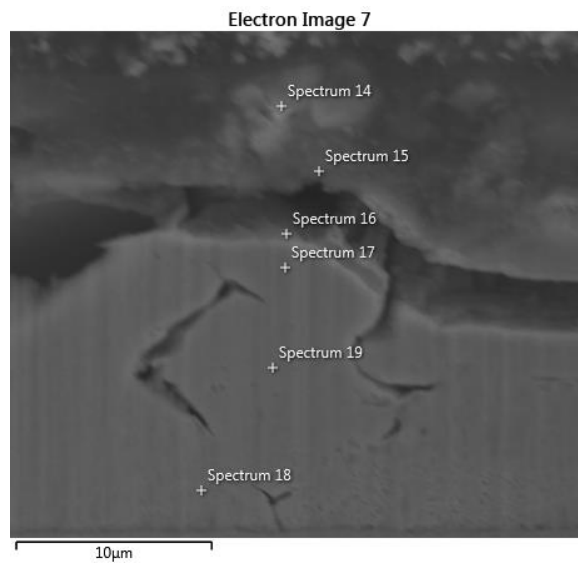


Figure 173. Secondary electron SEM image of delaminated area analysed by point and ID.



Figure 174. EDS spectrum of area 14 from Fig. 175.

4.6.2.4.5. Systems submerged in a cell up to 1000 hours.

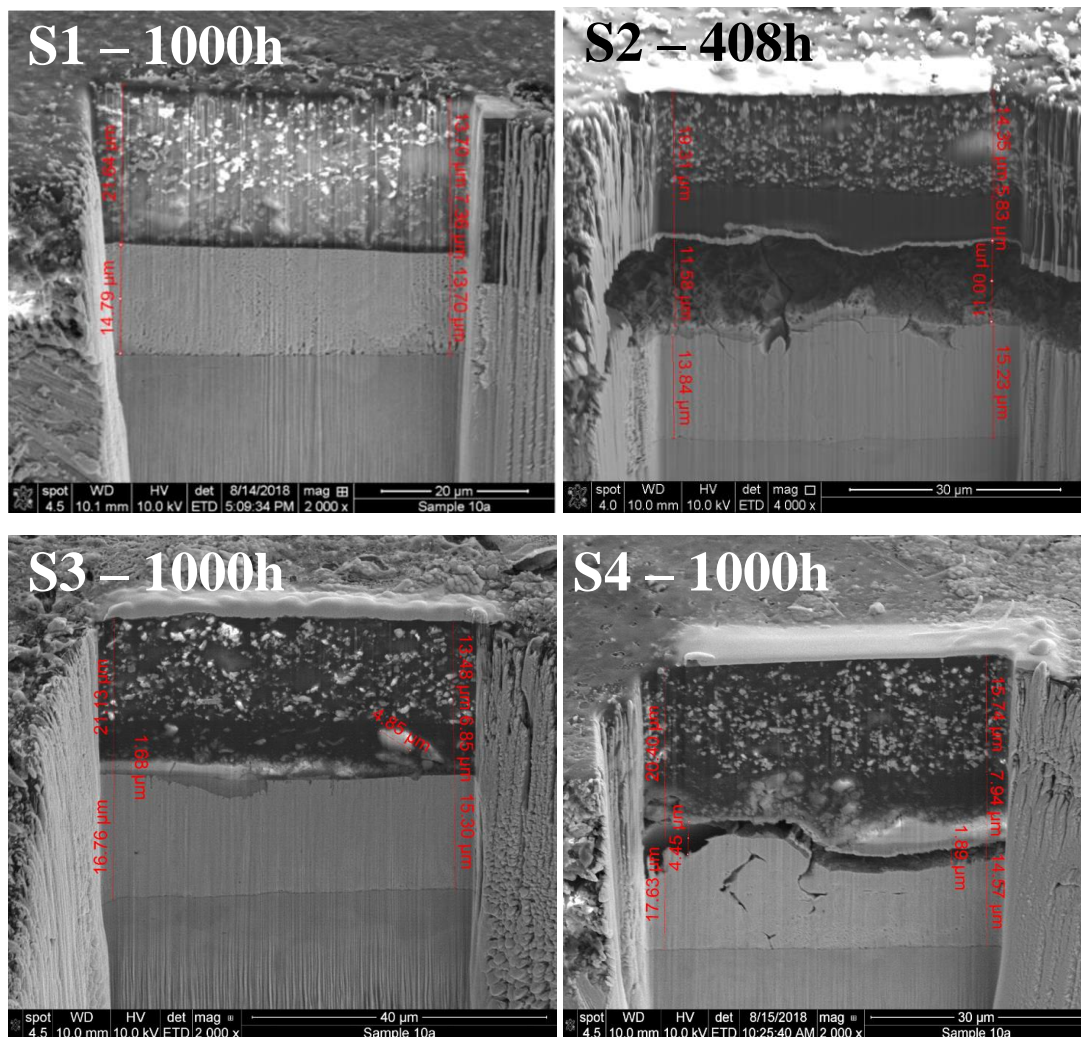


Figure 175. Secondary electron SEM images of exposed panel of systems 1 to 4.

The results of submerging the 4 systems in a cell are shown in Fig. 175. It shows that system 1 had no deterioration in the cross-sectioned areas after 1000 hours of exposure compared to the other 3 systems. System 2 is the worst and this can be seen after 408 hours exposure where the corrosion product has delaminated away from the zinc layer and the coating still adhered to the corroded area. Systems 3 and 4 started to corrode at 408 hours and deteriorated further after 1000 hours of exposure, with system 4 showing the worst performance out of the 2 systems. Delamination between the corrosion product and zinc layer can be seen in system 4, with the coating still adhered to the zinc. Also shown is the cracking in the zinc layer and this indicated that there was migration of ionic solution travelling through the coating into zinc and then to the steel.

4.7. Correlation of EIS and FIB/SEM data

4.7.1. Correlation of total impedance and corrosion products

A number of researchers have used impedance at 0.1Hz to show the total impedance of a coating [97] [125] [126], whereby a coating with $10^8 \Omega \text{ cm}^2$ or over impedance indicates no corrosion area is presented underneath the film. Between 10^6 and $10^8 \Omega \text{ cm}^2$ some corrosion is presence. Below $10^6 \Omega \text{ cm}^2$ represents a large area of corrosion products.

FIB/SEM images will be used to support the statements in the previous paragraph by showing what results were found when panels of different total impedance values, ranging from 10^4 to $10^8 \Omega \text{ cm}^2$ were cross-sectioned. The cross-sections were investigation on at least 2-3 samples, looking at 2 areas per sample so that it will be representative of that system under exposure.

4.7.1.1. Total impedance $>1 \times 10^8 \Omega \text{ cm}^2$ and the cross-sectioned area found.

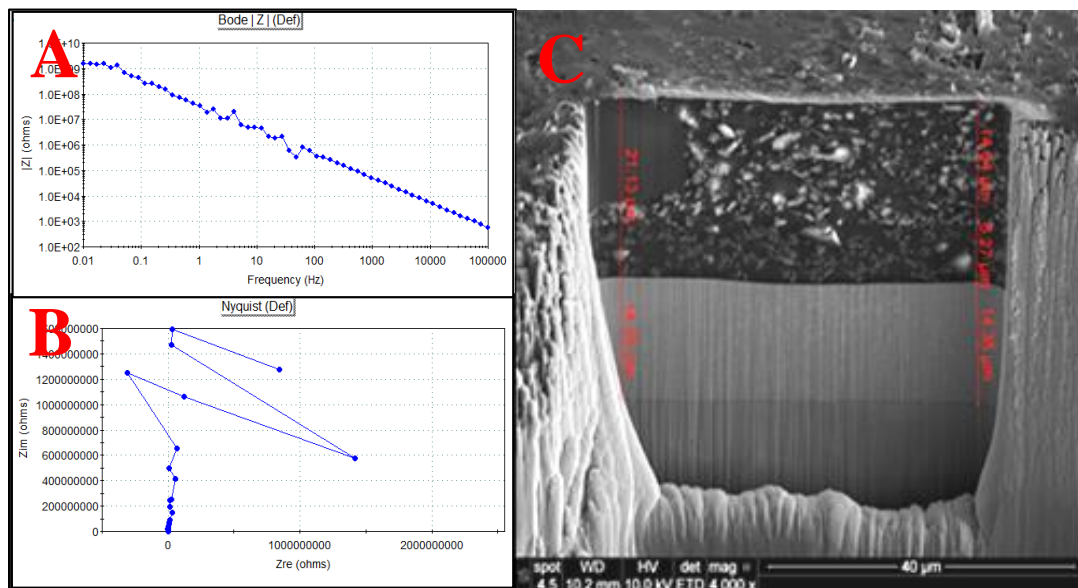


Figure 176. Bode impedance modulus (A) & Nyquist (B) plots of total impedance of $>1 \times 10^8 \Omega \text{ cm}^2$ and the cross-sectioned area observed for system 1 (C).

The result of total impedance greater than $1 \times 10^8 \Omega \text{ cm}^2$ is that no corrosion is seen in the cross-sectioned area of system 1 submerged in a cell for 1000 hours (See Fig. 176). The system is behaving as a leaky capacitor (b) with very high impedance

(a) and the result of this is good protection of the substrate with no sign of corrosion (c).

4.7.1.2. Total impedance $\sim 1 \times 10^7 \Omega \text{ cm}^2$ and the cross-sectioned area found.

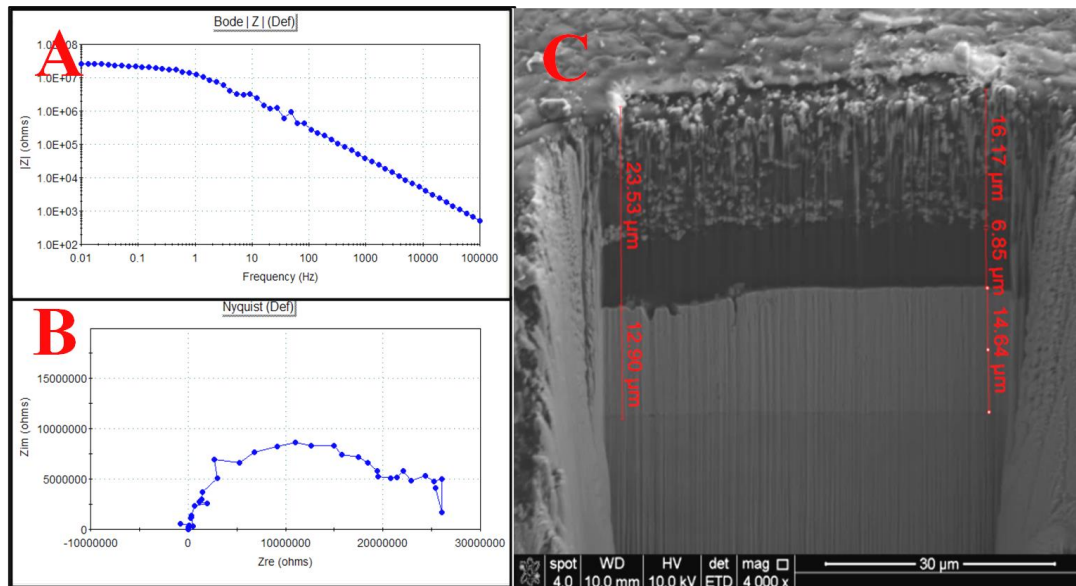


Figure 177. Bode impedance modulus (A) & Nyquist (B) plots of total impedance of $\sim 1 \times 10^7 \Omega \text{ cm}^2$ and the cross-sectioned area observed (C).

One or two corrosion products were found on top of the zinc layer for a total impedance of $\sim 1 \times 10^7 \Omega \text{ cm}^2$ (See Fig. 177). An example of this effect is found in system 2 submerged in a cell for 192 hours. The system has a high impedance value but allows electrolyte through to the metal surface, which reacts and forms corrosion product. This is supported by the second time constant found in the Nyquist plot, which is smaller in size than the first time constant represented by the coating.

4.7.1.3. Total impedance $\sim 1 \times 10^6 \Omega \text{ cm}^2$ and the cross-sectioned area found.

A few corrosion products were found on top of the zinc layer for a total impedance of $\sim 1 \times 10^6 \Omega \text{ cm}^2$ (See Fig. 178). An example of this effect is found in system 3 submerged in a cell for 408 hours. The system has a high impedance value but allows electrolyte through to the metal surface, which reacts and forms corrosion

product. This is supported by the second time constant found in the Nyquist plot, which is larger in size than the first time constant represented by the coating.

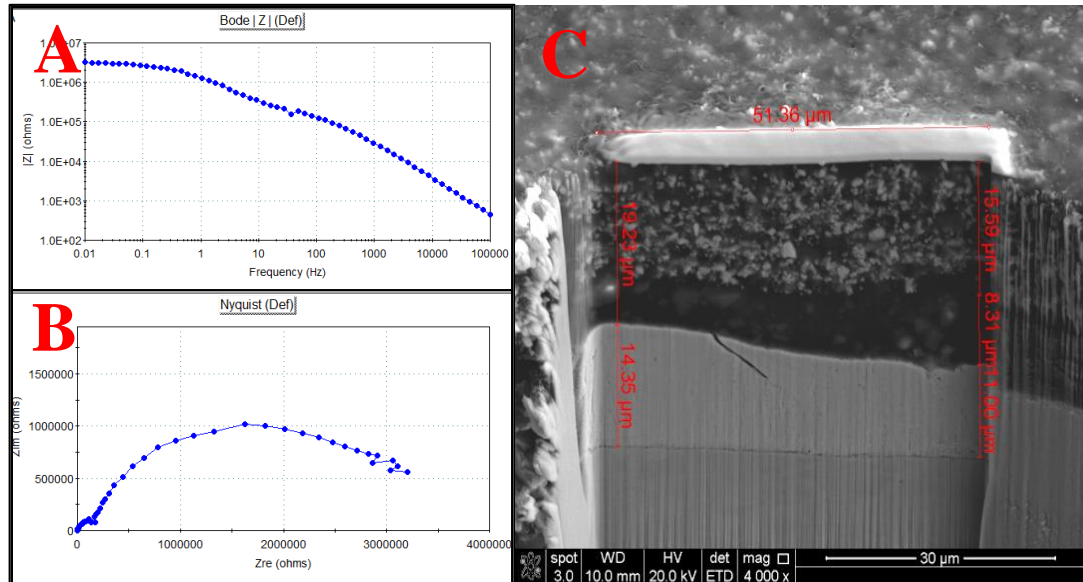


Figure 178. Modulus Bode (A) & Nyquist (B) plots of total impedance of $\sim 1 \times 10^6 \Omega \text{ cm}^2$ and the cross-sectioned area observed (C).

4.7.1.4. Total impedance $\sim 1 \times 10^5 \Omega \text{ cm}^2$ and the cross-sectioned area found.

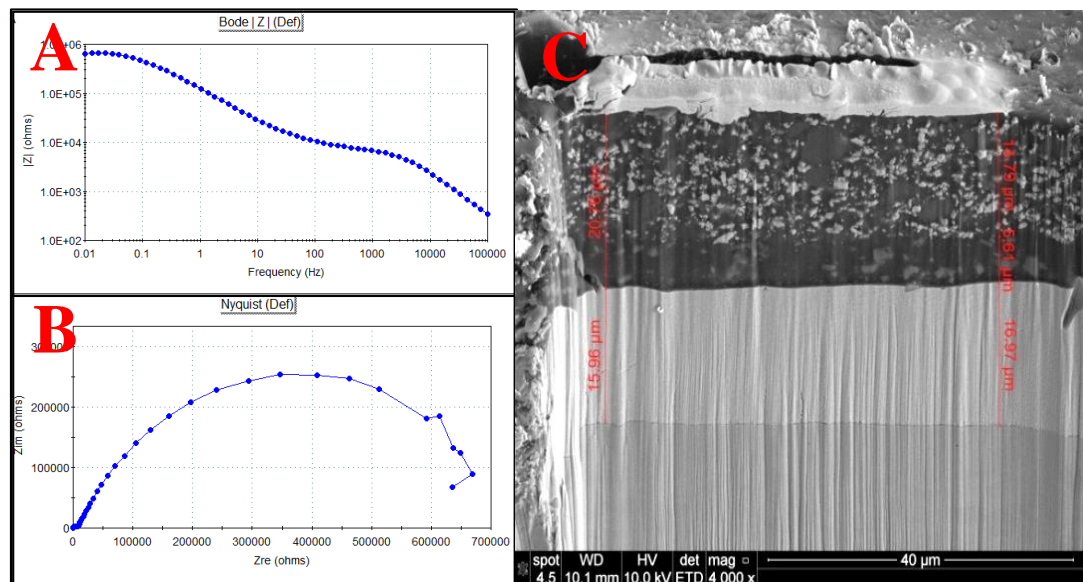


Figure 179. Modulus Bode (A) & Nyquist (B) plots of total impedance of $\sim 1 \times 10^5 \Omega \text{ cm}^2$ and the cross-sectioned area observed (C).

A few corrosion products were found on top of the zinc layer for a total impedance of around $\sim 1 \times 10^5 \Omega \text{ cm}^2$ (See Fig. 179). An example of this effect is found in system 3 submerged in a cell for 408 hours. The system has a medium impedance value but allows electrolyte through to the metal interface, which reacts and forms corrosion product. This is supported by the second time constant found in the Nyquist plot, which is larger in size than the first time constant represented the coating. Lower impedance value also supported this results.

4.7.1.5. Total impedance $\sim 1 \times 10^4 \Omega \text{ cm}^2$ and the cross-sectioned area found.

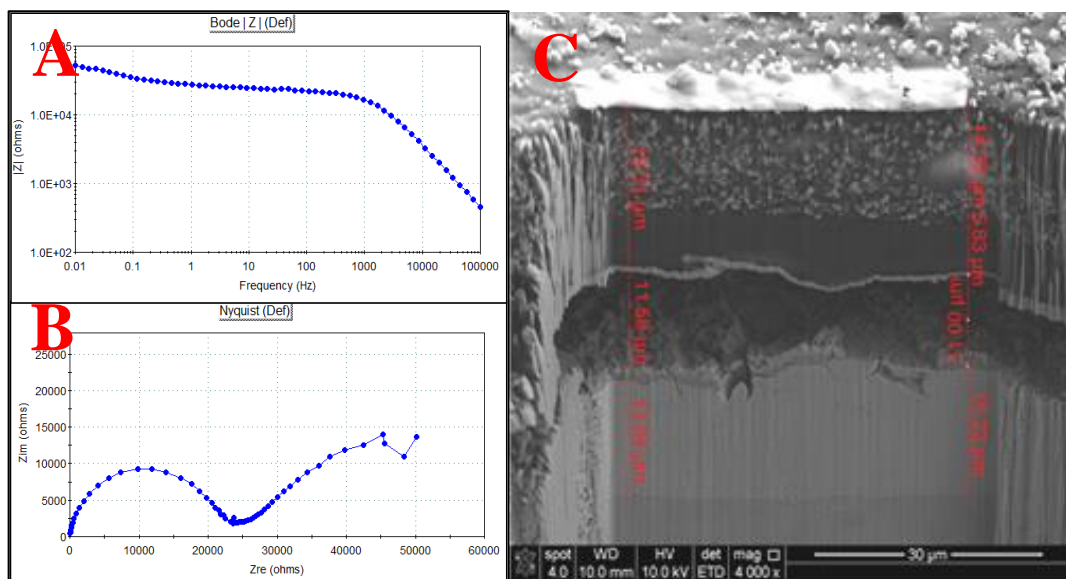


Figure 180. Modulus Bode (A) & Nyquist (B) plots of total impedance of $\sim 1 \times 10^4 \Omega \text{ cm}^2$ and the cross-sectioned area observed (C).

The breakup of corrosion products were found on top of the zinc layer for total impedance of $\sim 1 \times 10^4 \Omega \text{ cm}^2$ (See Fig. 180) An example of this effect is found in system 2 submerged in a cell for 408 hours. The system has a low impedance value and allows electrolyte through to the metal interface, which reacts and forms corrosion product. Over time, the corrosion product grows and delaminates.

Nyquist plot shows that there was corrosion products presence in the exposed sample represented by the formation of a second semi-circle but did not detect the breakup of corrosion products found in system 2. It may be that EIS only measured bulk area, not localised region. Whereas FIB/SEM could only analyse localised region

due to the time required to cross-section large area, in this case $\sim 50\ \mu\text{m}$ in length and $\sim 40\ \mu\text{m}$ in depth. However, the image from Fig. 181c shows further breakup of corrosion products at the cross-sectioned area walls.

Chapter 5. Conclusions and future work

5.1. Conclusions

This project successfully achieved the aims of acquiring the knowledge and understanding of the corrosion mechanisms of coil coated products that utilise a novel waterborne pretreatment using EIS and FIB/SEM. The key findings were:

- 1) Corrosion starts at defects in the zinc layer not necessarily at the zinc/ primer interface. Corrosion products were found to separate away from the zinc layer not from the coating as previously understood for blisters and delaminated coatings.
- 2) Blisters were observed at 408 hours, over 200 hours after the formation of corrosion products could be seen on the FIB/SEM.
- 3) FIB/SEM was found to correlate with EIS measurements and this supported other researchers who used total impedance values as an indication of corrosion products underneath the coating.
- 4) Development and optimisation of FIB/SEM was found to be a useful technique to study cross-sections of pre-painted metal. Information from secondary and backscattered electron images can reveal the quality of the coating (for example adhesion to substrate, pigment dispersion, interfacial properties etc.) and the thickness of the coating. Additionally it offers the ability to look at specific areas of interest such as defects, contamination and corroded areas. Elemental mapping using EDS measures the distribution and amount of elements within coatings.

Open circuit potential was used to monitor the electrical activity of the 4 systems tested over time. Most of the activities occurred between 0 and 240 hours, with the potential going either more negative or more positive. The potential generally stayed constant from 240 hours onward depending on which tests were used. In other accelerated tests, except for EIS cell, it was difficult to use OCP values to determine which systems were the best in corrosion protection.

Task 1: EIS was found to be precise and consistent in measuring electronic components with known values. The error of each component was less than 0.005%. Whereas in coatings the errors were high due to; the porosity of the materials, the

effect of test conditions such as electrolyte solutions, temperature and time. The EIS results for coatings were system and component dependent. Solvent-borne primer had the least percentage RSE compared to waterborne pretreatment primers. Film capacitance had a lower percentage RSE than film resistance and total impedance.

EIS measurements were used to characterise the performances of 4 systems tested in the cell, NSS, humidity and Bohus Malmö. The data were expressed as Bode impedance modulus and phase angles. The Nyquist plots were not used due to the difficulty in expressing different magnitudes of data on one scale.

In all of the systems, especially at the beginning of each experiment there were high levels of interference in the spectra at around 50 Hz. It was found that the spikes were caused by the coating. A good performing coating (system 1) gave rise to the spikes throughout the test period and a poor performing coating did not. Systems 2 to 4 represented this quite well, especially system 2 the spikes in the spectra decreased with increases in coating deterioration over time.

Task 2: ECMs were constructed for the 4 systems tested in different conditions. Different ECMs were used as the coatings deteriorated over time. The components of $Z_{0.1\text{Hz}}$, R_f and R_t are related to the resistance and decreased with time indicating decreases in corrosion protection. The components of X_o , C_f and C_d are related to capacitance and increased with time, indicating increased in water uptake in the coating and at the coating/ metal interface.

Cell exposures characterised by EIS showed that system 1 had the best performance with no corrosion, followed by systems 3 and 4 in that order and the worst was system 2. The total impedance and percentage water uptake supported this. The other individual components also supported these results and showed the importance of having anti-corrosive pigments in the coatings. Blistering was found to develop for systems 2 to 4. No blistering was observed in system 1, which was expected as there was no corrosion present. The blisters were observed at 408 hours, over 200 hours after corrosion product were detected by EIS and observed under FIB/SEM analysis.

NSS exposures characterised by EIS showed that all systems deteriorated over time. System 1 was the least affected by the test followed by system 3, system 4 and just slightly worse was system 2. Most of the deterioration started immediately and lasted until 408 hours after which the panels delivered reasonably constant in values. ECMs show that systems 2 to 4 had similar performance and the presence of an anti-corrosive pigment in the coating did not improve the results for systems 3 or 4. System 1 was the best with only a small amount of corrosion present. No blistering was found for system 1. The other 3 systems all had blisters on the exposed areas. Blistering started early for the un-pigmented system 2 at 48 hours. Systems 3 and 4 had anti-corrosive pigment in the coating which delayed the onset of blistering by about 200 hours. However, after 1000 hours they were all very bad, the only difference was the size of blisters formed.

Humidity exposures characterised by EIS showed that all systems deteriorated over time, not as severely as in NSS, but more than in the cell. System 1 was the least affected by the test followed by system 3, then system 4 and just slightly worse was system 2. After 24 hours of exposure the solvent-borne system could be distinguished from the 3 waterborne systems by comparing at the impedance moduli. Most of the deterioration started immediately and continued until 192 hours then it stayed reasonably constant to the end of the test.

ECM showed that systems 2 to 4 had similar performance and the presence of an anti-corrosive pigment in the coating did not improve the results for systems 3 or 4. System 1 was the best with small amount of corrosion present. No blistering was found for system 1. The other 3 systems, all had blisters on the exposed areas. Blisters were detected earlier for systems 2 and 4 at 240 hours. Blisters were observed for System 3 at 504 hours of exposure. However, after 1000 hours they had similar deterioration to each other systems.

The degree of blistering in the humidity test was not as severe as in the EIS cell. The worst blistering results were in the NSS chamber. The high salt content in NSS may be the influencing factor in producing blisters, not the test temperature. The humidity test used no salt whereas the other 2 tests (NSS and cell) used 29 g/l and 50

g/l sodium chloride solution respectively. The temperature of the humidity test was the highest at 40 °C, followed by 35 °C for NSS, and lowest was 21°C for the cells.

Task 3: Outdoor weathering exposures characterised by EIS show that all systems deteriorated over a 2 year period. North facing panels were generally worse than panels facing South. The only exception was system 1 for which panels facing North and South produced similar results. This might not be the case if the system was exposed for a longer period.

System 1 was the least affected by the exposure followed by systems 4, 3 in that order and the worst was system 2. The results show the importance of using anti-corrosive pigment in the coating. No pigment was used in system 2 and outdoor exposure results reflected this. Whereas accelerated testing did not show this, all three waterborne pretreatment primers were virtually the same. System 1 was the best with small amount of corrosion present. Some blisters were found for system 1 after 2 years. The other 3 systems all have blisters on the exposed areas, with system 2 being the worst. System 4 was only slightly better than system 3. They had blisters after one year and then had more blisters after the second year.

Task 4: FIB/SEM was used to observe the 4 systems submerged in cells for 1000 hours. EDS was used to analyse the areas of interest such as; defects, contamination and corroded areas. Initial assessment of unexposed systems showed that phase differences existed between solvent-borne topcoat and waterborne pretreatment primers, whereas between solvent-borne topcoat and primer there was no phase difference. Sometime it was difficult to see this effect due to the quality of SEM images produced. It can be related to how the samples interacted with the electron beam.

Task 5: SEM and BSED images of system 1 tested for 1000 hours show no sign of corrosion product at coating/ metal interface during the entire period of testing. When analysed by EDS small traces of chlorine were detected in the coating only. At the coating/ metal interface there was no sign of chlorine, only silicon which suggested that a barrier layer of silicate had formed there to inhibit the electrolytic activity and protect the metal.

In system 2, corrosion activity started early and after 192 hours, corrosion products were formed. When analysed by EDS, no chlorine was detected only elements of C, Zn, O, Fe, S and P. The corrosion product was distinguished from pure zinc using BSED images. Pure zinc was found to be brighter than zinc containing materials. This indicates that the corrosion products are either zinc oxide or zinc hydroxide. The other elements found may be from the surrounding materials in the coating.

After 408 hours of exposure, system 2 was severely deteriorated and when investigated at the edge of a blister, it was found that the coating was still adhered to the corrosion product even though the corrosion product had parted from the zinc layer. In the corroded areas crystal like structures were found and the width of these range between 85 and 250 nm. About 7% chlorine was detected in the corroded areas. Corrosion product was also observed in cross-sectioned area that had no blisters.

After 1000 hours of exposure, system 2 was severely blistered and even when investigated in an area of good appearance, corrosion product was found at the coating/metal interface. The crystal like structure size of the corrosion product ranged from few hundreds nanometres to 2.15 micrometres.

System 3 was better in protecting the steel from corrosion than system 2, but not by much. SEM and BSED images supported this whereby corrosion products were found after 192 hours, at the same time as system 2. However, the extent of the corrosion was not as severe as system 2. It may be due to the silicate layer forming at certain regions of the coating/metal interface. A trace of chloride was detected in the corrosion product.

System 3 only got worse after 1000 hours of exposure whereby corrosion product was observed along the entire coating/metal interface in the cross-sectioned area. There were blistered areas, but they were difficult to find and cross-section. Chlorine was detected in this region and the quantities range from 2 to 5%. Little deterioration was found between 192 and 408 hours.

System 4 was found to be slightly worse than system 3 and the results supported the EIS measurements made earlier. After 192 hours, no corrosion product

was found and this may be due to number of sectioned areas analysed. Corrosion product was found after 408 hours and a small amount of chlorine was detected. At the coating/ metal interface Si and Ca were detected indicating a silicate barrier layer.

After 1000 hours of exposure, system 4 had some blistered areas and when investigated further, the corrosion product was found to part from the zinc layer. The coating was still adhered to the corrosion product. 0.7% of chlorine was detected in the cross-sectioned area. 7.5% of chlorine was detected in the corrosion product.

Final task: FIB/SEM was found to correlate and support the work of many researchers they used the total impedance values to indicate the presence of corrosion underneath the coating. No corrosion was found for total impedance value of $>1 \times 10^8 \Omega \text{ cm}^2$. Small amount of corrosion products were found for impedance values between 10^6 and $10^8 \Omega \text{ cm}^2$. Some corrosion products were found for impedance values between 10^5 and $10^6 \Omega \text{ cm}^2$. Relative large areas of corrosion products were observed for total impedance $<10^5 \Omega \text{ cm}^2$. In the blistered area the corrosion product was found to depart away from the zinc layer, but the coating still adhered to the corrosion product.

Overall, the work has shown the value of EIS and NSS in predicting the performance of coating systems in BM-N facing natural exposure. It would appear that the parameter that indicates potential failure most regularly is the double layer interfacial capacitance.

The formulation of silicate layers containing calcium at the interface indicates that the anti-corrosive pigment is functioning as has been described in the literature and that failure will happen without its presence. The fact that blistering starts within the zinc corrosion produced not at the interface backs up recent published work.

5.2. Further work

1. FIB/SEM analysis through a blister and montage the different sections of the blister together.
2. FIB/SEM analysis of panels exposed in NSS, humidity and Bohus Malmö and correlate them with EIS results.
3. Expose more systems in the cell and BM-N so that prediction is accurate and consistent.
4. Investigate the effectiveness of different anti-corrosive pigments towards corrosion by EIS and FIB/SEM.
5. Monitor, investigate, and characterise the effect of changing the anti-corrosive pigments, surfactants, degree of cure, and manufacturing methods on the corrosion resistance of water-borne chromate free pretreatment primers.
6. Monitor, investigate, and characterise the corrosion resistance of different layers that make up a coil coating products. The steel, the pretreatment on the steel, the primer on the pretreated steel and the topcoat on the primed steel should be investigated.
7. Investigate how different steel substrates have an effect on the corrosion resistance of the coil coating products.
8. Investigate the effect of cleanliness of steel substrates and how this affects the corrosion resistance of waterborne pretreatment primer. Cleaning solution concentrations and process (time and temperature) conditions should be investigated.
9. The different coating systems should be exposed in humidity, prohesion, neutral salt spray and natural weathering in Sweden.
10. Electrochemical impedance spectroscopy and scanning Kelvin probe should be used to monitor, investigate and characterise the corrosion resistance of the different coating systems.
11. Investigate how film formation and degree of cure affect the barrier property of waterborne chromate free pretreatment primers. The focus should be on how the stoving process, water and pigment concentration affects film formation.

References

- [1] G. Schmitt, "Global needs for knowledge dissemination, research, and development in materials deterioration and corrosion control," World corrosion organization, 2009. [Online]. Available: http://www.corrosion.org/images_index/whitepaper.pdf. [Accessed 10 12 2012].
- [2] K. Trethewey, J. Chamberlain, Corrosion for science and engineering, 1995, pp. 75-81.
- [3] J. Sander, "1.6 Applications of precoated metal," in *Coil coating*, Hanover, Vincentz Network, 2014, pp. 22-24.
- [4] F. Pilati, M. Toselli, M. Mrssori, H. Van Dyk, S. G. Yeates, B. Petterson, N. Tuck, B. Storer, D. Howell, G. Raynaer, D. C. Barder, Volume IV waterborne & solvent based saturated polyesters and their end user applications, Wiley, 1999, pp. 579-580.
- [5] "The process - the most advanced method for coating metal," National coil coating association, 2012. [Online]. Available: <https://www.coilcoating.org/how-to-paint-metal-coils>. [Accessed 11 10 2013].
- [6] V. Saarimaa, E. Kauppinen, A. Markkula, J. Juhanoja, B-J. Skrifvars, and P. Steen, "Microscale distribution of Ti-based conversion layer on HDG steel," *Surface & coating technology*, vol. 206, pp. 4173-4179, 2012.
- [7] A. R. Marder, "The metallurgy of zinc-coated steel," *Progress in materials science*, vol. 45, pp. 191-271, 2000.
- [8] J. Sander, European coatings conference tutorial: the basics of coil and can coating, 2010.
- [9] "<http://www.steel-sheet-metal.com/manufacturing-process-of-hot-dipped-galvanized-steel-coil>," Rich ward group. [Online]. [Accessed 31 12 2017].
- [10] "www.whitfordww.com/industrial/app-coil.html," Whitford. [Online]. [Accessed 31 12 2017].
- [11] M. Dornbusch, M. Hickl, "Corrosion protection mechanism of chromate-free coil coating systems," *Finishing processes*, pp. 231-236, 2008.
- [12] Metal cladding and roof manufacturers association, UK, statistics, 1991.

- [13] P.A. Ryan, R.P. Wolstenholme, D.M. Howell, Durability of cladding; a state of the art Report, WS/Atkins, Thomas Telford, 1994.
- [14] W. Lee, "Chromate-free anti-corrosive primers-ten years on," *Becker industrial coatings 2009 magazine*, pp. 6-11, 2009.
- [15] J. Maxted, "Short term testing and real time exposure," *Journal of corrosion science and engineering*, vol. 2, 1999.
- [16] F. Deflorian, F. Michele, R. Stefanol, "Artificial versus natural weathering tests," *European coatings journal*, vol. 10, pp. 18-23, 2012.
- [17] L. L. Shreir, Corrosion, Elsevier B. V., 2010.
- [18] N. Perez, Electrochemistry and corrosion science, Springer, 2016.
- [19] B. E. Roetheli, G. L. Cox, and W. B. Littreal, "Metal alloys," vol. 3, pp. 73-76, 1932.
- [20] A. R. Marder, "The metallurgy of zinc-coated steel," *Progress in materials science*, vol. 45, pp. 191-271, 2000.
- [21] X. G. Zhang, "Corrosion," vol. 55, pp. 787-794, 1999.
- [22] X. G. Zhang, Corrosion and electrochemistry of zinc, New York: Plenum press, 1996.
- [23] T.E. Graedel, *Journal of electrochemical society*, vol. 136, p. 193, 1989.
- [24] A. Philipe, P.E. Schweitzer, Metallic materials: physical, mechanical, and corrosion properties, New York, USA: Marcel Dekker, 2003.
- [25] D.A. Jones, Principles and prevention of corrosion, New Jersey, USA: Prentice Hall, Upper Saddle River, 1996.
- [26] Y. Miyoshi, J. Oka and S. Maeda, *Translation of the iron and steel institute of Japan*, vol. 23, p. 974, 1983.
- [27] T. Falk, J. E. Svensson, and L. G. Johansson, *Journal of electrochemical society*, vol. 145, pp. 39-44, 1998.
- [28] R. Lindstrom, J. E. Svensson, and L.G. Johansson, *J. Electrochem. Soc.*, vol. 147, pp. 1751-1757, 2000.
- [29] I. Odneval and C. Leygraf, *Journal of electrochemical society*, vol. 138, pp. 1923-1928, 1991.
- [30] I. Odneval and C. Leygraf, *Corrosion science*, vol. 34, pp. 1213-1229, 1993.

- [31] I. Odnevall and C. Leygraf, *Corrosion science*, vol. 36, pp. 1551-1567, 1994.
- [32] R. G. Duarte, A. C. Bastos, A. S. Castela, M. G. S. Ferreira, "A comparative between Cr(VI) containing and Cr-free Films for coil coating systems," *Progress in organic coatings*, vol. 52, pp. 320-327, 2005.
- [33] C. Gabrielli, M. Keddam, F. Minouflet-Laurent, K. Ogle, H. Perrot, *Electrochimica Acta*, vol. 48, p. 965, 2003.
- [34] M. Kendig, A. J. Davenport, H. S. Isaacs, *Corrosion Science*, *Corrosion science*, vol. 41, p. 31, 1993.
- [35] "Background document for strontium chromate," ECHA, 29 11 2012. [Online]. Available: <http://echa.europa.eu/documents/10162/abc0fe7a-ded9-4e17-8c1d-aa2451e5c804>. [Accessed 1 12 2012].
- [36] S. Le Manchet, J. Landoulsi, C. Richard and D. Verchere, "Study of a chromium-free treatment on HDG Steel: electrochemical behaviour and performance in a saline medium," *Surface & coating technology*, vol. 205, pp. 475-482, 2010.
- [37] Becker industrial coatings.
- [38] Gnot, M. Zubielewicz and W., "Mechanisms of non-toxic anti-corrosive pigments in organic waterborne coatings," *Progress in organic coatings*, vol. 49, pp. 358-371, 2004.
- [39] C.R. Bacon, J.J. Smith and F.M. Rugg, "Electrolytic resistance in evaluating protective merit of coatings on metals," *Industrial & engineering chemistry research*, Vols. 40, No1, pp. 161-167, 1948.
- [40] E.M. Kinsella and J.E.O. Mayne, "Ionic conduction in polymer films: I. influence of electrolyte on resistance," *British polymer journal*, vol. 1, pp. 173-176, July 1969.
- [41] N. L. Thomas, "The barrier properties of paint coatings," *Progress of organic coating*, vol. 19, pp. 101-121, 1991.
- [42] D. Greenfield and D. Scantlebury, "The protective action of organic coatings on steel: A review," *Journal of structural and construction engineering*, 2000.
- [43] A.R. Filho, E.S. da Costa, *Journal of coating technology*, vol. 65, p. 67, 1993.
- [44] A.Z. Gad, H.A. Gomoa, *Journal of oil & colour chemists association*, vol. 2, p. 50, 1988.

- [45] L. Fedrizzi, F. Deflorian, G. Boni, P.L. Bonora, E. Pasini, "EIS study of environmentally friendly coil coating performances," *Progress in organic coatings*, vol. 29, pp. 89-96, 1996.
- [46] J. Sinko, "Challenges of chromate inhibitor pigments replacement in organic coatings," *Progress in organic coatings*, vol. 42, pp. 267-282, 2001.
- [47] Y. Liu, X. Zhou, S. B. Lyon, R. Emad, T. Hashimoto, A. Gholinia, G. E. Thompson, D. Graham, S. R. Gibbon, and D. Francis, "An organic coating pigmented with strontium aluminium polyphosphate for corrosion protection of zinc alloy coated steel," *Progress in organic coatings*, vol. 102, pp. 29-36, 2017.
- [48] S. C. Attwood, *Journal of oil & colour chemists association*, vol. 4, no. 75, p. 128, 1992.
- [49] M. Beland, *American paint & coatings journal*, vol. 76, p. 43, 1991.
- [50] G. Meyer, *Farbe Lack*, vol. 71, p. 508, 1965.
- [51] J. Vogelsang, in *European coatings conference*, Berlin, 2000.
- [52] W. Kozłowski, J. Flis, *Corrosion science*, vol. 8, no. 32, p. 861, 1991.
- [53] J. Ruf, *Farbe lack*, vol. 11, no. 101, p. 922, 1996.
- [54] A. Bittner, J. Ruf, *Polymer paint colour journal*, no. 187, p. 23, 1997.
- [55] A. Amirudin, C. Barreau, R. Hellouin, D. Thierry, *Progress in organic coatings*, no. 25, p. 339, 1995.
- [56] U. Rammelt, G. Rainhard, *Progress in organic coatings*, no. 24, p. 309, 1994.
- [57] C.H. Hare, *Journal of coating technology*, vol. 910, no. 79, p. 21, 2000.
- [58] B.P.E. Goldie, *Protection coating europe 8*, vol. 12, p. 26, 2001.
- [59] M. Deya, V.F. Vetere, R. Romagnoli, B. Del Amo, *Surface coating international part B 86*, vol. B1, p. 79, 2003.
- [60] B.P.F. Goldie, G.G. Othen, "Chemical inhibitors for corrosion control special publication No. 1," *Polymer science of chemistry*, p. 121, 1990.
- [61] C.H. Hare, *Modern paint & coatings*, vol. 7, p. 26, 1996.
- [62] B.P.F. Goldie, *Paint resin*, vol. 1, p. 16, 1985.

- [63] B.P.F. Goldie, *Journal of oil & colour chemists association*, vol. 9, no. 71, p. 257, 1998.
- [64] T. Flether, *Polymers paint colour journal*, vol. 182, p. 147, 1992.
- [65] "<https://grace.com/coatings-and-inks/en-us/anti-corrosion-pigments>," Grace. [Online]. [Accessed 03 01 2018].
- [66] *PRA Paint technology course 2002*, PRA.
- [67] "<http://www.industrialpaintquality.com/education/inthecan/vs02.html>," Paint quality institute. [Online]. [Accessed 03 01 2018].
- [68] PRA, "Principles of waterborne coatings," 2017.
- [69] P.A. Steward, *Advances colloid interface science*, pp. 195-267, 2000.
- [70] M. Barbour, J. Clarke, D. Fone, A. Hoggan, Volume 1 waterborne & solvent based acrylics and their end user application, SITA Technology Ltd., 1996.
- [71] N. A. Swartz, T. L. Clare, "Understanding the differences in film formation mechanisms of two comparable solvent based and waterborne coatings on bronze substrates by electrochemical impedance spectroscopy," *Electrochimica acta*, no. 62, pp. 199-206, 2012.
- [72] J. L. Keddie, P. Meredith, R. A. Jones, and A. M. Donald, "<http://pubs.acs.org/doi/pdf/10.1021/ma00112a012>," [Online]. [Accessed 31 12 2017].
- [73] R. Posner, K. Wapner, S. Amthor, K.J. Roschmann, G. Grundmeier, "Electrochemical investigation of the coating/substrate interface stability for styrene/acrylate copolymer films applied on iron," *Corrosion science*, vol. 52, pp. 37-44, 2010.
- [74] M. A. Winnik, "Latex film formation," *Current opinion in colloid & interface science*, vol. 2, no. 2, pp. 192-199, 1997.
- [75] S.S. Voyutskii, "Autohesion and adhesion of high polymers.," in *Polymer reviews vol 4*, Wiley-Interscience, 1963.
- [76] A. Turshatov, J. Adams, D. Johannsmann, *Macromolecules*, vol. 41, no. 5365, p. 14, 2008.
- [77] H. J. Butt, R. Kuroпка, B. Christensen, *Colloid polymer science*, vol. 272, p. 1218, 1994.

- [78] J. Zhang, S. Hu, J. Rieger, S. V. Roth, R. Gehrke, Y. Men, *Macromolecules*, vol. 41, p. 4353, 2008.
- [79] J.N. Yoo, L.H. Sperling, C.J. Glinka, A. Klein, *Macromolecules*, vol. 24, p. 2868, 1991.
- [80] B.J. Roulstone, M.C. Wilkinson, J. Hearn, *Polymer International*, vol. 27, p. 42, 1992.
- [81] "<http://polymerdatabase.com/polymer%20physics/GlassTransition.html>," [Online].
- [82] P.J. Gay, "Blistering of paint films metal," *Journal of oil & colour chemists association*, vol. 32, no. 352, pp. 488-498, 1949.
- [83] J.E.O Mayne, "The blistering of paint film. Part II blistering in the presence of corrosion.," *Journal of oil & colour chemists association*, vol. 31, no. 12, pp. 538-547, 1950.
- [84] "<https://www.linkedin.com/pulse/blistering-mehdi-mehdizadeh>," [Online]. [Accessed 31 12 2017].
- [85] W. Funke, "Toward a unified view of the mechanism responsible for the paint defects by metallic corrosion," *Industrial & engineering chemistry product research development*, vol. 24, no. 3, pp. 343-347, 1985.
- [86] L.A. van der Meer-Lerk and P.M. Heertjes, "Mathematical model of growth of blisters in varnish films on different substrates," *Journal of oil & colour chemists association*, vol. 62, pp. 256-263, 1979.
- [87] E.L. Koehler, "Underfilm corrosion currents as the cause of failure of protective organic coatings," *Corrosion control by organic coatings*, pp. 87-96, 1981.
- [88] W. Schwenk, "Adhesion loss for organic coatings causes and consequences for corrosion protection.," *Corrosion control by organic coatings*, pp. 103-110, 1981.
- [89] D. Greenfield and J.D. Scantlebury, "Blistering and delamination process on coated steel," *The journal of corrosion science and engineering*, vol. 2, p. 26, 2000.
- [90] "www.reddit.com/r/corrosion/comments/713noy/filiform_corrosion_on_a_painted_aluminium_sample/," [Online].
- [91] W. Furbeth and M. Stratmann, "The delamination of polymeric coatings from electrogalvanised steel - a mechanistic approach. Part 1: delamination from a defect with intact zinc layer," *Corrosion science*, no. 43, pp. 207-227, 2001.

- [92] "www.novasys.com.au/suppliers-a-h/ascott/," Novasys Group. [Online]. [Accessed 30 12 2017].
- [93] Sander, J., Coil coating, Vincentz Network, 2014, pp. 49-67.
- [94] "www.diazepamresource.com," [Online]. [Accessed 30 12 2017].
- [95] EG&G Prince Applied Research, *Application note AC-1 basic of electrochemical impedance spectroscopy (EIS)*, 1980.
- [96] G. W. Walter, "A review of impedance plot methods used for corrosion performance analysis of painted metals," *Corrosion science*, vol. 26, pp. 681-703, 1986.
- [97] M. O'Donoghue, R. Garrett, V. Datta, P. Roberts, T. Aben, "Electrochemical impedance spectroscopy: testing coatings for rapid immersion service," *Corrosion abstracts*, vol. 36, pp. 36-41, 2003.
- [98] Yu.N. Michailovskki, v.V. Leonov, N.D. Tomasky, *Kor. Met. Spanov*, vol. 201, 1965 .
- [99] M. Kendig, F. Mansfeld and S. Tsai, *Corrosion science*, vol. 23, p. 317, 1983.
- [100] D. M. Brasher, A.H. Kingsbury, *Journal of applied chemistry*, vol. 4, no. 2, p. 62, 1954.
- [101] "[https://en.wikipedia.org/wiki/Double_layer_\(surface_science\)](https://en.wikipedia.org/wiki/Double_layer_(surface_science))," [Online]. [Accessed 29 1 2018].
- [102] J. N. Murray, L. D. Stephenson and A. Kumar, "Electrochemical and physical evaluations of coil coatings on metal-coated steels for roofing applications," *Progress in organic coatings* , vol. 47, pp. 136-146, 2003.
- [103] E. D. Schachinger, R. Braidt, B. Strauss, A. W. Hassel, "EIS study of blister formation on coated galvanised steel in oxidising alkaline solutions," *Corrosion science*, vol. 96, pp. 6-13, 2016.
- [104] M. Delucchi, A. Barbucci and G. Cerisola, "Optimisation of coil coating systems by means of EIS," *Electrochimica Acta* 44, pp. 4297-4305, 1999.
- [105] J. W. Martin, S. C. Saunders, F. L. Floyd, J. P. Wineburg, "Methodologies for predicting the service lives of coating systems," *NIST building science series*, vol. 172, pp. 39-48, 1989.
- [106] T. Prosek, A. Nazarov, U. Bexell, D. Thierry, J. Serak, "Corrosion mechanism of model zinc-magnesium alloys in atmosphere conditions," *Corrosion science*, vol. 50, pp. 2216-2231, 2008.

- [107] A.C. Bastos, C. Ostwald, L. Engl, G. Grundmeier, A.M. Simoes, "Formability of organic coatings - an electrochemical approach," *Electrochimica acta* 49, pp. 3947-3955, 2004.
- [108] J. Goldstein, et al., "Scanning electron microscopy and X-ray microanalysis," *Springer science + business media, New York*, pp. 1-20, 2003.
- [109] "SEM A to Z - Basic knowledge for using The SEM," [Online]. Available: http://www.jeolusa.com/DesktopModules/Bring2mind/DMX/Download.aspx?Command=Core_Download&EntryId=598&PortalId=2&TabId=320. [Accessed 5 February 2015].
- [110] "www.intechopen.com," [Online]. [Accessed 30 12 2017].
- [111] "www.ammrf.org.au/myscope/analysis/eds/xraygeneration/," [Online]. [Accessed 30 12 2017].
- [112] R. Levi-Setti, "Proton scanning microscopy: feasibility and promise scanning electron microscopy," *Scanning electron microscopy*, vol. 125, pp. 125-134, 1974.
- [113] J. Goldstein, et al., "Scanning electron microscopy and X-ray microanalysis," New York, Springer science and business media, 2003.
- [114] L. A. Giannuzzi and F. A. Stevie, "Introduction to focused ion beams," *Instrumentation, theory, techniques and practice, Springer science + business media*, pp. 107-132, 2010.
- [115] N. P. Picard, et al, "Focused ion beam-shaped microtools for ultra-precision machining of cylindrical components," *Precision engineering*, vol. 27, no. 1, pp. 59-69, 2003.
- [116] H.W. Sun, et al, "Optimization and experimentation of nanoimprint lithography based on FIB fabricated stamp," *Microelectronic engineering*, vol. 82, no. 2, pp. 175-179, 2005.
- [117] W. Brostow, B.P. Gorman, O. Olea-Mejia, "Focused ion beam milling and scanning electron microscopy characterization of polymer + metal hybrids," *Materials letters*, vol. 61, no. 6, pp. 1333-1336, 2007.
- [118] "www.ifw-dresden.de," [Online]. [Accessed 30 12 2017].
- [119] J. Li, et al., "Recent advances in FIB-TEM specimen preparation techniques," *Materials characterization*, vol. 57, no. 1, pp. 64-70, 2006.

- [120] S. Zanini, et al, "Surface properties of HMDSO plasma treated polyethylene terephthalate," *Surface and coatings technology*, vol. 200, no. 1, pp. 953-957, 2005.
- [121] R.J. Bailey, et al., "Evaluating focused ion beam induced damage in soft materials," *Micron*, vol. 50, pp. 51-56, 2013.
- [122] S. Brunner, et al, "Investigation or multilayered aluminum coates polymer laminates by focused ion beam (FIB) etching," *Surfure and coatings technology*, vol. 200, pp. 5908-5914, 2006.
- [123] F. Mansfeld, "Recording and analysis of AC impedance data for corrosion studies," *Nationl association of corrosion engineers*, vol. 36, no. 5, pp. 301-307, 1981.
- [124] V.S. Bonitz, "Random and systematic error as a function of sample area in electrochemical impedance spectroscopy," *Progress in organic coatings*, vol. 77, pp. 2100-2106, 2014.
- [125] J.R. Scully, *Journal of electrochemical society*, vol. 136, p. 979, 1989.
- [126] A.R. Di Sarli, E.E. Schwiderke and J.J. Podesta, "Proceedings of the 10th international congress on metallic corrosion," Madras, 1987.
- [127] S.Z. Abdullah, P. R. Berube and D. J. Horne, "SEM imaging of membranes: Importance of sample preparation and imaging parameters," *Journal of membrane science*, vol. 463, pp. 113-125, 2014.
- [128] E. Huttunen-Saarivirta, V.E. Yudin, L.A. Myagkova and V.M. Svetlichnyi, "Corrosion protection of galvanised steel by polyimide coatings: EIS and SEM investigations," *Progress in organic coatings*, vol. 72, pp. 269-278, 2011.
- [129] M. Akbarian, ME. Olya, M. Mahdavian and M. Ataefard, "Effects of nanoparticulate silver on the corrosion protection performance of polyurethane coatings on mild steel in sodium chloride solution," *Progress in organic coatings*, vol. 77, no. 8, pp. 1233-1240, 2014.
- [130] H. Vakilli, B. Ramezanzadeh and R. Amini, "The corrosion performance and adhesion properties of the epoxy coating applied on the steel substrates treated by cerium-based conversion coatings," *Corrosion science*, vol. 94, pp. 466-475, 2015.
- [131] M. Huang, H. Zhang and J. Yang, "Synthesis of organic silane microcapsules for self-healing corrosion resistant polymer coatings," *Corrosion science*, vol. 65, pp. 561-566, 2012.

- [132] O. Lunder, C. Simensen, Y. Yu and K. Nisancioglu, "Formation and characterisation of Ti-Zr based conversion layers on AA6060 aluminium," *Surface and coatings technology*, vol. 184, no. 2, pp. 278-290, 2004.
- [133] J.H. Nordlien et al, "Formation of a zirconium-titanium based conversion layer on AA 6060 aluminium," *Surface and coatings technology*, vol. 153, no. 1, pp. 72-78, 2002.
- [134] C. Le Pen, C. Lacabanne, N. Pebere, "Characterisation of waterbased coatings by electrochemical impedance spectroscopy," *Progress in organic coatings*, no. 46, pp. 77-83, 2003.
- [135] "www.substech.com," [Online]. [Accessed 30 12 2017].
- [136] [Online]. Available: <http://www.statstutor.ac.uk/resources/uploaded/spearmans.pdf>. [Accessed 24 August 2018].
- [137] [Online]. Available: <https://www.york.ac.uk/depts/maths/tables/spearman.pdf>. [Accessed 24 August 2018].
- [138] [Online]. Available: <http://www.real-statistics.com/statistics-tables/pearsons-correlation-table/>. [Accessed 24 August 2018].
- [139] [Online]. Available: <https://caspar.bgsu.edu/~courses/Ethology/Labs/Habituation/SpearmanRhoTable.pdf>. [Accessed 24 August 2018].
- [140] E.B. Bradford, *Journal of colloid science*, vol. 6, p. 108, 1957.
- [141] A. Burkil, *Journal oil & colour chemists association*, no. 81, p. 274, 1998.
- [142] G. L. Brown, "Formation of films from polymer dispersions," *Journal of polymer science*, vol. 22, p. 423, 1956.
- [143] A. Belghazi, S. Bohm, J.H. Sullivan, D.A. Worsley, "Zinc runoff from organically coated galvanised architectural steel," *Corrosion science* 44, vol. 8, pp. 1639-1653, 2002.
- [144] A. D. Zeeuw, M. Roth and J. Sander, "Chromium-free, thermally curable corrosion protection composition". U.S. Patent 20090214883a1, 27 August 2009.
- [145] Fischer instrumentation LTD, *Fischerscope multi 650/750 C manual*, 1988.
- [146] R.A. Dickie, A.G. Smith, "How paint arrests rusts," *Chemtech*, pp. 31-35, 1980.

- [147] "Member section - statistics 2008," European coil coatings association, 2013. [Online]. Available: http://www.prepaintedmetal.eu/members_section/members/statistics. [Accessed 10 1 2014].
- [148] J. Kawafuku, J. Katoh, M. Toyama, K. Iikeda, H. Nishimoto, H. Sato, "Properties of zinc alloy coated steel sheets obtained by continuous vapour deposition pilotline," in *Proceedings of the 5th automotive corrosion & prevention conference on Oct 21-23, MI, U.S., 1991*.
- [149] "Thermax 10 level strips," TMC Hallcrest, 2008. [Online]. Available: http://www.tmchallcrest.com/industrial.php?switch=TMC_Hallcrest&medical_product=68&sublvl_id=5&subcat_id=6&cat_id=68. [Accessed 5 2 2014].
- [150] A. Komatsu, T. Tsujimura, K. Watanabe, N. Yamaki, and A. Andoh and T. Kittaka , "Hot dip Zn-Al-Mg coated steel sheet excellent in corrosion resistance and surface appearance and the process for the production thereof". Patent EP0905270, Nisshin steel corporation 1999.
- [151] W. R. G. & Co., "<https://grace.com/coatings-and-inks/en-us/Documents/SHIELDEX%20Brochure%20-%20English.pdf>," W. R. Grace & Co., 2013. [Online].

Word count

Chapter 1 (Introduction) = 1829

Chapter 2 (Literature review) = 12712

Chapter 3 (Methodology) = 3472

Chapter 4 (Results & discussions) = 19347

Chapter 5 (Conclusions and future work) = 2417

Total word count = 39777

Appendix I – Supplementary information to chapter 4.6.1.

1. Unexposed panels of the 4 systems

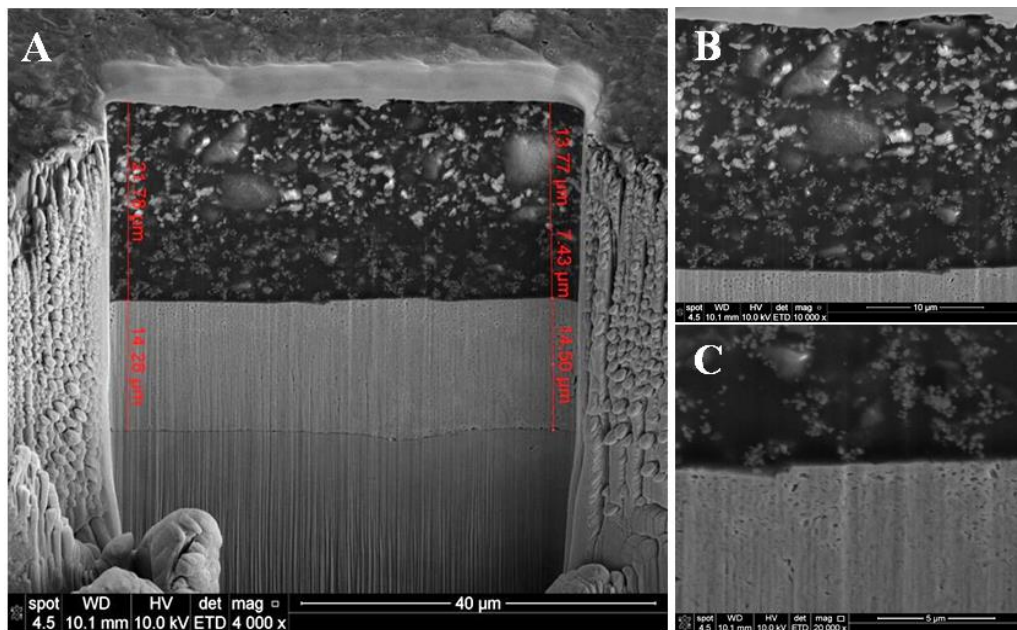


Figure 181. Secondary electron SEM images of an unexposed panel of system 1, area 2. Cross-section area (a), topcoat/ primer/ zinc area (b) and primer/ zinc area (c).

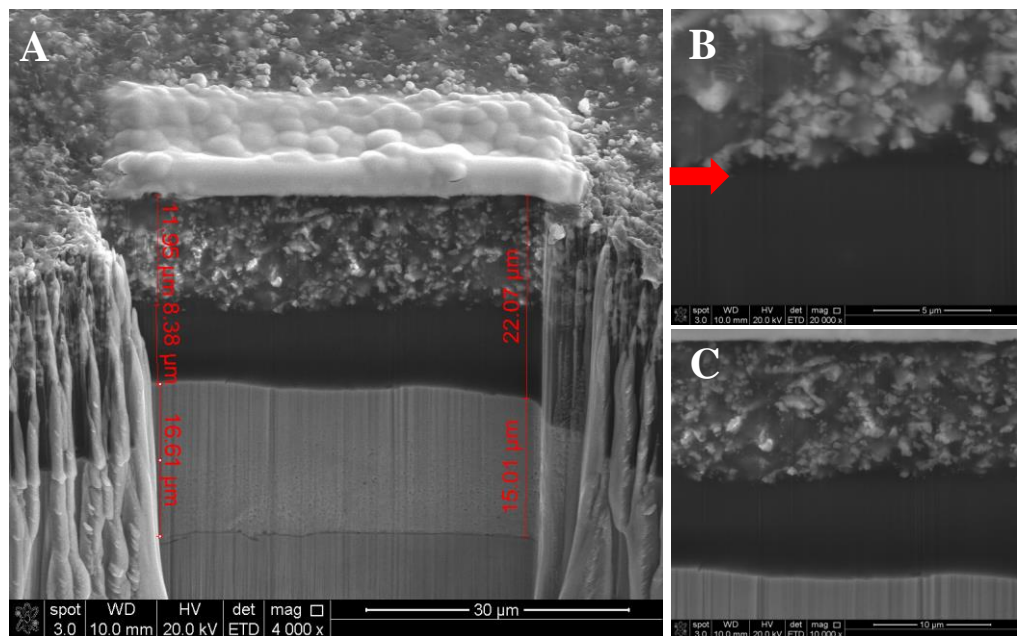


Figure 182. Secondary electron SEM images of an unexposed panel of system 2. Cross-section area (a) , topcoat/ primer/ zinc area (b) and primer/ zinc area (c). A red arrow represents the phase difference between topcoat and primer.

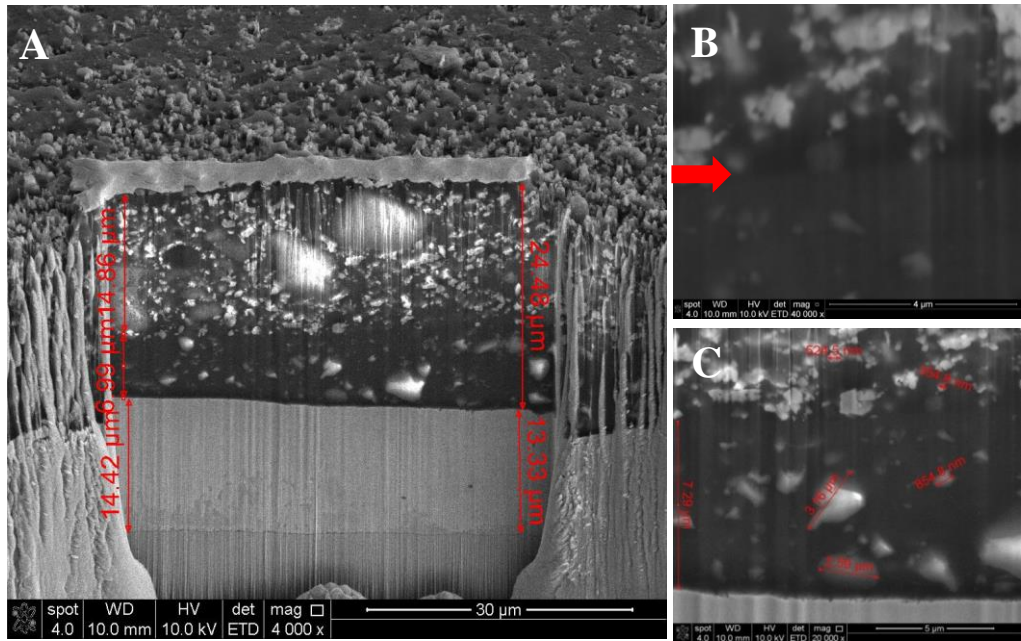


Figure 183. Secondary electron & back scattered electron SEM images of an unexposed panel of system 3, area1. Cross-section area (a), topcoat/ primer/ zinc area (b) and primer/ zinc area (c). A red arrow represents the phase difference between topcoat and primer.

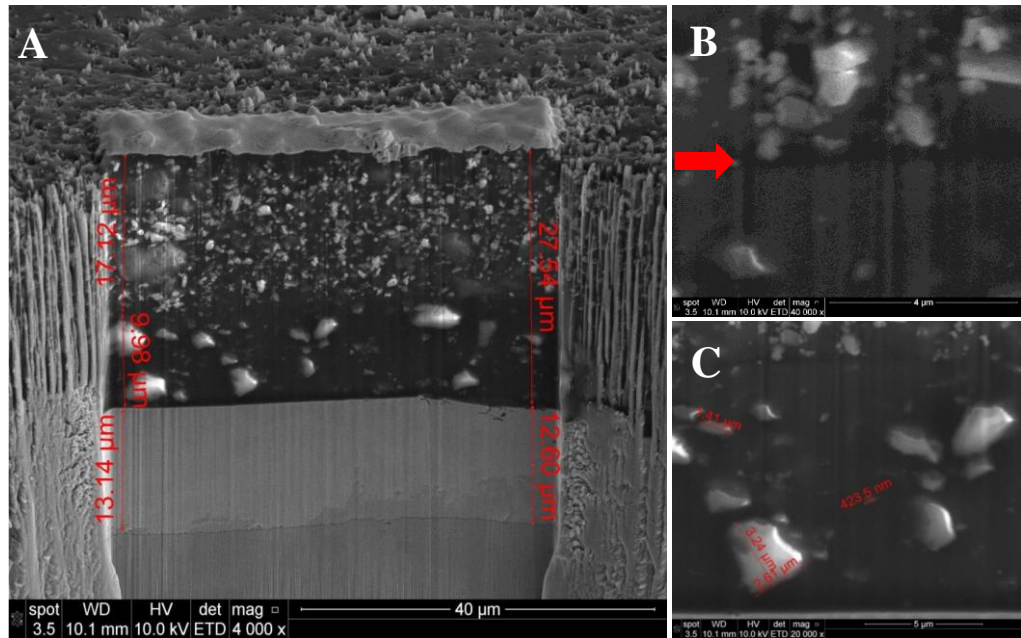


Figure 184. Secondary electron SEM images of an unexposed panel of system 4, area 1. Cross-section area (a), topcoat/ primer/ zinc interface (b) and primer/ zinc interface (c). Red arrow pointing towards the phase difference between topcoat and primer.

Appendix II – Supplementary information to chapter 4.6.2.

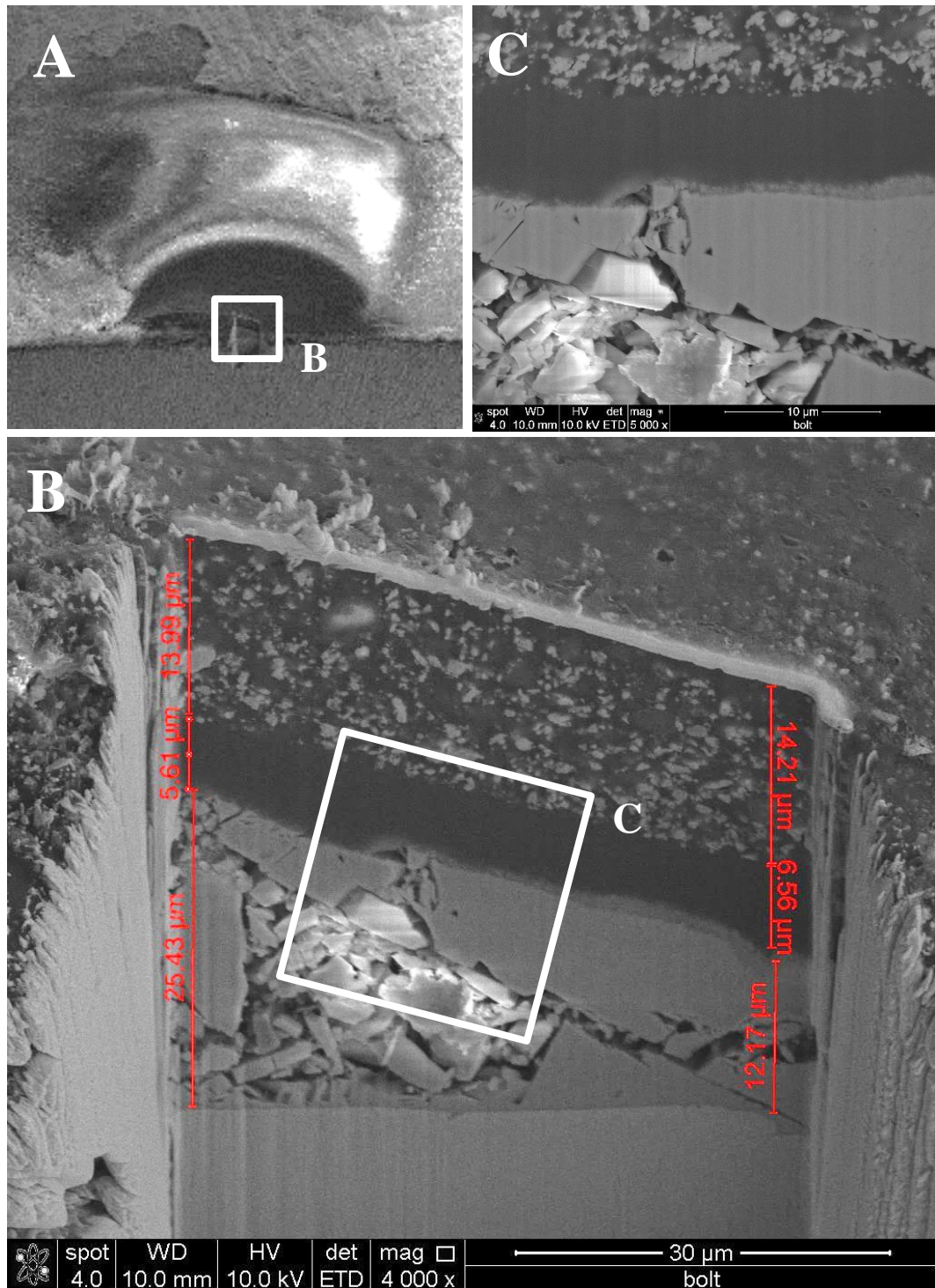


Figure 185. Secondary electron images of an exposed panel of system 2 submerged in a cell for 408 hours. A blister in the centre of image (a), cross-section of a blister in A (b) and zoom in corroded area in B (c).

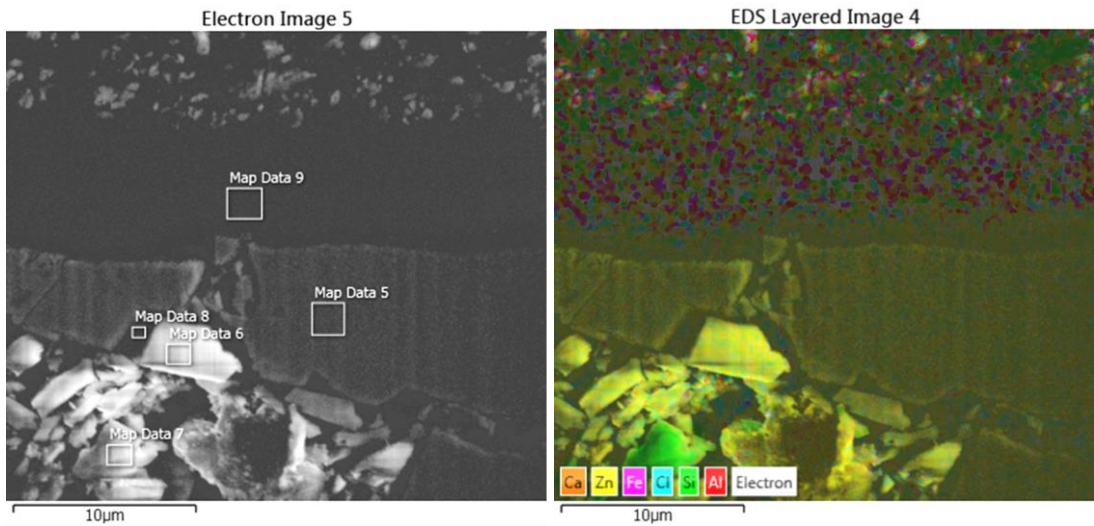
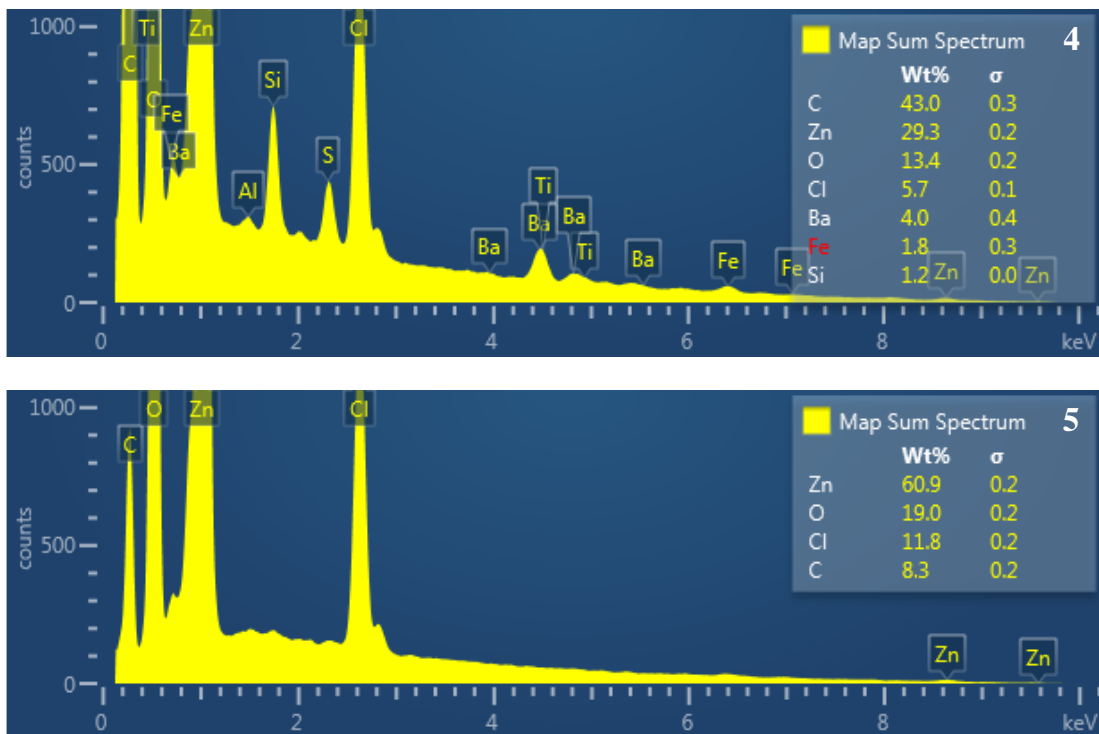


Figure 186. Secondary electron SEM image (left) and the results of EDS mapping (right) of an exposed panel of system 2 submerged in a cell for 408 hours. Results are shown in Fig. 187.



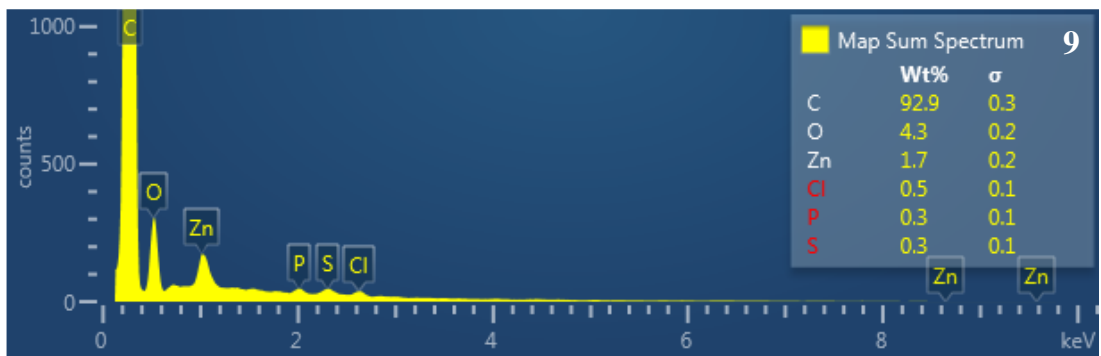
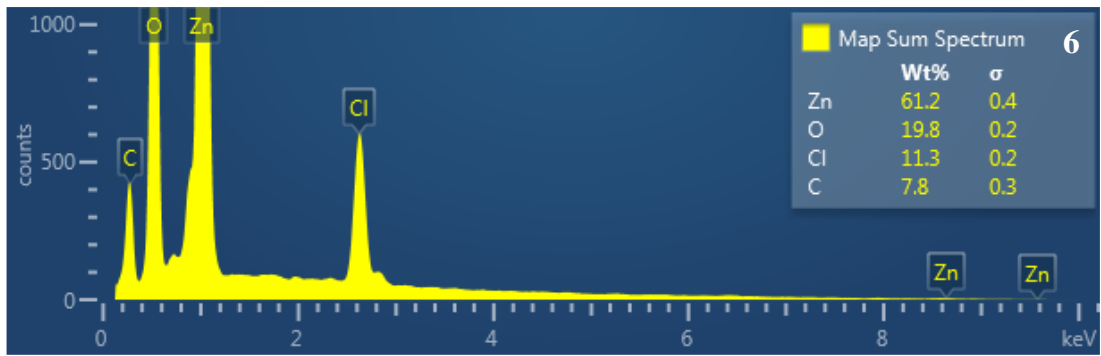


Figure 187. EDS spectra of an exposed panel from Fig. 186.

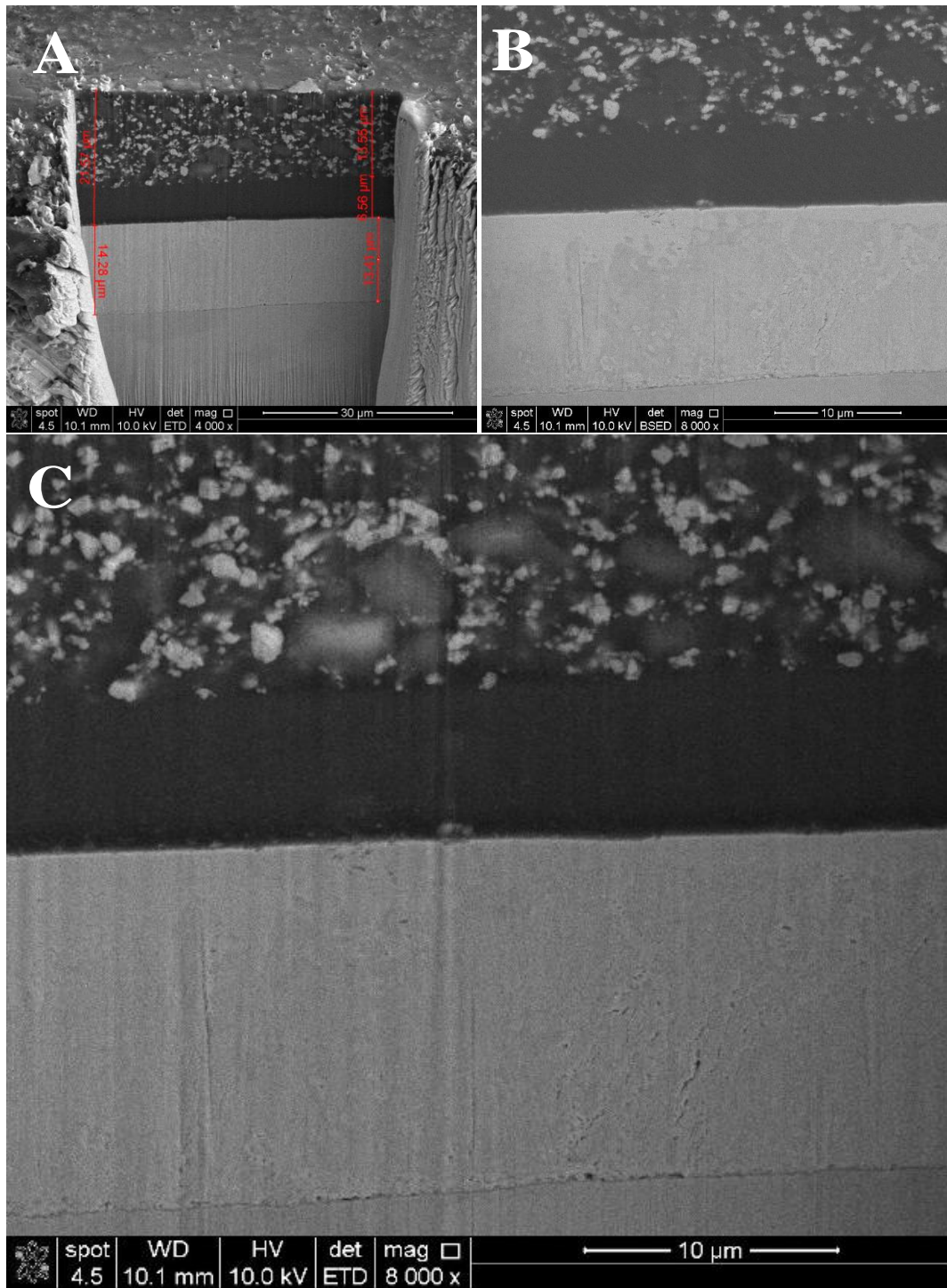


Figure 188. Secondary (a & c) & backscattered (b) electron SEM images of an exposed panel of system 2 submerged in a cell for 408 hours, area 2. Cross-sectioned area (a), BSED image of zoom in area (b) and SE image of zoom in area (c)

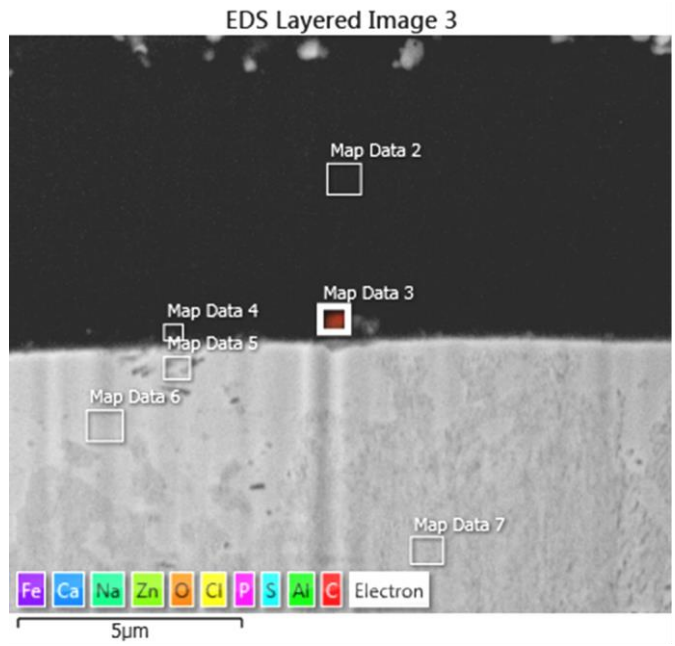


Figure 189. Secondary electron SEM image showing areas that was mapped.

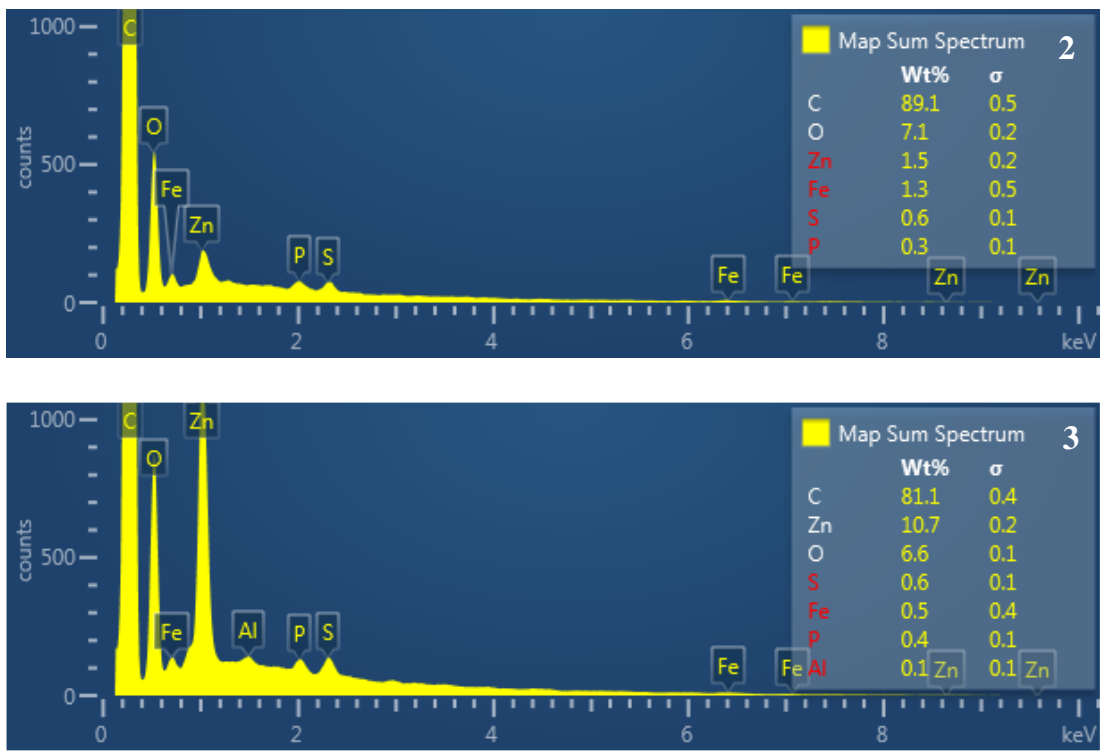


Figure 190. EDS spectra of analysed areas in Fig. 189.

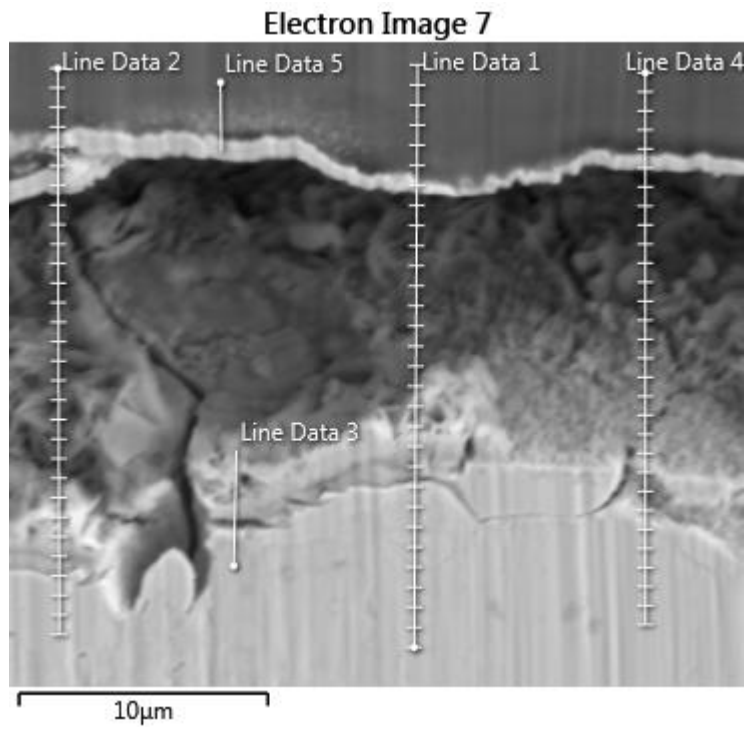


Figure 191. Secondary electron SEM image of system 2 submerged in a cell for 408 hours.



Figure 192. EDS line scan 2 of Fig. 191.

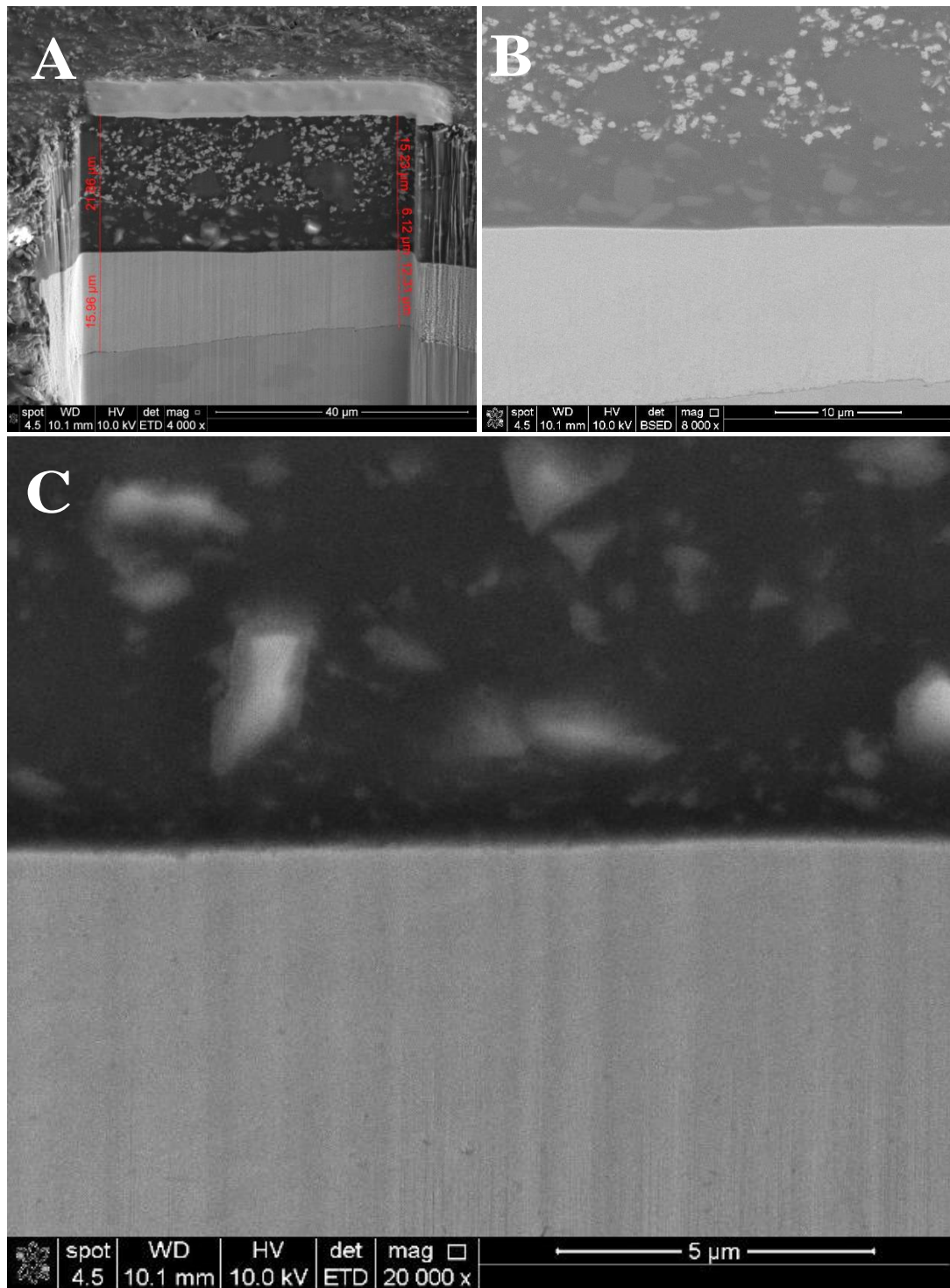


Figure 193. Secondary (a & c) & backscattered electron (b) SEM images of an exposed panel of system 3 submerged in a cell for 408 hrs. Cross-section of milled area (a), primer/ zinc interface (b) and another example of primer/ zinc interface (c).

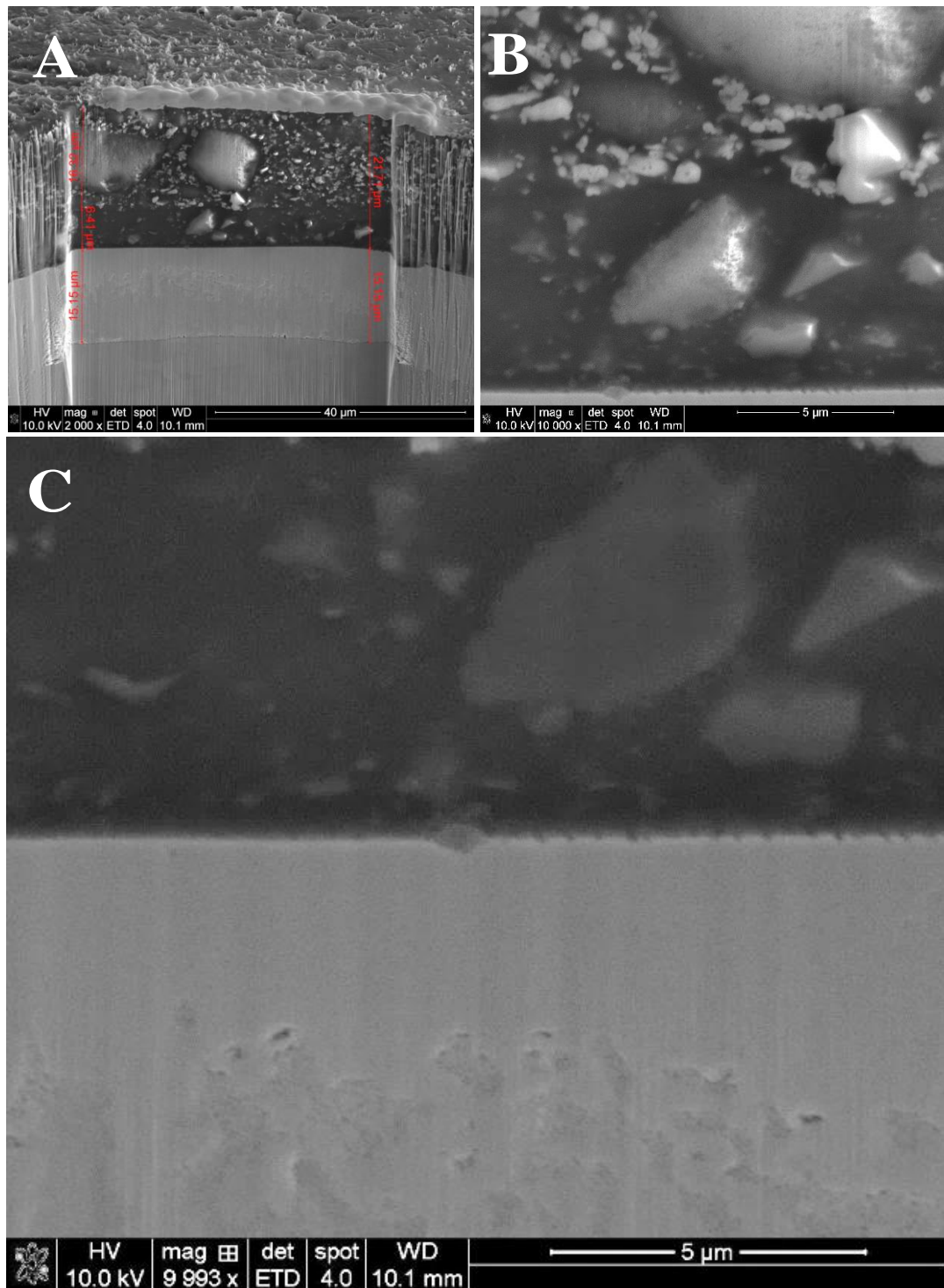


Figure 194. Secondary electron SEM images of an exposed panel of system 4 submerged in a cell for 408 hrs. Cross-section of milled area (a), topcoat/ primer/ zinc interface (b) and primer/ zinc interface (c).

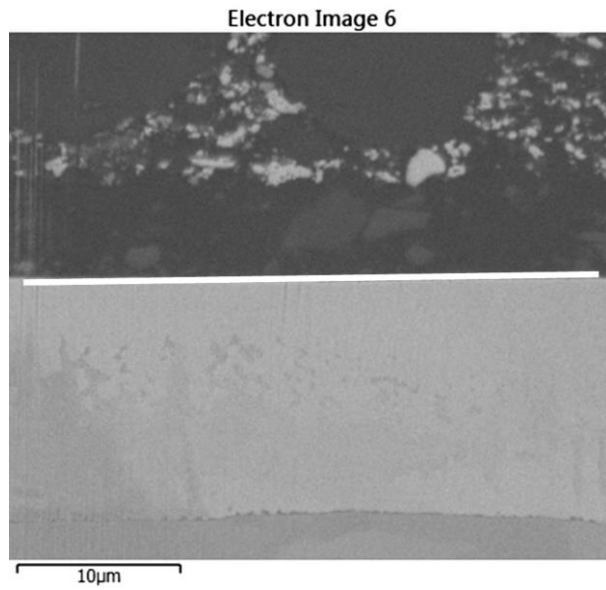


Figure 195. Secondary electron SEM image of primer and zinc area that was mapped at the primer/ zinc interface.

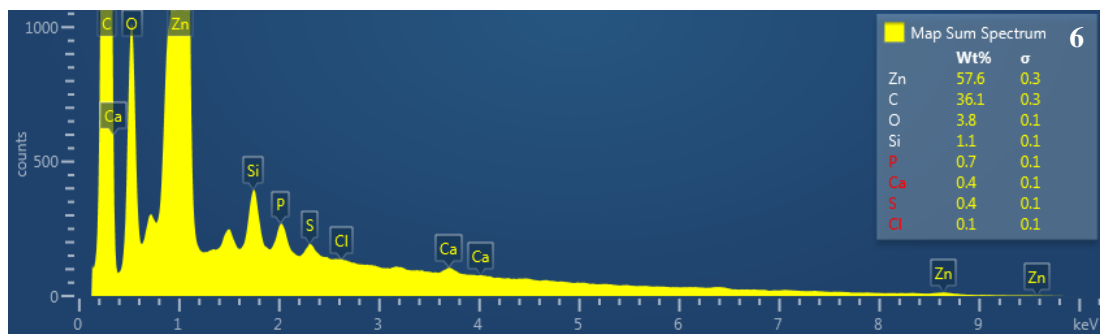


Figure 196. EDS spectrum results at the primer/ zinc interface of Fig. 195.